APR 2 2 1985

Ames 830-11-14

NAS 1.26: 3269

COMPLETED

ORIGINAL

NASA Contractor Report 3269

High Resolution Vertical Profiles of Wind, Temperature and Humidity Obtained by Computer Processing and Digital Filtering of Radiosonde and Radar Tracking Data From the ITCZ Experiment of 1977

Edwin F. Danielsen, R. Stephen Hipskind,
and Steven E. Gaines

CONTRACT NAS2-10023
APRIL 1980

MICROFILMED FROM
BEST AVAILABLE COPY

NASA

117

NASA Contractor Report 3269

High Resolution Vertical Profiles of Wind, Temperature and Humidity Obtained by Computer Processing and Digital Filtering of Radiosonde and Radar Tracking Data From the ITCZ Experiment of 1977

Edwin F. Danielsen
Beam Engineering, Inc., Sunnyvale, California
R. Stephen Hipskind
Oregon State University, Corvallis, Oregon
Steven E. Gaines
San Jose State University, San Jose, California

Prepared for
Ames Research Center
under Contract NAS2-10023

NASA
National Aeronautics
and Space Administration

Scientific and Technical
Information Office

1980

A

INTRODUCTION

Current concern with the affects of transport on atmospheric chemistry, in particular the ozone chemistry, have regenerated and strengthened interest in the mass exchange between the troposphere and stratosphere. It is well known from aircraft experiments (Danielsen, 1964; 1968), synoptic analyses (Danielsen, 1959; Reiter, 1963; Reiter and Mahlman, 1965; Mahlman, 1965 and others) and numerical model simulations (Mahlman and Moxim, 1978) that stratospheric air is intermittently transported into the mean troposphere by wave motions during cyclogenesis in extratropical latitudes. Although numerical estimates of the amount of mass leaving the stratosphere each year by this process vary considerably, there is general agreement that it is a significant fraction of the total stratospheric mass. There also is general agreement that the corresponding inflow of tropospheric air to the stratosphere occurs at lower latitudes. But it remains to be determined what percentage of the inflow is at tropical latitudes, and whether the physical process is predominately a zonal mean transport by the upward branch of the Hadley cells, or a combination of mean and wave or eddy transports.

The NASA-Ames Research Center's Inter-Tropical Convergence Zone (ITCZ) Experiment was organized to study tropospheric-stratospheric transport associated with the ITCZ by means of aircraft observations of several important trace species, including ozone, nitric oxide, water vapor, chlorofluromethanes and aerosols. Although the emphasis was on determining the mean transport rates, the experiment was designed to resolve spatial and temporal variations in some of these trace species and, in the meteorological variables, to objectively determine their existence and to reliably establish their frequencies, amplitudes and relative phase relationships. In support of this secondary objective the recording rates for several U-2 measurements were increased and special arrangements were made to permit high resolution determinations of the vertical profiles of temperature, relative humidity, ozone and the horizontal wind velocity.

This report deals specifically with the temperature, relative humidity and wind velocity profiles resulting from objective computer processing methods applied to digitally recorded radio-ozonesonde data. In particular, the wind velocities are derived directly from special radar tracking data, which eliminate the major sources of errors that limit accuracy of the conventional rawinsonde system. In addition, by having a completely independent set of tracking measurements the accuracy of the conventional measurements can be assesed. The accuracy of the computed winds can be directly determined, of course, but also from differences in the radiosonde computed heights and the radar heights, the less direct effects of systematic temperature and pressure errors can be estimated. These results are of major significance in the tropics because the height variations are small and the signal-to-noise ratio is easily swamped by the instrumental and/or data processing errors.

The experiment involved the cooperation of several governmental agencies whose technicians were asked to provide non-conventional data and/or special recording methods. It follows quite logically that difficulties would arise in the data recording and processing. Indeed, many were encountered. However, by persistent efforts and subtle detective work we overcame the obstacles and are proud of the final data set. There are unavoidable gaps in the processed data but the original objective has been met. Also, since the entire set of observations were digitally recorded at 1 or 2 per second, it was possible to design and apply low-pass digital filters to each variables' vertical profile. Most importantly, by subtracting these filtered profiles, i.e., by effectively applying narrow band-pass filters, individual wave modes can be isolated. Thus, for the first time, we can isolate examples of the Kelvin wave mode, the Rossby-gravity modes, etc., and compare their vertical wavelengths, amplitudes and phases to those dervied from perturbation theory.

Recognizing that meteorologists usually work only with processed data, we are presenting sufficient background and discussion to enable one to appreciate the unique advantages of this data set, and how these objective processing methods differ from conventional methods. However, to avoid a myopic preoccupation with details, many explicit steps have been eliminated. They will be supplied upon request.

RATIONALE FOR RADAR TRACKING AND DIGITAL RECORDING

In principal, radar tracking of a radiosonde balloon system has several advantages over the usual GMD-1 rawinsonde tracking. Because the radar transmits a short pulse of energy and measures the time for this pulse to go to and return from the target, it obtains a direct measurement of the slant range with minimum interference from refracted or reflected waves arriving later due to their increased path. The radar always points toward the most direct path to the target, slightly curved by a gradient in the index of refraction. On the other hand, the GMD antenna can err in its direction angles because it senses only the direction of maximum radio signal intensity, and this maximum can be the result of interference between a most direct ray and a more refracted or reflected ray. As shown by Danielsen and Duquet (1967), the seriousness of this interference error increases rapidly as the elevation angles decrease to 15 degrees or less. During the ITCZ Experiment the elevation angles remained larger, so interference did not produce serious errors, but the effects of interference can be demonstrated.

Another advantage of radar tracking (for this experiment the major advantage) is that the radar alone supplies a necessary and sufficient set of measurements for wind computations. Knowing the azimuth and elevation angles, plus the slant range from the radar to the target, one can directly compute the three-dimensional position of the target over the curved earth as a function of time. Then, by finite differencing the horizontal positions for a constant time interval, one can compute a time-averaged velocity. The difficulty with the GMD-1 is its lack of a slant range measurement. To determine the radiosonde transmitter's three-dimensional position over the curved

earth, it is necessary to compute the height from the radiosonde observations of temperature, relative humidity and pressure, and then use this height in combination with the measured azimuth and elevation angles. As will be shown, errors in pressure and temperature (especially errors in pressure) contribute to large height errors at high altitudes where the ambient pressure is low. If the measured pressure is too low, the apparant slant range is too large and the horizontal distance out is also too large. Since an error in the computed winds depends on relative errors in position, an increasing error in position is most serious. Such is the case when the pressure error is constant; then the percentage error increases as the balloon ascends to lower pressures.

In addition to the errors in the computed wind vectors, an error in pressure produces an error in the pressure or height to which the wind is assigned. Again, such phase errors tend to increase with decreasing pressure, increasing height. It follows that the geopotential heights and winds dervied from radiosonde-GMD-1 data are most accurate at low elevations and their accuracy degrades as the balloon ascends. For these reasons it has been standard practice to increase the finite differencing interval above the 7 km level. For example, at operational rawinsonde stations, the azimuth and elevation angles are recorded only once per minute. The successive positions are plotted graphically, and a two-minute average wind velocity is computed by central finite differencing. Above 7 km this difference interval is doubled, yielding a four-minute average wind. Because the balloon ascends at an average velocity of 5 m sec^{-1}, these time averaged winds correspond to a 600 m average below 7 km and 1.2 km average above 7 km.

Here, in processing the winds from the radar tracking data, we have used a constant 200 m average, for the following reasons. Based on precision radar tracking data from an FPS-16 radar digitally recorded at 20 times per second, Danielsen and Duquet (1967) showed that a 2 sec averaged wind resolved even the torroidal motions of the balloon. Power spectra analyses indicated these balloon-induced oscillations had periods ranging from 6 to 20 sec, perhaps extending to 30 or 40 sec. In general, there was a distinct minimum in the power or variance spectra from 40 to 60 seconds; therefore, to eliminate spurious oscillations caused by eddy shedding from the ascending balloon, it is convenient to use a 40-second difference in the wind computations. At an average ascent rate of 5 m sec^{-1} this corresponds to a 200 m difference in height. We changed the independent variable from time to height when we discovered that there were rather large systemmatic differences in the ITCZ Experiment's balloon ascent rates. These differences altered the effective vertical wavelengths of the digital filters, an alteration which is unacceptable. Ordering the data at a constant 5 m interval, by interpolating in the 1 second data, eliminated this balloon-dependent effect. Thus, the filters pass only those vertical wavelengths exceeding a prescribed wavelength.

Clearly, since the winds are derived from differencing position coordinates, relative errors in horizontal position are more important than absolute errors. However, to take advantage of the additional radar tracking capability, i.e., to use the radar

derived heights to assess errors in the radiosonde system, we must consider the absolute errors. The heights for the radiosonde are computed from the hydrostatic approximation and the equation of state for a mixture of ideal gases. Explicitly, the appropriate equation is

$$Z = Z_o + \int_p^{p_o} \frac{R}{g} T_v d(\ln p) \qquad (1)$$

where Z is the height at the pressure p, R is the specific gas constant for the mixture of diatomic molecules in dry air, g is the acceleration of gravity and $T_v = T(1 + .612\, X_v)$ is the virtual temperature, augmented by the specific humidity X_v to account for the reduction in mean density by the lighter-than-air water molecules. Here, X_v is expressed in grams of water per kilogram of moist air.

The appropriate value for R is 2.87×10^6 ergs $gm^{-1} deg^{-1}$, a constant. It is customary, also, in meteorology to treat g as a constant, 980 cm sec^{-2} and then to refer to Z as a "geopotential" height. On the other hand, the height determined from the radar is the geometric height. Thus, before direct comparisons are made the geometric must be converted to geopotential height, or vice-versa. Here we have made the former conversion and will then assess the errors in the geopotential heights in terms of errors in T_v and P. The full potentials of this method could not be realized in the ITCZ Experiment due to the limitations of the tracking radars and the difficulties the radar technicians encountered getting the radars on target for automatic tracking.

During the ITCZ Experiment we were fortunate to have the cooperation and support of the U.S. Army Signal Corps, who provided radar tracking of the ozonesonde balloons and the U-2 and Lear Jet aircraft. Two NIKE radars, normally used for rocket tracking, were made available for the experiment. However, they did not have a digital readout capability, so technicians from NASA-Wallops Island facility supplied portable digital recorders and made the necessary modifications and adaptations on site. Considering the inherent difficulties in this task and the time limitations they were very successful, but occasionaly the digitizers failed, producing some gaps in the tracking data.

Major delays in processing the data were caused by systematic errors in the radar's tracking measurements. Errors were detected in both angle measurements and in the slant range. Fortunately, by comparing the GMD-1 and radar tracking of elevation and azimuth angles for each balloon ascent over the complete set of ascents, the relative errors were determined as a function of time. Then from a few cases, where both radars were simultaneously tracking the same balloon or the same aircraft, reasonable absolute errors could be assigned to both radars and to the GMD. The most troublesome and least understood errors were in the radar's measurements of the slant range. The simultaneous tracking data sets indicated unusually large errors in slant range which remained constant during each flight but which differed from flight to flight. To overcome this problem we were forced to reverse our logic and use the radiosonde-determined heights to determine the error in slant range for each balloon ascent.

The effects of this reversal in logic are not as bad as they would appear to be. We used only the first minute of radar tracking data, after we were sure the radar was on target, to calibrate the radar slant range. Because it took some 6 to 10 minutes to get the radar on target, the calibration minute corresponds to pressures of 700-600 mb. In this pressure range the radiosonde heights are quite accurate with standard errors of about 10 to 20 m. As will be shown, the errors increase with height to hundreds, even to thousands of meters, so the initial calibration does not preclude the higher altitude error determinations.

Finally, to provide tracking data for the entire ascent and, therefore, to permit computations of the complete wind velocity profiles, we transformed the GMD tracking angles to the radar site, eliminating the parallax errors, and converted the radiosonde heights to an equivalent slant range from the time of balloon release until the calibration minute. The justification for this extension of the data comes from the excellent correspondence between the GMD-1 and radar tracking measurements at the generally large elevation angles which occurred during the experiment. Before presenting and discussing the results we will breifly outline the logic used to prepare and process the data, including the relevant equations.

DATA PREPARATION

The radar tracking data were digitally recorded at a rate of 2 per second, but since two radars were usually in operation the data from the two were alternately recorded on one channel. This alternation reduced the data rate for most ascents to 1 per second, so this rate was accepted as standard. Data preparation included correcting for systematic errors in azimuth and elevation angles and a special correction for slant range, which was determined by the computer after the radiosonde data were prepared and processed. In view of the dependence on the radiosonde data, we will defer the slant range calibration discussion and focus first on the radiosonde data preparation.

Because of the time constraints, the most practical operational procedure was to attach the ozone instrument to the balloon train and to use the radiosonde's radio transmitter for both sets of measurements. This means that 8 different signals are transmitted in 4 to 16 second bursts, in a semiorganized sequence, and all data could be recorded on one channel. Obviously, the system was not designed for digital recording and computer processing. Nevertheless, we were stuck with these limitations or no digital recording at all. We accepted the challenge to unscramble the data.

The first step was to develop a logic for separating the ozone data from the radiosonde data. In this discussion the following symbols will be used for the 8 separate frequencies.

OZONE DATA	RADIOSONDE DATA
OZZ - Ozone zero	RTF - Radiosonde temperature
OZC - Ozone calibration constant	RHF - Radiosonde humidity
OZB - Box temperature	RLR - Low reference
OZF - Ozone signal	RHR - High reference

Under normal operations the radiosonde data are transmitted sequentially in an order determined by a mechanical baroswitch. There are some 150 switches from RTF to RHF

or from RTF to RLR or RHR in the $1\frac{1}{2}$ to 2 hours it takes for the balloon to reach its maximum altitude, or about 36 seconds per contact. Usually the RTF is transmitted for six-tenths of this time and the other for four-tenths. Again, it must be stressed that the system is designed for manual-graphical readout and processing which accounts for the long transmission times for each signal. But, of course, when only one signal is transmitted at a time there are large data gaps in each signal's trace. In graphical processing, the operator visually ignores these gaps by following the trends of the recorded segments. Here, we must fill the gaps after the data are separated.

Adding the transmission requirement of the ozone instruments increases the number and, to a lesser degree, the duration of data gaps. Transmission of the ozone data is controlled by a battery-driven commutator which interrupts and overrides the radiosonde's baroswitching. A complete cycle takes about 128 seconds and includes 9 four-second bursts of ozone data: 1-OZZ, 1-OZC, 1-OZB and 6-OZF's with the intervening radiosonde data bursts ranging from 8 to 16 seconds. Being battery-driven and mechanical, the cycle times were not constant; therefore, the computer algorithm had to include a method for determining the individual cycle periods.

The method for determining periods is based on filtering the data with three comparatively narrow frequency gates, which pass only the slowly-varying OZZ, OZC and OZB signals, followed by a systemmatic contraction and expansion of the time gates to minimize the number of nonzero entries from those three ozone signals. All frequencies recorded within the OZF's time gates are then stored without applying an OZF frequency gate since this signal can vary more rapidly. The remaining frequencies are then considered to be radiosonde data and the problem remains to separate the four types of signals.

First, narrow frequency gates are derived to isolate the RLR and RHR, reference signals. By referring to the ozone time gates, all gaps in RLR and RHR are filled by linear interpolation. Then using the prescribed sequence of alteration between RLR and RHR the individual contacts are numbered and checked against initial and final contact information coded from visual inspection of the recorder trace. From contact 5 to contact 135 in multiples of 5, these reference frequencies are preceded and followed by RTF unless the ozone data interfere. Using the means of these RTF signals, the trends in the temperature frequencies are determined and these trends are used to establish frequency gates to isolate RTF. Then all remaining frequencies are stored in RHF. For all contacts greater than 135, humidity frequencies are no longer transmitted and the transmission alternates between temperature and reference frequencies which are easily separated.

Next, the RHR's, which are transmitted only to aid the operator visually identify certain contact numbers, are converted to RLR's, and then the contacts which are not divisible by 5, between the first and No. 135, are identified and numbered. The identification is based on a change from RTF to RHF. Where an ozone signal interfers with this change the contact is assigned to the center of the four-second interruption.

Finally, the reason for identifying and numbering the contacts is to determine the pressure versus time. From a pressure calibration chart, the pressure is known only when each contact is actuated. No other pressure data are available. To complete the data preparation all of the gaps must be filled and spurious signals eliminated. Spurious signals can occur if the counter is active while the frequency is switching, and when the signals are weak or noisy.

The methods used to identify spurious signals and to fill data gaps depends upon the expected variability of the signal and the number of data points in a given data burst or interval. For slowly-varying frequencies, such as OZZ, OZB, OZC and RLR, the mean and standard deviation σ are computed for each interval. Points whose deviations exceed 3σ are rejected, new means are computed and linear interpolation is used to fill the gaps between the means. For more rapidly-varying frequencies, such as OZF, RTF and RHF, a linear root-mean-square, RMS, fit and σ are computed if the data contain less than or equal to 8 data points (4 seconds). Again, points whose deviations exceed 3σ are rejected, the linear RMS fit is recomputed and then the value of the central frequency and its derivative are used to interpolate across the gap with a cubic interpolation function. Thus, f and $\delta f/\delta t$ are continuous from data burst to data burst.

The remaining gaps in RTF and RHF, which now exceed 8 data points, are first fitted by a cubic RMS function. Next, the value of f and $\delta f/\delta t$ at 0.5 sec from the data intervals' boundaries are used to provide continuity for a cubic interpolation formula. Finally, the pressures are interpolated from the contact versus time data by linear interpolation in lnp. This completes the ozone-radiosonde data preparation which yields a 10-column matrix including: TIME·INDEX·OZZ·OZF·OZB·OZC·RTF·RHF·PRESSURE·σ.

The methodology for this data preparation was written by E. Danielsen and programmed by Steve Gaines. Steve is commended for his careful and painstaking efforts which successfully unscrambled what first appeared to be a hopeless maze of data.

Two consecutive examples of the computer-generated plots of the separated and interpolated data are presented in Figures 1 and 2. Note that decreasing RTF corresponds to decreasing temperature, but decreasing RHF to increasing relative humidities. In these figures the slow but persistent drifts in the calibration frequencies are evident as is the large variability in RHF. Note the general increase in relative humidity during the six hours implied by the decrease in RHF's. These two figures illustrate also the large differences in ascent rates (compare the elapsed time to contact 150 or 155).

At this point we can return to the radar data preparation. The difficulties here are to identify and reject spurious data, to interpolate across data gaps when the digitizer failed and to determine the systemmatic tracking errors. That the latter existed and were large was evident when the radar and GMD tracking angles were plotted as a function of time on the same diagram. In Figure 3, for example, the two traces are almost parallel while the elevation angle varied from approximately 30 to 70°, but are systemmatically offset. The difference angle, plotted on an expanded scale to the right, includes a systemmatic offset of approximately 0.7° which increases to approximately 1.0° due to parallax. Superimposed on these combined effects are high frequency

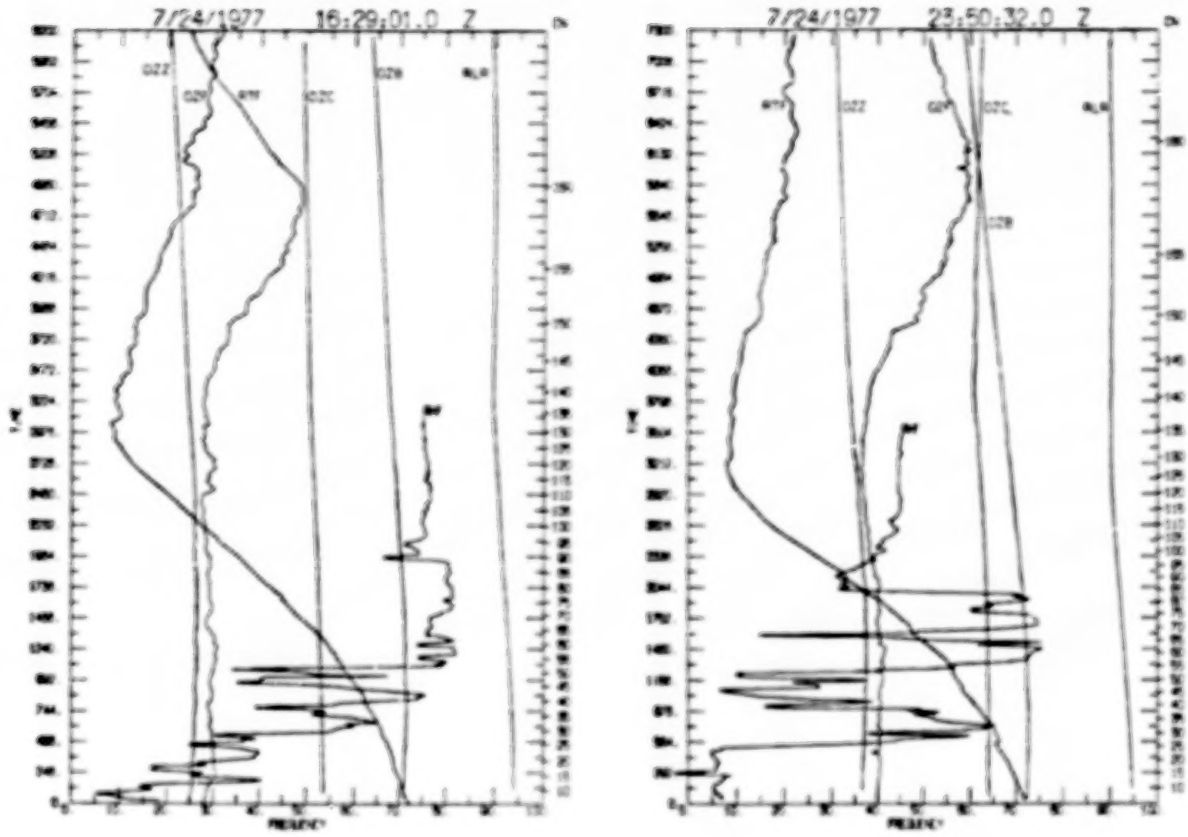

Figures 1 (left) and 2 (right). Ozonesonde and Radiosonde frequencies separated and interpolated. See text for symbols.

oscillations which come from the GMD tracking data. These are the fluctuations produced by interference between direct and refracted (or reflected) rays, referred to earlier. Notice that their amplitudes are less than or equal to 0.2^{O} in this example.

Systemmatic errors in azimuth angles can be identified in Figure 4. Here the GMD trace in the left diagram has been offset by 2^{O} to provide a visual comparison of relative tracking accuracy. Again, the relative tracking capability is excellent. All significant variations are reproduced. The actual angle differences plotted to the right include a systemmatic difference of approximately 0.2^{O} which varies from $+0.5$ to -0.5^{O} due to parallax. From these data one could deduce that the GMD was located to the NNE of the radar. Comparing the right diagrams of Figures 3 and 4, it is clear that the interference effects are not as large nor as organized in the azimuth as they are in the elevation angles.

To determine whether the systemmatic differences in azimuth and deviation angles were constant through the experiment, separate plots like Figures 3 and 4 were made for each balloon flight. From these plots it was determined that the calibration of the northern radar, hereafter referred to as Radar No. 1, was changed twice. After the

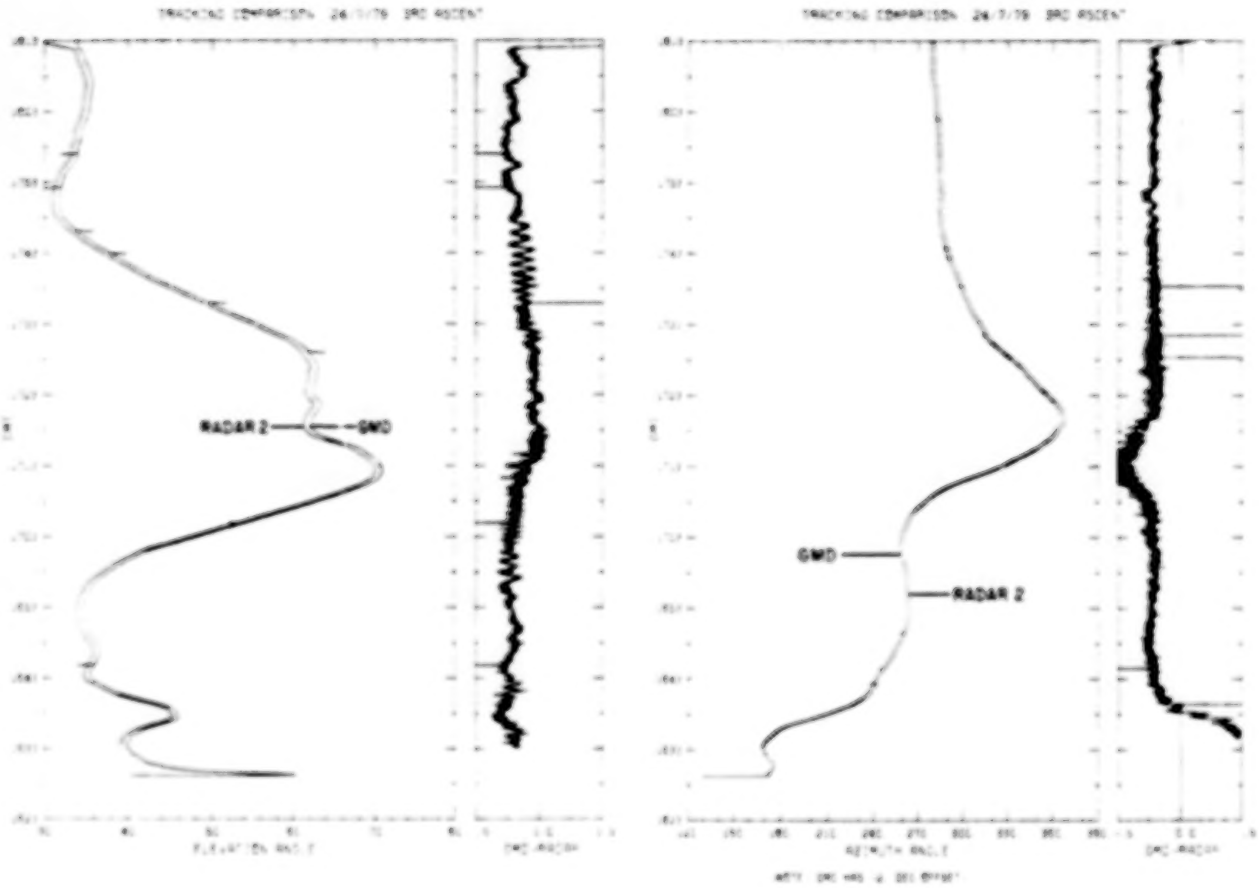

Figures 3 (left) and 4 (right). Tracking angle comparisons between GMD-1 and Radar 2.

first flight or the 16th the azimuth angle was adjusted by 3.3°, and after the second flight on the 18th the elevation angle was adjusted by 0.66° to agree with Radar No. 2. No adjustements were made to Radar No. 2 and this radar was finally judged to be most accurately calibrated. The GMD calibration for elevation angles was changed on the 30th after it was recognized that a sudden jump of approximately 1° had occurred during the first flight. The effect of this jump is evident in Figure 5 where the elevation angle difference between the GMD and Radar 1 is approximately 1.6°. For this flight only, both radars and the GMD were tracking the radiosonde target. In the left diagram, Radar 2's data were offset by -1° to permit visual comparison. Without this displacement Radar 1's trace overlaps that of Radar 2. Consequently, the difference plot GMD-Radar 2 would also overlap the righthand plot. These simultaneous measurements confirm the conclusion that the oscillations are in the GMD trace, not in the radar tracking. Again, we see the amplitudes are less than or equal to 0.2°.

Having established the relative errors between the three systems, it was still necessary to assess the absolute errors. Obviously only one set of errors had to be assessed

and then all others could be computed from the relative errors. The final judgement was based on the stability of the Radar 2 measurements and the fact that the GMD could be calibrated only to an accuracy of $\pm 2^{o}$. The following corrections were therefore added to all measurements prior to data processing:

Elevation Angle Corrections

Radar 2	$\Delta\epsilon = -0.35$
Radar 1	$\Delta\epsilon = +1.03$ thru 18th
	$\Delta\epsilon = -0.375$ 19th-31st
GMD	$\Delta\epsilon = -1.15^{o}$ thru 29th
	$\Delta\epsilon = -2.125$ on 2nd & 3rd flights on 30th
	$\Delta\epsilon = -0.14$ 31 July

Azimuth Angle Corrections

Radar 2	$\Delta\alpha = 0$
Radar 2	$\Delta\alpha = -2.5^{o}$ for 1st & 2nd flight on 16th
	$\Delta\alpha = +0.823$ for all remaining flights
GMD	$\Delta\alpha = +0.20$

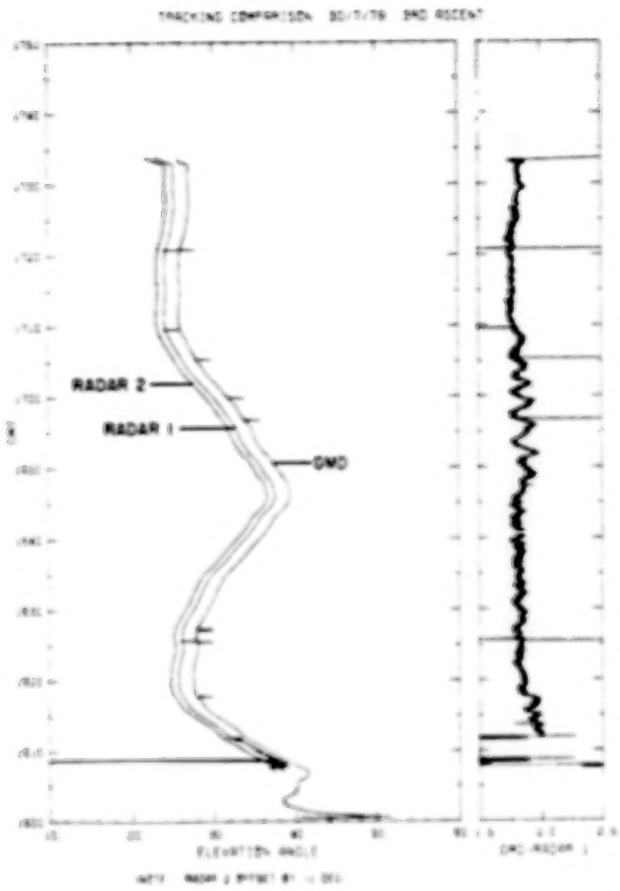

Figure 5. Tracking angle comparisons between GMD-1 and Radars 1 and 2.

Finally it was necessary to determine the accuracy of the slant range measurements, and this was not an easy task. Initially we were told that there were no slant range errors. However, when the heights computed from the radar were compared to those computed from the radiosonde, it was obvious that the differences greatly exceeded the errors in the radiosonde. Communications with the radar technician produced systemmatic errors which had inadvertently been overlooked. Further work revealed that these errors were off by an order of magnitude, but still the data were inconsistent from flight to flight. At this point we turned to the aircraft tracking data, selecting all examples when both radars tracked the same aircraft. On the basis of these simultaneous tracking sets it was determined that the slant range measurements were inconsistent but that the relative range error remained almost constant during each flight. Most of these tests involved low elevation angles, therefore, the distances-out were not sensitive to errors in the elevation angles.

Because the slant range errors held constant during each flight but varied from flight to flight, we decided to use the first minute of reliable radar tracking data to calibrate the

slant range for each balloon ascent. Reference to Figures 3 to 5 indicates that approximately ten minutes elapse before the radar is on automatic tracking. For the earlier ascents, approximately 20 minutes were required by the radar operators to find the target - so the calibration minute is always at altitudes where the radiosonde accuracy is of the order of ±20m. All subsequent height errors exceeding these limits can be determined.

DATA PROCESSING: RADIOSONDE AND RADAR DATA

The radiosonde temperature and relative humidity frequencies are first corrected for frequency drift, determined by the change with time of the low reference frequency. Then the temperatures and relative humidities are computed from the equations supplied by the radiosonde manufacturer. Details of the method will be supplied upon request. Having determined the temperature, the computer uses the Smithsonian Tables water vapor equations to determine the saturation pressure over a water surface. Multiplication by the relative humidity yields the actual vapor pressure. Then the specific humidity X_v is computed and used to calculate the virtual temperature.

$$T_v = T(1 + .612X_v) \tag{2}$$

where T is expressed in ^{o}Kelvin and X_v in grams kgrams^{-1}.

The following potential temperatures are computed also:

1. Potential Virtual Temperature θ_v

$$\theta_v = T_v\left(\frac{1000}{p}\right)^{.286} \tag{3}$$

where p is the total pressure.

2. Equivalent Potential Virtual Temperature θ_{ve}

$$\theta_{ve} = \theta_v \exp\left[\frac{X_v L}{c_p T_c}\right] \tag{4}$$

where T_c is the condensation temperature, the latent heat L is a function of T_c and c_p is the specific heat at constant pressure. A special numerical method for computing T_c was developed for these computations which yields excellent accuracy in two steps. Convective instability, so important in the tropics, is determined from the vertical derivative of θ_{ve}. Instability is present when this derivative is negative.

The geopotential heights, of course, are computed from (1). Because the data are at a constant 0.5 second interval, a linear mean of T_v is sufficiently accurate for each integration step. Again we stress that these heights are geopotential not geometric heights.

The radar data require special treatment. Occasionally, when the digitizer failed, zeros were recorded for azimuth, elevation and slant range, or values somewhere between

zero and the proper signals. To identify these, the second differences are first computed and then the standard deviation of these second differences. Values exceeding 3σ are then examined for successive sign changes. When data gaps are identified they are filled by linear interpolation. In a few cases exceptionally noisy data segments proved to be too difficult to correct by objective computer methods, so special manual adjustments were necessary. All corrections are indicated in the printout.

After the radar azimuth and elevation corrections are made the slant range correction is evaluated. For each second of the 1 minute calibration segment the geopotential heights of the radiosonde are converted to geometric heights and these heights and elevation angles are used to compute the slant range from

$$r = -R_e \sin\epsilon + \sqrt{(R_e \sin\epsilon)^2 + (Z^2 + 2R_e Z)} \qquad (5)$$

where R_e is the radius of the earth and Z is the geometric height above sea level (see Figure 6). The observed radar slant ranges are subtracted from these computed values and the mean value is used to correct all radar slant range measurements for that particular balloon ascent.

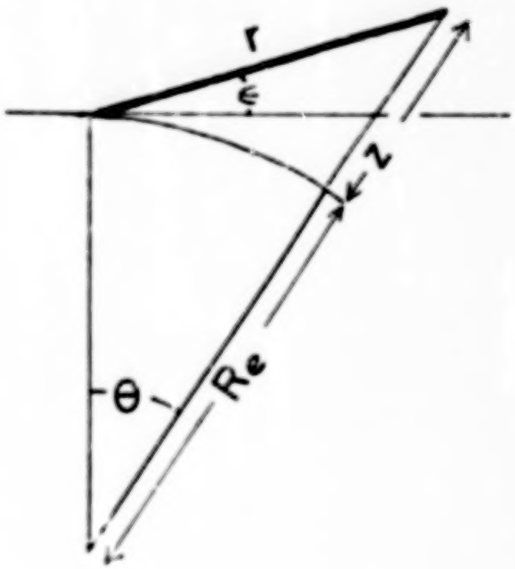

Figure 6. Slant range r as a function of height Z and elevation angle ϵ. R_e is the radius of the earth.

From the time of the balloon release until the time of the calibration minute the missing radar measurements are supplied from the radiosonde measurements. To assure continuity in the measurements at the interfacial time, the GMD tracking angles are calibrated by transforming the radar angles, during the minute overlap, to the GMD site removing the parallax effects. Subtracting these transformed angles from the GMD angles provides a correction for the latter. Generally, these corrections are small, less than or equal to 0.2°. Again, the values used are printed out for each ascent. After these corrections are determined the radiosonde heights and elevation angles are used to compute slant ranges, then these and the azimuth and elevation angles are transformed to the radar site to complete the radar data set.

At this stage the data are ready for filtering with time as the independent variable. The filters to be discussed in the next section were initially designed as low-pass filters with their 50% transmission at 0.5, 3 and 9 minutes. For the reason discussed earlier we changed from time to height as the independent variable. Thus, instead of ordering

the data, including the height at 1 second intervals, the data and time are ordered at 5 m intervals. Having established a complete set it is a simple matter for the computer to determine the geometric height from the elevation angle and slant range

$$Z = R_e\left[\left(1 + \frac{2r\sin\epsilon}{R_e} + \frac{r^2}{R_e^2}\right) - 1\right] \tag{6}$$

and the distance out over the curved earth

$$D = R_e\theta = R\left[\cos^{-1}\left(\frac{\cos\epsilon}{1+\frac{Z}{R_e}}\right) - \epsilon\right]$$

where θ is defined in Figure 6.

FILTER DESIGN AND APPLICATIONS

In keeping with our objective to detect wave modes in the ITCZ data, and to be able to study their amplitudes and phase relations in the height rather than the vertical wave number domain, we have designed several low-pass, non-recursive filters and applied them to each of the computed variables. To significantly reduce any aliasing, the response of each filter is designed to closely approximate the desired response illustrated in Figure 7. Here $k = 2\pi/L$ where L is the vertical wavelength and L_D is the grid distance or vertical distance between successive data points. For our filters L_D is greater than or equal to 5 m, the minimum grid distance.

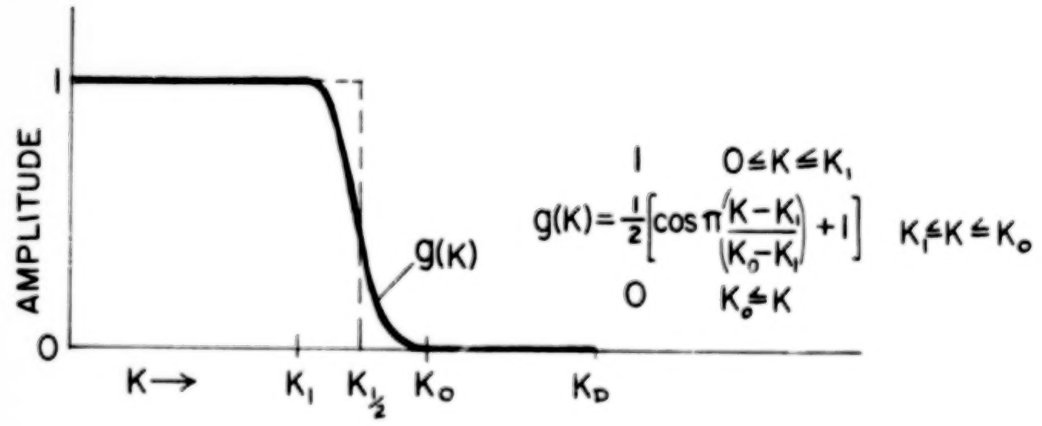

Figure 7. Response function for digital low-pass filter.

Each filter will be identified by the wavelength associated with the 50% response which corresponds to $k_{1/2} = \frac{k_0 + k_1}{2} = \frac{2\pi}{L_{1/2}}$

Applying two filters with $k_{1/2}(1)$ greater than $k_{1/2}(2)$ and subtracting the output of the second from the first is equivalent to applying a band-pass filter as illustrated in Figure 8.

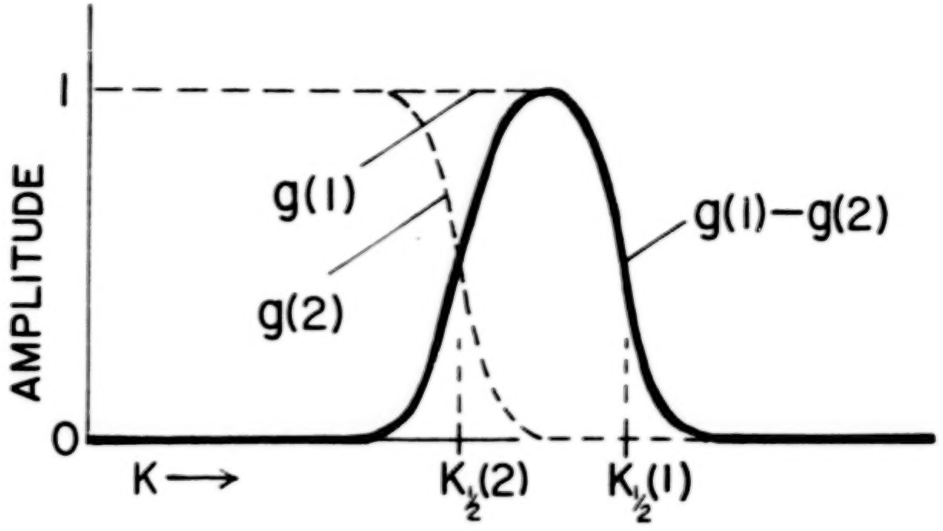

Figure 8. Band-pass filter derived from two low-pass filters.

The width of this band-pass depends, of course, on the difference between $k_{1/2}(1)$ and $k_{1/2}(2)$ and upon the width of the transition zone k_0-k_1 for each filter. As will be shown, reducing the width of the transition zones tends to increase aliasing because the actual response for a filter with finite number of weights oscillates about the desired response. To reduce the aliasing it is then necessary to increase the number of weights, which increases the distance required for the filter.

When the filter is applied to 2N+1 data points the filtered value at height index j_0 is given by

$$\bar{X}(j_0) = f(0)X(j_0) + \sum_{j'=1}^{N} f(j')\left[X(j_0+j') + X(j_0-j')\right] \tag{8}$$

where $j'=j-j_0$. The weights $f(j)$, normalized by $\sum_{j=-N}^{N} f(j) = 1$, are derived from the Fourier transform of $g(k)$, see Figure 7.

$$\begin{aligned} f(Z) &= 2\int_0^{\infty} g(k)e^{-ikZ}dk \\ &= \frac{\sin k_0 Z + \sin k_1 Z}{\pi Z\left[1 - \left(\frac{k_0-k_1}{\pi}\right)^2 Z^2\right]} \\ &= \frac{2}{\pi}\left[\frac{\sin\left(\frac{k_0+k_1}{2}\right)Z}{Z}\right]\left[\frac{\cos\left(\frac{k_0-k_1}{2}\right)Z}{1 - \left(\frac{k_0-k_1}{\pi}\right)^2 Z^2}\right] \end{aligned} \tag{9}$$

The first bracketed term is the Fourier transform of a step function, the step being located at $k = (k_0+k_1)/2 = k_{1/2}$, see the dotted line in Figure 7. The transform $(\sin k_{1/2}Z)/Z$ represents a damped oscillation with its maximum amplitude at $Z = 0$. The weights corresponding to this term will oscillate in sign and damp in magnitude away from the central point of the filter. As $k_{1/2}$ increases, the relative importance of the central weight and its closest neighbors also increases, so the total number of weights can be decreased accordingly. However, when $k_{1/2}$ is small, as in most of our applications, excessively large numbers of weights are required for such a step-type filter.

The second bracketed term determines the effects of the finite transition zone. As k_0-k_1 increases, the square term in the denominator eventually dominates and then rapidly reduces the magnitude of all subsequent weights. Therefore, increasing the width of the transition zone permits a reduction in the number of weights for a given threshold of aliasing, but it decreases the slope of the filter response at $k_{1/2}$. Generally, one must compromise and increase k_0-k_1 as $k_{1/2}$ decreases to avoid use of excessive numbers of weights. On the other hand, if the number of weights is kept constant as $k_{1/2}$ decreases then k_D must also decrease, i.e., the data interval increases by reducing the density of points. The effect is much the same as before but fewer computations are required.

Changing the independent variable from height Z to the index j eliminates the height interval L_D in all terms except the linear term in the denominator of the first bracket, thus (9) becomes

$$f(jL_D) = \frac{2}{\pi L_D}\left[\frac{\sin\frac{2\pi j}{M}}{j}\right]\left[\frac{\cos\frac{\pi j}{T}}{1-\left(\frac{2j}{T}\right)^2}\right] \qquad (10)$$

where M is the number of data (height) intervals between $L_{1/2}$ and L_D, and T is the number of intervals between the effective transition wavelength L_T and L_D. This effective wavelength is defined by $L_T = L_0L_1/L_1-L_0$ and it approaches infinity when L_1 and $L_0 \longrightarrow L_{1/2}$. From (10) we can see that the normalized f(j) will be independent of L_D. Therefore, the weights for a given filter depend on M, T and N. If these three quantities are held constant, increasing L_D increases the wavelength at the 50% response and spreads the transition zone over a larger wavelength range.

For the first three filters illustrated in Figure 9 the data interval $L_D = 5$ m is kept constant and the number of weights $n = 2N+1$ is increased a $k_{1/2}$ is decreased. Filter No. 1, which passes the largest wave numbers, shortest vertical wavelengths, has M = 30, T = 37.5 and N = 90. Filter No. 2 has M = 180, T = 140.6 and N = 162. Filter No. 3 has M = 540, T = 500 and N = 453. Since $L_D = 5$ m, the wavelengths corresponding to the 50% response are $L_{1/2}(1) = 150$ m, $L_{1/2}(2) = 900$ m and $L_{1/2}(3) = 2.7$ km. At an average ascent rate of 5 m sec^{-1} these correspond to 30 second, 3 minute and 9 minute filters. These filters are applied to the primary data sets, then the secondary

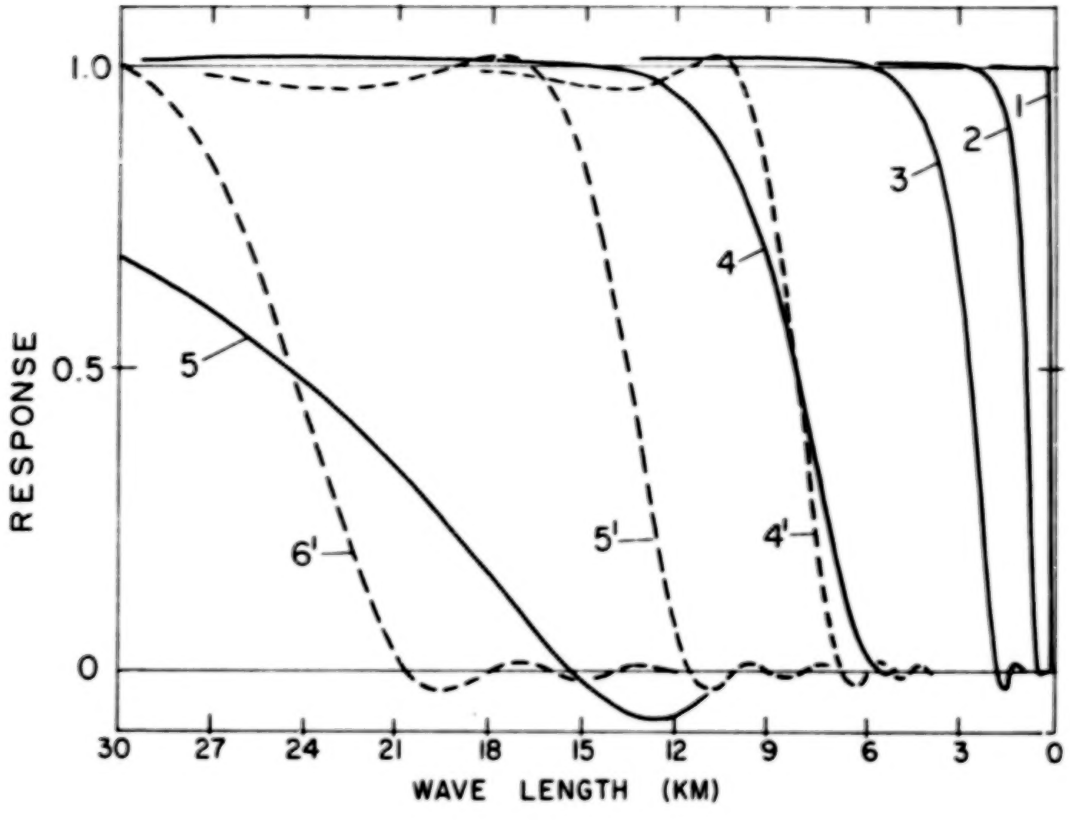

Figure 9. Actual filter response for the low-pass filters used in data processing.

data are computed from the filtered values. For example, the winds are computed from the finite differences between filtered positions and filtered times corresponding to ±100 m. This means that all reported winds are finite differences over 200 m or approximately 40 seconds.

After studying many of the plotted profiles of the filtered wind components, including the band-pass profiles, it seemed desirable to extend the filtering to still longer vertical wavelengths. In particular, the midpoint wavelengths were increased to 8.1 and 24.3 km, to determine whether the Kelvin wave could be separated, and to determine its vertical wavelength. Decreasing $k_{1/2}$ to such low values increased M from 30 to 1620 and 4860 for Filters 4 and 5. To avoid using correspondingly large numbers of weights we reduced M by a factor of 20, by increasing L_D to 100 m, and then limited N to less than or equal to 149. Despite the rather poor filter response of the 8.1 and 24.3 km filters (see Figure 9), the results were rewarding and we will discuss them briefly. Also, they stimulated further refinements of the long wavelength filters, including the introduction of another filter with the 50% response at 13 km. The response for these three filters, Nos. 4', 5' and 6', are plotted as dashed lines in Figure 9. Being much steeper than Filters 4 and 5, they also oscillate more around 0 and 1.

Before discussing the results we want to credit Steve Hipskind for an excellent job of writing the computer codes for processing the radiosonde and radar data and for writing all of the plot codes.

PRESENTATION AND DISCUSSION OF RESULTS

A total of 40 soundings were processed and plotted for this report. As indicated earlier, failures of the digitizers were responsible for most of the omissions. A few cases were omitted because of erratic radar slant range measurements which produced erroneously large winds and balloon ascent rates. Using the third sounding on 24 July as an example, Table 1 reproduces the first 50 lines of the computer output from Filters 1 to 3. The results are printed at a constant height interval of 100 m. These results are stored on a disk at Ames Research Center and will be made available upon request. Note that the last column gives the ascent rate of the balloon, averaged as are the winds over a 200 m interval. The fourth column gives the geopotential height error between the radar and the radiosonde computations. Figure 10 shows the two heights as a function of time and the differences plotted to the right. In this example the height accuracy of the radiosonde is quite good from the surface to 25 km. Above this height the errors increase rapidly to about 1 km at 35 km. Errors 2 to 3 times this large were found in some ascents and these were attributable to errors in pressure. A more complete analysis of the height errors is possible, time permitting.

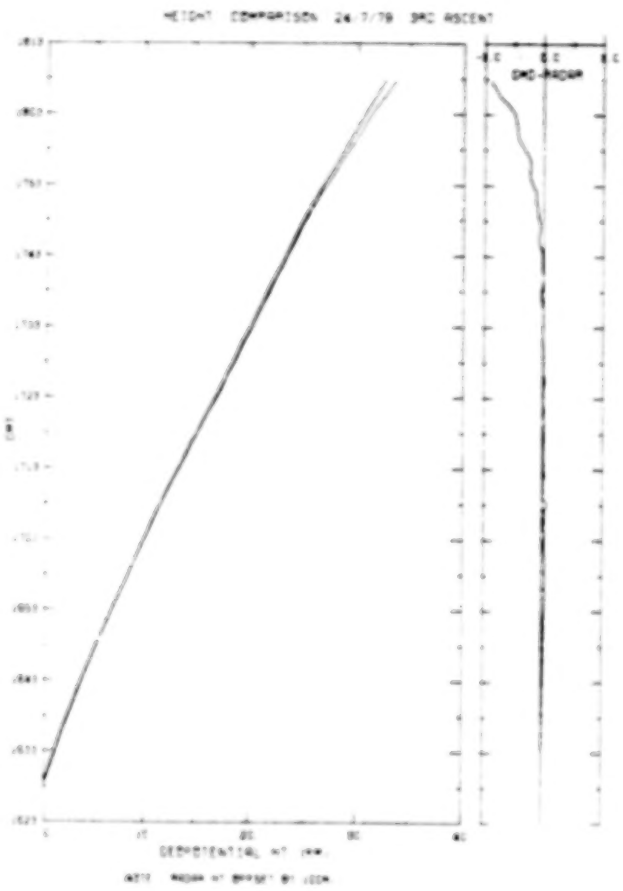

Figure 10. Error in geopotential heights computed from radiosonde.

An example of the filtered profiles is presented in Figure 11, left and right pages. Starting with the upper left side, the profiles from the low-pass Filter No. 3 are plotted across the page. The profiles include Relative Humidity, Temperature, Zonal Wind, u component and Meridional Wind, v component. Winds from the west and south are positive in these plots. Along the second row on the left, profiles of the 0.9-2.7 km band-pass are plotted against the same height scale, but with appropriate changes in the scales on the abscissa. At the lower left, the band pass components are added to the Filter No. 3 profiles to show the relative amplitudes and how the waves add structure to the profiles.

0.5 MIN FILTER APPLIED TO PANAMA DATA 7/26/1977

Z(M) A100		UT MIN	Z(SFC) GPUT/M	DELZ GPUT/M	PP (MB)	TEMP (C)	MM	R (MM)	AV (G/KG)	TV (K)	THV (K)	THVE (K)	WD (DEG)	WS (M/S)	U (M/S)	V (M/S)	W (M/S)
0	16	29 0	0.00	0.00	1005.20	28.20	83.00	32.511	20.366	305.10	304.65	334.83	340.00	2.00	.00	-1.00	
1	16	29 35	99.42	-.00	993.96	25.70	92.37	30.513	19.319	302.39	302.91	334.20					
2	16	29 54	199.61	.01	982.82	25.18	93.44	30.751	19.565	301.90	303.40	333.48	334.18	3.09	.07	-3.04	0.31
3	16	30 21	299.41	.01	971.77	24.21	91.99	29.125	19.249	300.93	303.40	334.37	331.18	3.13	.22	-3.13	0.40
4	16	30 43	399.22	.01	960.82	24.11	89.88	27.003	17.868	300.98	303.93	331.27	334.85	3.95	.04	-3.95	0.00
5	16	31 5	499.02	.00	949.97	23.54	88.78	25.169	17.067	299.78	304.22	344.93	334.45	3.92	.08	-3.91	0.38
6	16	31 29	598.80	.02	939.23	22.94	88.04	24.646	16.485	299.08	304.49	344.74	330.81	3.74	.94	-3.66	0.22
7	16	31 52	698.60	.01	928.57	22.68	77.04	21.222	14.340	298.42	304.82	343.67	341.24	3.73	1.85	-3.44	0.29
8	16	32 16	798.38	.01	918.03	22.42	73.36	19.903	13.397	298.03	305.41	342.44	344.82	0.08	1.67	-3.84	0.32
9	16	32 38	898.19	-.00	907.58	21.57	80.95	20.852	14.416	297.32	305.89	344.94	343.48	0.01	1.51	-3.82	0.32
10	16	33 2	997.92	.05	897.23	20.84	79.88	19.889	13.749	296.46	305.80	344.31	342.14	3.78	1.77	-3.30	0.22
11	16	33 26	1097.36	.36	887.00	20.02	85.52	20.020	14.100	295.72	306.03	344.63	340.45	3.71	1.34	-3.55	0.13
12	16	33 50	1195.19	2.33	877.03	19.41	88.95	19.599	14.018	295.07	306.35	344.87	338.48	3.03	.31	-3.02	0.00
13	16	34 15	1298.70	-1.41	866.58	19.22	79.08	17.744	12.635	294.81	306.98	342.26	1.28	0.82	-.01	-0.78	0.05
14	16	34 40	1401.44	-0.77	856.28	19.17	76.45	17.424	12.755	294.81	307.98	343.20	21.27	0.69	-1.70	-0.37	0.07
15	16	35 10	1499.98	-3.13	846.59	18.54	73.30	15.851	11.588	293.78	308.09	340.22	37.82	0.16	-2.52	-3.27	0.47
16	16	35 37	1602.39	-5.79	836.56	18.22	72.61	15.197	11.377	293.41	308.71	340.44	48.08	3.95	-2.96	-2.04	0.02
17	16	36 5	1706.46	-10.10	826.48	17.76	72.76	14.796	11.211	292.91	309.32	340.04	81.19	0.47	-3.92	-2.15	0.47
18	16	36 28	1798.95	-2.83	817.61	17.12	74.08	14.575	11.103	292.26	309.58	340.80	78.18	0.01	-5.84	-1.44	0.45
19	16	36 50	1898.52	-2.85	808.15	16.51	80.54	15.120	11.725	291.74	310.07	342.83	83.77	1.47	-1.45	-.59	0.06
20	16	37 11	1998.94	-3.32	798.78	16.24	78.32	14.892	11.668	291.35	310.70	341.75	92.83	0.78	-0.76	.48	0.77
21	16	37 32	2103.08	-1.71	789.00	15.31	73.55	12.793	10.169	290.26	310.81	339.25	91.47	10.36	-10.36	.27	0.77
22	16	37 52	2202.84	-1.73	779.78	14.69	73.02	12.204	9.742	289.51	310.92	338.85	87.98	10.80	-10.80	-.38	0.17
23	16	38 14	2296.95	-2.10	771.17	13.91	76.34	12.130	9.842	288.80	311.08	338.98	89.51	10.97	-10.97	-.09	0.75
24	16	38 35	2400.76	-12.17	761.21	13.65	84.30	13.049	10.653	288.68	311.65	339.24	92.98	10.72	-10.70	.56	0.76
25	16	38 55	2509.64	-15.35	751.98	13.54	81.74	12.575	10.258	288.09	312.36	339.44	91.85	11.86	-11.85	.38	0.73
26	16	39 17	2598.09	-4.03	744.14	13.07	89.59	13.984	11.521	287.33	312.91	338.83	89.95	13.22	-13.22	-.01	0.69
27	16	39 38	2700.33	-8.54	735.14	12.12	98.82	14.315	11.865	286.31	312.87	333.34	87.92	13.75	-13.74	-.50	0.34
28	16	40 1	2803.68	-10.16	726.14	11.77	94.09	13.484	11.223	286.04	313.46	332.24	89.78	13.70	-13.64	-1.25	0.48
29	16	40 24	2905.11	-11.87	717.39	11.12	97.42	13.595	11.312	285.43	313.87	333.15	93.72	13.73	-13.64	-1.50	0.45
30	16	40 46	3005.87	-12.92	708.79	10.37	91.54	12.763	10.623	284.71	314.16	334.08	92.71	13.31	-13.20	-1.69	0.49
31	16	41 8	3102.37	-9.69	700.62	9.79	83.82	11.126	9.888	284.14	314.58	334.89	92.41	12.00	-11.89	-1.58	0.53
32	16	41 30	3203.23	-10.84	692.17	9.08	82.86	10.653	9.544	283.37	314.81	334.00	91.13	11.37	-11.24	-1.75	0.59
33	16	41 52	3303.94	-11.85	683.81	8.26	84.90	10.624	9.568	282.61	315.06	335.43	78.39	11.41	-11.18	-2.30	0.56
34	16	42 14	3403.68	-11.88	675.81	7.69	81.97	9.908	9.014	281.88	315.33	333.12	80.19	11.73	-11.56	-2.00	0.53
35	16	42 36	3506.93	-15.43	667.20	7.07	87.70	9.805	9.029	281.15	315.65	331.78	80.08	12.30	-12.12	-2.12	0.59
36	16	42 57	3610.92	-14.71	658.82	6.70	92.11	9.133	8.911	280.53	316.09	327.97	82.56	11.28	-11.19	-1.66	0.73
37	16	43 18	3708.34	-17.44	651.06	6.74	87.38	8.678	8.521	280.50	317.13	327.91	88.41	9.27	-9.26	-.28	0.72
38	16	43 40	3806.16	-15.56	643.34	6.23	85.21	8.345	8.240	279.94	317.58	327.60	93.86	8.22	-8.20	.55	0.62
39	16	44 1	3906.24	-15.95	635.53	5.71	87.11	8.317	8.230	279.59	318.29	331.18	104.52	7.88	-7.80	1.97	0.65
40	16	44 23	4004.91	-18.93	627.80	4.80	96.18	8.833	8.804	278.78	318.50	333.07	109.50	7.76	-7.31	2.59	0.68
41	16	44 44	4104.41	-18.74	619.99	3.87	99.92	8.828	8.858	277.85	318.58	333.28	116.49	7.13	-6.92	3.45	0.70
42	16	45 5	4203.89	-14.55	612.75	3.21	88.99	8.305	8.403	277.28	318.98	335.23	123.58	8.15	-6.79	4.50	0.83
43	16	45 26	4307.84	-16.82	604.95	2.81	70.38	8.261	8.427	276.86	319.69	338.12	121.76	8.38	-7.11	4.40	0.00
44	16	45 45	4407.40	-18.71	597.56	1.99	70.70	8.984	9.204	276.02	319.81	335.58	118.07	8.07	-7.12	3.79	0.08
45	16	46 5	4508.65	-20.24	590.11	1.23	58.29	8.893	9.114	275.08	319.81	332.53	113.02	7.87	-7.25	3.08	0.10
46	16	46 25	4611.29	-23.25	582.64	.87	63.18	9.110	9.399	274.76	320.67	334.18	112.84	7.92	-7.30	3.07	0.17
47	16	46 44	4712.79	-23.08	575.33	.11	64.95	9.001	9.337	274.00	320.93	334.25	114.18	7.98	-7.28	3.27	0.32
48	16	47 2	4808.61	-21.24	568.49	-.64	71.15	9.151	9.559	273.28	321.18	335.18	110.37	8.10	-8.18	3.03	0.30
49	16	47 21	4896.15	-9.12	562.30	-.82	99.06	8.538	8.810	272.81	321.04	338.52	107.20	9.54	-9.11	2.82	0.29

3 MIN FILTER APPLIED TO PANAMA DATA 7/24/1977

Z(M) A100	UT HMS	Z:SFC(C) GPOT/M	DELZ GPOT/M	PV (MM)	TEMP (C)	MM	E (MB)	AV (G/KG)	TV (K)	THV (K)	THVE (K)	WD (DEG)	WS (M/S)	U (M/S)	V (M/S)	W (M/S)
0	16 24 0	0.00	0.00	1005.20	29.20	65.00	32.511	20.366	305.10	304.65	334.05	340.00	2.00	.00	-1.00	
1	16 24 28	99.81	.00	993.94	26.78	89.43	31.478	19.937	303.59	304.12	330.91					
2	16 29 55	199.61	.01	982.80	25.53	92.48	30.238	19.363	302.22	303.72	329.47	353.15	4.00	.48	-3.97	3.82
3	16 30 20	299.42	.01	971.76	24.55	93.33	28.794	18.639	301.10	303.58	329.31	2.82	5.34	-.24	-5.33	4.05
4	16 30 44	399.23	-.01	960.82	23.86	91.81	27.173	17.781	300.23	304.70	331.24	5.21	6.23	-.57	-6.22	4.28
5	16 31 7	499.03	-.03	949.98	23.39	89.36	25.467	16.848	299.54	306.02	334.29	1.32	6.49	-.15	-6.49	4.41
6	16 31 30	598.82	.00	939.23	22.94	86.76	23.741	15.908	299.02	306.43	347.33	353.17	6.31	.75	-6.26	4.44
7	16 31 52	698.60	.11	928.60	22.57	81.89	22.355	15.111	298.65	306.84	345.74	344.96	6.08	1.58	-5.87	4.40
8	16 32 15	798.12	.27	918.06	22.06	80.10	21.240	14.522	297.83	305.20	344.60	340.32	5.93	2.00	-5.54	4.34
9	16 32 38	897.71	.48	907.63	21.46	80.06	20.443	14.158	297.11	305.52	343.97	340.08	5.82	1.99	-5.47	4.29
10	16 33 2	997.42	.55	897.28	20.84	80.91	19.965	13.929	296.58	305.84	343.80	342.74	5.68	1.89	-5.42	4.21
11	16 33 26	1097.48	.27	886.99	20.25	81.68	19.398	13.716	295.91	306.19	343.78	347.84	5.41	1.16	-5.28	4.10
12	16 33 51	1198.01	-.49	876.75	19.73	81.53	18.746	13.408	295.29	306.61	343.33	355.30	5.01	.41	-4.99	3.97
13	16 34 16	1298.97	-1.67	866.57	19.29	80.27	17.957	12.991	294.71	307.04	342.78	5.72	4.60	-.46	-4.57	3.83
14	16 34 43	1400.08	-3.02	856.47	18.91	78.24	17.097	12.511	294.29	307.63	342.17	10.75	4.27	-1.37	-4.04	3.75
15	16 35 10	1501.07	-4.24	846.49	18.54	76.27	16.288	12.055	293.85	308.19	341.59	14.16	4.16	-2.33	-3.44	3.73
16	16 35 36	1601.84	-5.05	836.84	18.15	74.95	15.613	11.698	293.54	308.74	341.25	50.81	4.48	-3.40	-2.79	3.81
17	16 36 2	1701.62	-5.26	826.96	17.78	74.66	15.163	11.454	293.49	309.25	341.19	65.31	5.09	-4.63	-2.13	3.98
18	16 36 27	1801.22	-5.10	817.40	17.17	75.20	14.724	11.285	293.33	309.68	341.25	78.32	6.19	-6.02	-1.48	4.21
19	16 36 50	1900.80	-4.93	807.94	16.59	75.90	14.326	11.103	293.71	310.98	341.17	83.04	7.53	-7.48	-.83	4.47
20	16 37 11	2000.69	-5.06	798.54	15.97	76.12	13.807	10.865	294.04	310.38	340.81	88.19	8.85	-8.85	-.28	4.68
21	16 37 32	2101.03	-5.66	789.18	15.36	75.32	13.141	10.483	294.35	310.69	340.05	90.83	9.94	-9.94	.14	4.81
22	16 37 53	2201.71	-6.60	779.89	14.78	73.35	12.328	9.990	294.81	311.02	338.98	92.05	10.71	-10.70	.38	4.85
23	16 38 14	2302.42	-7.57	770.67	14.25	70.32	11.419	9.488	295.03	311.34	337.76	92.19	11.25	-11.24	.43	4.82
24	16 38 34	2402.97	-8.38	761.56	13.76	66.68	10.492	8.814	295.43	311.74	336.42	91.53	11.71	-11.70	.31	4.77
25	16 38 56	2503.29	-8.91	752.57	13.30	63.02	9.621	7.990	295.85	312.23	335.18	90.40	12.20	-12.20	.09	4.70
26	16 39 17	2603.27	-9.21	743.68	12.82	59.96	8.874	7.455	296.28	312.87	334.19	89.13	12.76	-12.72	-.19	4.62
27	16 39 39	2703.24	-9.45	734.89	12.30	58.12	8.315	7.085	296.69	313.50	333.59	87.84	13.18	-13.17	-.50	4.56
28	16 40 1	2803.26	-9.75	726.18	11.73	57.83	7.985	6.851	296.98	313.99	333.45	86.51	13.40	-13.43	-.82	4.51
29	16 40 23	2903.33	-10.09	717.55	11.09	59.07	7.798	6.787	297.43	313.83	333.84	85.02	13.38	-13.41	-1.17	4.48
30	16 40 46	3003.45	-10.50	709.00	10.40	61.30	7.732	6.811	296.74	314.17	334.04	83.35	13.20	-13.12	-1.53	4.48
31	16 41 8	3103.66	-10.94	700.52	9.69	63.41	7.627	6.808	296.93	314.46	334.31	81.64	12.78	-12.84	-1.86	4.50
32	16 41 30	3204.07	-11.38	692.10	9.00	64.98	7.352	6.634	297.39	314.74	334.19	80.17	12.32	-12.14	-2.10	4.53
33	16 41 52	3304.73	-12.04	683.75	8.36	65.39	6.856	6.281	297.84	315.05	333.48	79.29	11.92	-11.71	-2.22	4.56
34	16 42 14	3405.56	-13.76	675.46	7.79	64.27	6.162	5.694	298.43	315.41	332.25	79.34	11.56	-11.36	-2.14	4.59
35	16 42 36	3506.52	-15.01	667.24	7.31	62.58	5.381	5.032	298.83	315.85	330.87	80.58	11.16	-10.97	-1.86	4.62
36	16 42 57	3607.55	-16.14	659.12	6.89	61.05	4.678	4.427	299.21	316.31	329.71	83.28	10.47	-10.40	-1.22	4.64
37	16 43 19	3707.64	-16.93	651.11	6.48	59.62	4.217	4.038	299.53	316.93	329.17	87.79	9.84	-9.83	-.37	4.65
38	16 43 40	3807.68	-17.29	643.22	6.02	58.53	4.082	3.957	299.65	317.49	329.56	94.30	8.78	-8.75	.66	4.66
39	16 44 2	3907.59	-17.29	635.43	5.46	57.10	4.243	4.163	299.53	318.01	330.66	102.27	8.11	-7.93	1.72	4.67
40	16 44 23	4007.15	-17.18	627.74	4.81	55.81	4.547	4.518	299.24	318.45	332.13	110.18	7.78	-7.30	2.68	4.71
41	16 44 44	4106.47	-17.30	620.10	4.11	54.91	4.834	4.853	298.89	318.81	333.97	116.27	7.73	-6.93	3.42	4.76
42	16 45 5	4207.20	-17.86	612.51	3.37	54.52	5.005	5.099	298.54	319.14	335.92	119.74	7.81	-6.78	3.87	4.84
43	16 45 25	4307.74	-18.76	604.96	2.65	54.51	5.018	5.178	298.28	319.45	337.11	120.78	7.89	-6.79	4.03	4.94
44	16 45 45	4408.46	-19.76	597.49	1.96	54.42	4.869	5.101	298.28	319.78	337.68	119.70	7.92	-6.88	3.92	5.04
45	16 46 5	4508.88	-20.51	590.10	1.32	54.14	4.620	4.884	298.29	320.12	338.47	117.43	7.92	-7.03	3.65	5.13
46	16 46 24	4608.93	-20.49	582.81	.71	53.88	4.428	4.723	298.53	320.48	338.30	114.54	8.01	-7.29	3.33	5.20
47	16 46 43	4708.51	-20.41	575.61	.16	53.65	4.363	4.693	298.81	320.81	338.31	111.75	8.29	-7.70	3.07	5.25
48	16 47 2	4807.73	-20.35	568.55	-.35	52.79	4.144	4.447	298.38	321.29	337.82	109.72	8.82	-8.30	2.97	5.28
49	16 47 21	4906.71	-19.84	561.56	-.82	49.22	3.544	3.823	298.81	321.75	336.68	108.87	9.55	-9.04	3.06	5.28

BEST AVAILABLE COPY
DISCONTINUED FROM

* 4TH FILTER APPLIED TO PANAMA DATA 7/24/1977

Z(M) A100	UT HMS	Z(SFC) GPDT/M	DZ GPDT/M	PP (MB)	TEMP (C)	RH	t (MB)	AV (G/MB)	TV (K)	THV (K)	THDV (K)	DD (DEG)	DS (M/S)	U (M/S)	V (M/S)	W (M/S)
0	16 29 0	0.00	0.00	1005.20	25.20	85.00	32.711	20.366	305.10	304.65	324.05	340.00	2.00	.00	-1.00	
1	16 29 25	99.18	.03	993.40	27.38	84.91	30.957	19.604	304.13	304.66	325.47					
2	16 29 49	199.31	.11	982.72	26.56	84.86	29.884	19.019	304.17	304.69	325.00	334.96	3.27	1.38	-2.96	+.04
3	16 30 14	299.49	.14	971.80	25.75	84.79	28.896	18.180	302.23	304.72	323.74	340.17	3.08	1.32	-3.05	+.04
4	16 30 34	399.11	.11	960.71	24.98	84.84	28.163	17.512	301.31	304.78	323.48	344.42	4.31	1.17	-4.35	+.04
5	16 31 4	498.97	.05	949.86	24.20	84.55	27.535	16.895	300.43	304.88	323.38	349.24	5.10	.95	-5.01	+.04
6	16 31 28	598.83	-.01	939.13	23.47	84.39	26.942	16.315	299.58	305.01	324.96	353.1-	5.03	.67	-5.59	+.04
7	16 31 53	698.73	-.12	928.44	22.77	84.13	26.386	15.762	298.77	305.18	327.04	356.83	4.96	.34	-6.05	+.04
8	16 32 18	798.64	-.29	917.95	22.10	83.76	25.866	15.235	298.00	305.39	329.73	.49	4.15	-.03	-6.35	+.04
9	16 32 43	898.72	-.53	907.50	21.47	83.25	25.380	14.735	297.28	305.64	345.61	3.75	3.49	-.42	-6.48	+.04
10	16 33 7	998.80	-.83	897.14	20.87	82.62	24.930	14.262	296.59	305.94	344.12	7.43	2.96	-.84	-6.42	+.06
11	16 33 32	1098.96	-1.19	886.87	20.30	81.83	24.497	13.789	295.93	306.27	343.48	11.38	2.32	-1.27	-6.19	+.07
12	16 33 57	1199.11	-1.58	876.70	19.77	80.98	24.060	13.346	295.31	306.64	343.21	10.47	2.06	-1.72	-5.81	+.09
13	16 34 21	1299.29	-1.99	866.62	19.25	80.09	23.673	12.924	294.72	307.03	342.55	22.40	3.75	-2.19	-5.32	+.12
14	16 34 45	1399.49	-2.42	856.63	18.75	79.20	23.231	12.534	294.14	307.45	342.02	29.51	5.41	-2.69	-4.76	+.15
15	16 35 4	1499.71	-2.84	846.73	18.26	78.30	22.823	12.175	293.58	307.89	341.51	31.71	5.68	-3.23	-4.18	+.18
16	16 35 33	1599.97	-3.34	836.92	17.78	77.35	22.439	11.781	293.03	308.33	341.03	40.53	5.63	-3.81	-3.61	+.21
17	16 35 57	1700.25	-3.84	827.20	17.30	76.24	22.033	11.399	292.48	308.79	340.52	55.17	5.40	-4.43	-3.08	+.25
18	16 36 20	1800.51	-4.41	817.57	16.83	75.03	21.615	11.009	291.93	309.29	340.00	62.94	5.71	-5.08	-2.60	+.29
19	16 36 43	1900.82	-4.95	808.04	16.35	73.75	21.208	10.620	291.38	309.70	339.48	64.49	6.17	-5.78	-2.16	+.33
20	16 37 8	2001.14	-5.53	798.54	15.88	72.34	20.835	10.210	290.82	310.15	338.92	70.81	6.75	-6.51	-1.77	+.38
21	16 37 29	2101.45	-6.09	789.23	15.37	70.90	20.378	9.813	290.23	310.58	338.29	74.05	7.40	-7.26	-1.41	+.40
22	16 37 52	2201.77	-6.66	779.97	14.86	69.43	19.932	9.409	289.68	311.01	337.69	82.36	8.11	-8.03	-1.08	+.43
23	16 38 16	2302.08	-7.23	770.74	14.34	68.03	19.515	9.020	289.08	311.43	337.11	83.10	8.98	-8.87	-.78	+.46
24	16 38 37	2402.38	-7.79	761.70	13.80	66.62	19.104	8.625	288.47	311.82	336.49	87.70	9.78	-9.75	-.54	+.48
25	16 38 59	2502.67	-8.35	752.71	13.25	65.19	18.723	8.241	287.85	312.21	335.88	88.74	10.52	-10.52	-.34	+.52
26	16 39 21	2601.98	-8.96	743.79	12.70	63.76	18.361	7.865	287.23	312.60	335.22	91.34	11.09	-11.09	-.20	+.54
27	16 39 43	2701.34	-9.54	734.95	12.14	62.30	18.041	7.517	286.60	312.99	334.70	92.08	11.53	-11.53	-.14	+.57
28	16 40 5	2801.72	-10.20	726.22	11.57	61.41	17.811	7.200	285.98	313.38	334.21	93.63	11.91	-11.89	-.15	+.59
29	16 40 27	2901.05	-10.81	717.57	11.00	60.48	17.633	6.903	285.35	313.77	333.89	94.15	12.18	-12.15	-.08	+.60
30	16 40 49	3000.39	-11.43	708.99	10.42	59.60	17.527	6.630	284.73	314.16	333.58	94.30	12.34	-12.31	-.02	+.61
31	16 41 10	3100.77	-12.10	700.50	9.84	58.84	17.460	6.370	284.10	314.55	333.22	94.15	12.43	-12.40	-.00	+.62
32	16 41 31	3200.18	-12.74	692.09	9.25	58.38	17.417	6.144	283.47	314.94	333.05	93.81	12.44	-12.42	.03	+.63
33	16 41 53	3300.53	-13.44	683.76	8.66	58.11	17.320	5.953	282.85	315.33	332.95	93.33	12.38	-12.36	.12	+.64
34	16 42 15	3400.83	-14.05	675.52	8.07	58.01	17.249	5.774	282.22	315.72	332.83	92.82	12.18	-12.17	.00	+.65
35	16 42 38	3500.13	-14.63	667.37	7.47	58.01	17.202	5.613	281.59	316.12	332.83	92.41	11.91	-11.90	.30	+.67
36	16 42 57	3600.41	-15.20	659.30	6.87	57.91	17.150	5.443	280.95	316.51	332.73	92.19	11.55	-11.55	.44	+.69
37	16 43 19	3700.66	-15.75	651.30	6.28	57.88	17.117	5.298	280.34	316.91	332.74	92.03	11.13	-11.12	.44	+.71
38	16 43 40	3800.83	-16.25	643.40	5.68	57.82	17.089	5.169	279.71	317.32	332.88	92.71	10.64	-10.63	.30	+.73
39	16 44 1	3900.91	-16.72	635.57	5.09	57.84	17.050	5.065	279.09	317.72	332.87	93.60	10.12	-10.10	.03	+.76
40	16 44 22	4000.98	-17.20	627.82	4.50	57.65	16.923	4.993	278.47	318.13	332.74	95.00	9.60	-9.56	-.04	+.80
41	16 44 43	4100.91	-17.55	620.15	3.91	55.56	16.578	4.935	277.85	318.53	332.49	97.02	9.13	-9.07	1.12	+.84
42	16 45 3	4200.77	-18.02	612.55	3.33	55.02	16.430	4.909	277.23	318.93	332.17	99.06	8.75	-8.63	1.46	+.86
43	16 45 24	4300.54	-18.36	605.04	2.75	54.54	16.313	4.891	276.62	319.31	332.22	100.58	8.48	-8.27	1.65	+.93
44	16 45 44	4400.34	-18.54	597.61	2.18	53.24	15.901	4.871	276.01	319.69	332.02	103.36	8.33	-8.03	2.29	+.98
45	16 46 4	4500.15	-18.48	590.24	1.62	51.48	15.535	4.835	275.41	320.05	331.78	104.23	8.31	-7.89	2.80	+.02
46	16 46 24	4600.03	-18.21	582.93	1.08	49.44	15.252	4.791	274.81	320.40	331.51	110.48	8.38	-7.88	2.93	+.05
47	16 46 43	4700.17	-18.48	575.80	.52	47.11	14.984	4.735	274.22	321.11	331.23	112.15	8.53	-7.90	3.22	+.08
48	16 47 3	4800.10	-18.73	568.55	-.02	44.54	14.714	4.674	273.63	321.51	330.94	113.28	8.75	-8.04	3.46	+.11
49	16 47 22	4900.45	-18.42	561.43	-.56	41.91	14.441	4.611	273.05	322.04	330.67	113.81	9.03	-8.26	3.65	+.13

This page intentionally left blank.

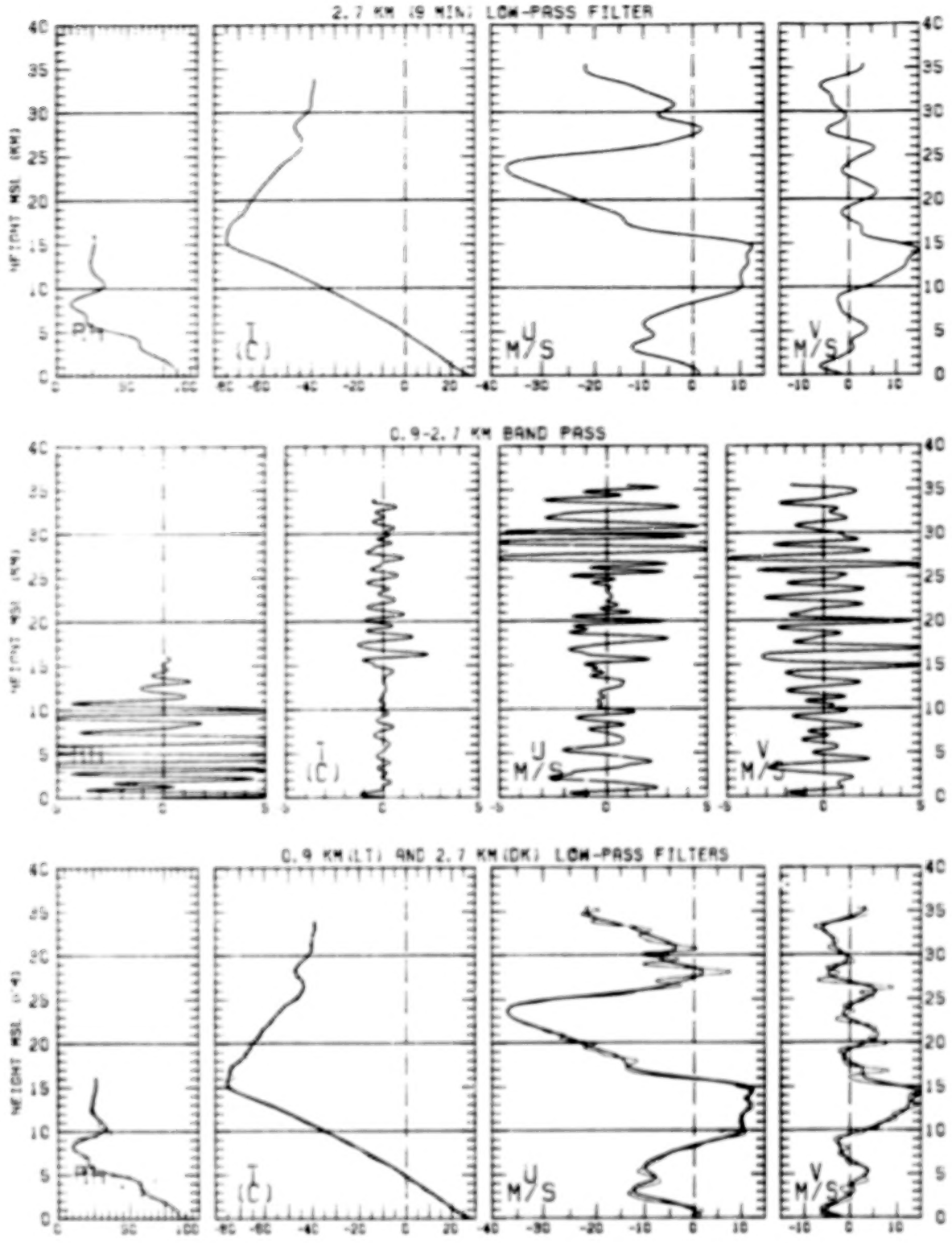
2.7 KM (9 MIN) LOW-PASS FILTER
0.9-2.7 KM BAND PASS
0.9 KM (LT) AND 2.7 KM (DK) LOW-PASS FILTERS
HEIGHT MSL (KM)
P (MB)
T (C)
U M/S
V M/S

Figure 11

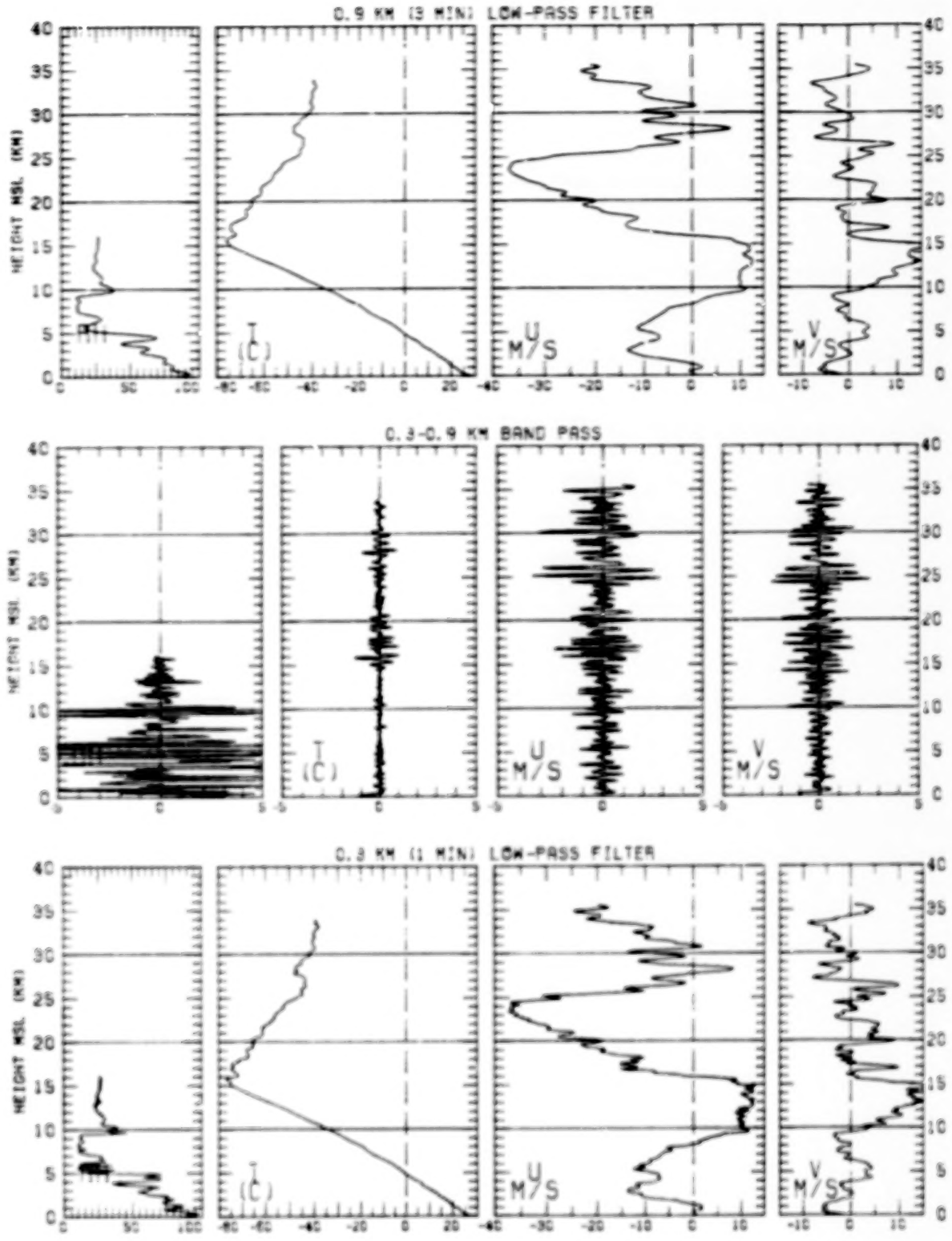
0.9 KM (3 MIN) LOW-PASS FILTER
0.3-0.9 KM BAND PASS
0.3 KM (1 MIN) LOW-PASS FILTER
HEIGHT MSL (KM)
T (C)
U M/S
V M/S

Figure 11

The sums, the light lines in the lower left row, are repeated in the upper right row. These profiles represent the low pass for the 0.9 km filter, Filter No. 2. Below them are the 0.15-0.9 km band-pass profiles and in the lowest row are the profiles resulting from applying Filter No. 1 to the unfiltered data. Note that the 0.3 km heading for the middle row and the 0.3 km (one minute) heading for the lower row are incorrect by a factor of two. Filter No. 1 has a 50% response at 0.15 km which is equivalent to 0.5 minute for an average balloon ascent rate.

These are the basic diagrams for displaying the results. They are completely automated and were drawn to scale for ease in reproduction. All ordinates are identical and correspond to geometric not geopotential heights. Each figure contains a vast amount of information and the compressed vertical scale obscures some of the phase relations, especially those of the shorter wavelength components. But by being able to see the entire set, without turning pages and losing one's visual reference, it has definite advantages for those who "see" what they are looking at.

The band-pass profiles clearly establish the presence of waves with a short vertical wavelength. A survey of all of these plots, Figures 15 to 54, indicates that they are always present and that they contribute to the fine structure of the temperature and relative humidity profiles as well as to the u and v velocity components. In general, amplitudes of the two velocity components are comparable within a given band pass, with decreasing amplitudes associated with decreasing wavelengths. There is evidence also for nodes at approximately 11 and 22 km in these band-pass profiles, the latter being the approximate height of the easterly jet.

Evidence of left and right circular polarizations, elliptical and linear polarizations are to be seen in the 0.9-2.7 band-pass profiles. For example, in Figure 11, left side, middle row, the band-pass wind at approximately 1 km is from the west at 2.5 m sec^{-1}. With increasing height the wind component changes to blow from the south, then from the east, then from the north and finally back again from the west at approximately 4 km. This counterclockwise rotation (cyclonic), by analogy to the righthand rule, will be called right circular polarization. At approximately 15 km the polarization is reversed and at approximately 28 km the u and v components are almost linearly polarized. Internal gravity waves are linearly polarized, but only where the larger scale winds have little vertical shear, i.e., where the thermal field is quasibarotopic. As shown by Danielsen (1966), vertical advection of the larger scale wind shear produces a relative phase shift between u and v which approaches quadrature when the shear is large.

Amplitudes of the 0.9 to 2.7 km band-pass components are often 3 to 5 m sec^{-1}, definitely nontrivial. Associated with these wind oscillations are temperature perturbations of approximately 0.5^{o} in the troposphere which increase to approximately 1 to 2^{o} in the stratosphere. Apparently the adiabatic compression and expansion, not horizontal advection, dominates for the local temperature change. Note that the relative humidity changes are quite the reverse. They maximize in the troposphere and indicate a dependence on horizontal gradients.

The same pattern of changes in perturbation amplitudes versus height can be found in the shorter wavelength band-pass, middle row, right figure. Again the tendency for a node at approximately 22 km is evident. However, all the amplitudes are about a factor of 2 smaller except those of relative humidity. This difference supports the relative importance of horizontal gradients for humidity perturbations. It is highly probable that these waves and those of the 0.9 to 2.7 km band-pass have high frequencies and consequently cannot be resolved from synoptic radiosonde, rawinsonde observations. However, it is clear that they contribute a complexity to tropopause identification. The low-pass profiles in the upper left are more representative of the "synoptic" scale structures, but the temperature profile is curved rather than discontinuous in slope, i.e., the tropopause is a second order discontinuity in T or a place where the curvature increases rapidly.

It is evident from the band-pass profiles that the amplitudes of the short, vertical wavelength oscillations are rather large. Velocity amplitudes of 2 to 5 m sec^{-1} have a potential for affecting the transport of trace gases and aerosols between the troposphere and stratosphere and within the stratosphere itself. The relative importance of these waves to transport at tropical latitudes remains to be established, but their presence can no longer be neglected nor denied. A significant eddy-type transport in the tropical stratosphere was deduced by Louis (1974) as being essential to maintaining the ozone concentrations below the chemically active altitudes against the upward and difluent transports by the mean circulations.

Having demonstrated the presence of the short, vertical waves, we decided to apply two additional low-pass filters to separate the longer vertical, wavelength components. Despite the broad transition zone of these two filters, especially that of Filter 5, Figure 12 reveals some interesting results. The 24-8 km band-pass, middle row, left, shows a distinctly different wavelength for the zonal than for the meridional components. Oscillating between ± 15 m sec^{-1}, the zonal winds have a vertical wavelength of approximately 16 km. A similar wavelength dominates the temperature deviations, with the phase lag similar to that of a Kelvin wave (Wallace and Kousky, 1968). The linearly-polarized Kelvin wave with velocity components restricted to the X, Z plane is a special type of internal gravity wave restricted to equatorial latitudes where $f = 2\omega \sin\Phi$, the vertical component of the earth's vorticity, approaches zero, ω being the angular speed of the earth's rotation. In the Kelvin wave, these zonal winds are in geostrophic balance. Although f approaches 0 as Φ approaches 0 , u_g remains finite when the pressure surfaces have a maximum (or minimum) elevation at the equator. The transition from westerly to easterly winds then requires negative temperature departures, as seen in Figure 12, which changes the curvature of the pressure surfaces from negative to positive with increasing heights.

Because the 16 km wave is linearly polarized in the zonal direction with temperature departures in quadrature, one is tempted to identify it as a large vertical-wavelength Kelvin wave. However, any such temptation is thwarted when one examines its local phase propagation. To qualify as a Kelvin wave the local vertical phase propagation should be negative or downward and the horizontal phase propagation should be positive or eastward. But this 16 km wave, although fluctuating diurnally up and down, has only a very small downward phase propagation. For example, Figure 13 shows the same wave eight days earlier in almost the same phase as in Figure 12. We will establish its probable identity later.

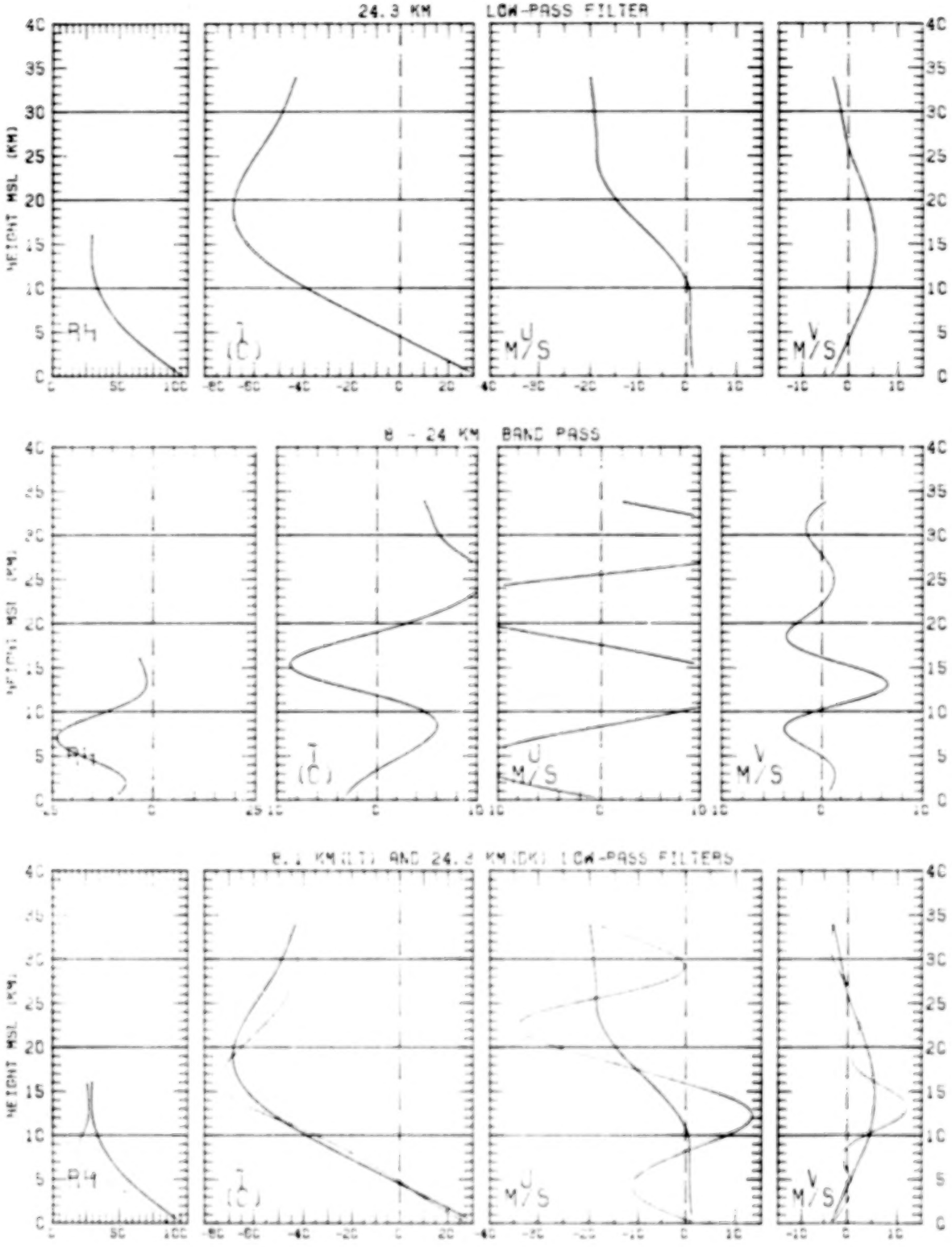
24.3 KM LOW-PASS FILTER
8 - 24 KM BAND PASS
HEIGHT MSL (KM)
RH
T (C)
U M/S
V M/S

Figure 12

PANAMA 24 JULY 1977 16.29UT

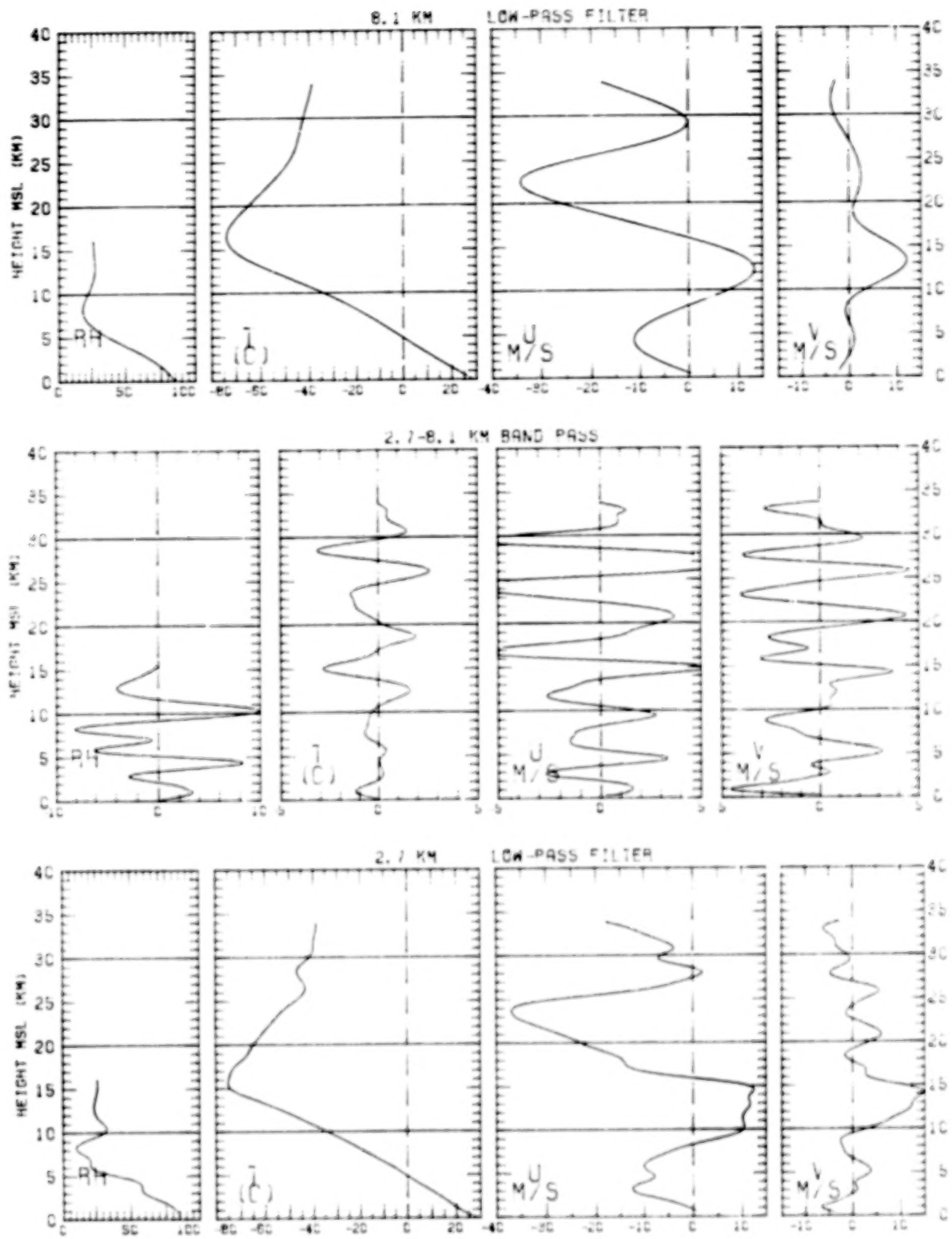

Figure 12

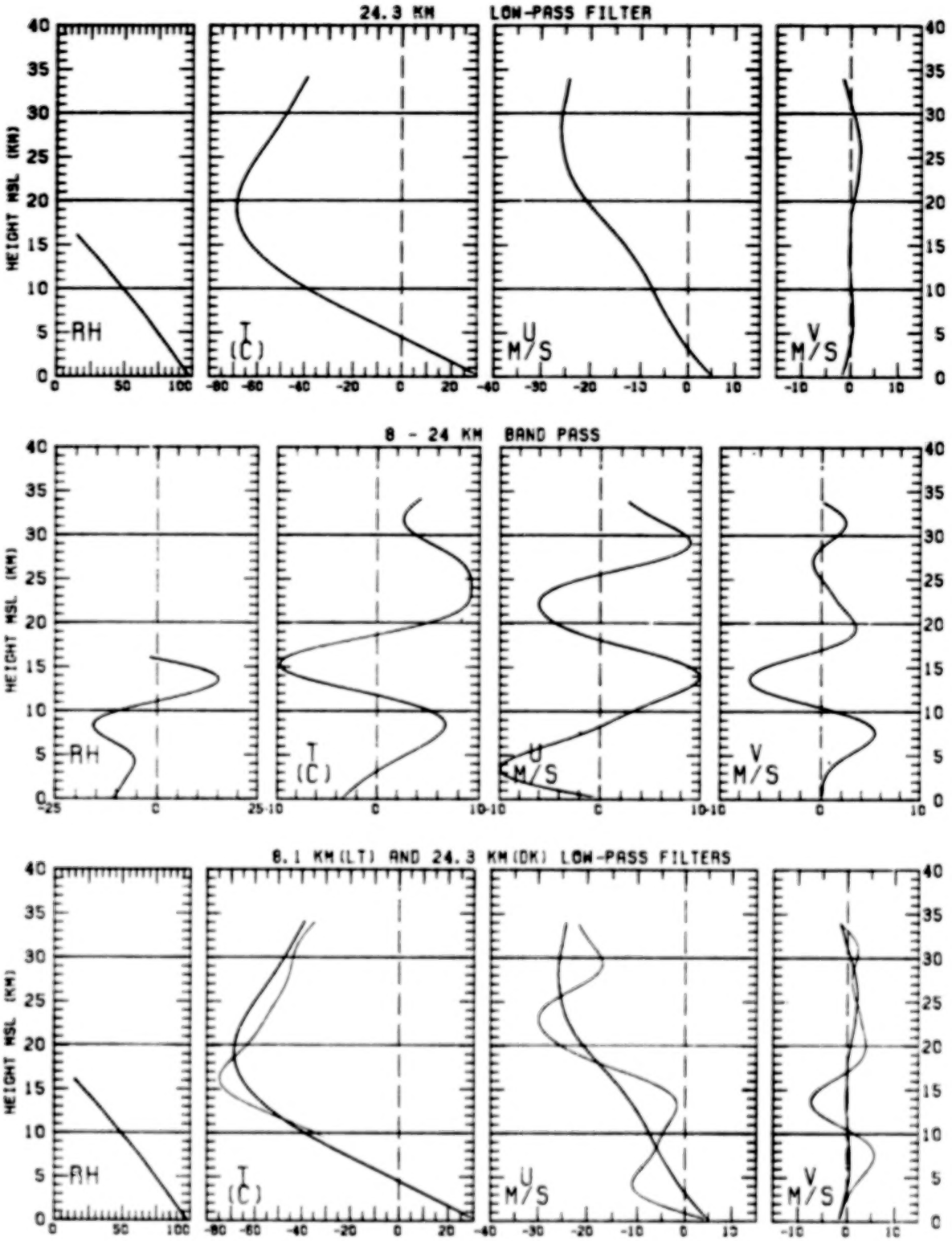
24.3 KM LOW-PASS FILTER
HEIGHT MSL (KM)
RH
T (C)
U M/S
V M/S
8 - 24 KM BAND PASS
8.1 KM(LT) AND 24.3 KM(DK) LOW-PASS FILTERS

Figure 13

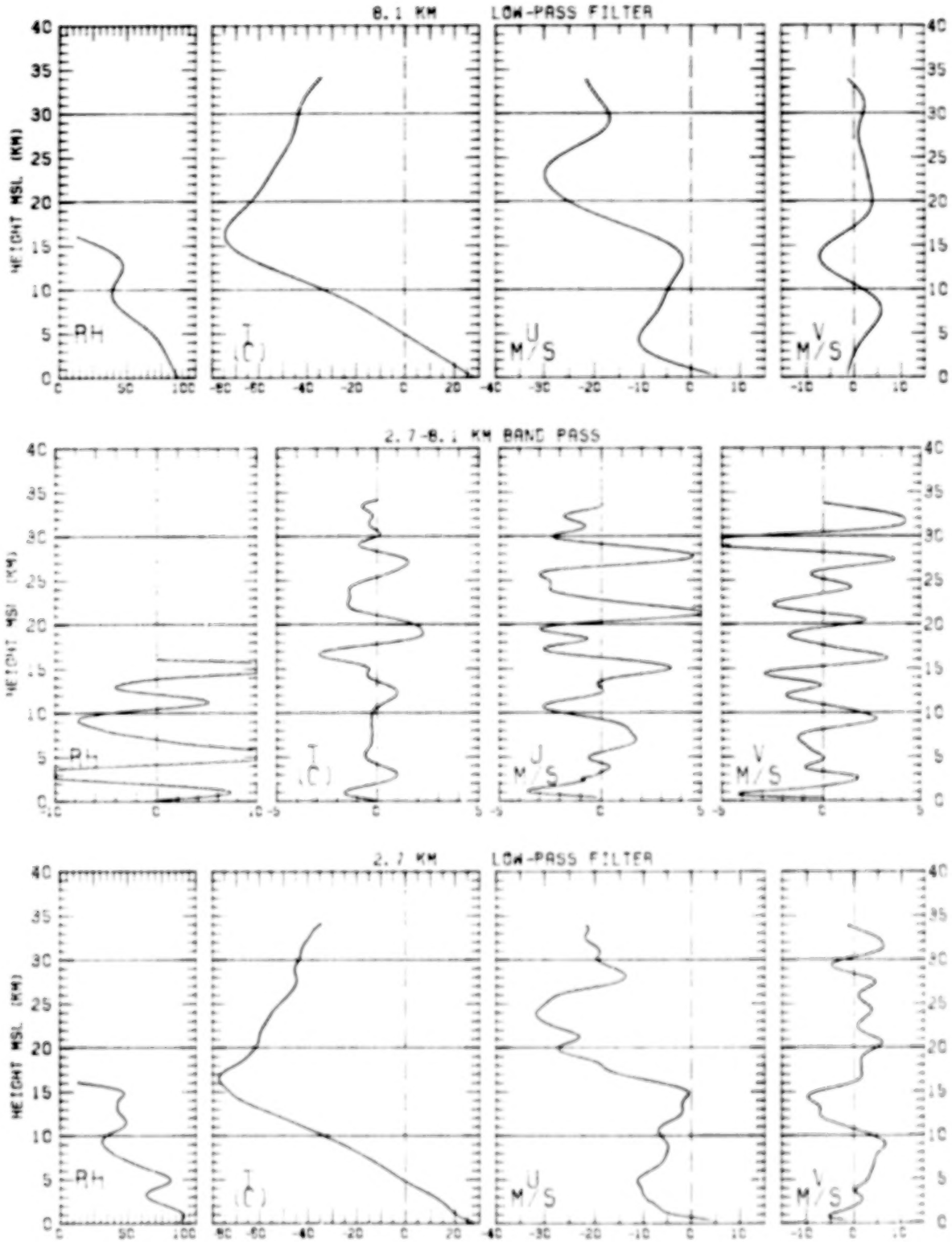
8.1 KM LOW-PASS FILTER
2.7-8.1 KM BAND PASS
2.7 KM LOW-PASS FILTER
HEIGHT MSL (KM)
RH
T (C)
U M/S
V M/S

Figure 13

In contrast to the quasistationary phase of the zonally polarized 16 km wave, the meridional components of an approximately 11 km wave have exactly reversed phase during the eight day period. A similar analysis for the 19th of July, not shown, indicates that this 11 km wave is produced by interference between upward and downward propagating wave modes. In other words, wave reflection or ducting is apparently taking place. The amplitude of this north-south oscillation is smaller by a factor of 3 or 4 than that of the east-west oscillation, but again, it is significant.

In addition to these two large-scale waves, there is evidence in the middle row, right of Figures 12 and 13, for rather large amplitude velocity components associated with approximately 5 km wavelengths. This vertical wavelength approximates that required for the Kelvin and gravity-modified Rossby waves but the phase of the temperature deviations doesn't fit well to either wave mode. In any case, the amplitudes of the wind components (less than or equal to 5 m sec^{-1}) are quite large, therefore, their potentials for transport cannot be ignored.

From these data it is an easy matter to compute the temperature or potential temperature flux in the zonal and meridional directions. The profiles in Figures 11, 12 and 13 suggest that these fluxes will be oscillatory but certainly significantly large in magnitude, with the largest fluxes produced by the largest vertical waves. It is interesting to note that the amplitude of the velocity deviations in meters per second is approximately equal to the vertical wavelength in kilometers; also, as is typical of internal gravity waves, the temperature perturbation in degrees is about 50% of the velocity perturbation in meters per second. From these general estimates one can deduce that the temperature flux increases as L_z^2, where L_z is the vertical wavelength. Since we have evidence here of waves with L_z ranging from 1 to 16 km, the heat flux produced by the largest waves are 100 to 200 times those of the 1 km waves.

Estimates of the meridional diffusion coefficient, K_{yy} a diagonal component of the diffusion tensor, can be made also from these data. For example, if we scale K_{yy} by τ

$$K_{yy} \simeq -\overline{u'v'}\tau \qquad (11)$$

use $v' = 10$ m sec^{-1}, and following Danielsen and Deaven (1974), we set $\tau = 4 \times 10^4$ sec we obtain a $K_{yy} \simeq -10^{10}$ cm^2 sec^{-1}. This agrees with the magnitude deduced by Louis (1974) for the equatorial zone.

Returning now to the enigmatic 16 km zonal wave which is quasistationary locally, it was recognized that, except for the forcing function, the generalized wave equation for stationary mountain waves in a nonuniform stability and wind regime (Danielsen and Bleck, 1970) would be applicable. This equation determines the total wave number squared as a complicated function of the stability and its vertical derivative, and the wind speed and its vertical derivatives. Then, knowing $k^2(Z)$ and k_x^2 one can solve for $k_z^2(Z)$. The computed k^2 values, based on the 24 km filters, yields k_z^2 values which are about 10 times too large, i.e., the L_z's would be closer to 5 than to 16 km. Again, the more general solution does not permit a free mode with such a large vertical wavelength.

However, this wave, which dominates the zonal wind profiles obtained from radar tracking of the radiosonde balloon, also dominates the wind profiles determined from radar tracking of the rockets which were released and tracked from the same site. Figure 14 shows the zonal wind profiles from our 8 and 24 km filters for the 24th of July with the rocket-derived winds from Schmidlin and Kloos (1978). Note that the latter and the former agree with respect to phase, but the rocket winds have a smaller amplitude. The mean profile, in the center, was drawn by hand and then these values were subtracted to produce the deviation profiles, at the right.

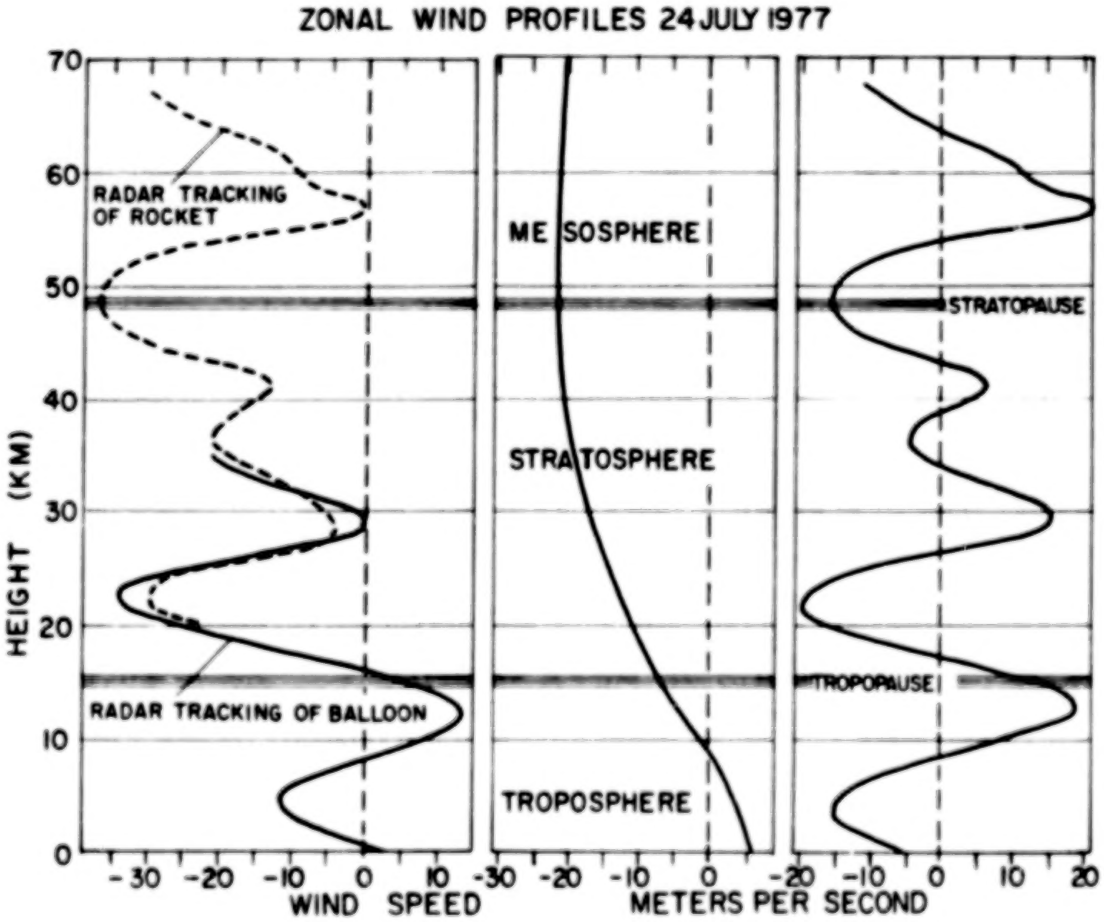

Figure 14. Zonal wind profiles from 24-8 km band-pass and from radar tracking of rocket.

From Figure 14, right, it is apparent that this oscillation extends from the surface through the troposphere, stratosphere, and into the mesosphere. The vertical wavelength varies from approximately 14 to 18 km and the amplitude is smallest near 40 km. Clearly, it dominates the zonal wind profile. After examining the entire set of rocket winds

it was obvious that the minimae and maximae fluctuated slightly in altitude and speed but there was no significant downward propagation. Thus, the rocket and radiosonde winds agree in all respects for this approximately equal-to-16 km wave.

The obvious implications are that this wave is forced and has a very long period. In general, it seems to fit the properties of the semiannual waves analyzed by Wallace (1973). Indeed, the profile for the summer of 1963 in Wallace's article is extremely similar to that in Figure 14. The mesospheric and upper stratospheric easterlies agree also with those illustrated in Figure 9.6 of Danielsen and Louis (1977). Here. the easterlies are attributed to the divergence produced by the heated hemisphere. The easterlies propagate across the equator, then reverse to become westerlies in the cooling winter hemisphere. Therefore, tropical easterlies are produced by both the northern and southern hemispheric summers. While they are approaching the equator in the heated hemisphere the winds from the east are approximately balanced by a warm anticyclone in the pressure field. However, a small ageostrophic meridional component advects the easterly winds across the equator where they experience a reversal of the coriolis force. As this force increases with increasing latitude, the resulting imbalance of forces produces rapid anticyclonic turning which reverses the flow's direction to westerly. Then, this westerly flow is approximately balanced by the cold cyclone in the pressure field of the winter hemisphere and the small ageostrophic meridional component continues the convergence toward the cooling pole, with an associated increase in zonal wind speeds. However, although this easterly momentum source during the solstices may explain the semiannual oscillation above about 35 km, it does not explain how the vertical wavelength is established.

SUMMARY

High resolution wind, temperature and relative humidity profiles have been derived by objective computer methods from a unique set of observations made in the vicinity of the Intertropical Convergence Zone. The set is unique because:

1) radiosonde-ozonesonde observations were made approximately every six hours for the latter half of July,

2) the balloon-borne system was simultaneously tracked by the conventional GMD-1 and by a NIKE radar, and

3) all data were digitally recorded at a rate of one or two per second.

Taking full advantage of the rapid recording rate, the data were objectively filtered by applying a series of non-recursive low-pass filters. The filtered data are presented as vertical profiles of the east-west and north-south wind components, the temperature and relative humidity.

The first filter removes the very short vertical waves and the majority of the instrumental and recording errors. The remaining filters remove progressively longer and longer waves to reveal the large-scale structures of the tropical atmosphere. The

largest scale wave, with a vertical wavelength of 16 ±2 km, dominates the zonal winds and the temperature profiles from the earth's surface through the troposphere, stratosphere and well into the mesosphere. This wave, with some of the properties of a Kelvin wave, does not have the proper intrinsic or local phase propagation for a Kelvin wave. It probably represents a semiannual oscillation generated in the upper atmosphere by heating in the summer hemisphere.

Of special significance to the initial research objectives are the profiles of the band-pass components, which firmly establish the existence of a broad range of mesoscale internal waves. The amplitudes of these waves decrease with decreasing wavelengths, but at all wavelengths they are significant. In particular, mesoscale waves in the wind with amplitudes greater than 5 m sec^{-1} are evident, especially in the stratosphere. The importance of these waves to stratospheric-tropospheric exchange and to eddy transports remains to be determined, but their potentials are now established.

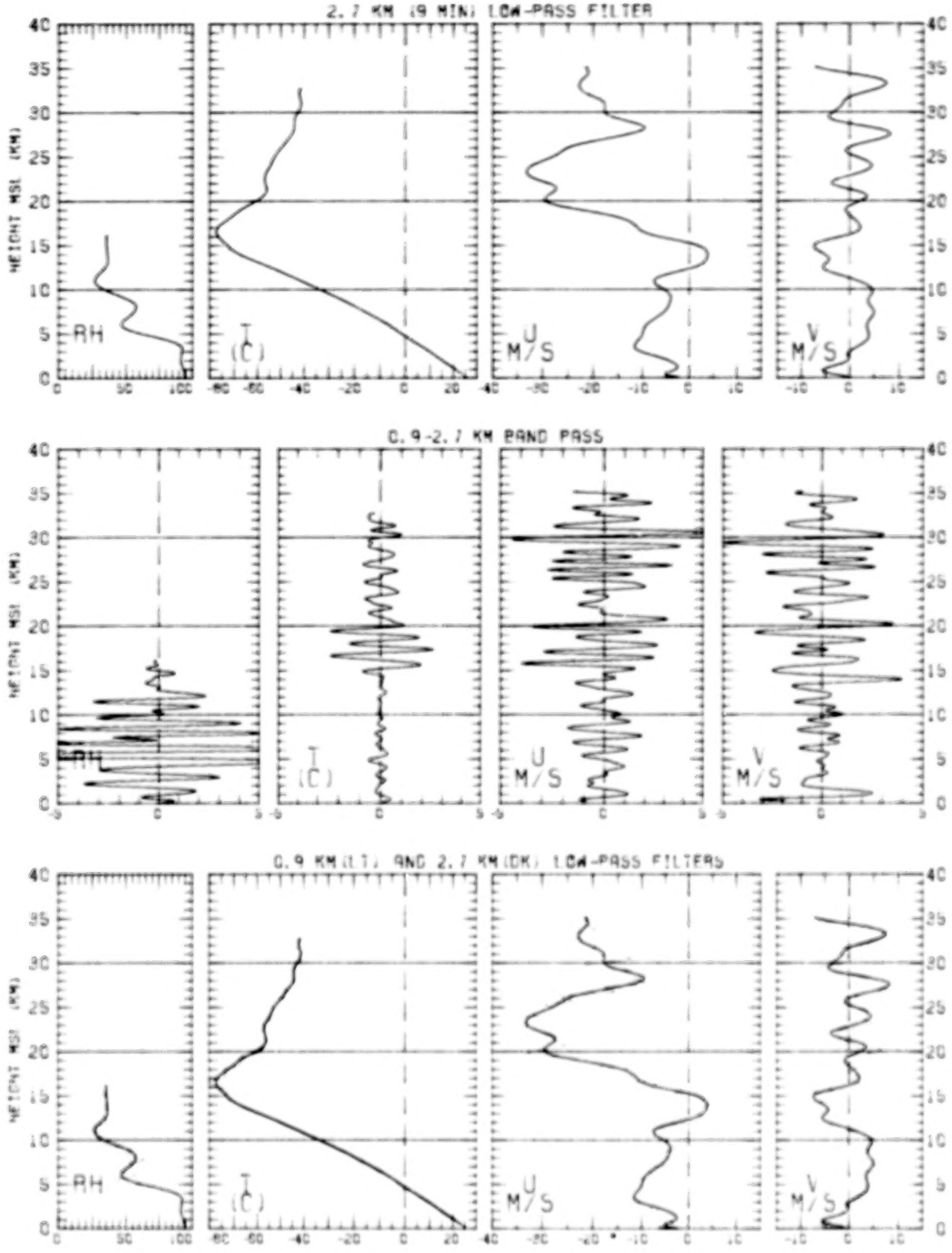
2.7 KM (9 MIN) LOW-PASS FILTER
HEIGHT MSL (KM)
RH
T (C)
U M/S
V M/S
0.9-2.7 KM BAND PASS
0.9 KM (LT) AND 2.7 KM (DK) LOW-PASS FILTERS

Figure 15

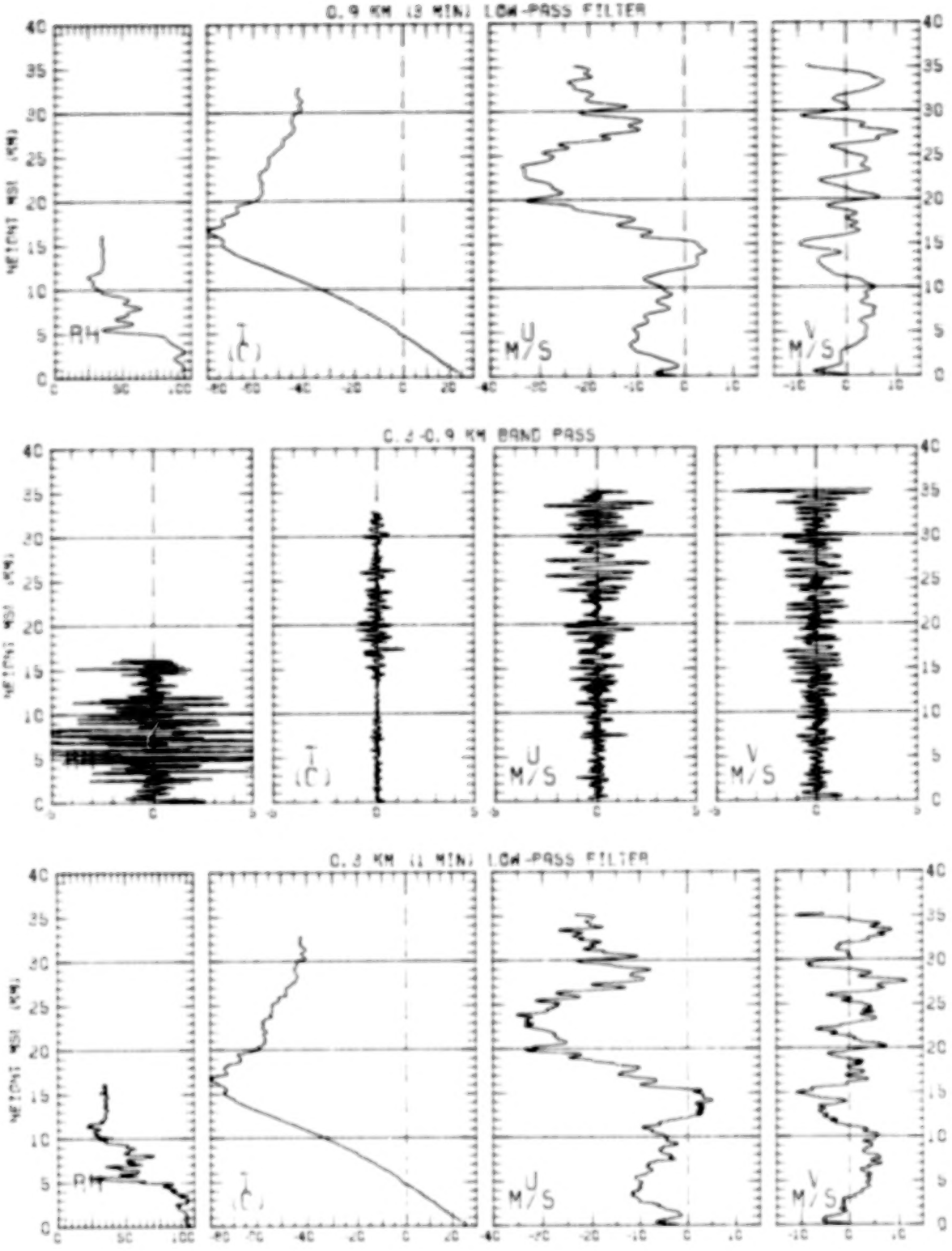
0.9 KM (3 MIN) LOW-PASS FILTER
0.3-0.9 KM BAND PASS
0.3 KM (1 MIN) LOW-PASS FILTER
HEIGHT MSL (KM)
RH
T (C)
U M/S
V M/S

Figure 15

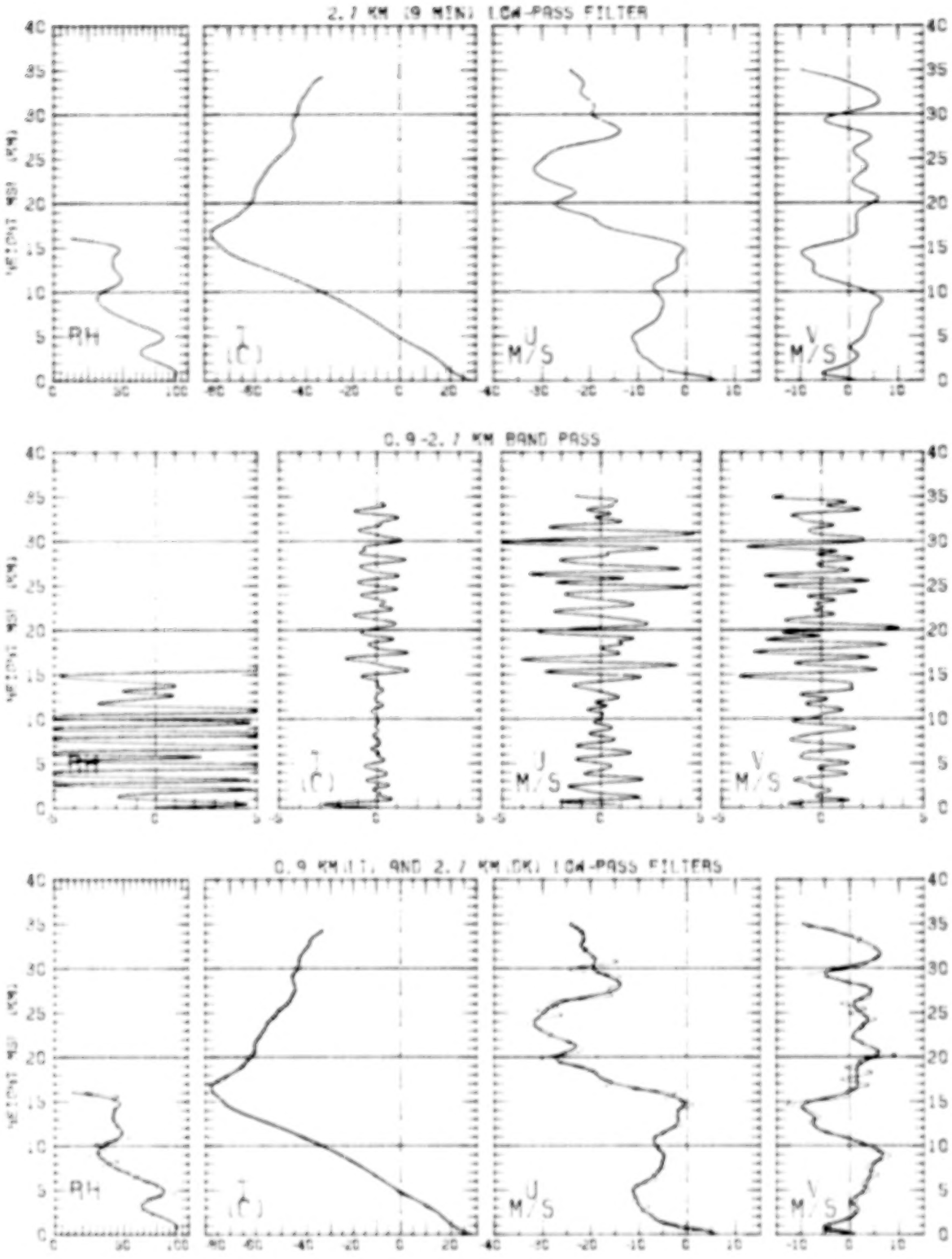
2.7 KM (9 MIN) LOW-PASS FILTER
0.9-2.7 KM BAND PASS
0.9 KM (3 MIN) AND 2.7 KM (9 MIN) LOW-PASS FILTERS
RH
T (°C)
U M/S
V M/S

Figure 16

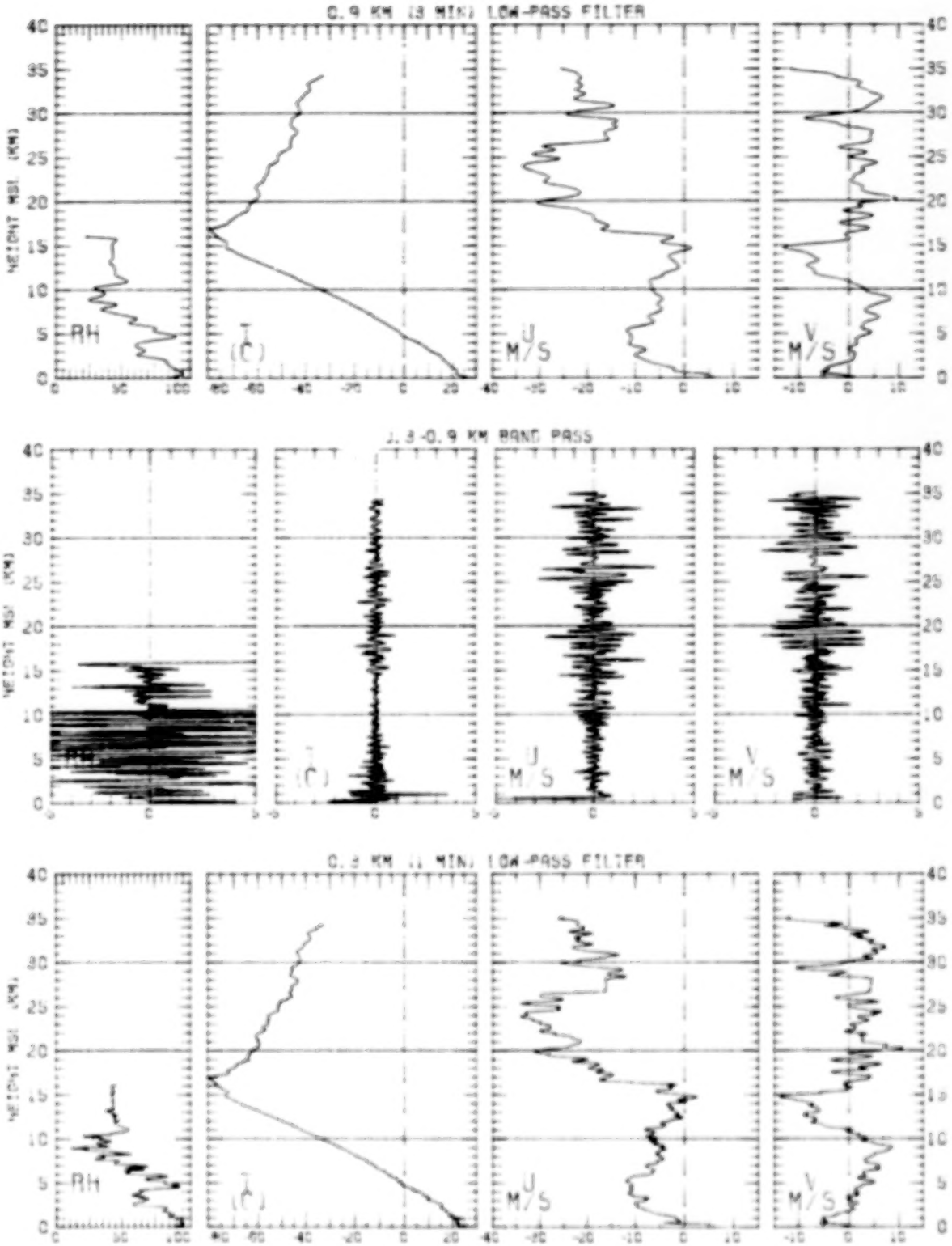
0.9 KM (3 MIN) LOW-PASS FILTER
HEIGHT MSL (KM)
RH
T (C)
U M/S
V M/S
2.3-0.9 KM BAND PASS
0.9 KM (3 MIN) LOW-PASS FILTER

Figure 16

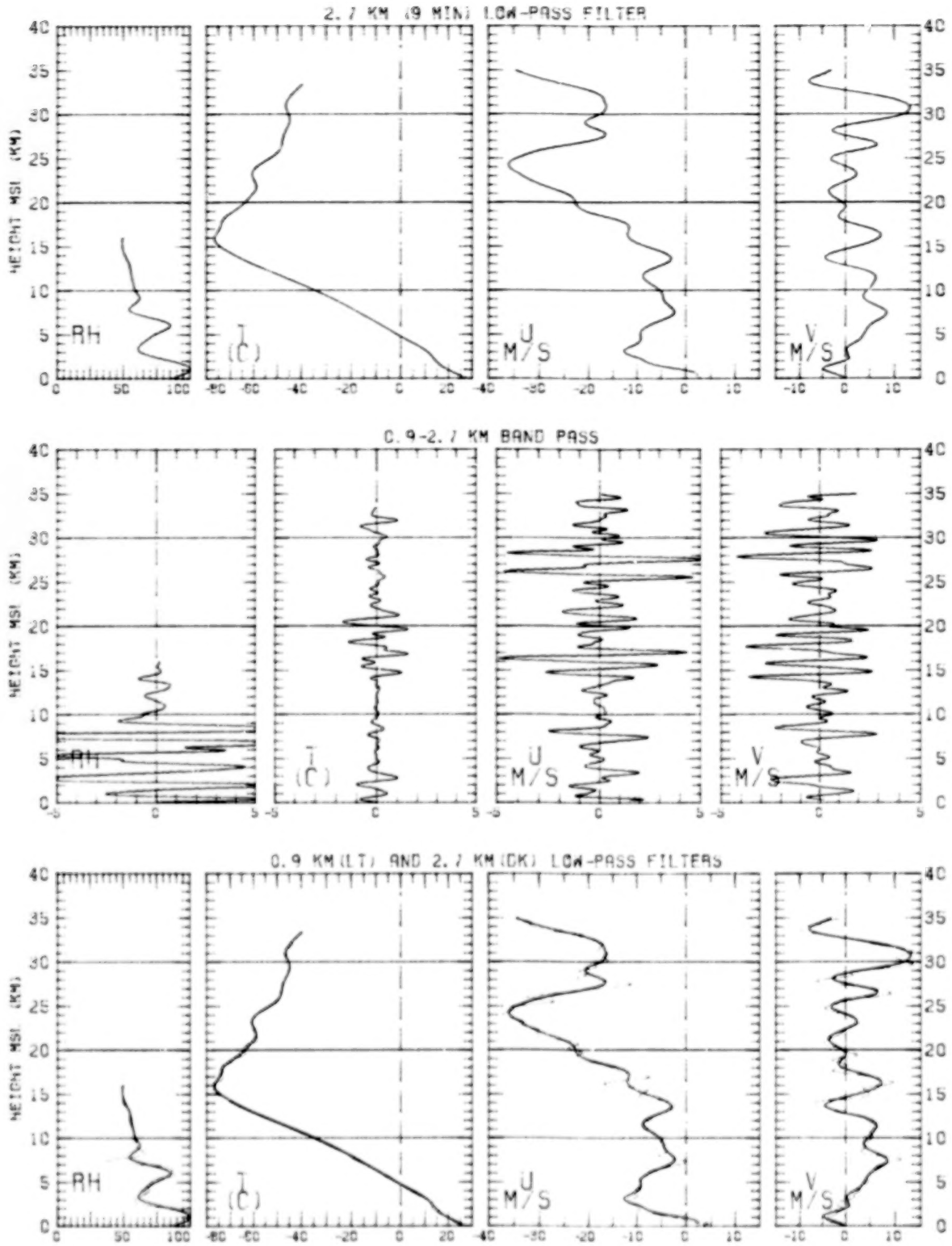
2.7 KM (9 MIN) LOW-PASS FILTER
HEIGHT MSL (KM)
RH
T (C)
U M/S
V M/S
0.9-2.7 KM BAND PASS
HEIGHT MSL (KM)
RH
T (C)
U M/S
V M/S
0.9 KM(LT) AND 2.7 KM(DK) LOW-PASS FILTERS
HEIGHT MSL (KM)
RH
T (C)
U M/S
V M/S

Figure 17

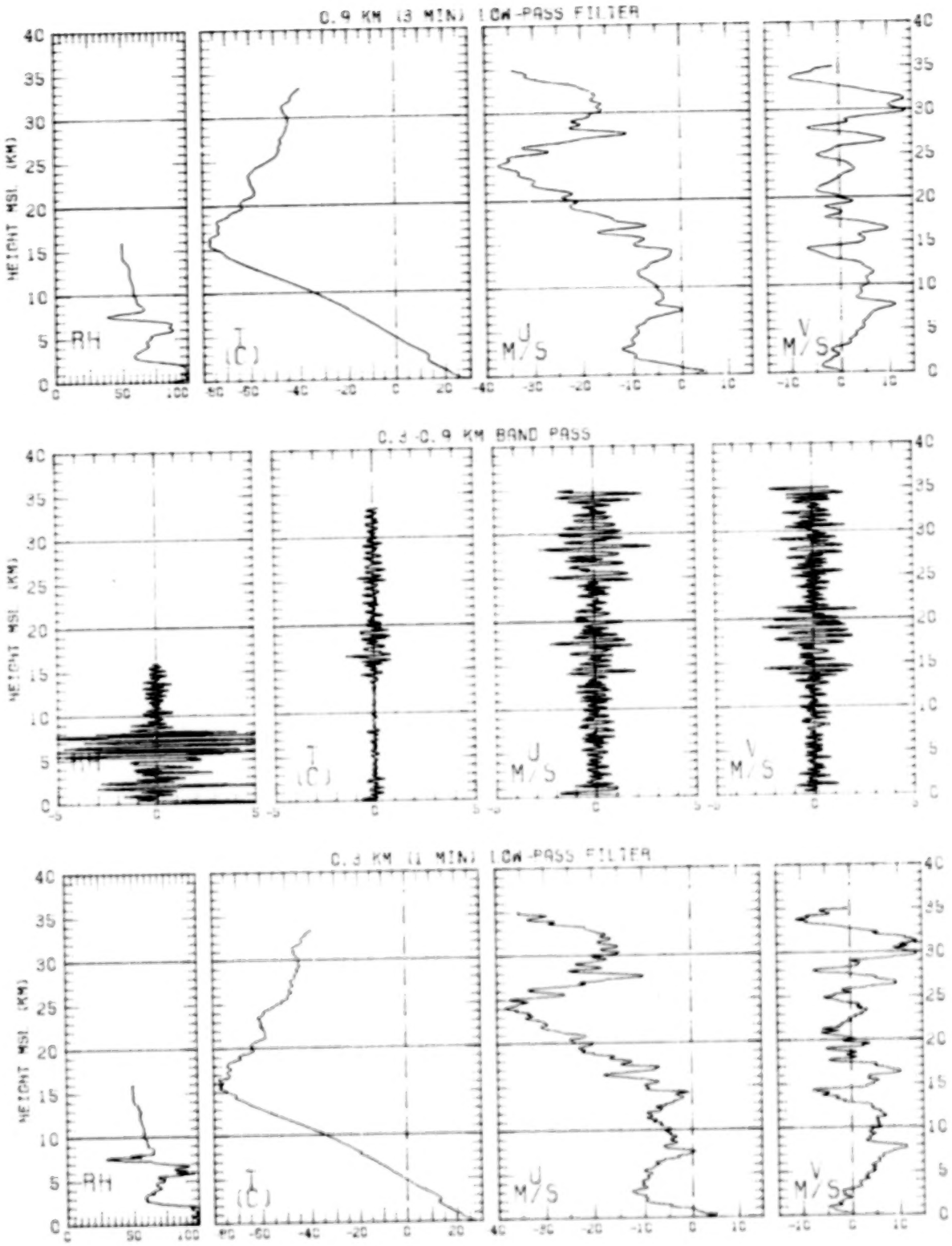
0.9 KM (3 MIN) LOW-PASS FILTER
HEIGHT MSL (KM)
RH
T (C)
U M/S
V M/S
0.3-0.9 KM BAND PASS
0.3 KM (1 MIN) LOW-PASS FILTER

Figure 17

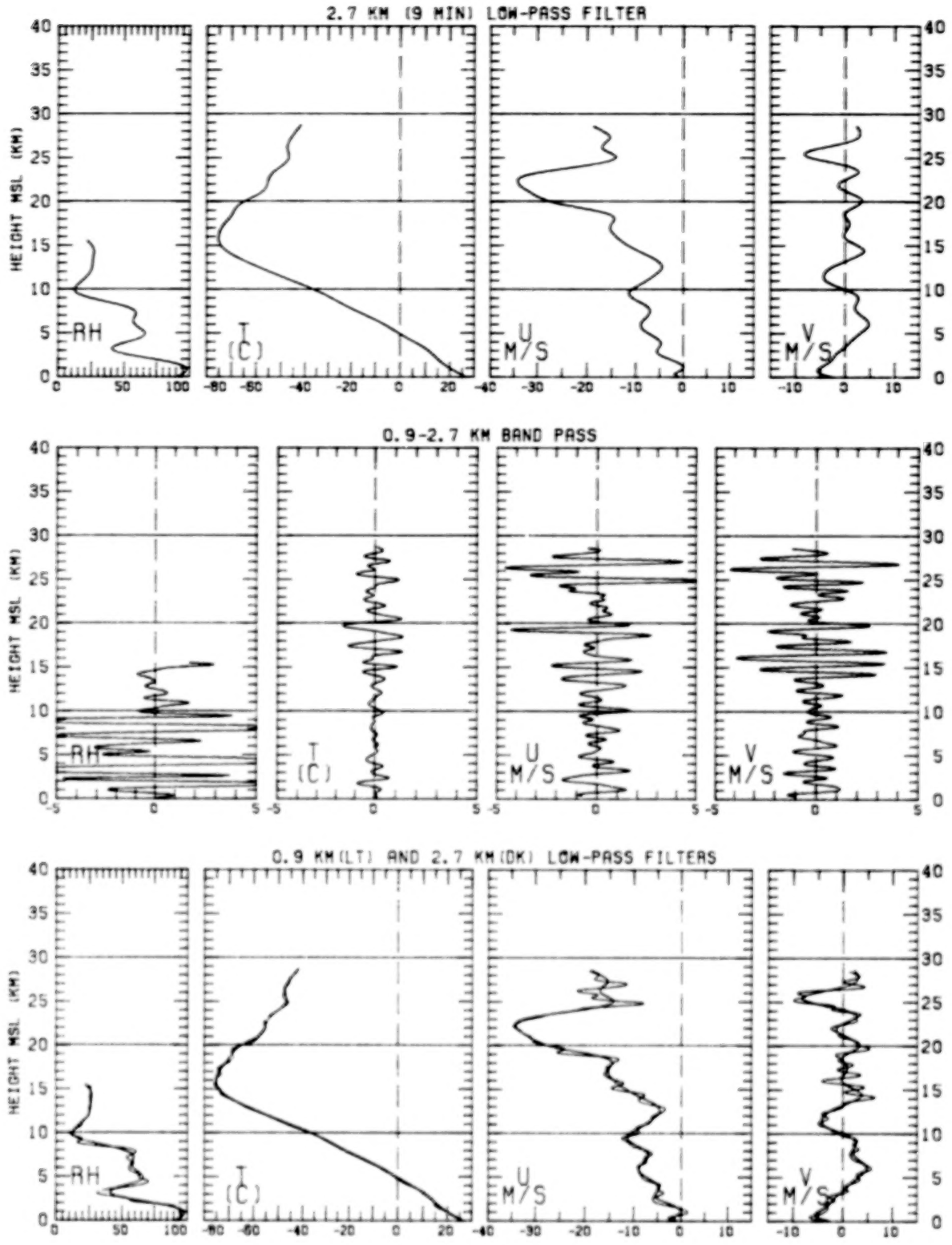
2.7 KM (9 MIN) LOW-PASS FILTER
HEIGHT MSL (KM)
RH
T (C)
U M/S
V M/S
0.9-2.7 KM BAND PASS
0.9 KM(LT) AND 2.7 KM(DK) LOW-PASS FILTERS

Figure 18

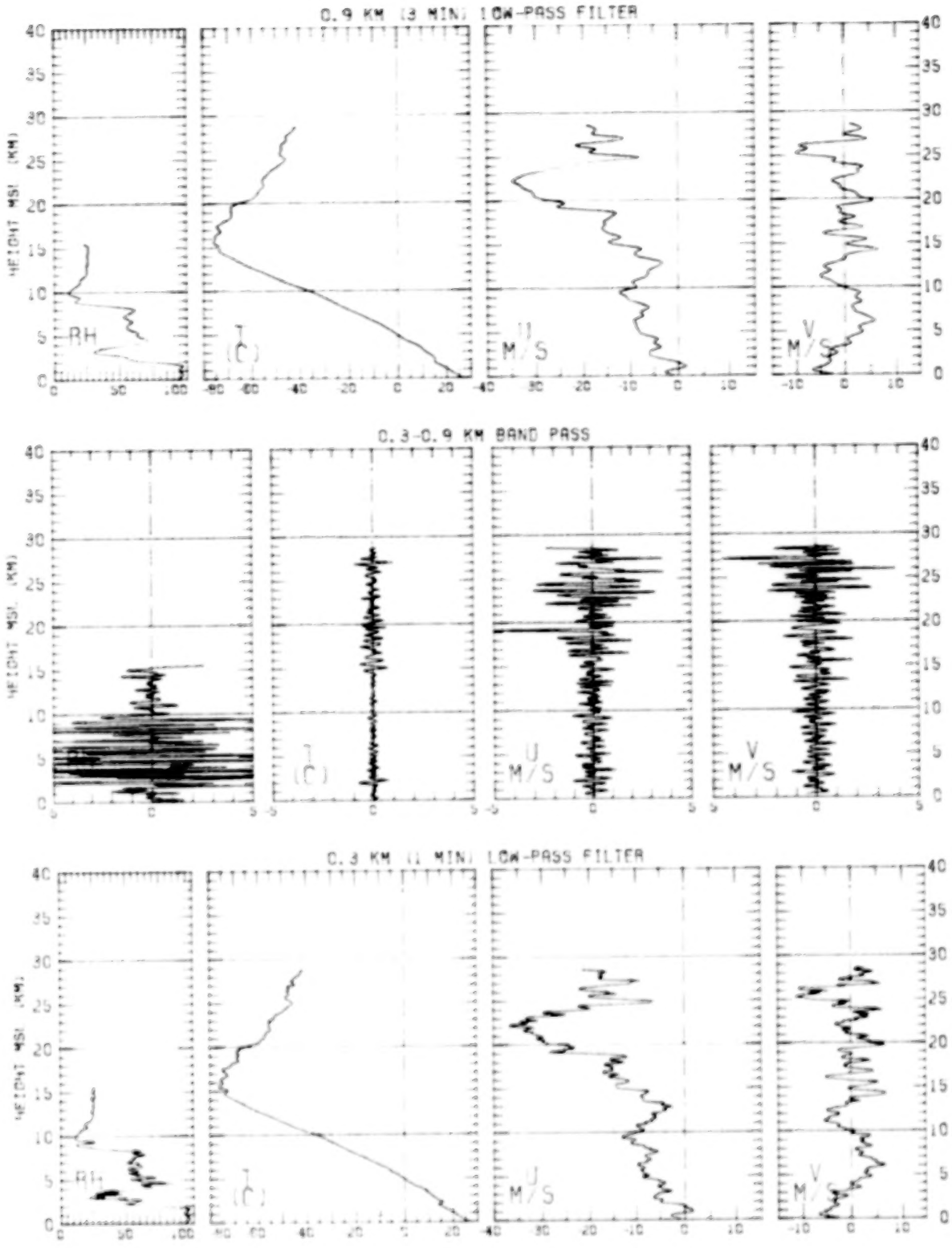
0.9 KM (3 MIN) LOW-PASS FILTER
HEIGHT MSL (KM)
RH
T (C)
U M/S
V M/S
0.3-0.9 KM BAND PASS
0.3 KM (1 MIN) LOW-PASS FILTER

Figure 18

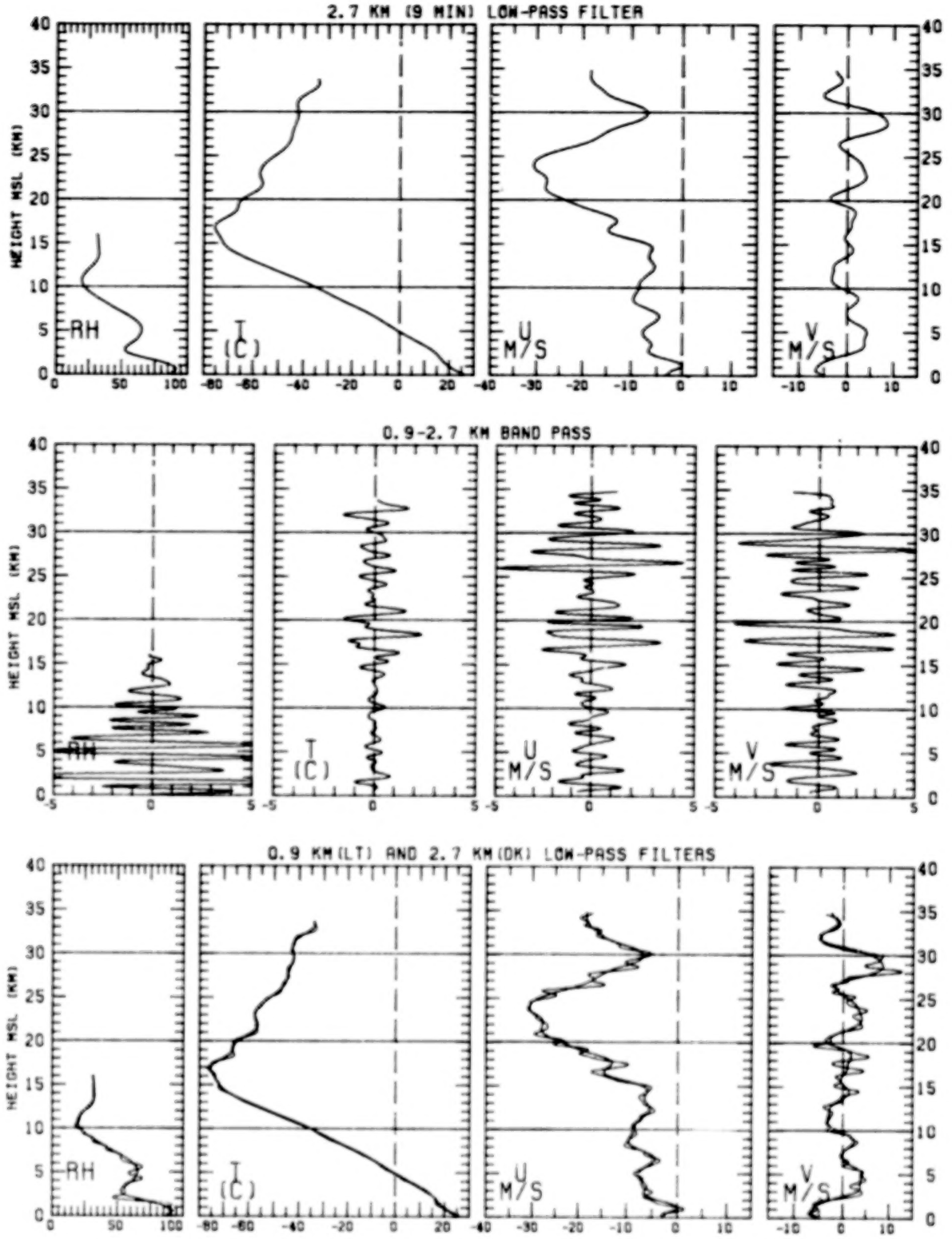
2.7 KM (9 MIN) LOW-PASS FILTER
HEIGHT MSL (KM)
RH
T (C)
U M/S
V M/S
0.9-2.7 KM BAND PASS
0.9 KM(LT) AND 2.7 KM(DK) LOW-PASS FILTERS

Figure 19

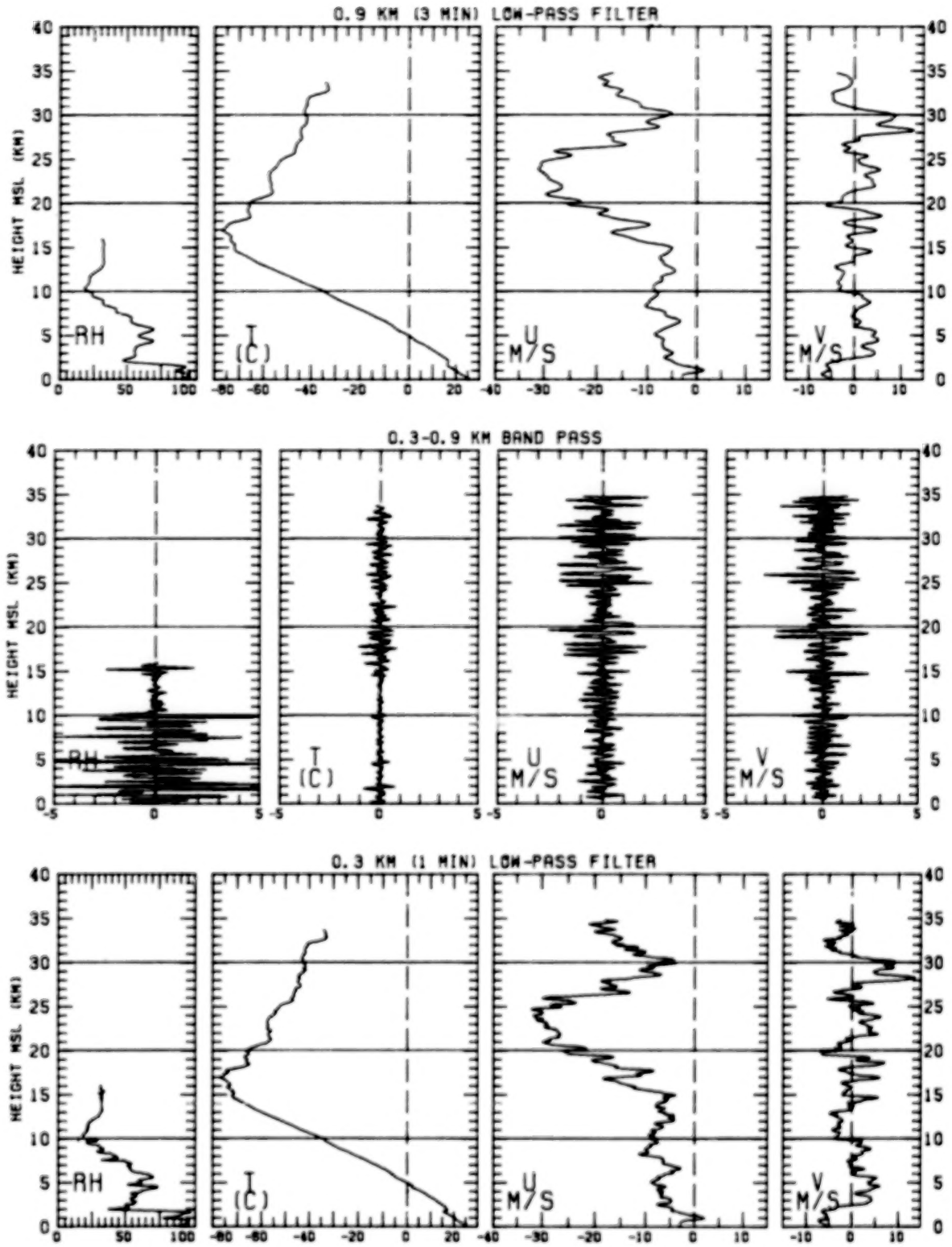
0.9 KM (3 MIN) LOW-PASS FILTER
0.3-0.9 KM BAND PASS
0.3 KM (1 MIN) LOW-PASS FILTER
HEIGHT MSL (KM)
RH
T (C)
U M/S
V M/S

Figure 19

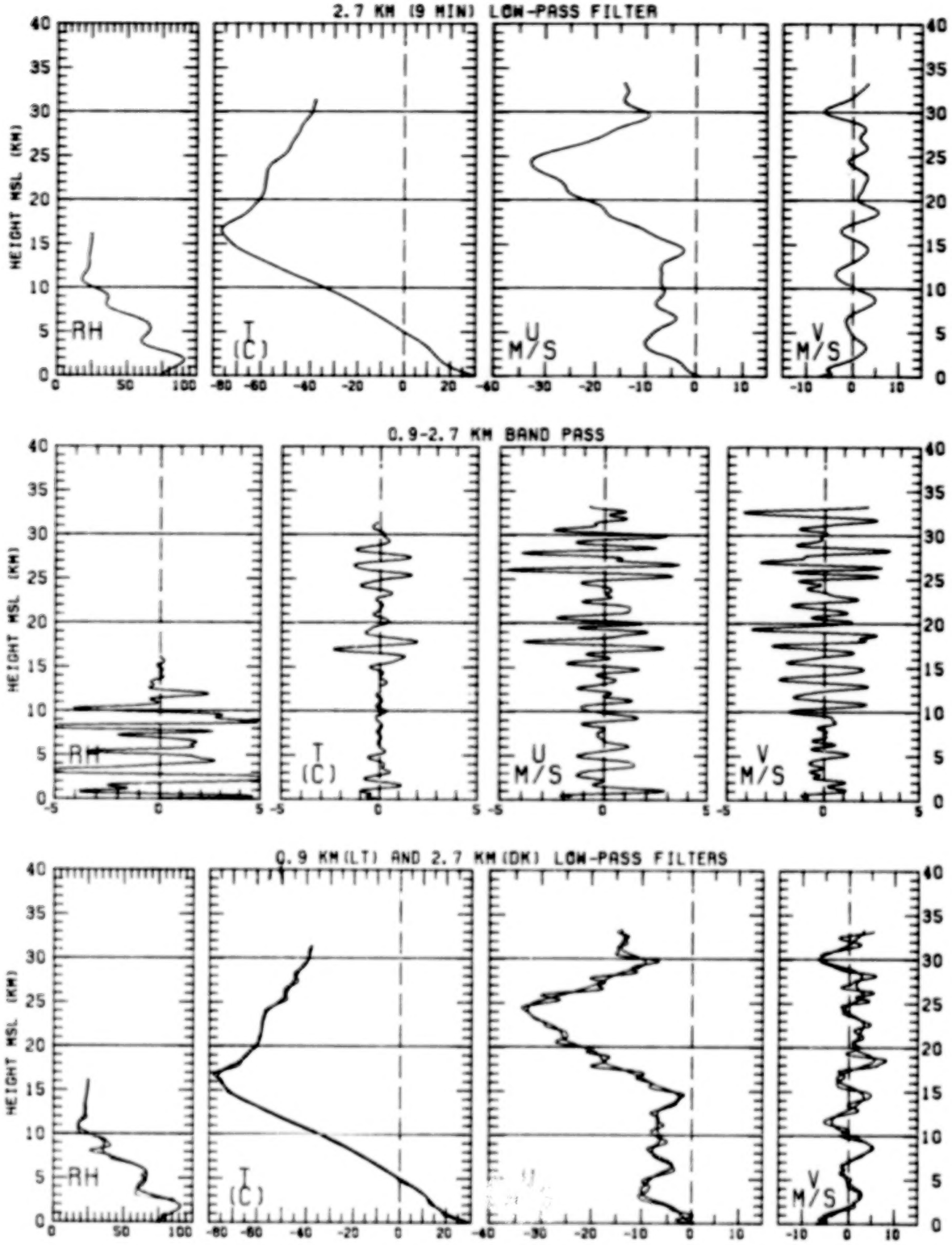
2.7 KM (9 MIN) LOW-PASS FILTER
HEIGHT MSL (KM)
RH
T (C)
U M/S
V M/S
0.9-2.7 KM BAND PASS
0.9 KM(LT) AND 2.7 KM(DK) LOW-PASS FILTERS

Figure 20

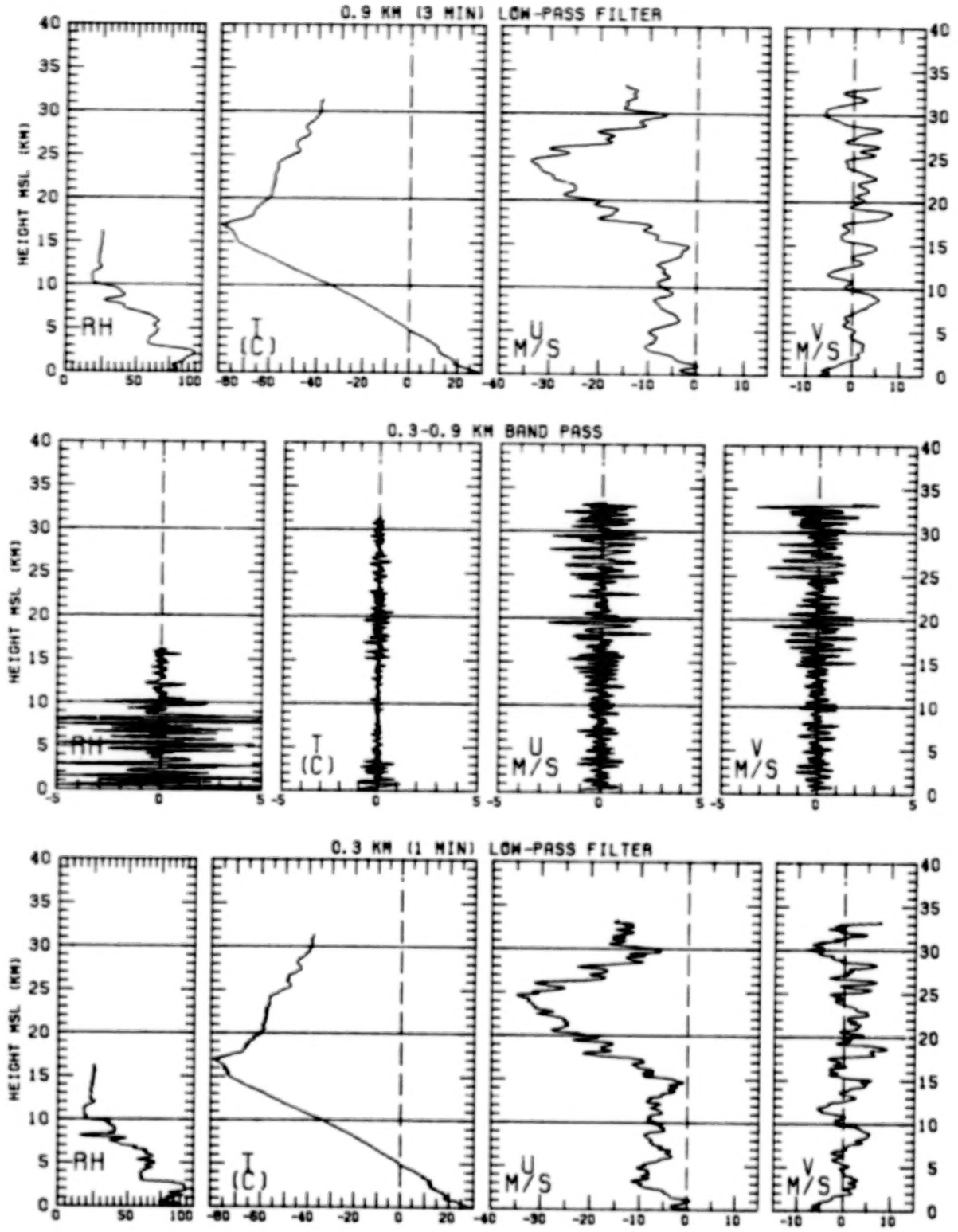
0.9 KM (3 MIN) LOW-PASS FILTER
HEIGHT MSL (KM)
RH
T (C)
U M/S
V M/S
0.3-0.9 KM BAND PASS
0.3 KM (1 MIN) LOW-PASS FILTER

Figure 20

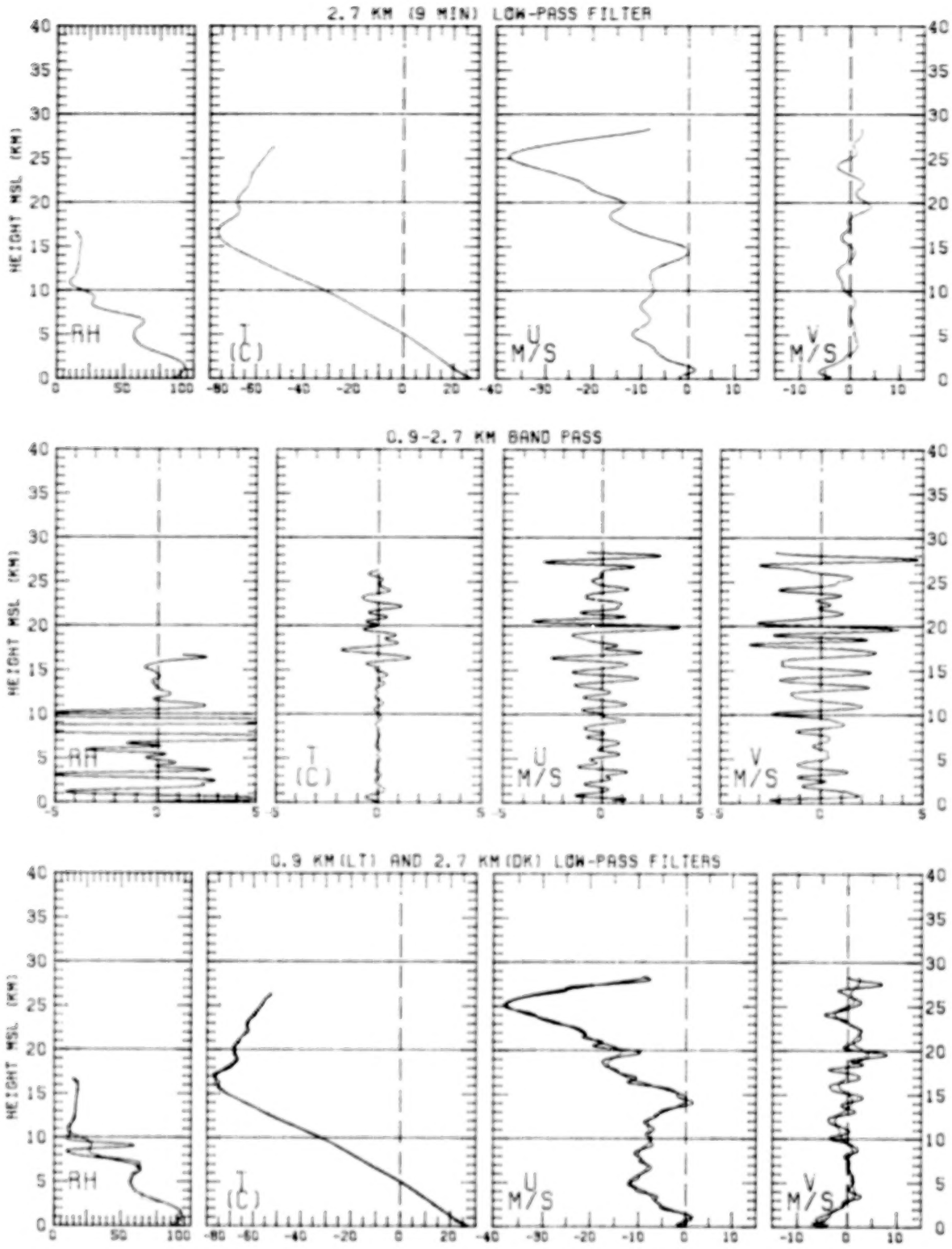
2.7 KM (9 MIN) LOW-PASS FILTER
0.9-2.7 KM BAND PASS
0.9 KM(LT) AND 2.7 KM(DK) LOW-PASS FILTERS
HEIGHT MSL (KM)
RH
T (C)
U M/S
V M/S

Figure 21

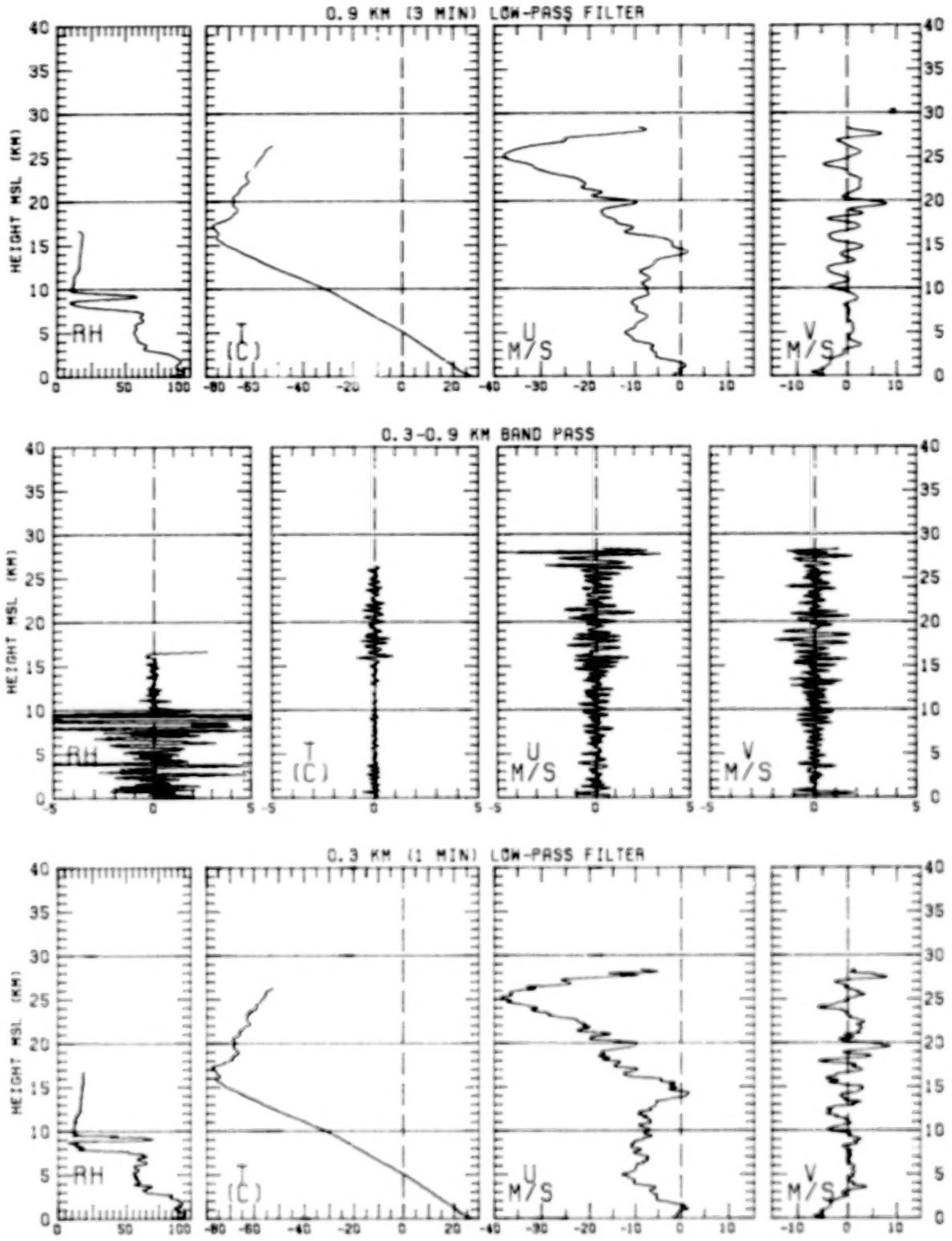
0.9 KM (3 MIN) LOW-PASS FILTER
HEIGHT MSL (KM)
RH
T (C)
U M/S
V M/S
0.3-0.9 KM BAND PASS
0.3 KM (1 MIN) LOW-PASS FILTER

Figure 21

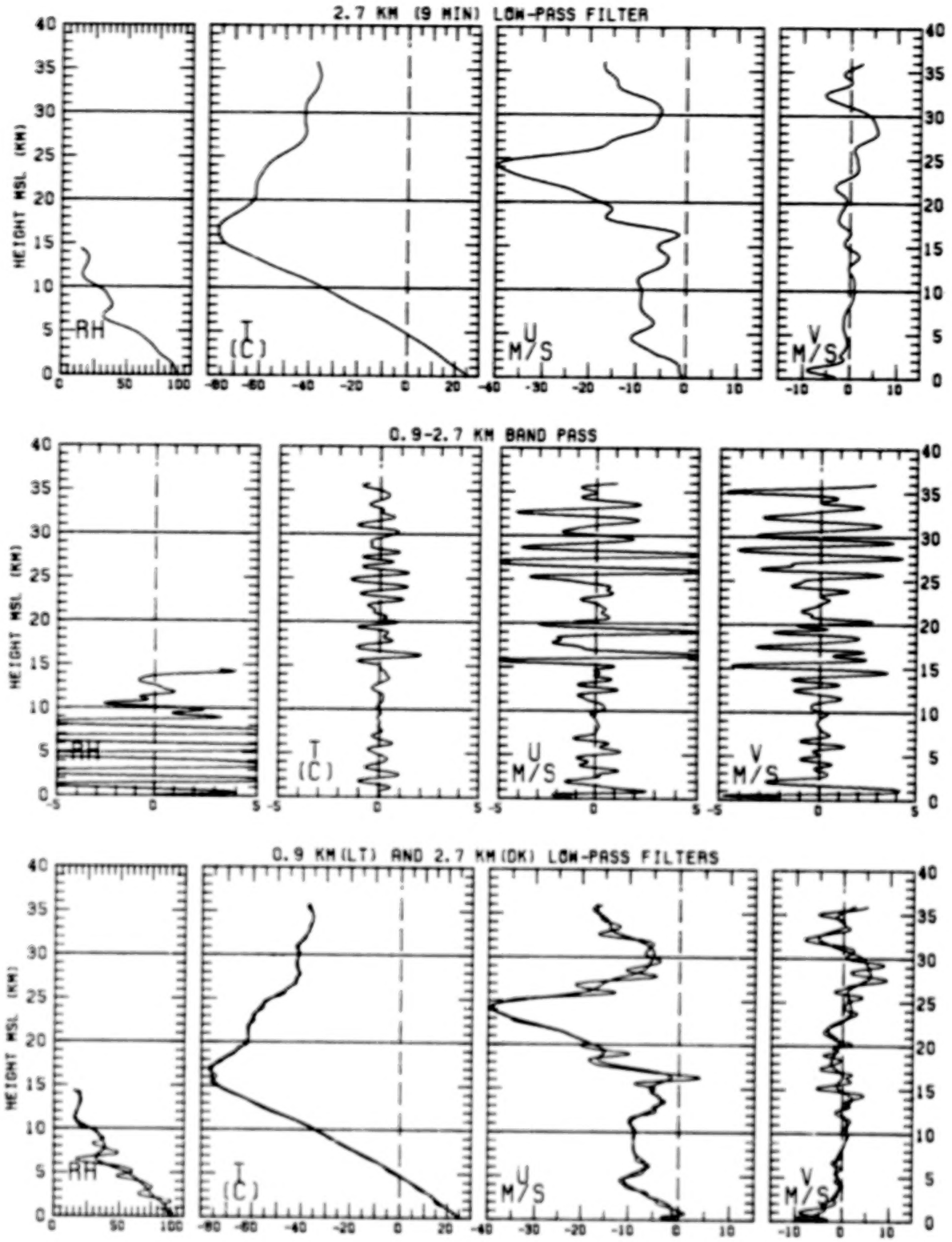
2.7 KM (9 MIN) LOW-PASS FILTER
HEIGHT MSL (KM)
RH
T (C)
U M/S
V M/S
0.9-2.7 KM BAND PASS
0.9 KM(LT) AND 2.7 KM(DK) LOW-PASS FILTERS

Figure 22

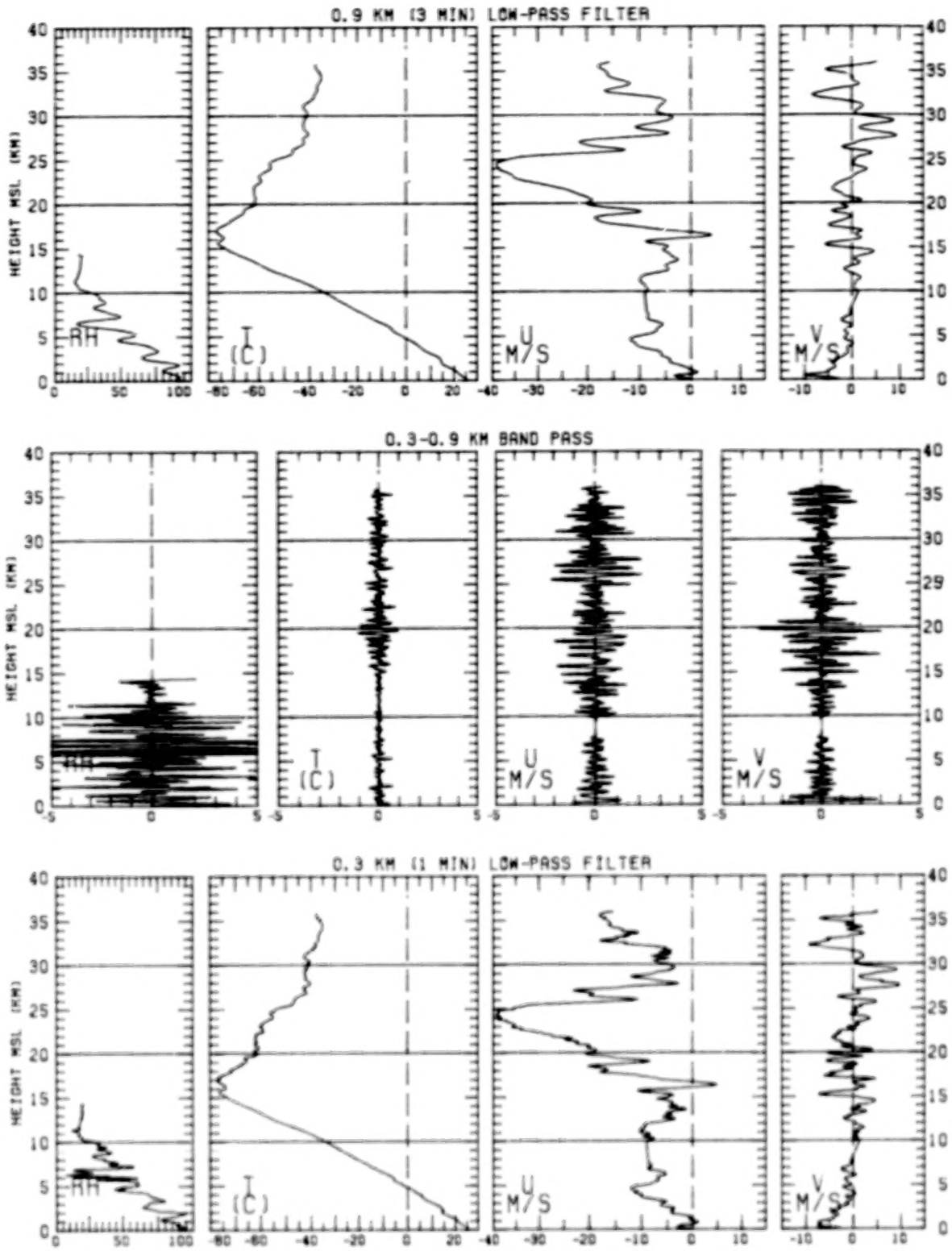
0.9 KM (3 MIN) LOW-PASS FILTER
HEIGHT MSL (KM)
RH
T (C)
U M/S
V M/S
0.3-0.9 KM BAND PASS
0.3 KM (1 MIN) LOW-PASS FILTER

Figure 22

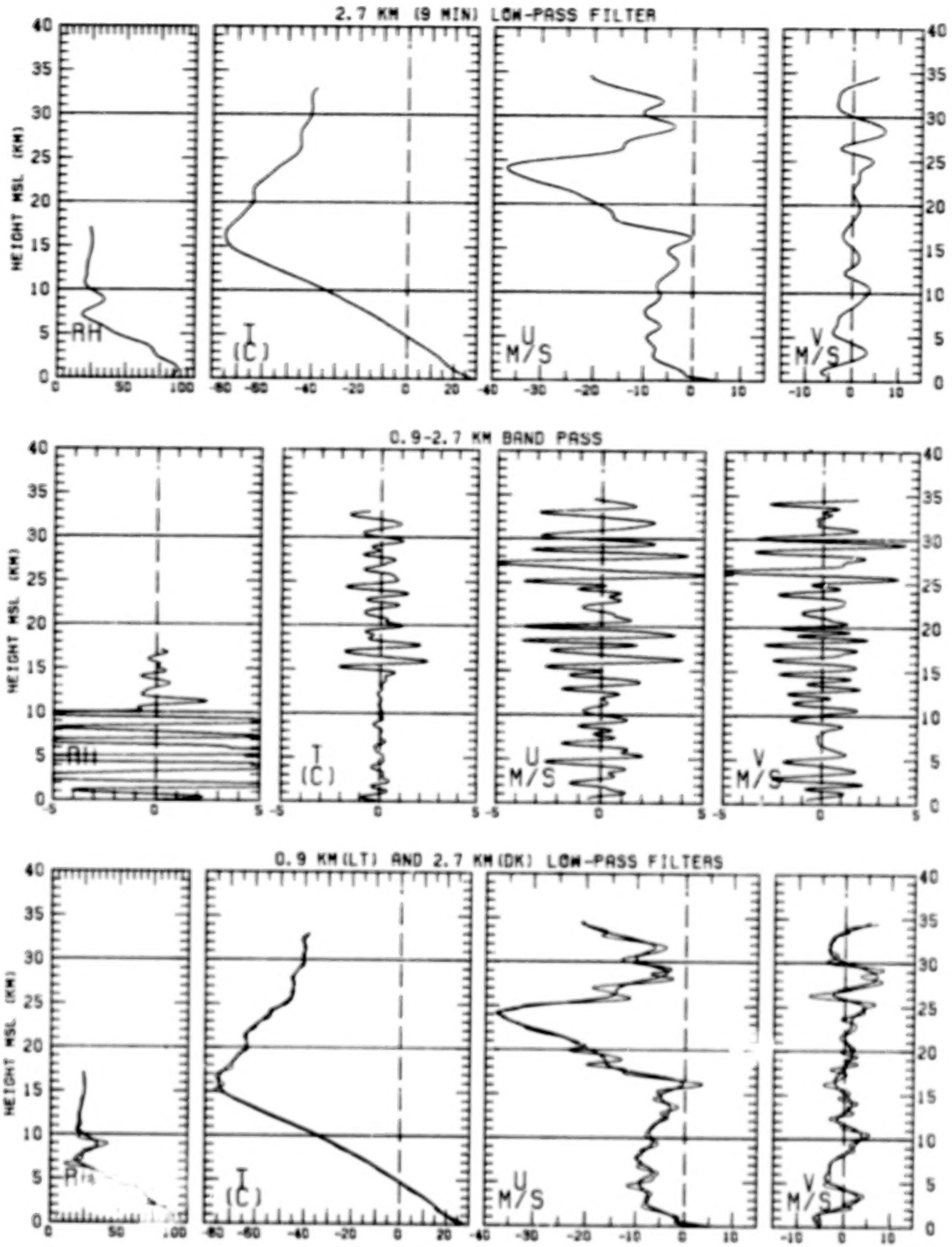
2.7 KM (9 MIN) LOW-PASS FILTER
HEIGHT MSL (KM)
RH
T (C)
U M/S
V M/S
0.9-2.7 KM BAND PASS
0.9 KM(LT) AND 2.7 KM(DK) LOW-PASS FILTERS

Figure 23

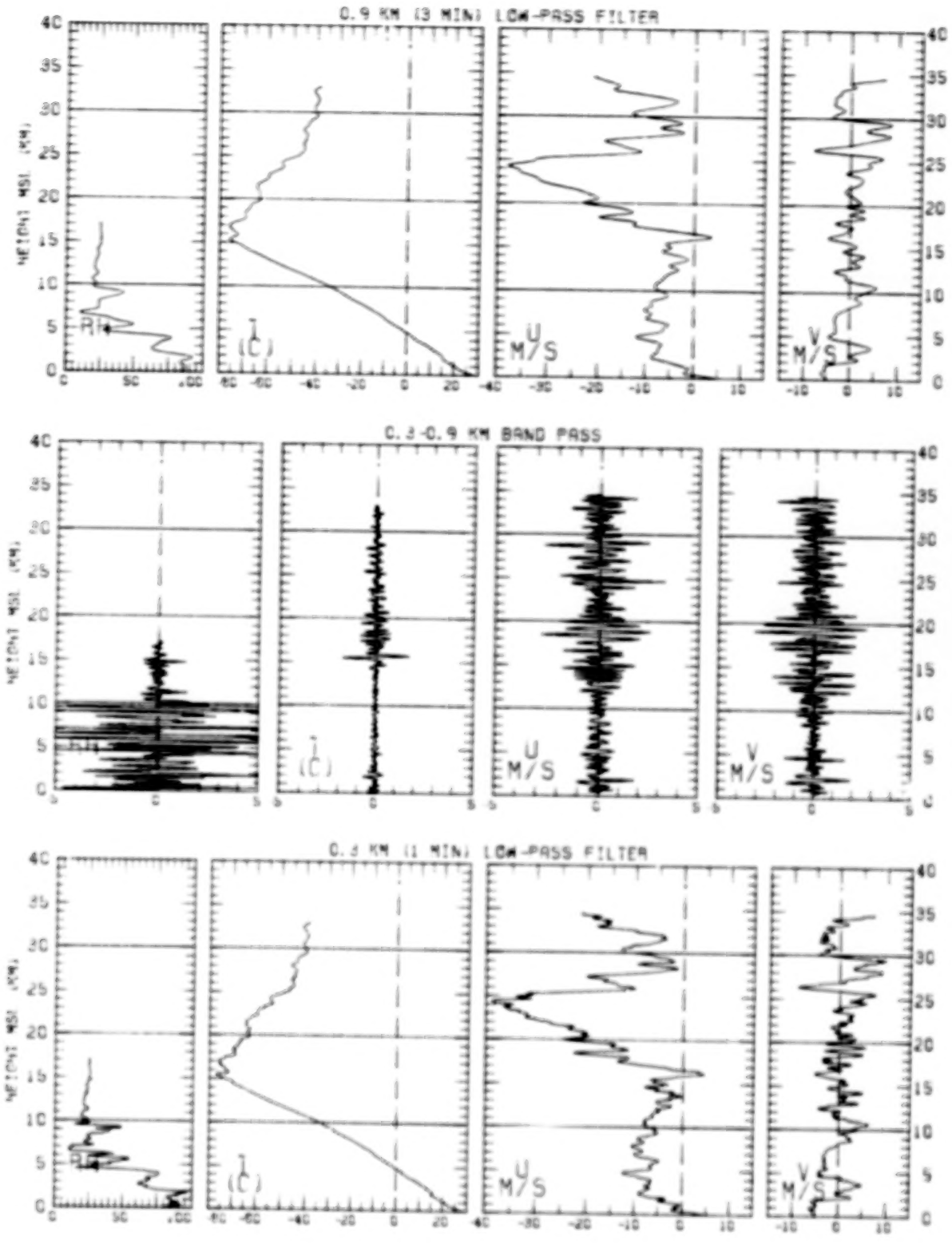
0.9 KM (3 MIN) LOW-PASS FILTER
0.3-0.9 KM BAND PASS
0.3 KM (1 MIN) LOW-PASS FILTER
HEIGHT MSL (KM)
RH
T (C)
U M/S
V M/S

Figure 23

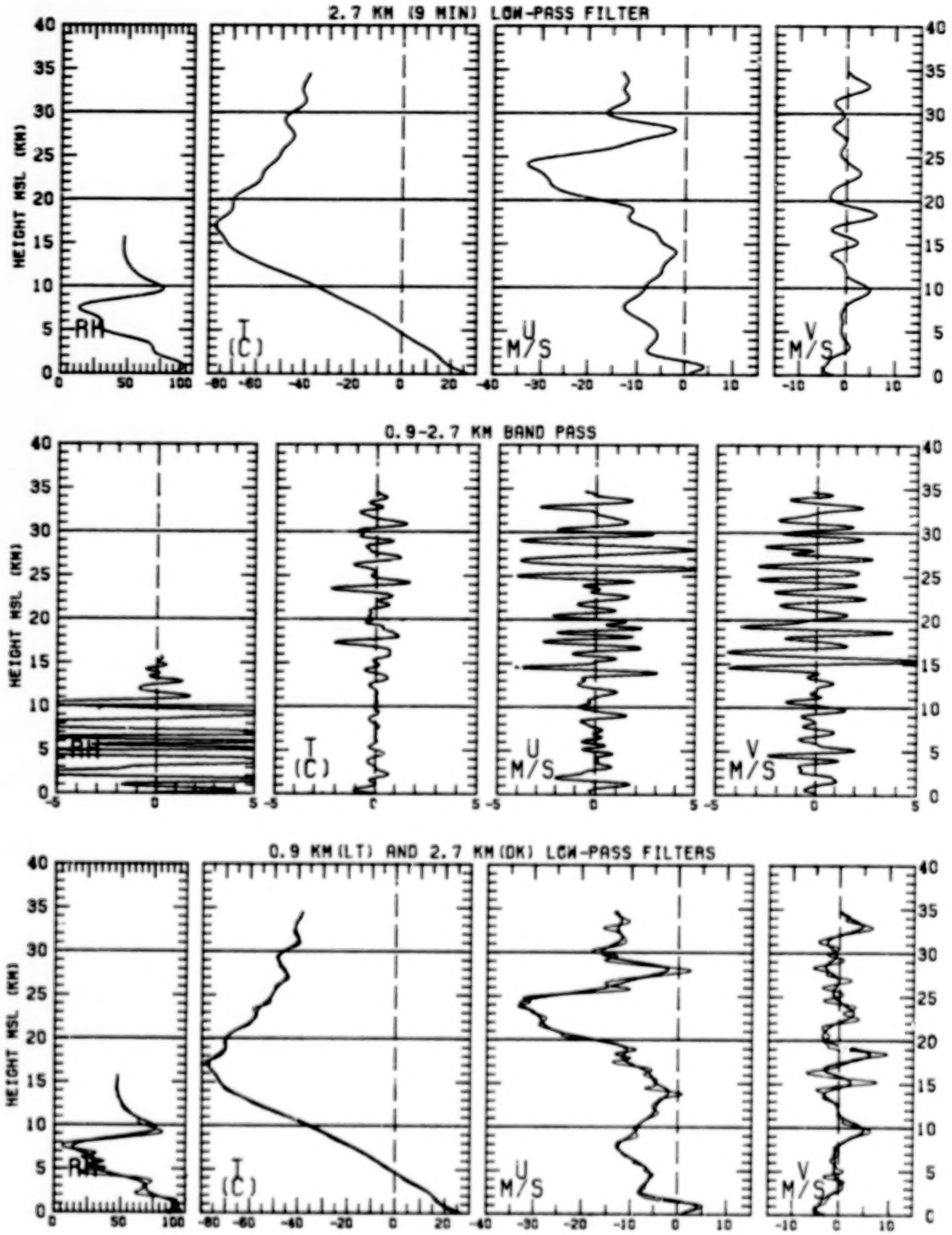
2.7 KM (9 MIN) LOW-PASS FILTER
HEIGHT MSL (KM)
RH
T (C)
U M/S
V M/S
0.9-2.7 KM BAND PASS
0.9 KM(LT) AND 2.7 KM(DK) LOW-PASS FILTERS

Figure 24

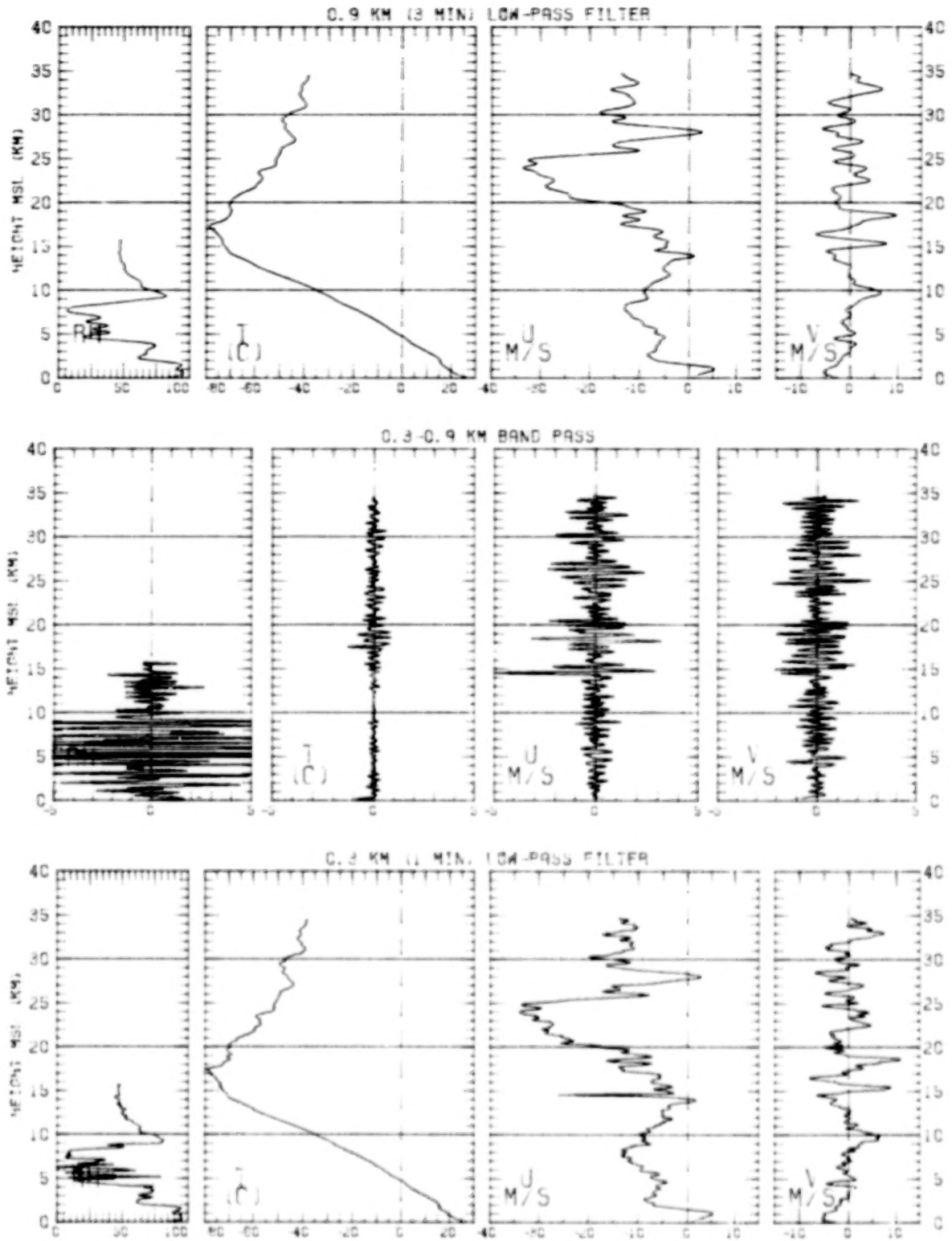
0.9 KM (3 MIN) LOW-PASS FILTER
HEIGHT MSL (KM)
R
T (C)
U M/S
V M/S
0.3-0.9 KM BAND PASS
0.3 KM (1 MIN) LOW-PASS FILTER

Figure 24

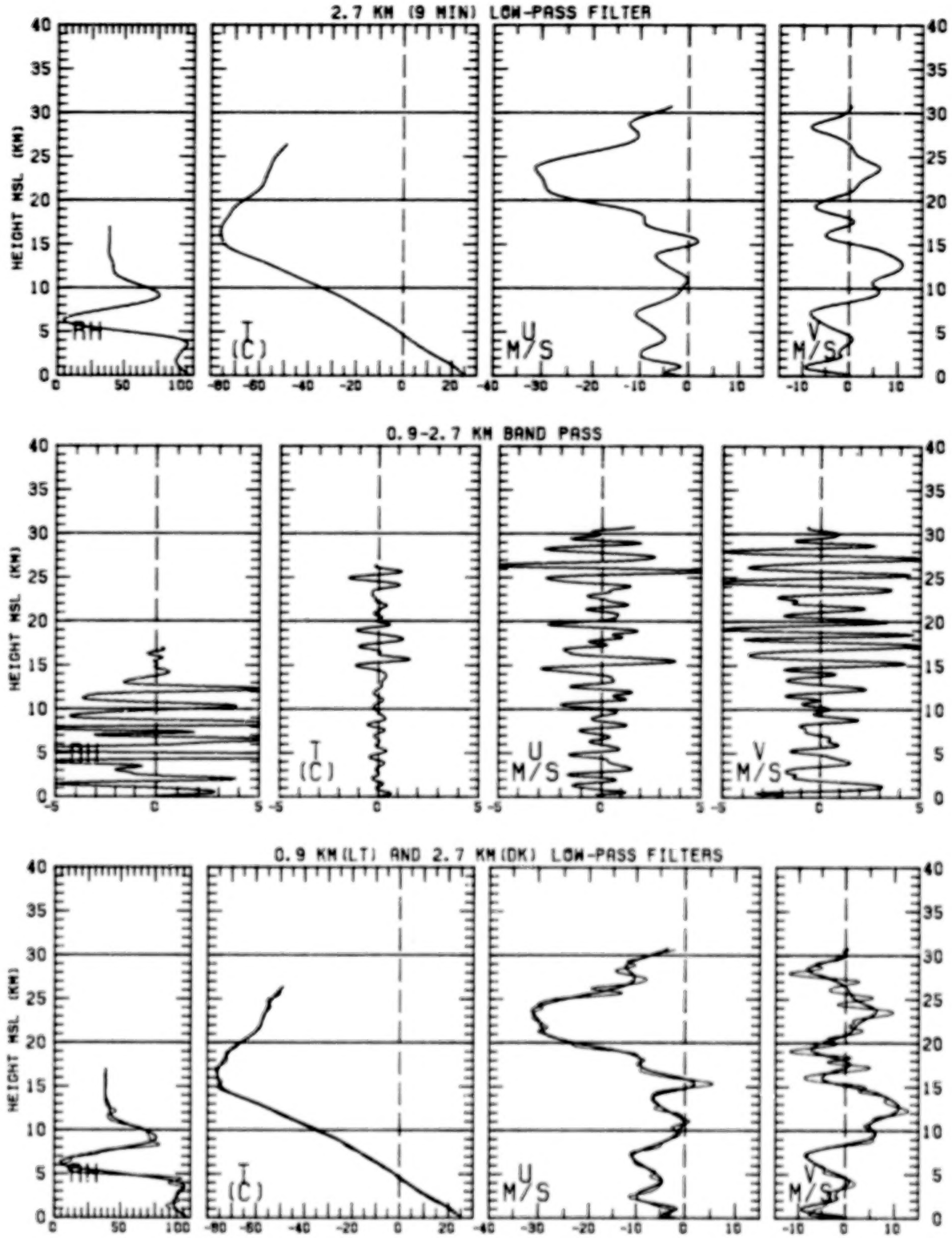
2.7 KM (9 MIN) LOW-PASS FILTER
HEIGHT MSL (KM)
RH
T (C)
U M/S
V M/S
0.9-2.7 KM BAND PASS
0.9 KM(LT) AND 2.7 KM(DK) LOW-PASS FILTERS

Figure 25

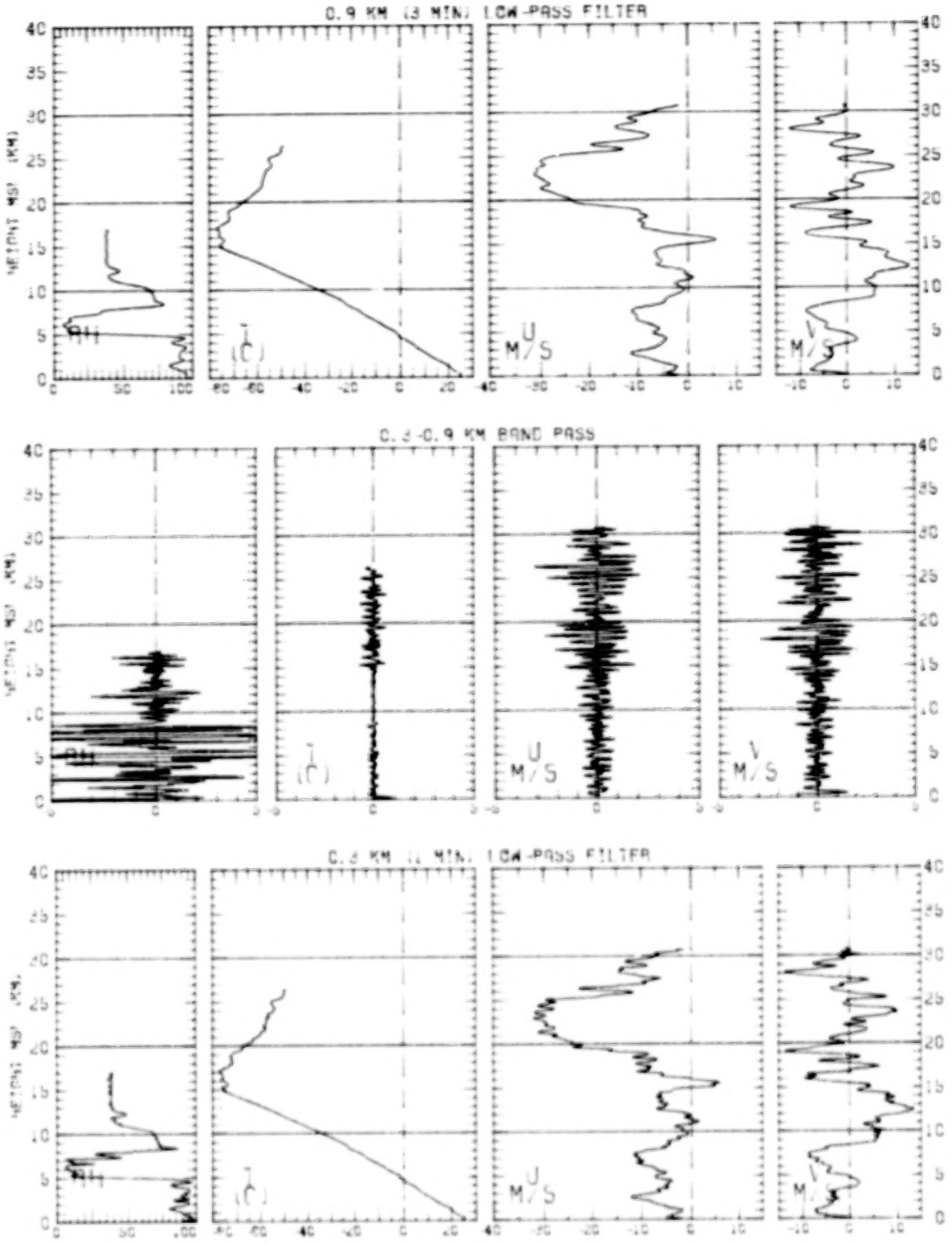
0.9 KM (3 MIN) LOW-PASS FILTER
0.3-0.9 KM BAND PASS
0.3 KM (1 MIN) LOW-PASS FILTER
HEIGHT MSL (KM)
RH
T (C)
U M/S
V M/S

Figure 25

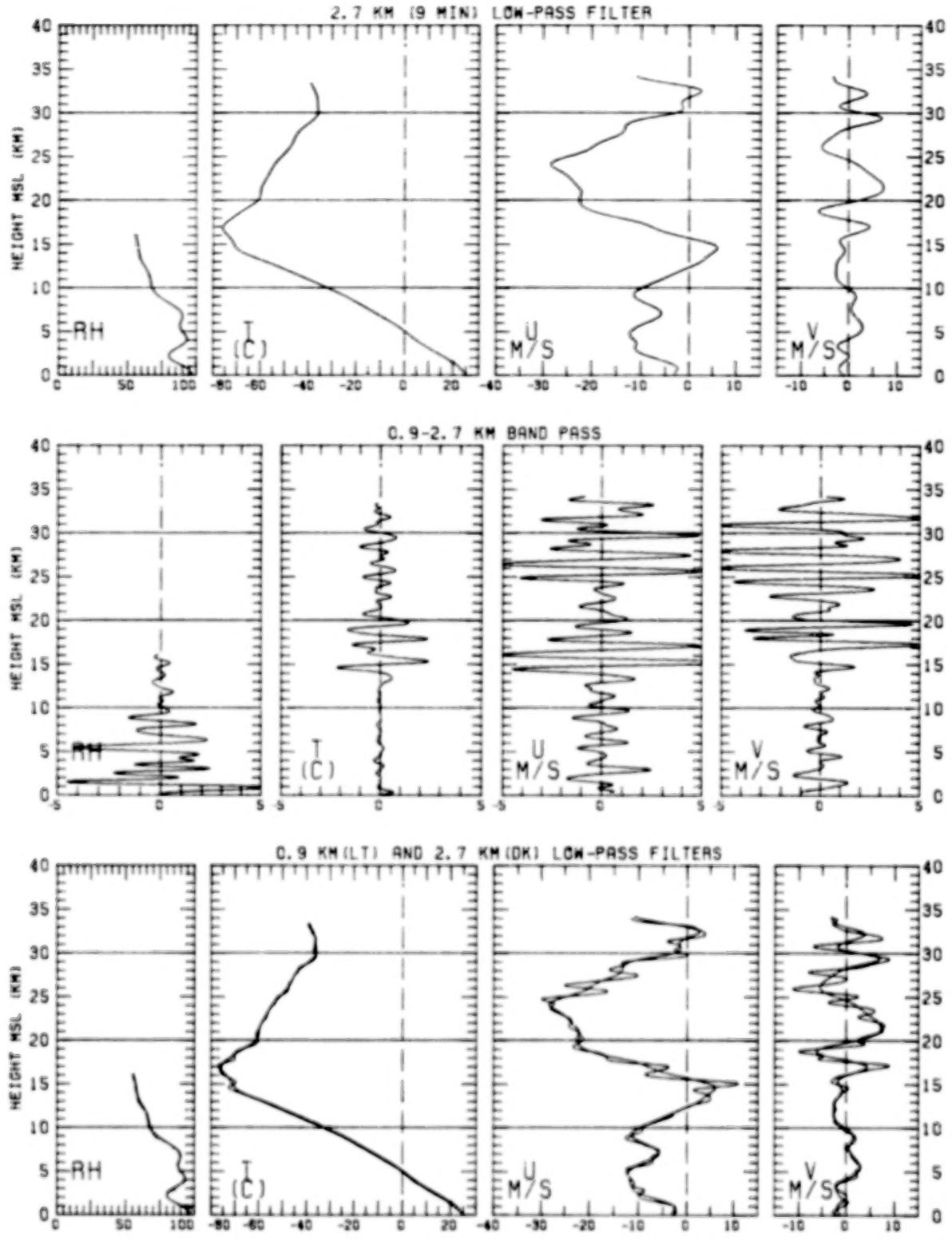
2.7 KM (9 MIN) LOW-PASS FILTER
HEIGHT MSL (KM)
RH
T (C)
U M/S
V M/S
0.9-2.7 KM BAND PASS
0.9 KM(LT) AND 2.7 KM(DK) LOW-PASS FILTERS

Figure 26

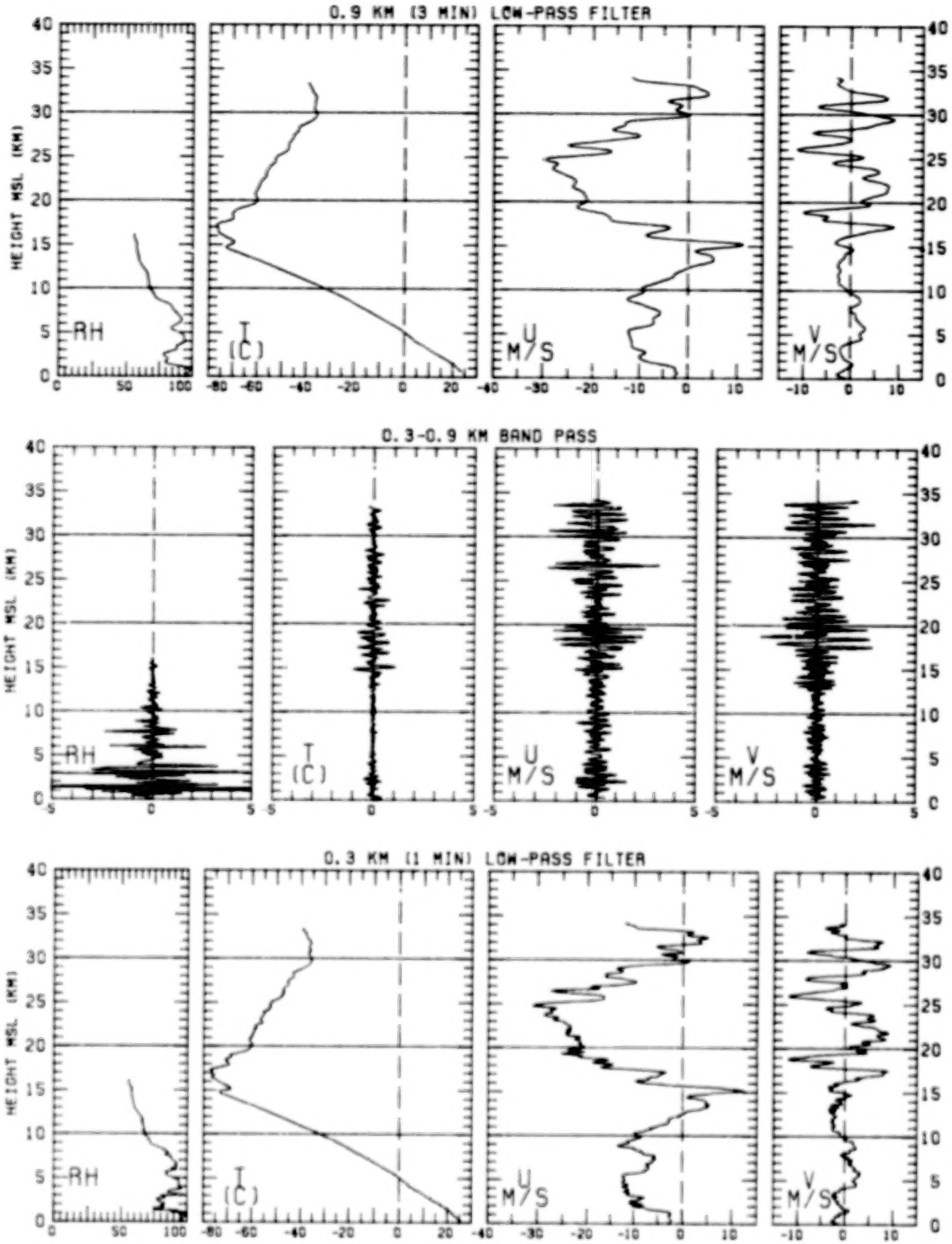
0.9 KM (3 MIN) LOW-PASS FILTER
HEIGHT MSL (KM)
RH
T (C)
U M/S
V M/S
0.3-0.9 KM BAND PASS
0.3 KM (1 MIN) LOW-PASS FILTER

Figure 26

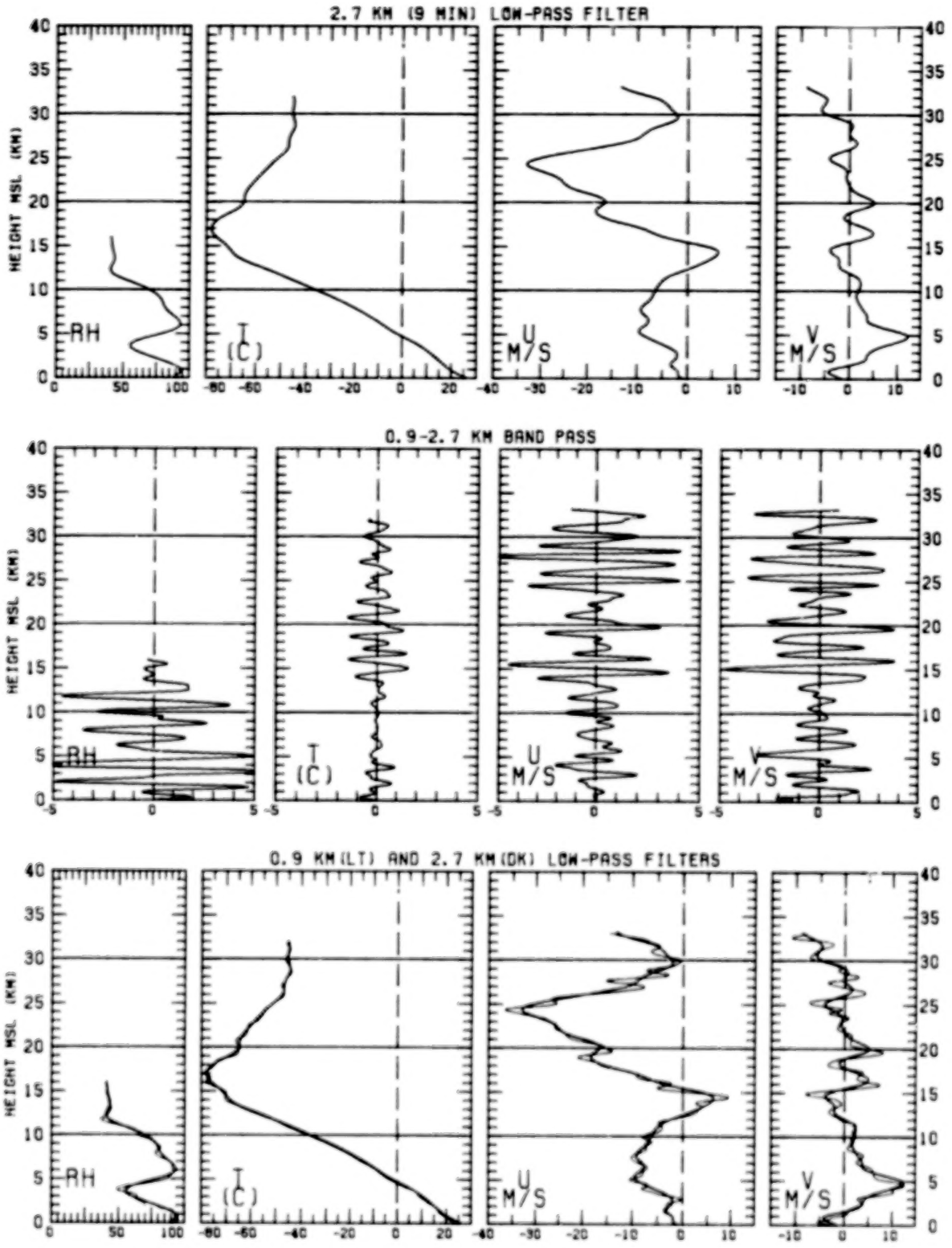
2.7 KM (9 MIN) LOW-PASS FILTER
0.9-2.7 KM BAND PASS
0.9 KM(LT) AND 2.7 KM(DK) LOW-PASS FILTERS
HEIGHT MSL (KM)
RH
T (C)
U M/S
V M/S

Figure 27

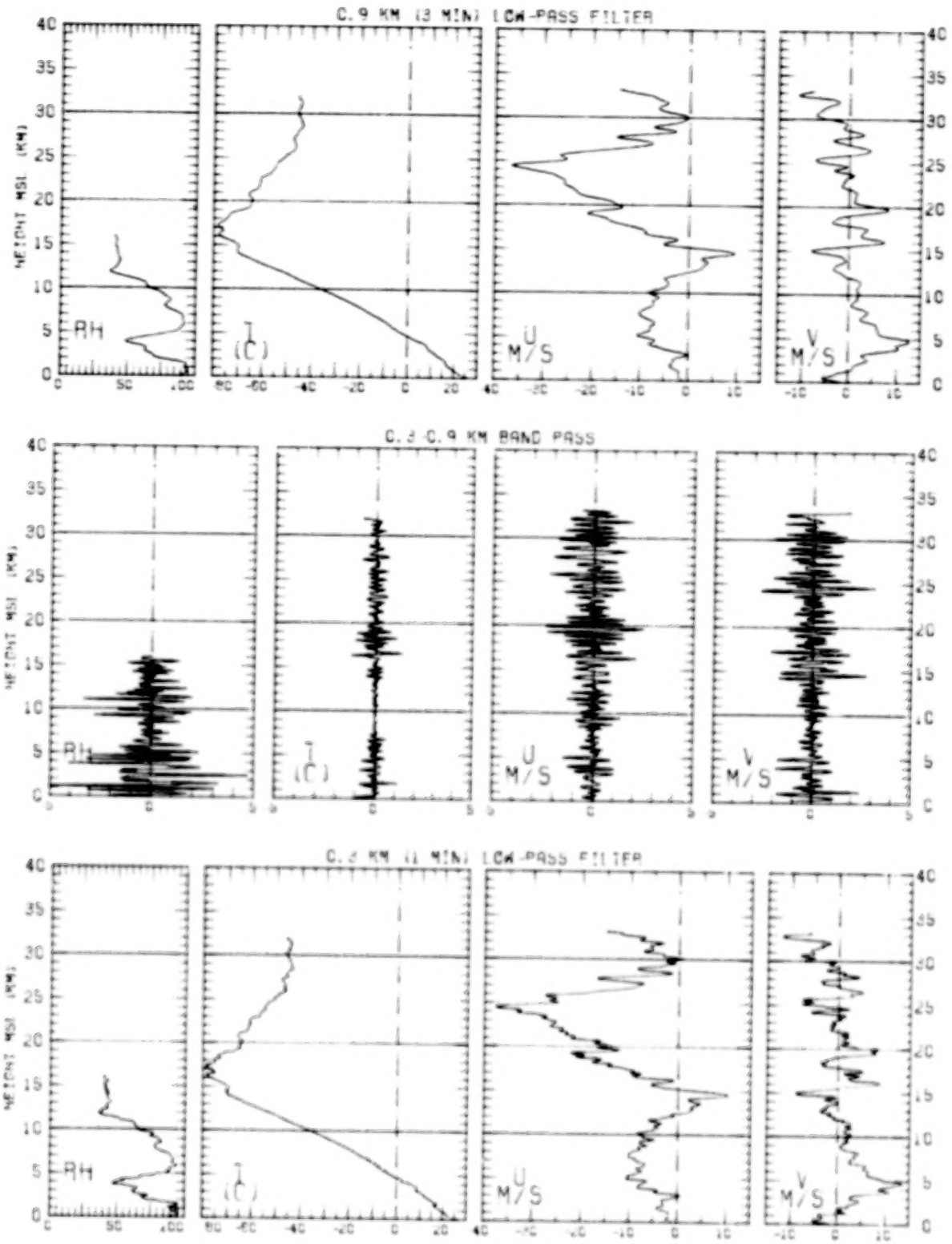
0.9 KM (3 MIN) LOW-PASS FILTER
HEIGHT MSL (KM)
RH
T (C)
U M/S
V M/S
0.3 0.9 KM BAND PASS
0.3 KM (1 MIN) LOW-PASS FILTER

Figure 27

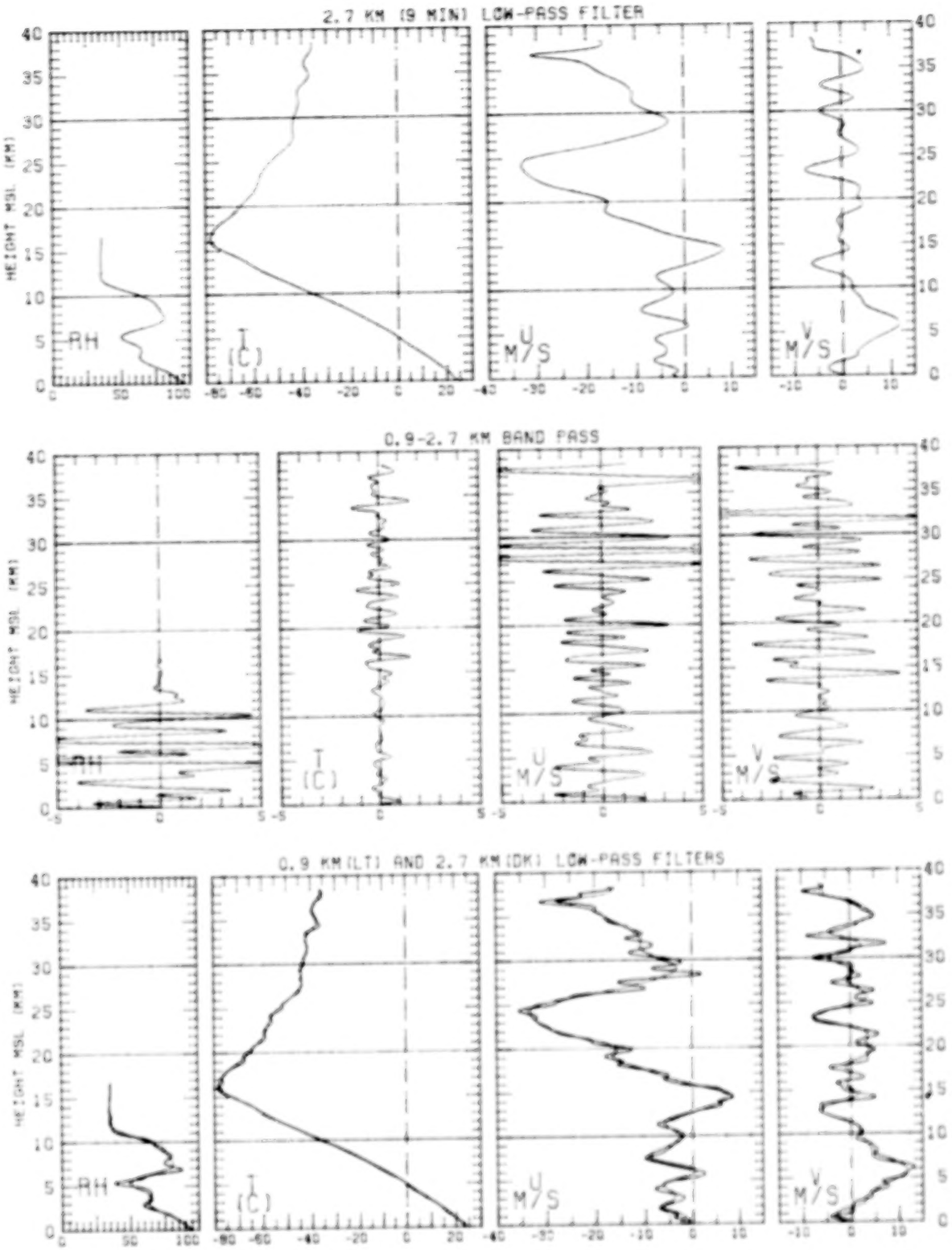
2.7 KM (9 MIN) LOW-PASS FILTER
HEIGHT MSL (KM)
RH
T (C)
U M/S
V M/S
0.9-2.7 KM BAND PASS
0.9 KM (LT) AND 2.7 KM (DK) LOW-PASS FILTERS

Figure 28

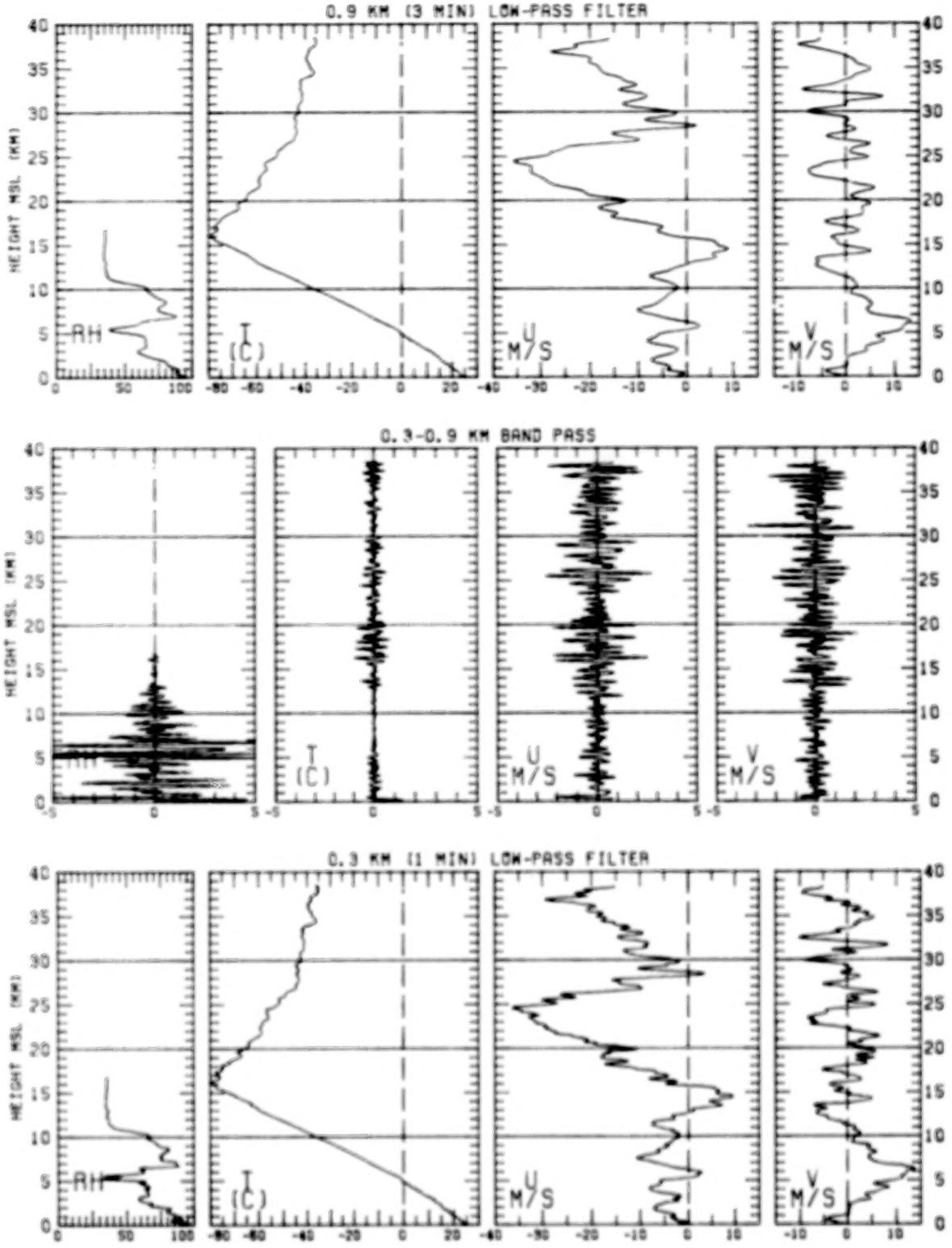
0.9 KM (3 MIN) LOW-PASS FILTER
0.3-0.9 KM BAND PASS
0.3 KM (1 MIN) LOW-PASS FILTER
HEIGHT MSL (KM)
RH
T (C)
U M/S
V M/S

Figure 28

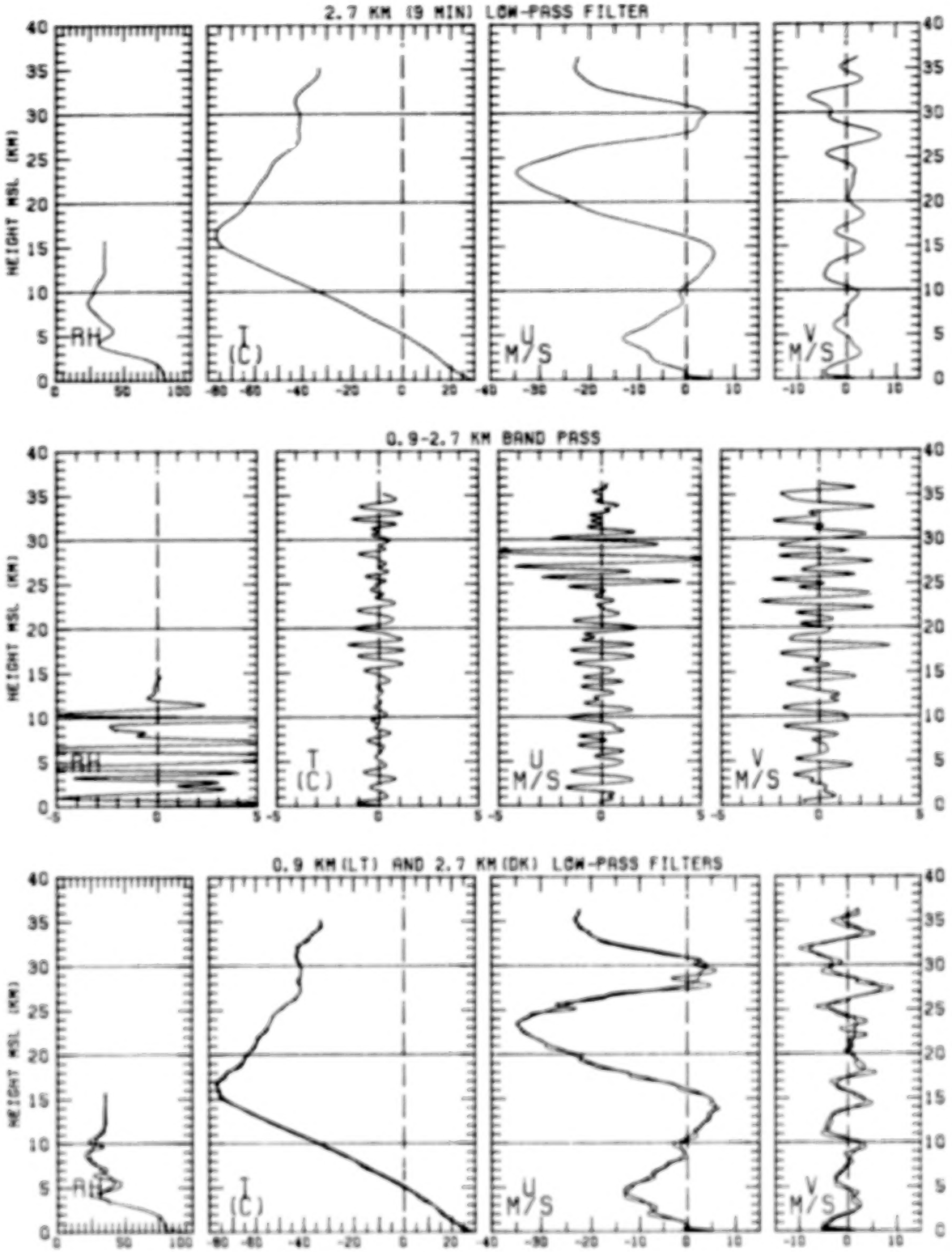
2.7 KM (9 MIN) LOW-PASS FILTER
HEIGHT MSL (KM)
RH
T (C)
U M/S
V M/S
0.9-2.7 KM BAND PASS
0.9 KM (LT) AND 2.7 KM (DK) LOW-PASS FILTERS

Figure 29

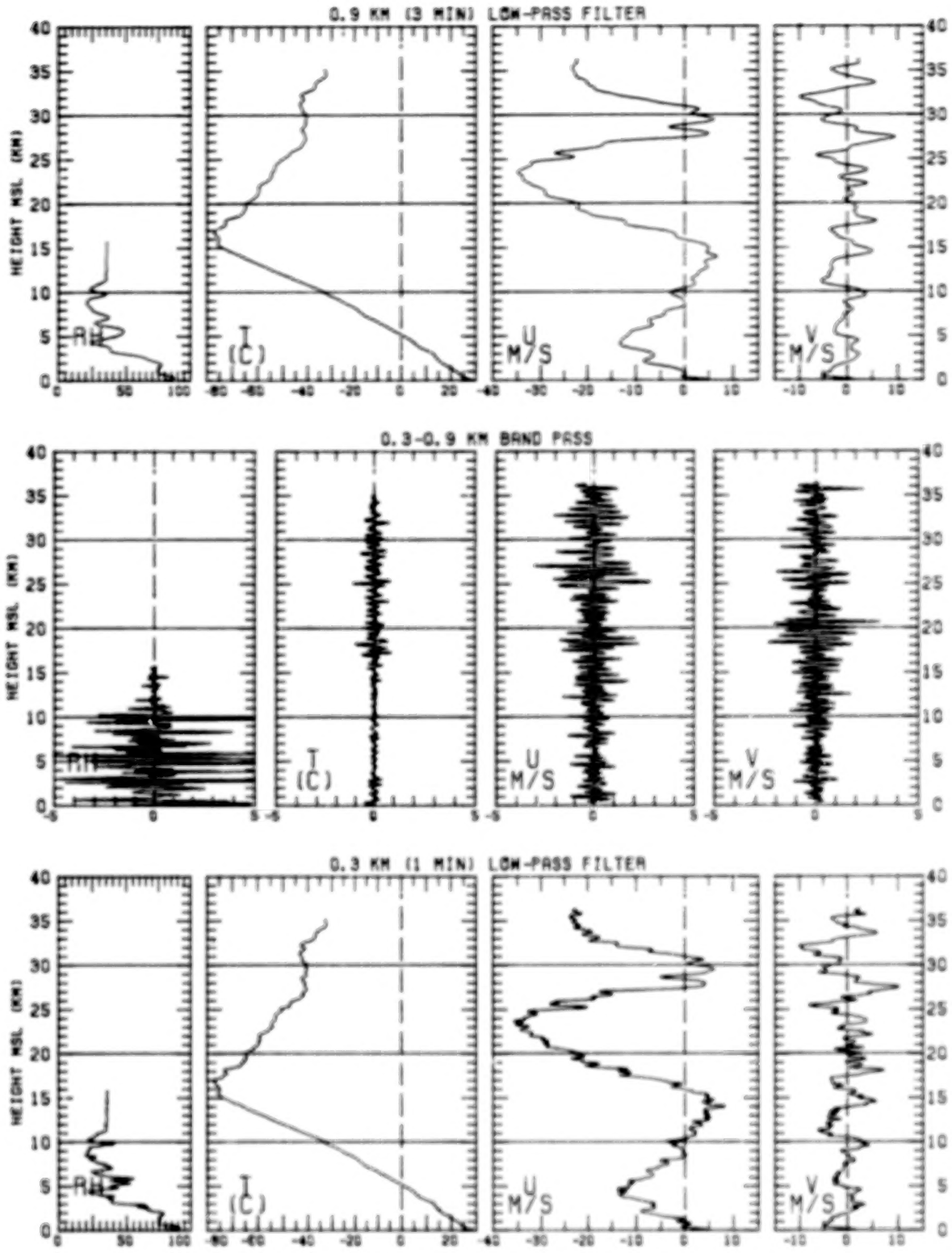
0.9 KM (3 MIN) LOW-PASS FILTER
0.3-0.9 KM BAND PASS
0.3 KM (1 MIN) LOW-PASS FILTER
HEIGHT MSL (KM)
RH
T (C)
U M/S
V M/S

Figure 29

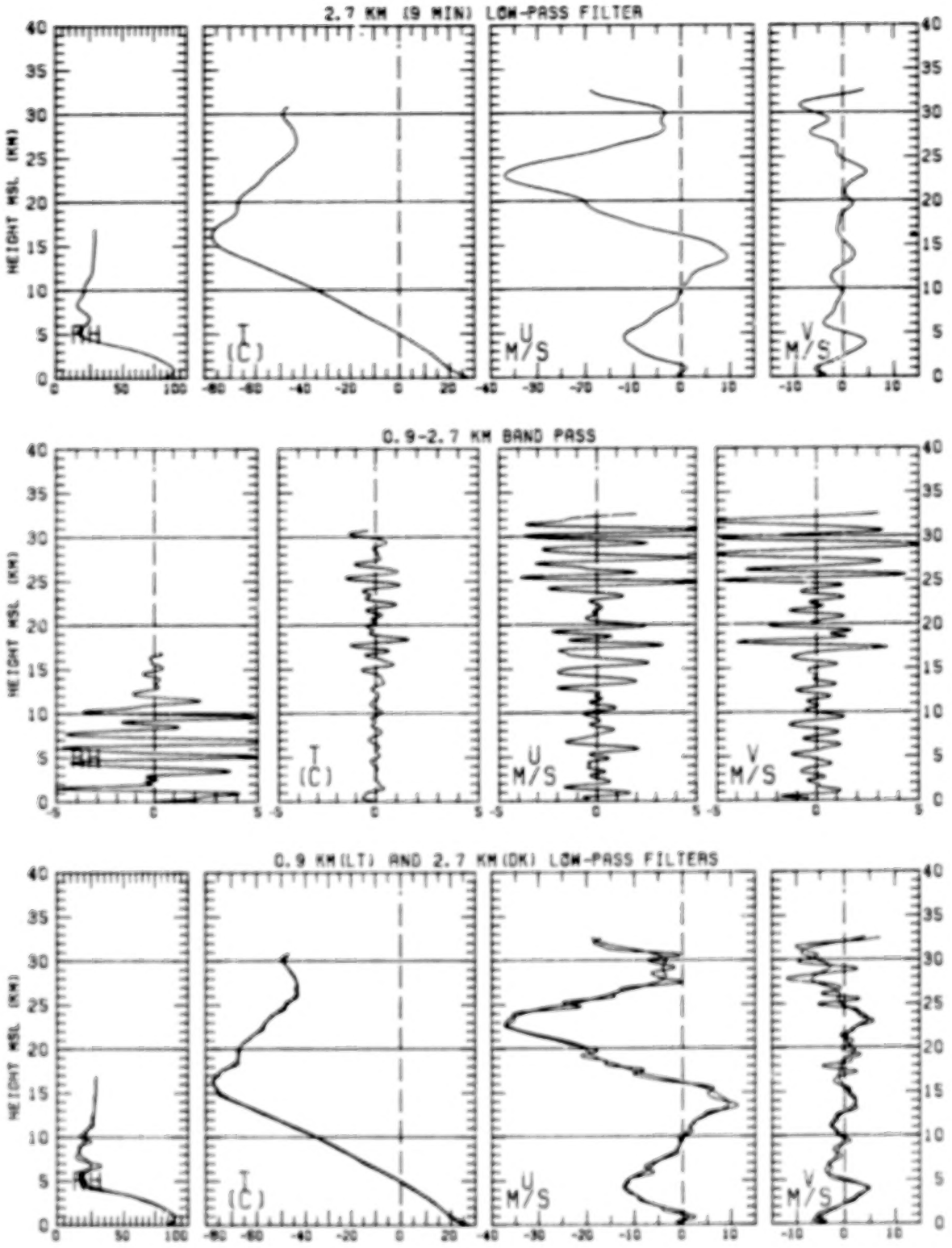
2.7 KM (9 MIN) LOW-PASS FILTER
HEIGHT MSL (KM)
RH
T (C)
U M/S
V M/S
0.9-2.7 KM BAND PASS
0.9 KM(LT) AND 2.7 KM(DK) LOW-PASS FILTERS

Figure 30

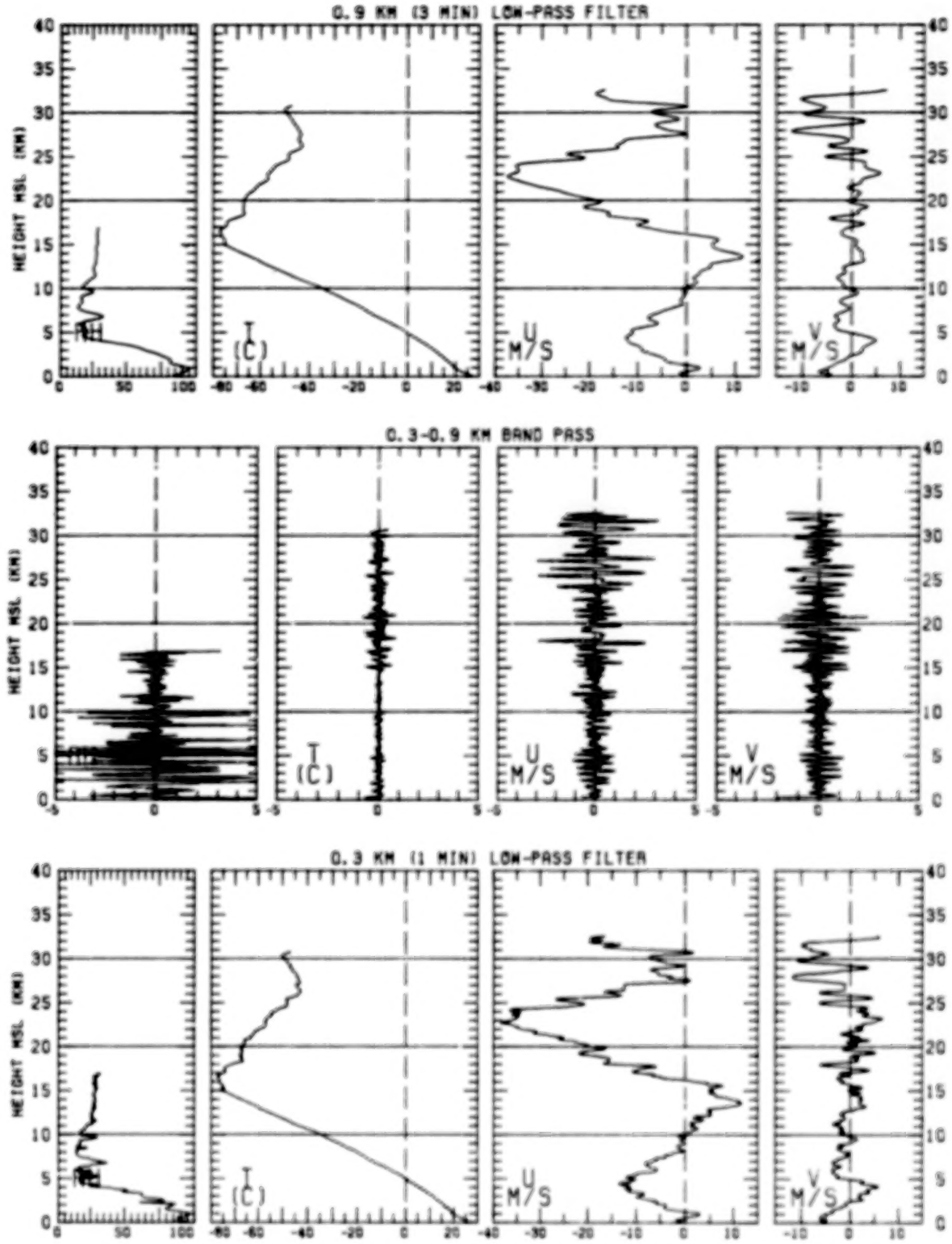
0.9 KM (3 MIN) LOW-PASS FILTER
0.3-0.9 KM BAND PASS
0.3 KM (1 MIN) LOW-PASS FILTER
HEIGHT MSL (KM)
RH
T (C)
U M/S
V M/S

Figure 30

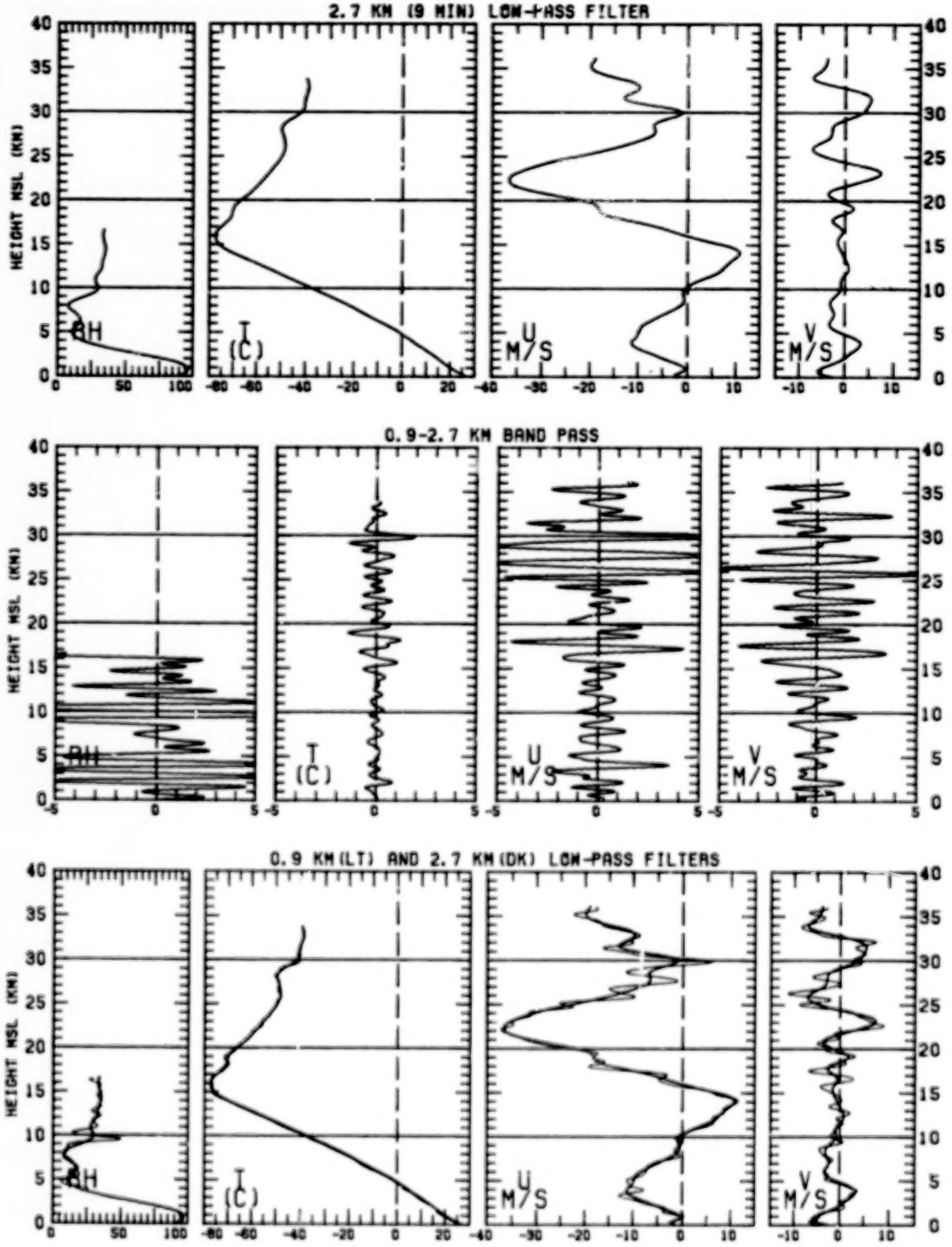
2.7 KM (9 MIN) LOW-PASS FILTER
0.9-2.7 KM BAND PASS
0.9 KM(LT) AND 2.7 KM(DK) LOW-PASS FILTERS
HEIGHT MSL (KM)
RH
T (C)
U M/S
V M/S

Figure 31

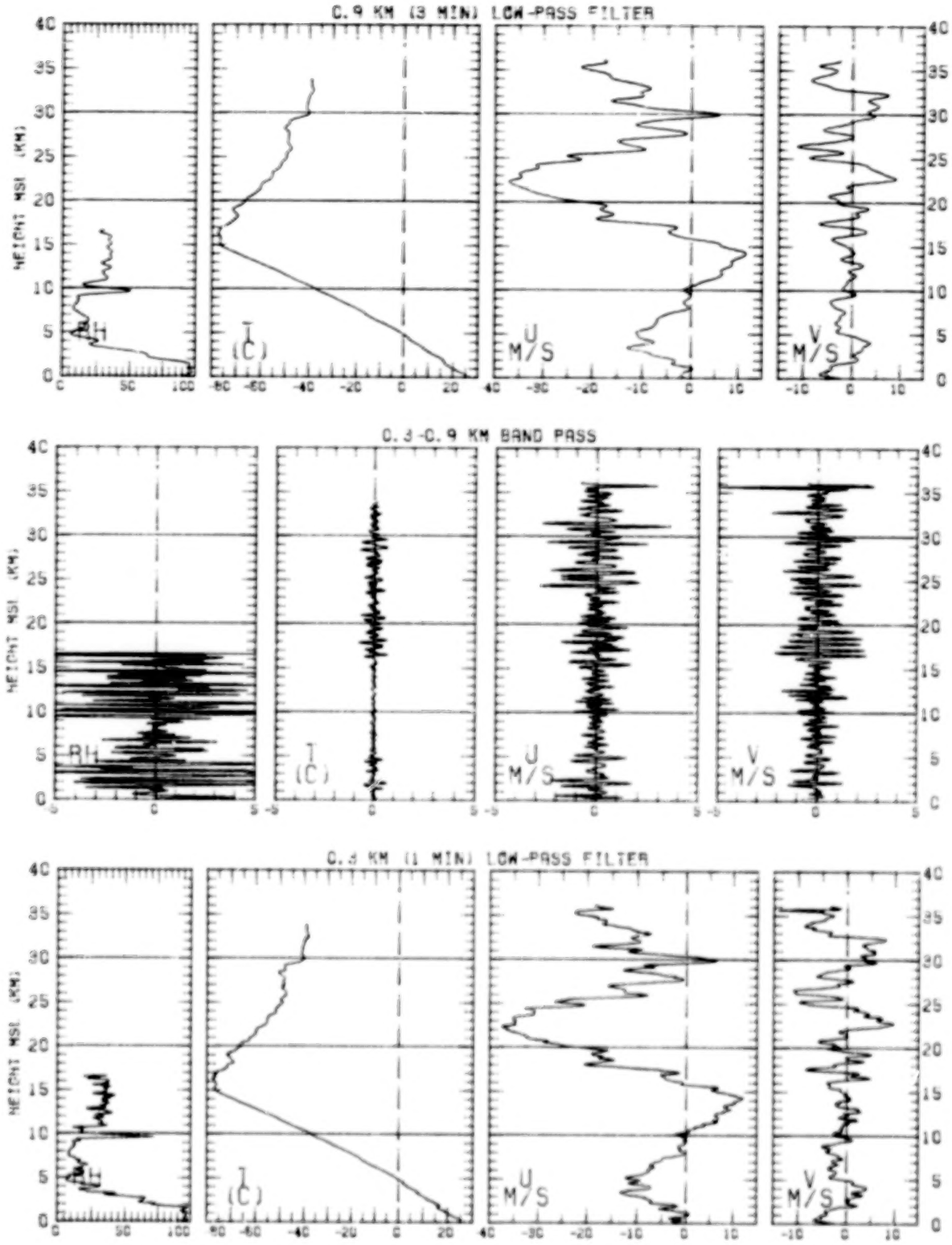
0.9 KM (3 MIN) LOW-PASS FILTER
HEIGHT MSL (KM)
RH
T (C)
U M/S
V M/S
0.3-0.9 KM BAND PASS
HEIGHT MSL (KM)
RH
T (C)
U M/S
V M/S
0.3 KM (1 MIN) LOW-PASS FILTER
HEIGHT MSL (KM)
RH
T (C)
U M/S
V M/S

Figure 31

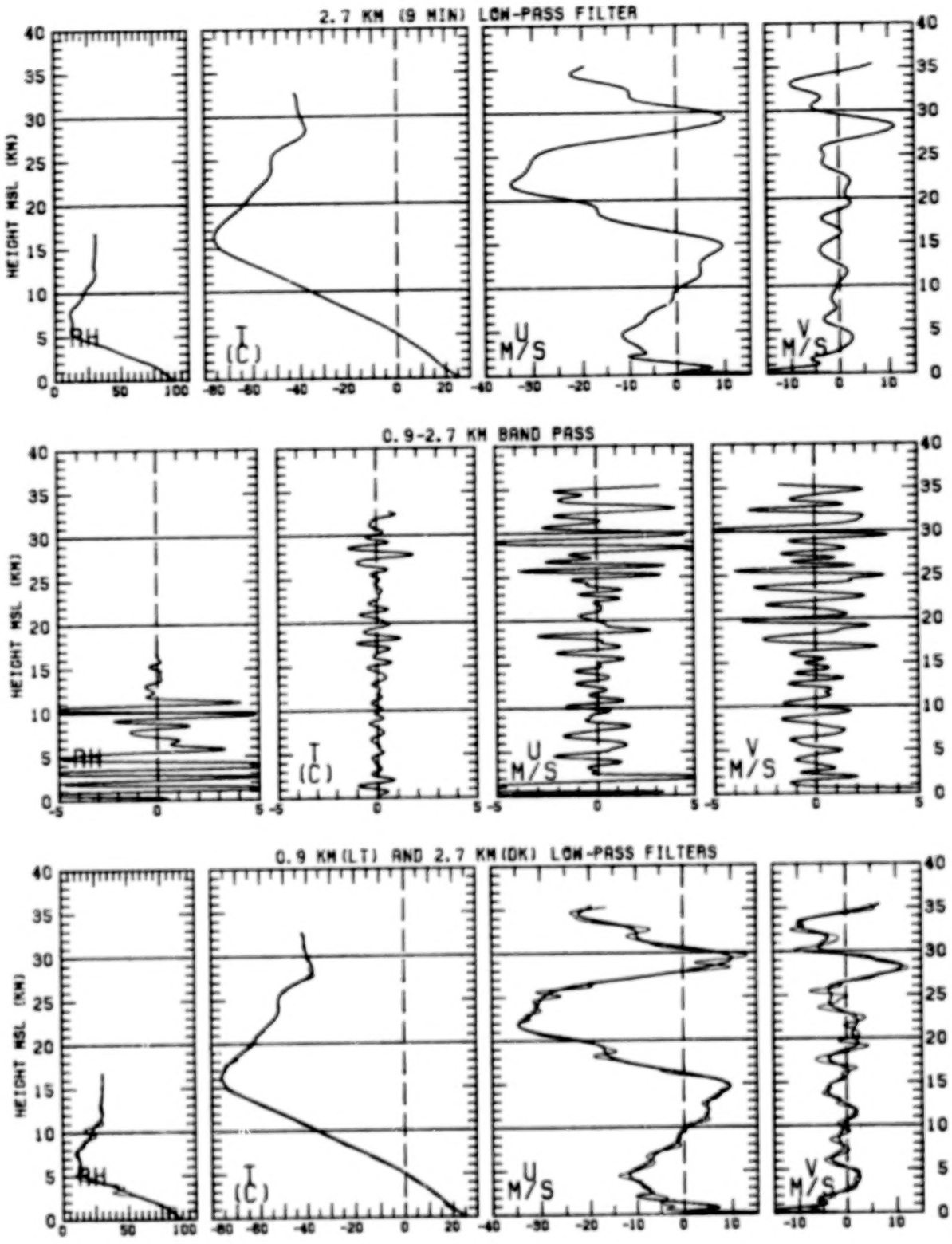
2.7 KM (9 MIN) LOW-PASS FILTER
HEIGHT MSL (KM)
RH
T (C)
U M/S
V M/S
0.9-2.7 KM BAND PASS
0.9 KM(LT) AND 2.7 KM(DK) LOW-PASS FILTERS

Figure 32

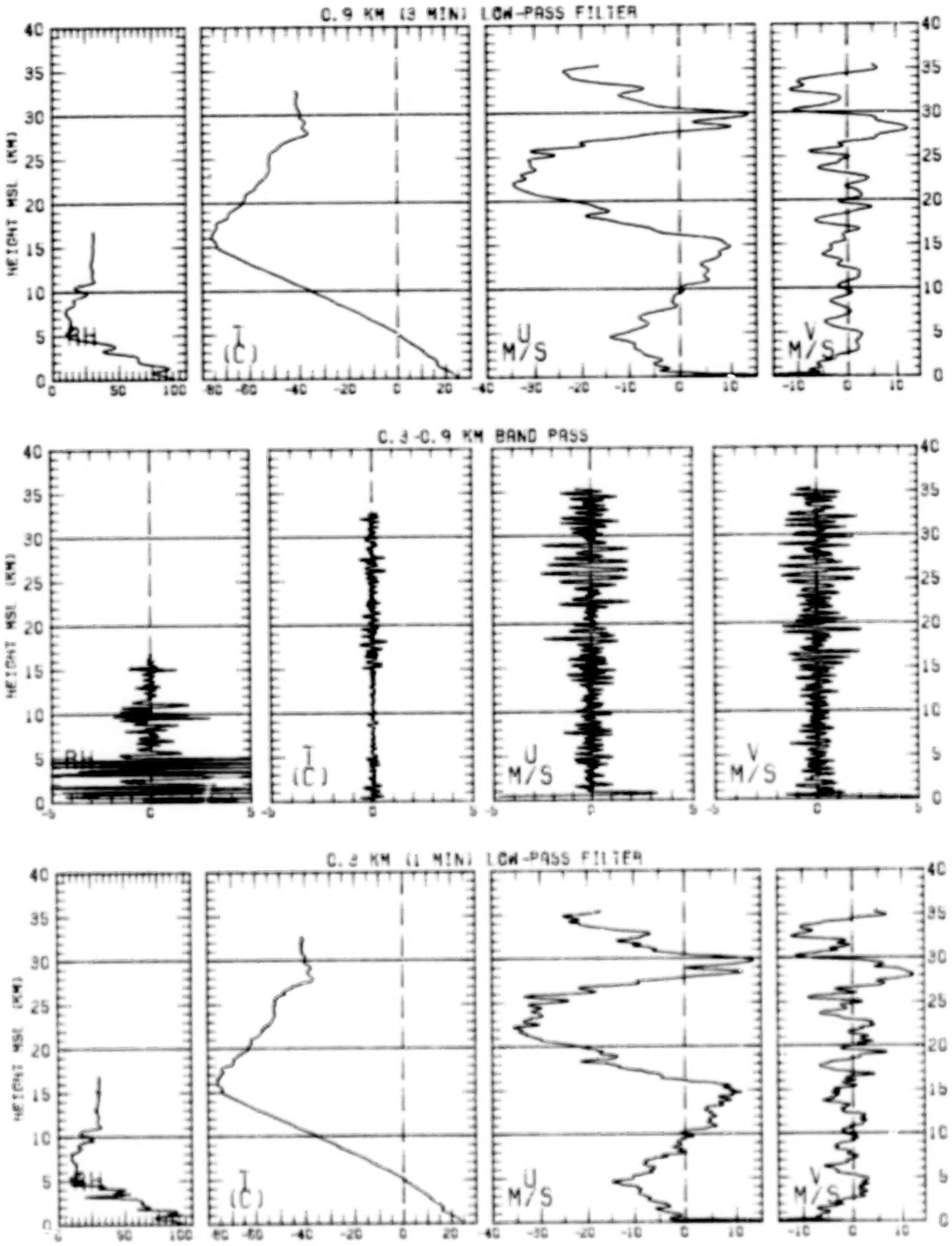
0.9 KM (3 MIN) LOW-PASS FILTER
HEIGHT MSL (KM)
RH
T (C)
U M/S
V M/S
0.3-0.9 KM BAND PASS
0.3 KM (1 MIN) LOW-PASS FILTER

Figure 32

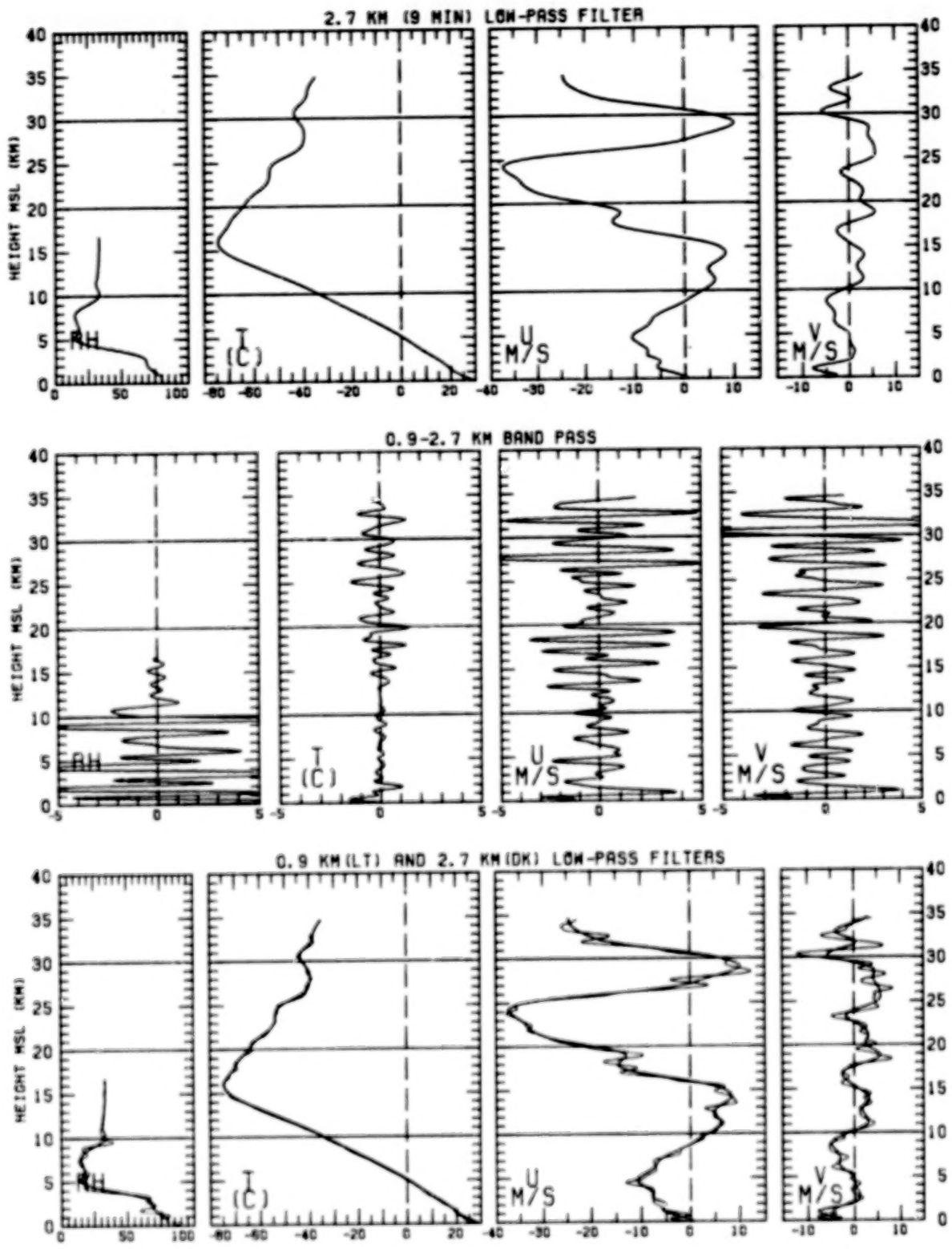
2.7 KM (9 MIN) LOW-PASS FILTER
HEIGHT MSL (KM)
RH
T (C)
U M/S
V M/S
0.9-2.7 KM BAND PASS
0.9 KM(LT) AND 2.7 KM(DK) LOW-PASS FILTERS

Figure 33

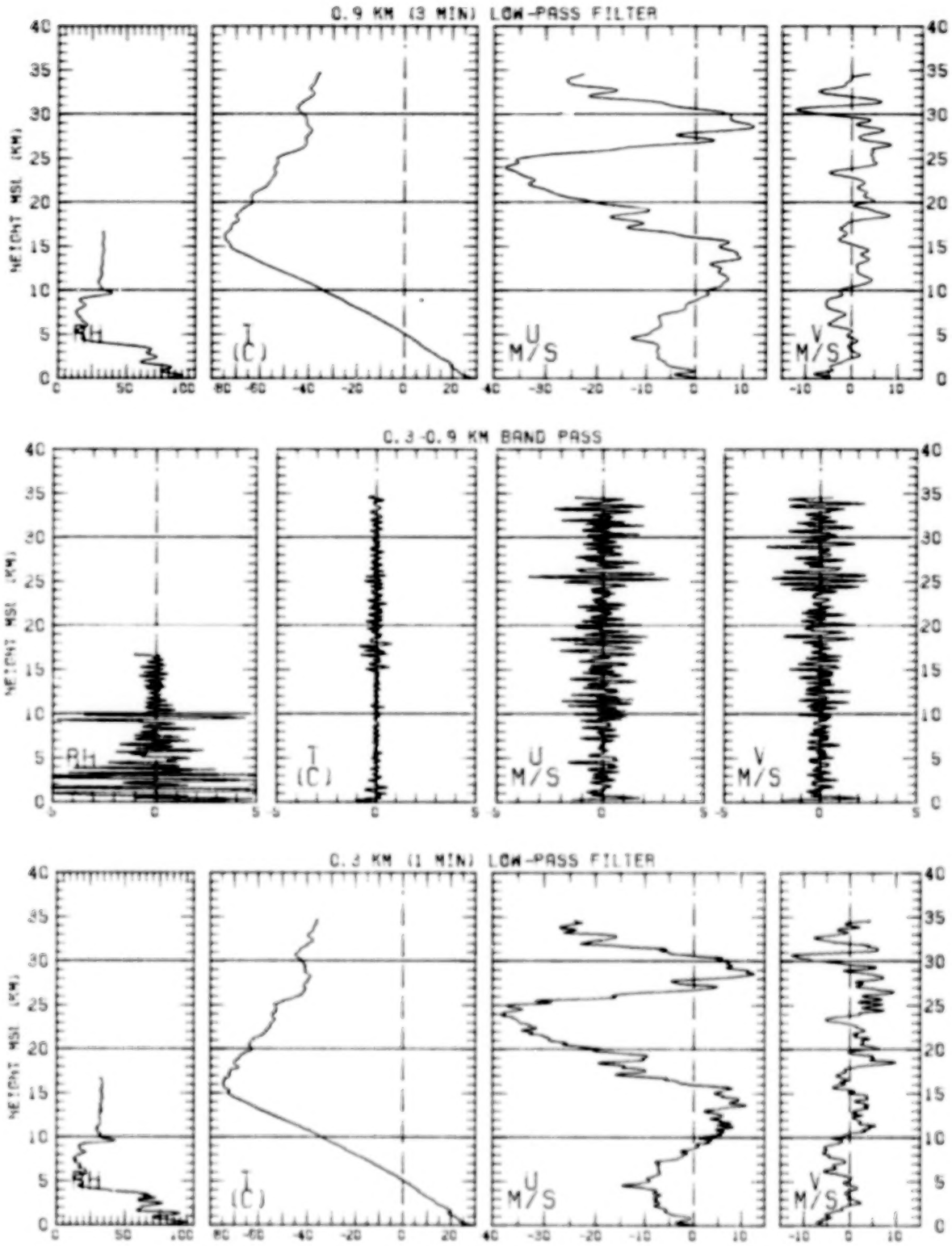
0.9 KM (3 MIN) LOW-PASS FILTER
0.3-0.9 KM BAND PASS
0.3 KM (1 MIN) LOW-PASS FILTER
HEIGHT MSL (KM)
RH
T (C)
U M/S
V M/S

Figure 33

PANAMA 24 JULY 1977 4:42UT

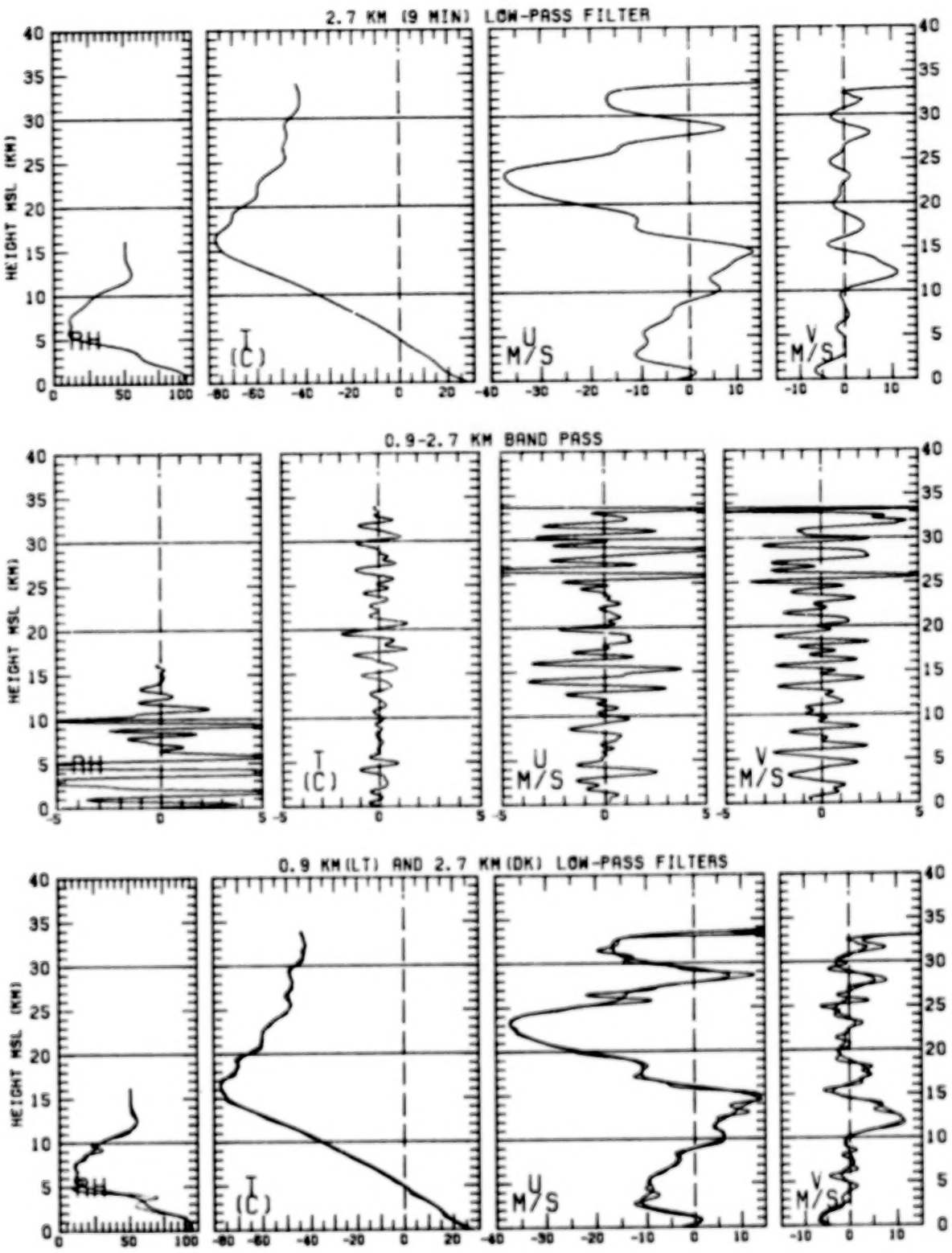

Figure 34

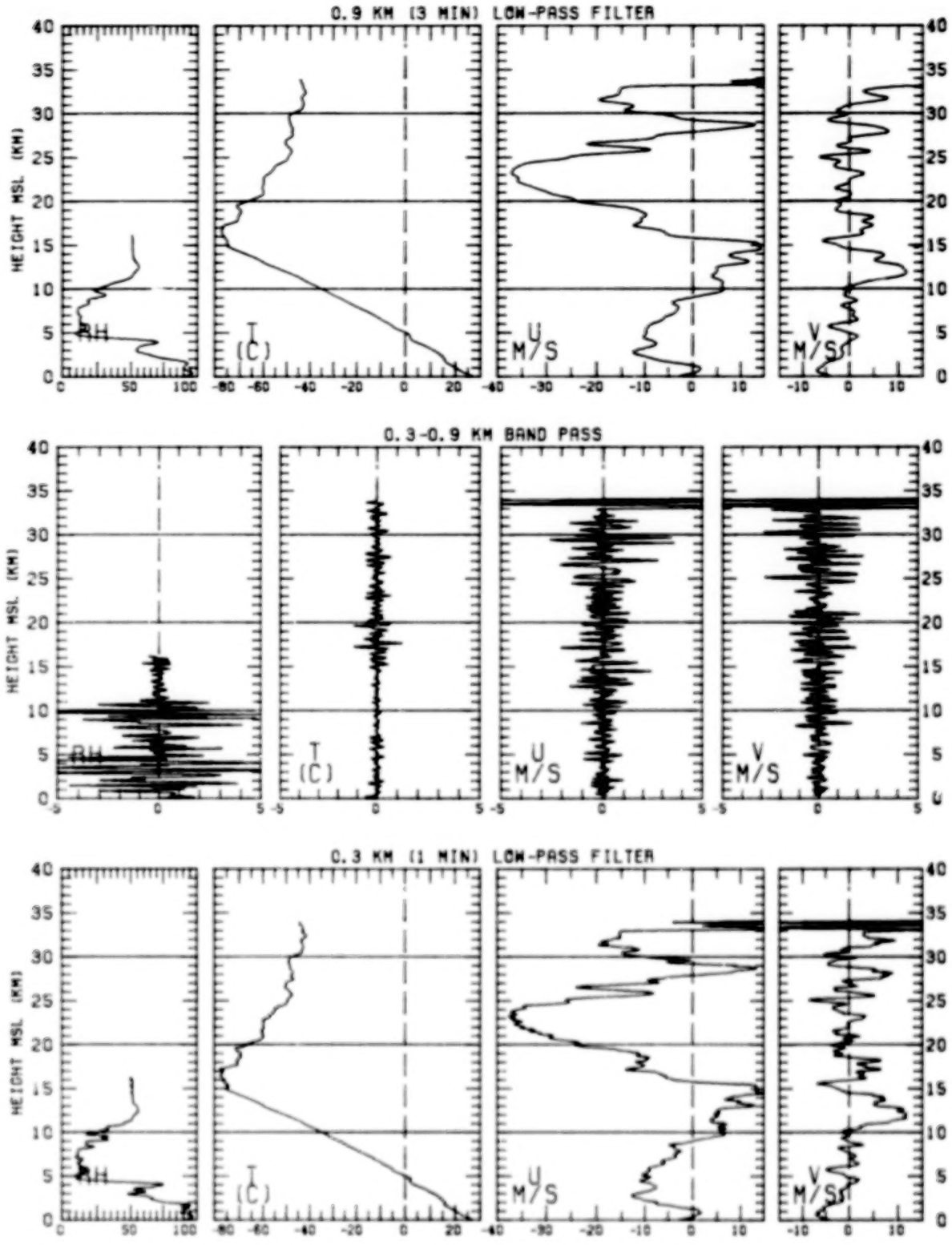
0.9 KM (3 MIN) LOW-PASS FILTER
HEIGHT MSL (KM)
RH
T (C)
U M/S
V M/S
0.3-0.9 KM BAND PASS
HEIGHT MSL (KM)
RH
T (C)
U M/S
V M/S
0.3 KM (1 MIN) LOW-PASS FILTER
HEIGHT MSL (KM)
RH
T (C)
U M/S
V M/S

Figure 34

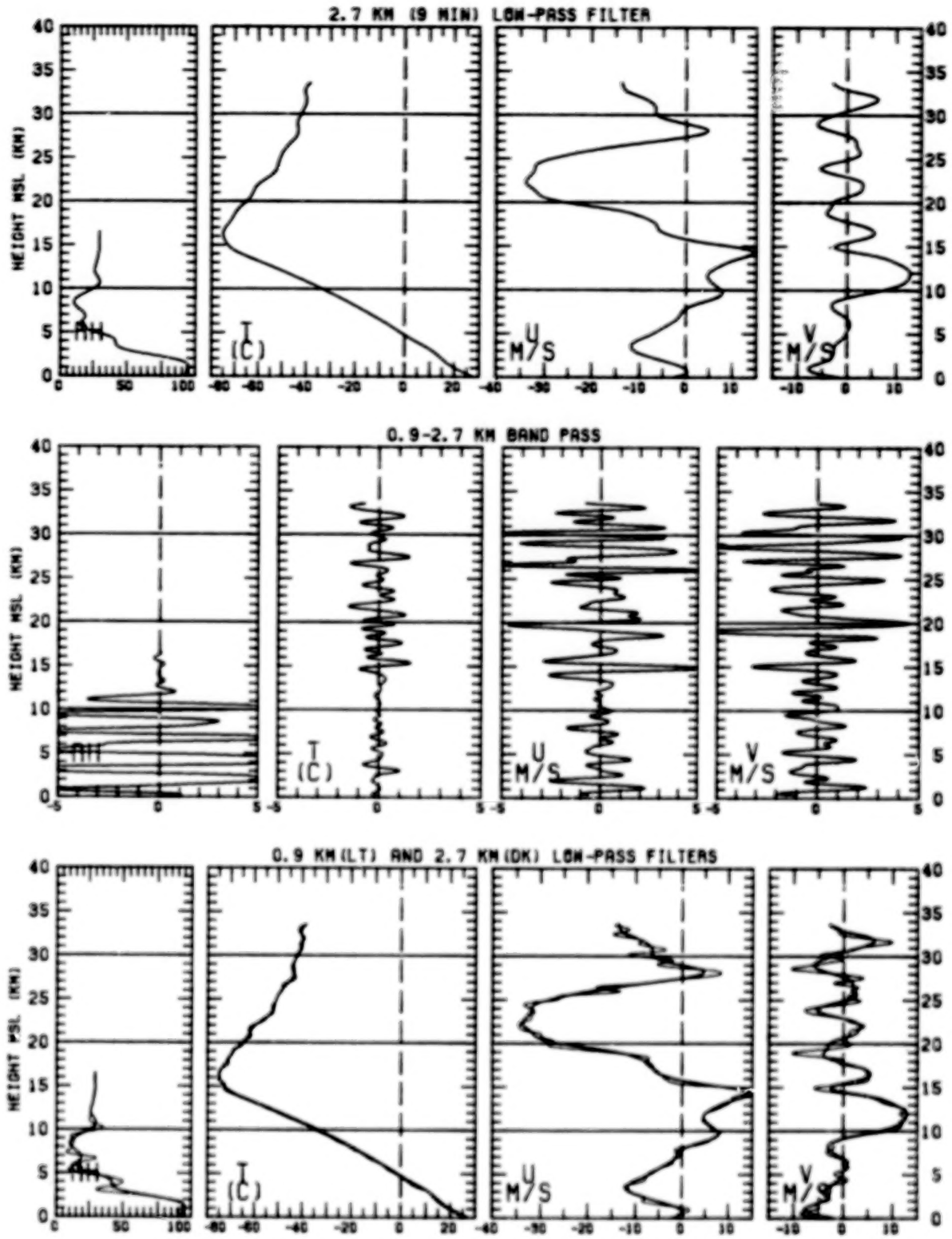
2.7 KM (9 MIN) LOW-PASS FILTER
HEIGHT MSL (KM)
RH
T (C)
U M/S
V M/S
0.9-2.7 KM BAND PASS
HEIGHT MSL (KM)
RH
T (C)
U M/S
V M/S
0.9 KM(LT) AND 2.7 KM(DK) LOW-PASS FILTERS
HEIGHT MSL (KM)
RH
T (C)
U M/S
V M/S

Figure 35

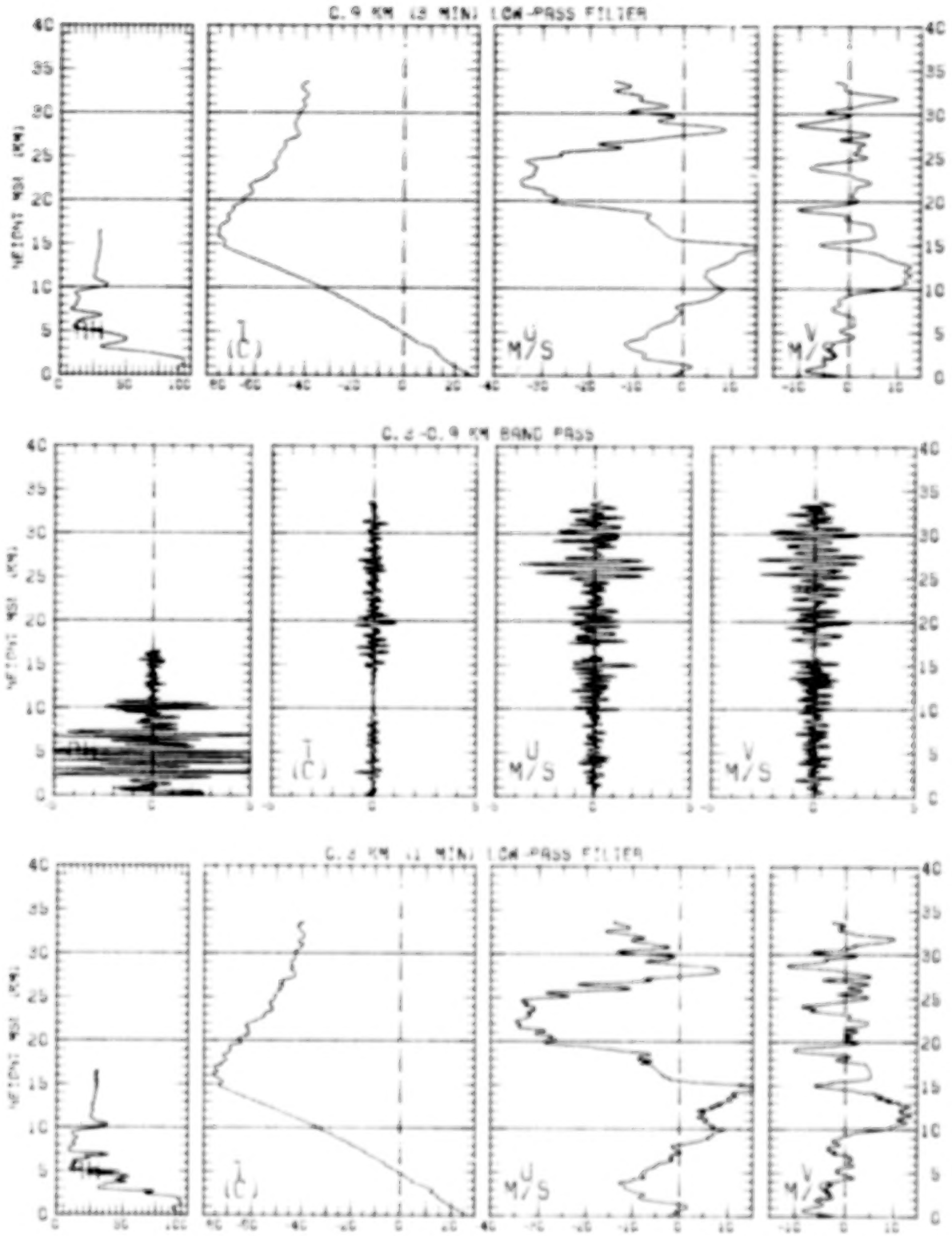
0.9 KM (8 MIN) LOW-PASS FILTER
HEIGHT MSL (KM)
T (C)
U M/S
V M/S
0.2-0.9 KM BAND PASS
0.2 KM (1 MIN) LOW-PASS FILTER

Figure 35

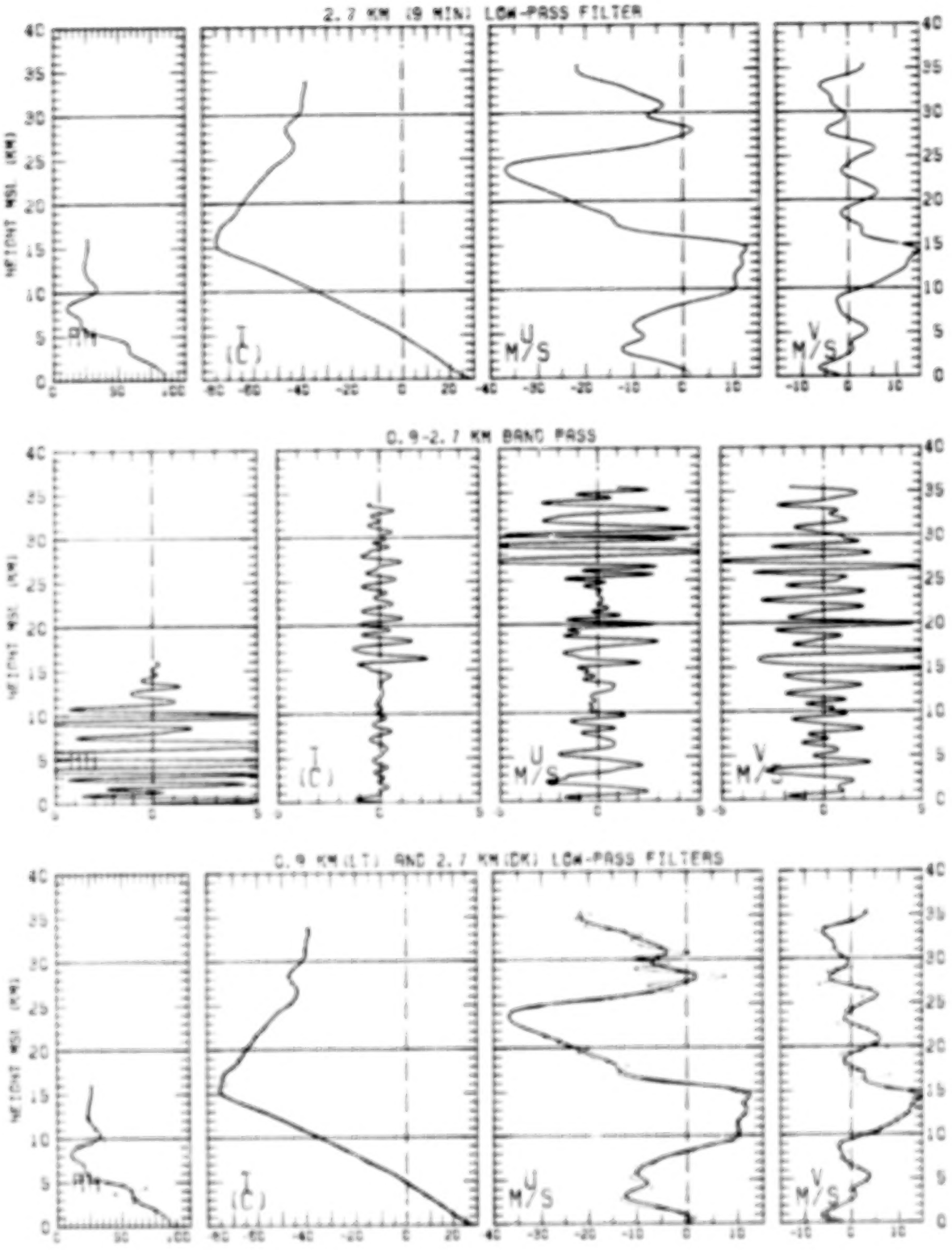
2.7 KM (9 MIN) LOW-PASS FILTER
HEIGHT MSL (KM)
RH
T (C)
U M/S
V M/S
0.9-2.7 KM BAND PASS
0.9 KM (LT) AND 2.7 KM (DK) LOW-PASS FILTERS

Figure 36

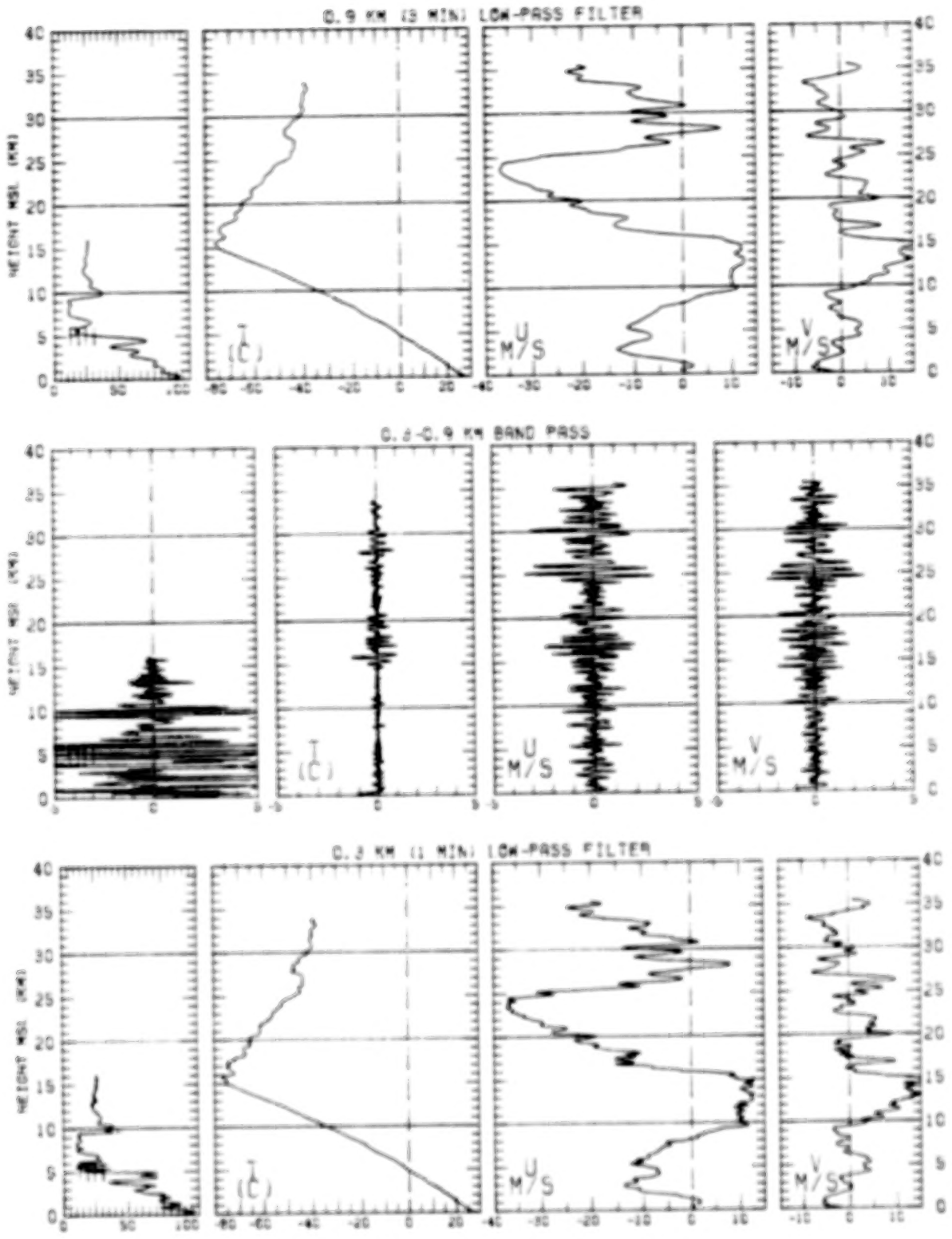
0.9 KM (3 MIN) LOW-PASS FILTER
HEIGHT MSL (KM)
T (C)
U M/S
V M/S
0.6-0.9 KM BAND PASS
0.3 KM (1 MIN) LOW-PASS FILTER

Figure 36

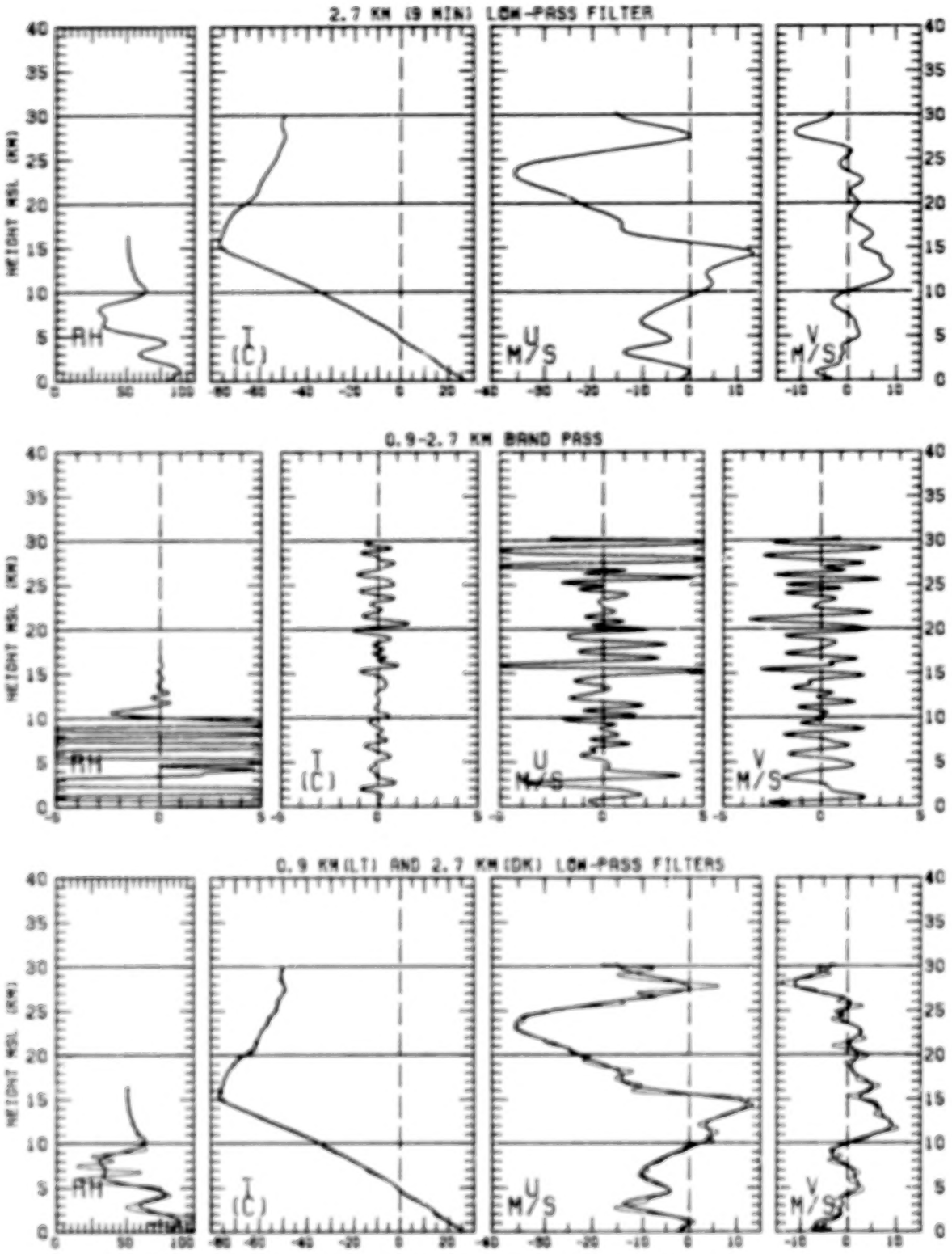
2.7 KM (9 MIN) LOW-PASS FILTER
0.9-2.7 KM BAND PASS
0.9 KM(LT) AND 2.7 KM(DK) LOW-PASS FILTERS
HEIGHT MSL (KM)
RH
T (C)
U M/S
V M/S

Figure 37

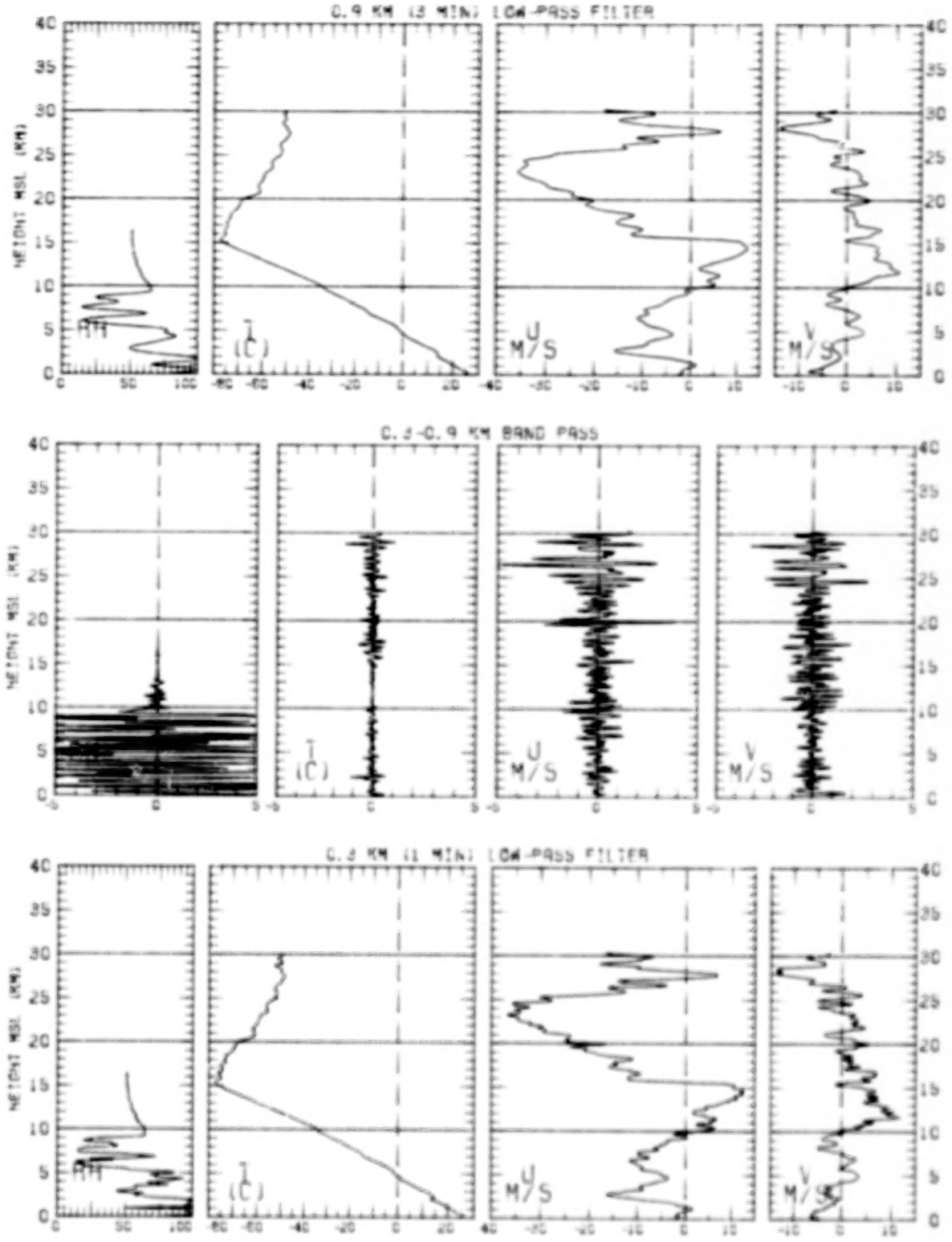
0.9 KM (3 MIN) LOW-PASS FILTER
0.3-0.9 KM BAND PASS
0.3 KM (1 MIN) LOW-PASS FILTER
HEIGHT MSL (KM)
RH
T (C)
U M/S
V M/S

Figure 37

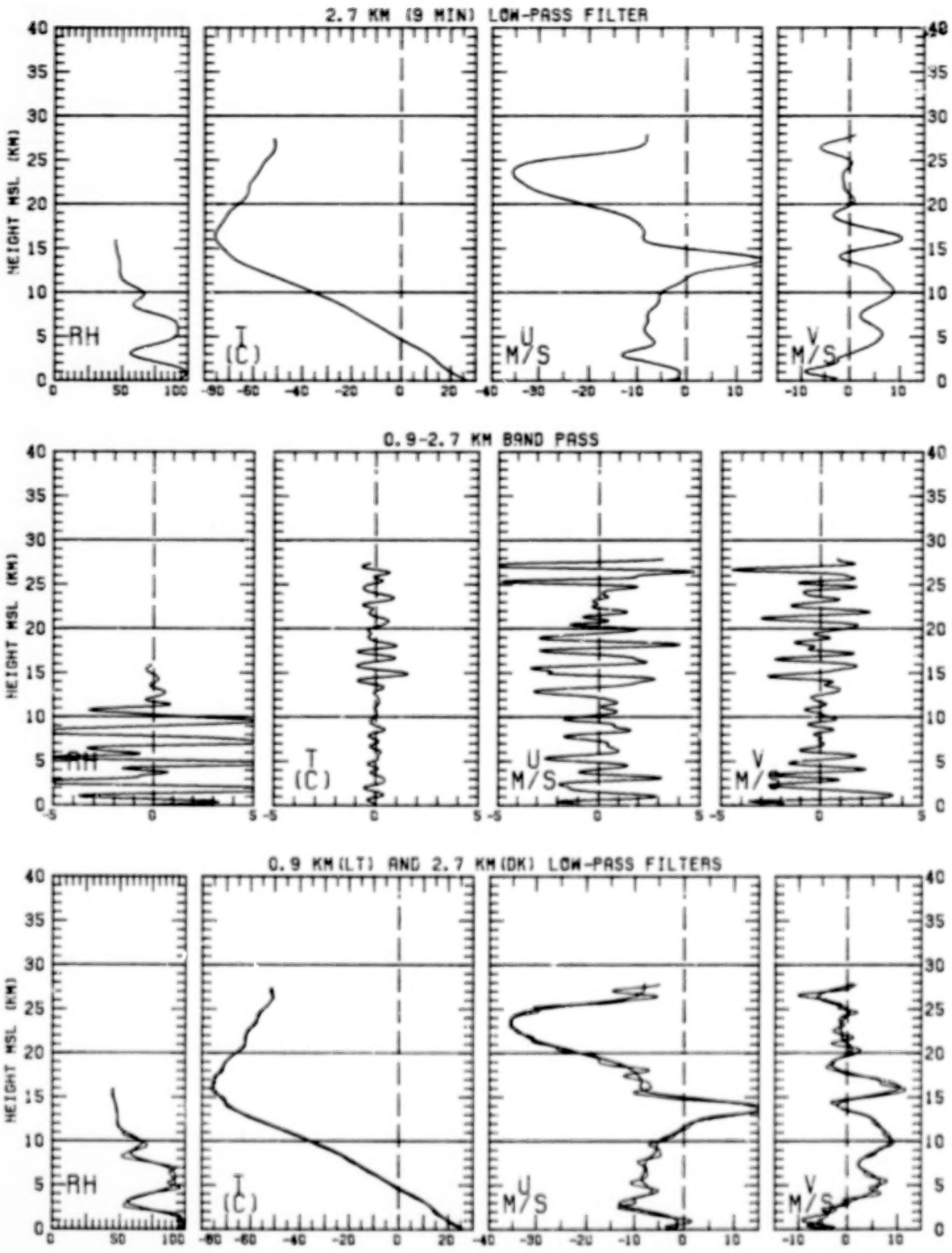
2.7 KM (9 MIN) LOW-PASS FILTER
0.9-2.7 KM BAND PASS
0.9 KM(LT) AND 2.7 KM(DK) LOW-PASS FILTERS
HEIGHT MSL (KM)
RH
T (C)
U M/S
V M/S

Figure 38

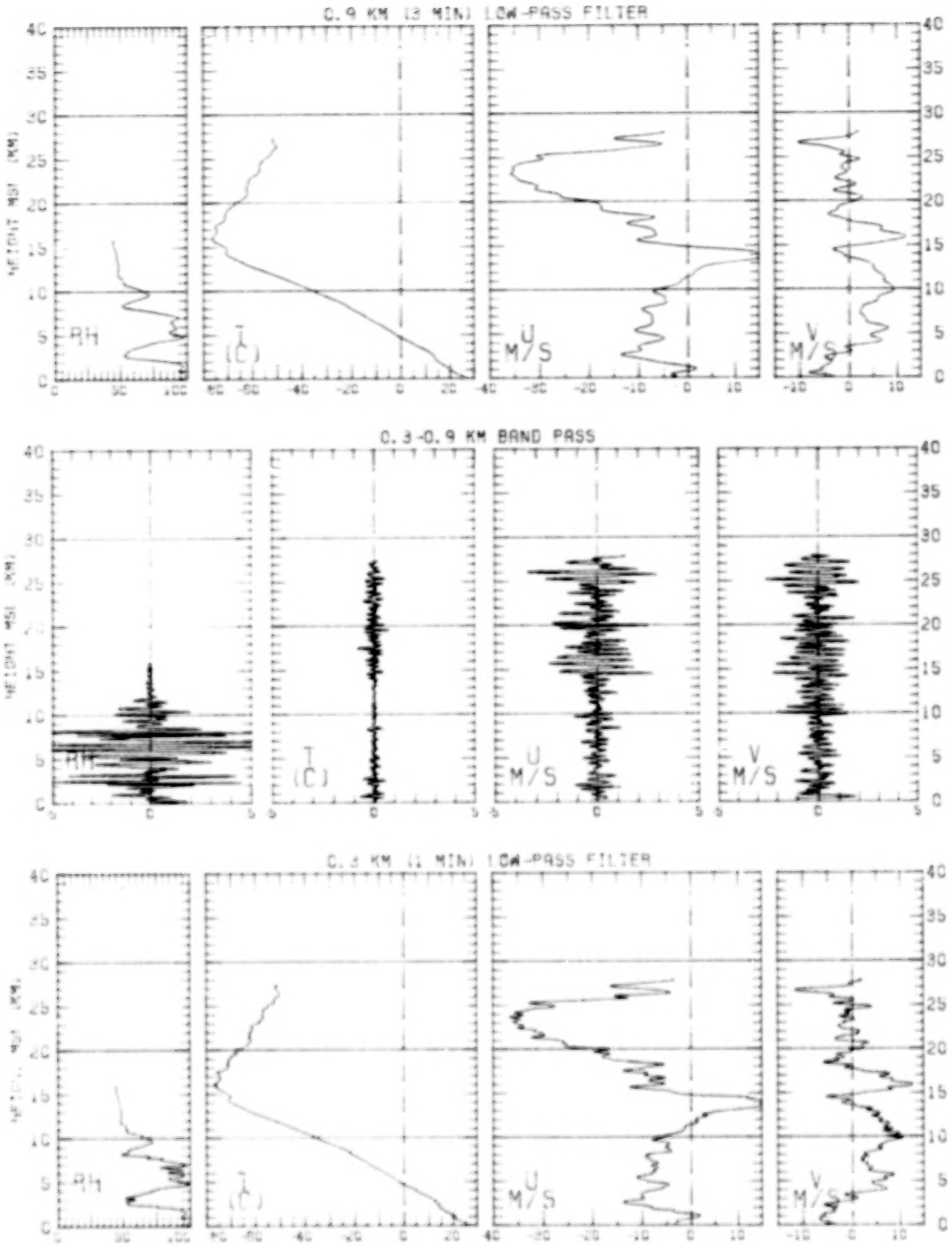
0.9 KM (3 MIN) LOW-PASS FILTER
HEIGHT MSL (KM)
RH
T (C)
U M/S
V M/S
0.3-0.9 KM BAND PASS
0.3 KM (1 MIN) LOW-PASS FILTER

Figure 38

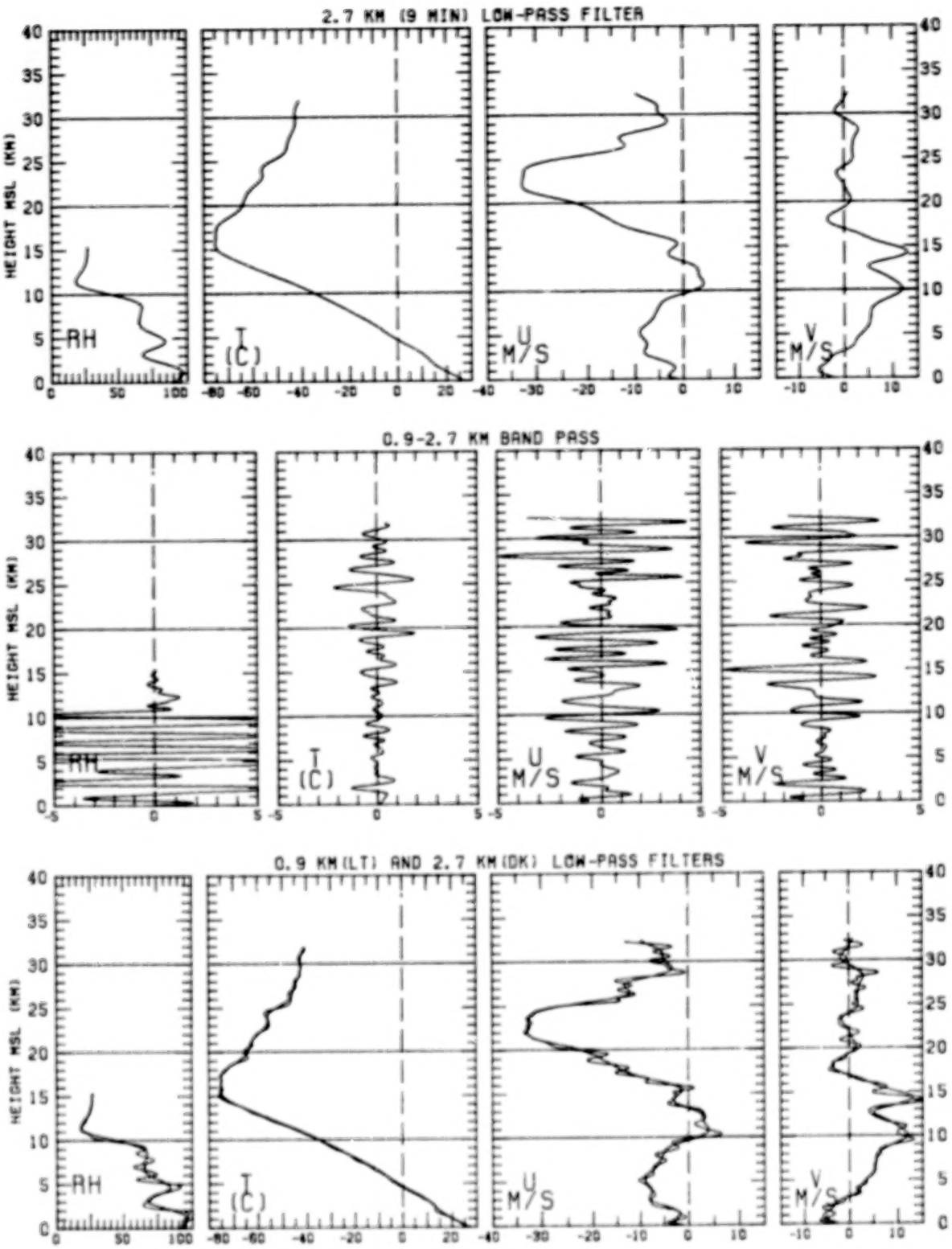
2.7 KM (9 MIN) LOW-PASS FILTER
HEIGHT MSL (KM)
RH
T (C)
U M/S
V M/S
0.9-2.7 KM BAND PASS
0.9 KM(LT) AND 2.7 KM(DK) LOW-PASS FILTERS

Figure 39

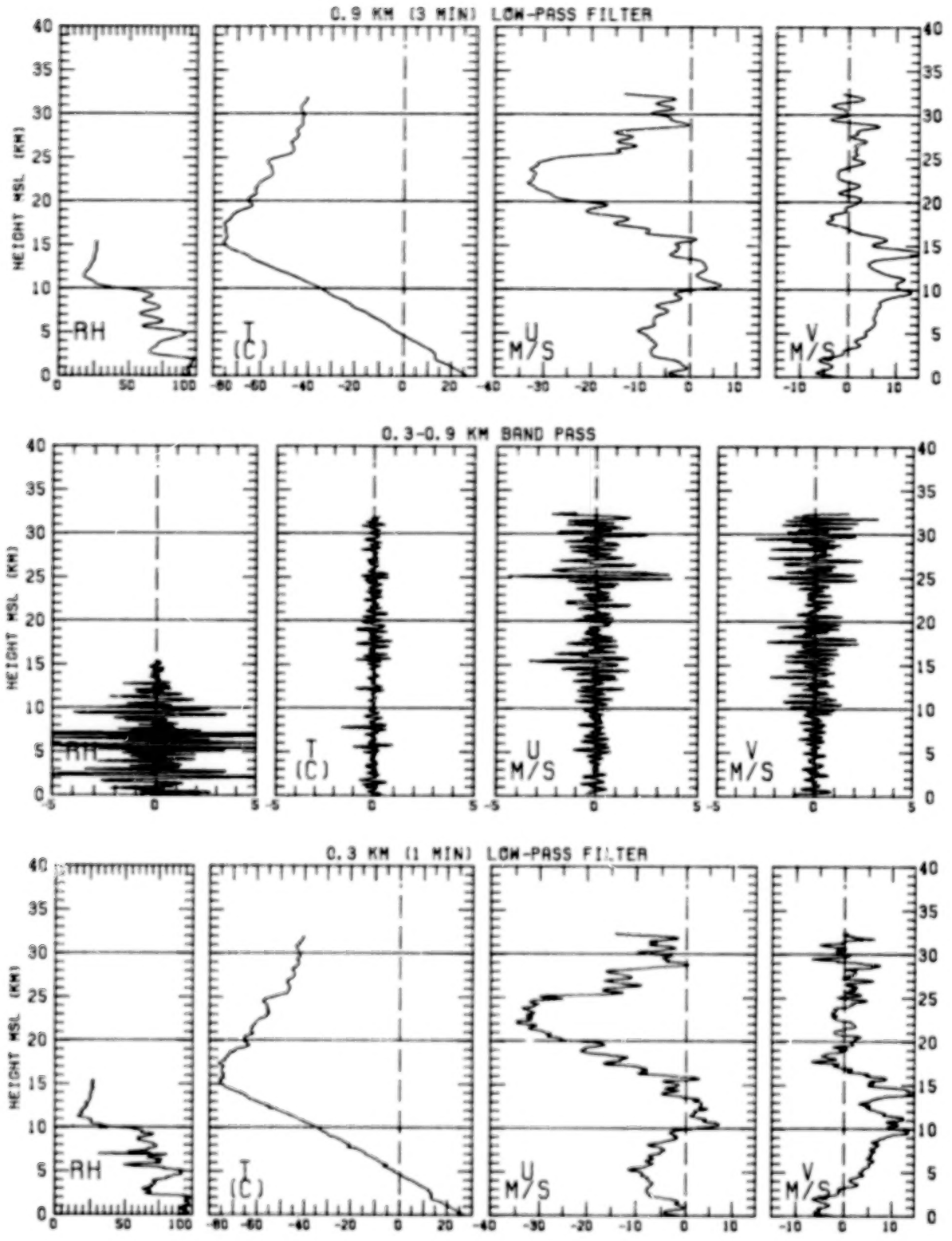
0.9 KM (3 MIN) LOW-PASS FILTER
0.3-0.9 KM BAND PASS
0.3 KM (1 MIN) LOW-PASS FILTER
HEIGHT MSL (KM)
RH
T (C)
U M/S
V M/S

Figure 39

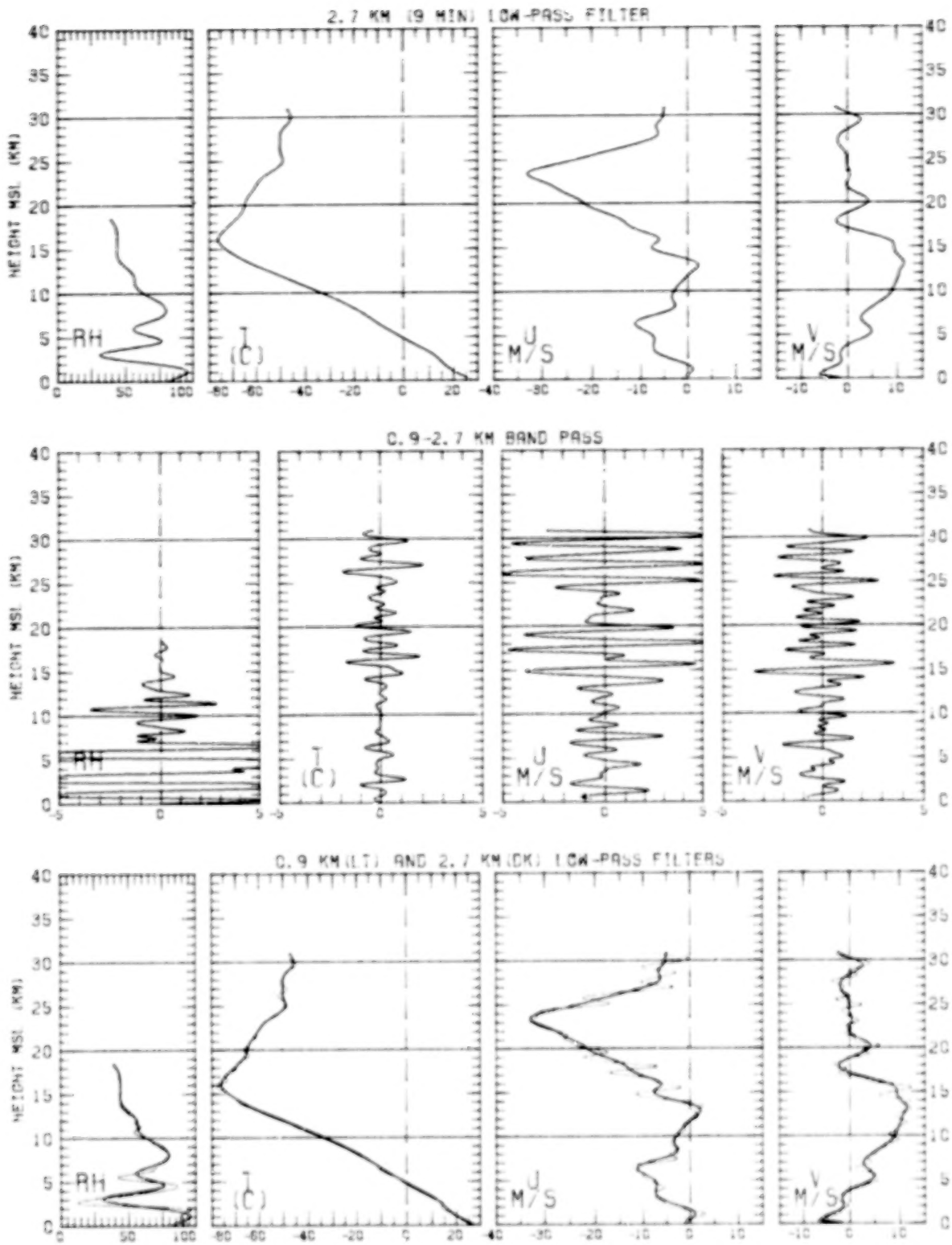
2.7 KM (9 MIN) LOW-PASS FILTER
HEIGHT MSL (KM)
RH
T (C)
U M/S
V M/S
0.9-2.7 KM BAND PASS
0.9 KM (LT) AND 2.7 KM (DK) LOW-PASS FILTERS

Figure 40

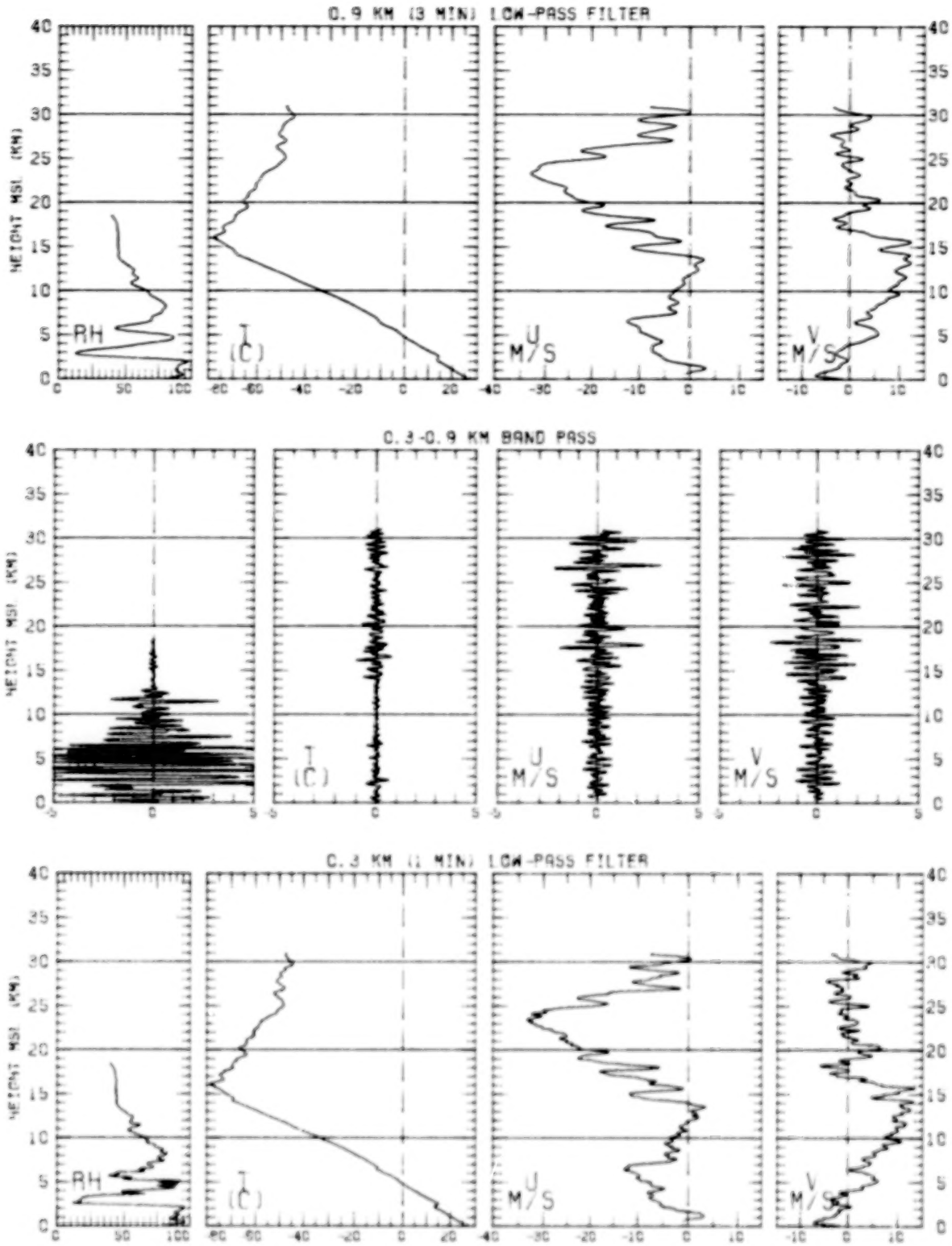
0.9 KM (3 MIN) LOW-PASS FILTER
0.3-0.9 KM BAND PASS
0.3 KM (1 MIN) LOW-PASS FILTER
HEIGHT MSL (KM)
RH
T (C)
U M/S
V M/S

Figure 40

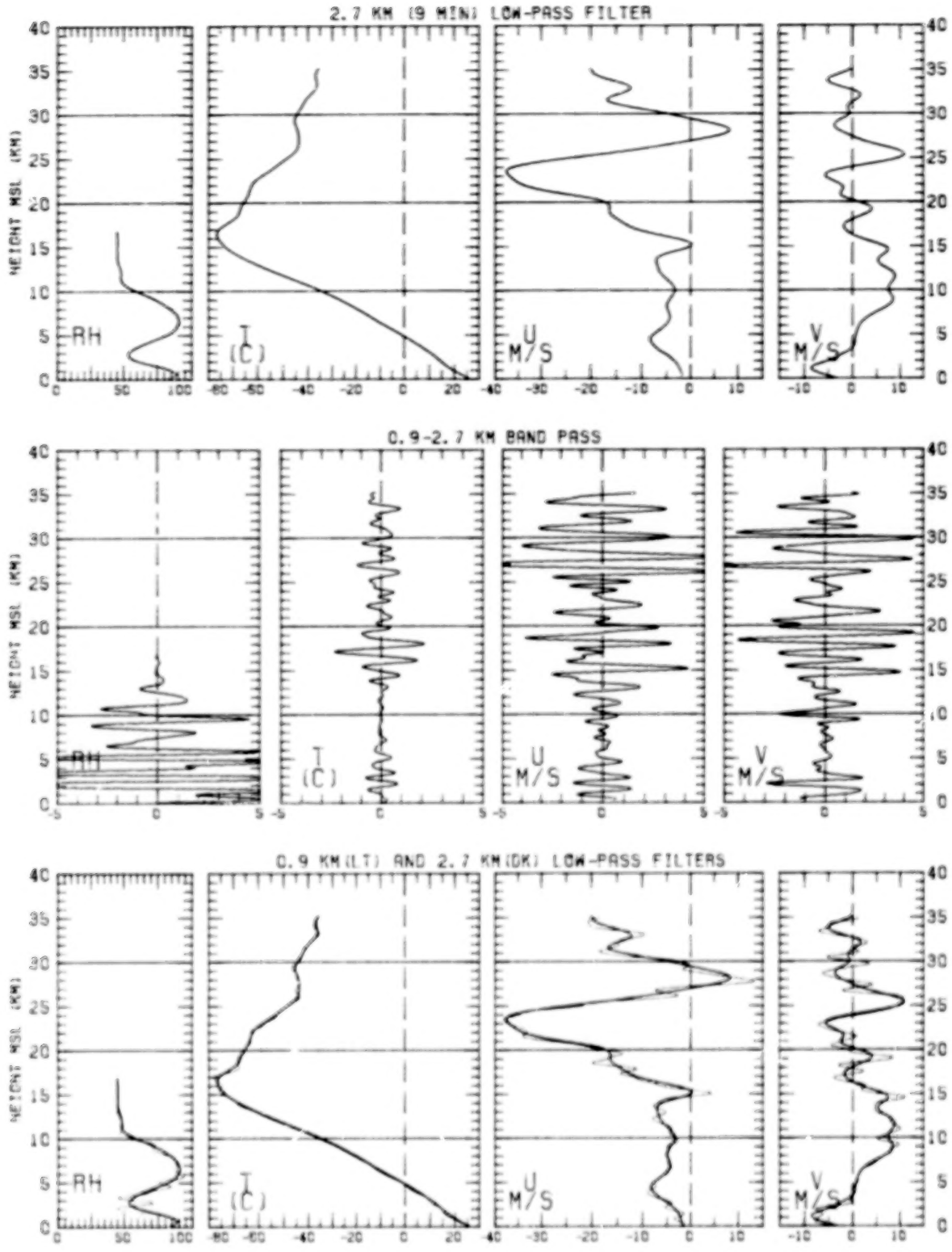
2.7 KM (9 MIN) LOW-PASS FILTER
0.9-2.7 KM BAND PASS
0.9 KM (LT) AND 2.7 KM (DK) LOW-PASS FILTERS
HEIGHT MSL (KM)
RH
T (C)
U M/S
V M/S

Figure 41

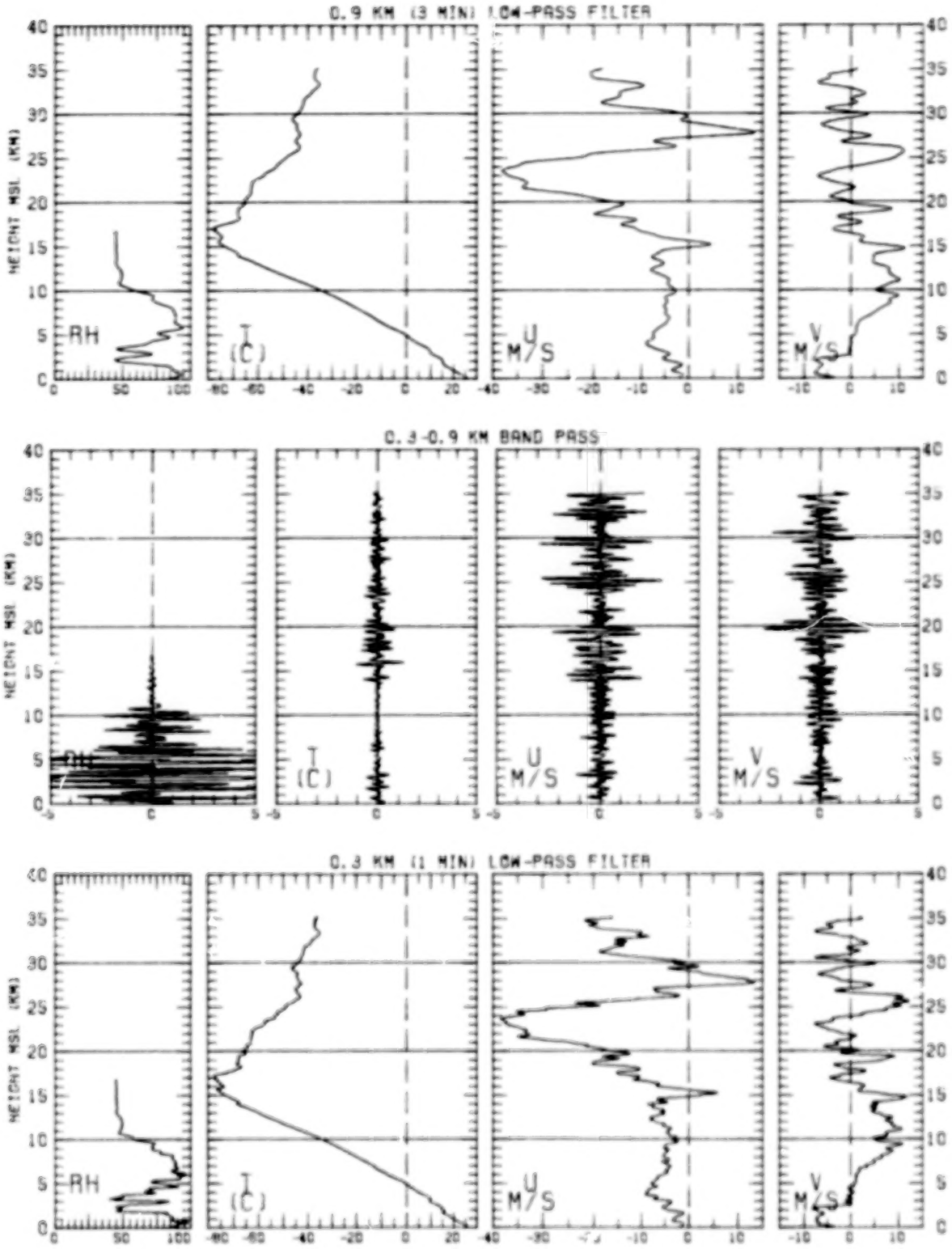
0.9 KM (3 MIN) LOW-PASS FILTER
HEIGHT MSL (KM)
RH
T (C)
U M/S
V M/S
0.3-0.9 KM BAND PASS
0.3 KM (1 MIN) LOW-PASS FILTER

Figure 41

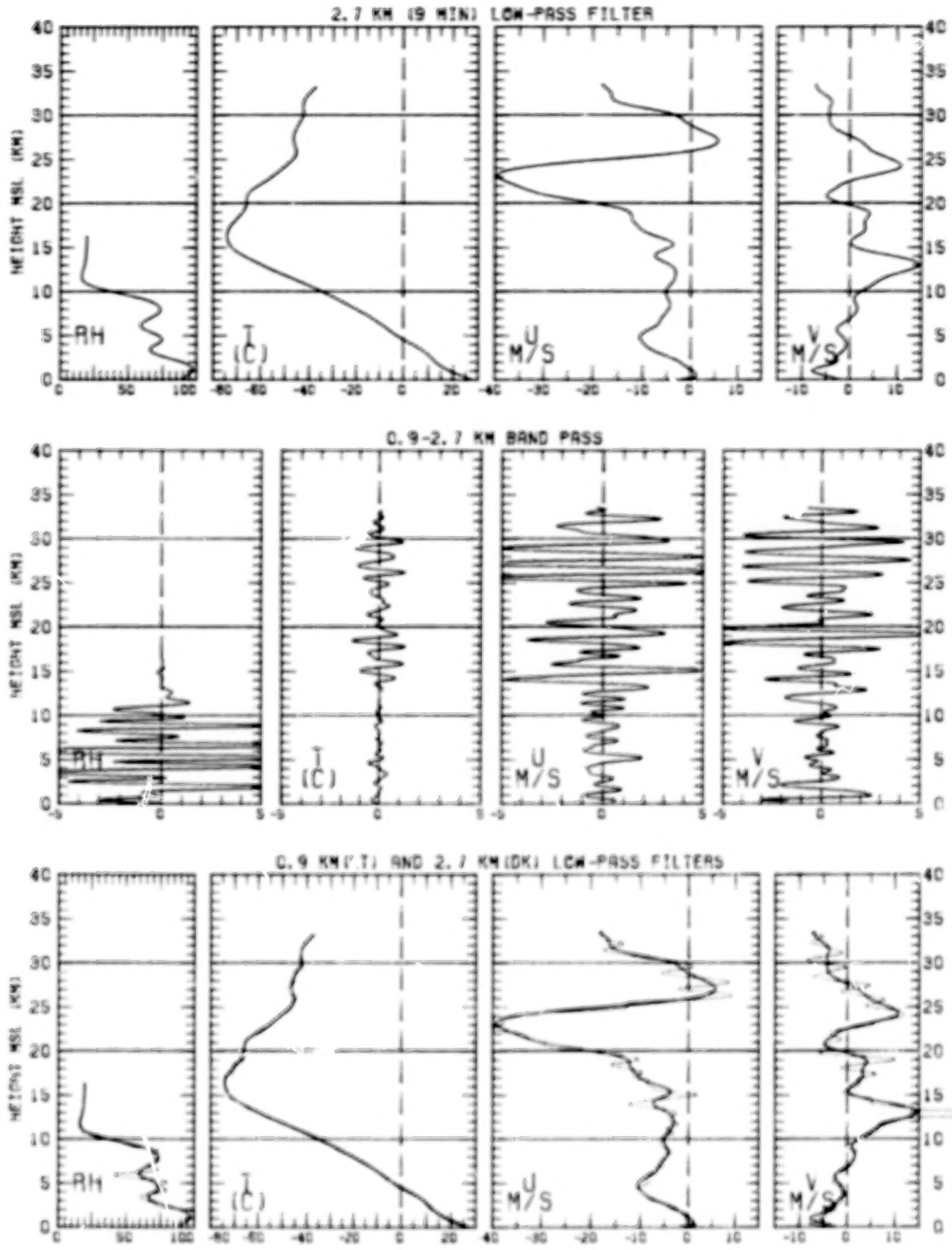
2.7 KM (9 MIN) LOW-PASS FILTER
HEIGHT MSL (KM)
RH
T (C)
U M/S
V M/S
0.9-2.7 KM BAND PASS
0.9 KM (FT) AND 2.7 KM (DK) LOW-PASS FILTERS

Figure 42

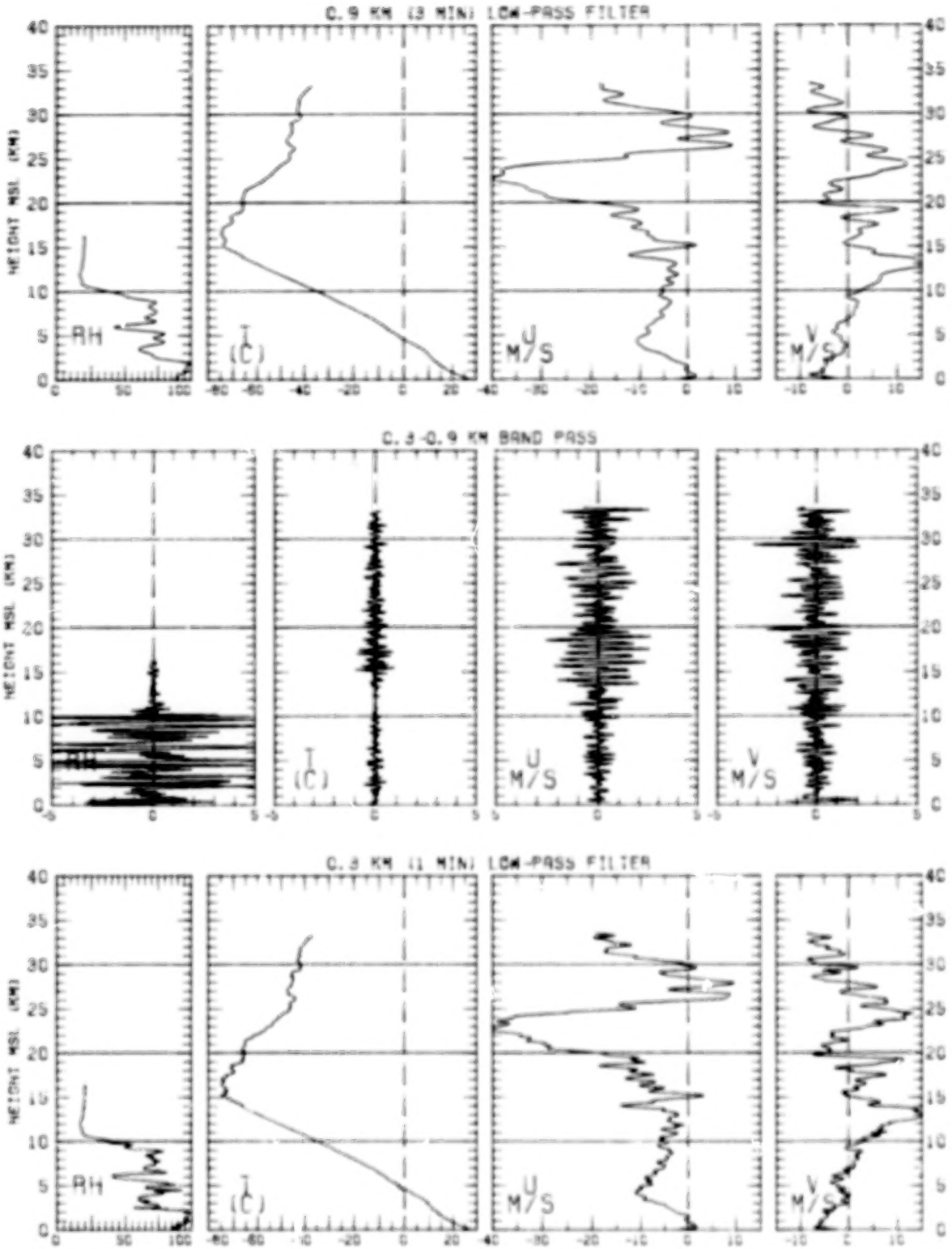
0.9 KM (3 MIN) LOW-PASS FILTER
0.3-0.9 KM BAND PASS
0.3 KM (1 MIN) LOW-PASS FILTER
HEIGHT MSL (KM)
RH
T (C)
U M/S
V M/S

Figure 42

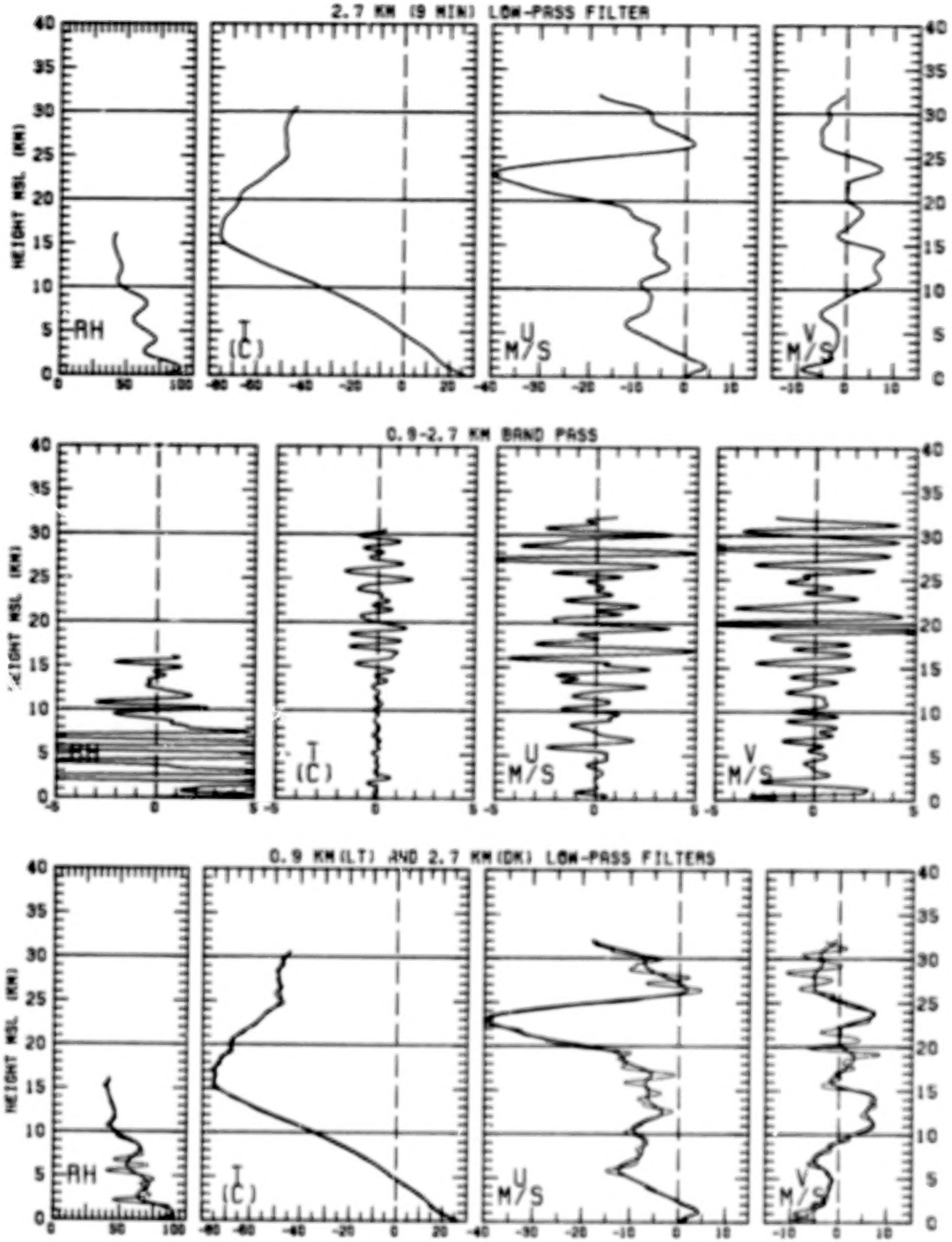
2.7 KM (9 MIN) LOW-PASS FILTER
HEIGHT MSL (KM)
RH
T (C)
U M/S
V M/S
0.9-2.7 KM BAND PASS
0.9 KM (LT) AND 2.7 KM (DK) LOW-PASS FILTERS

Figure 43

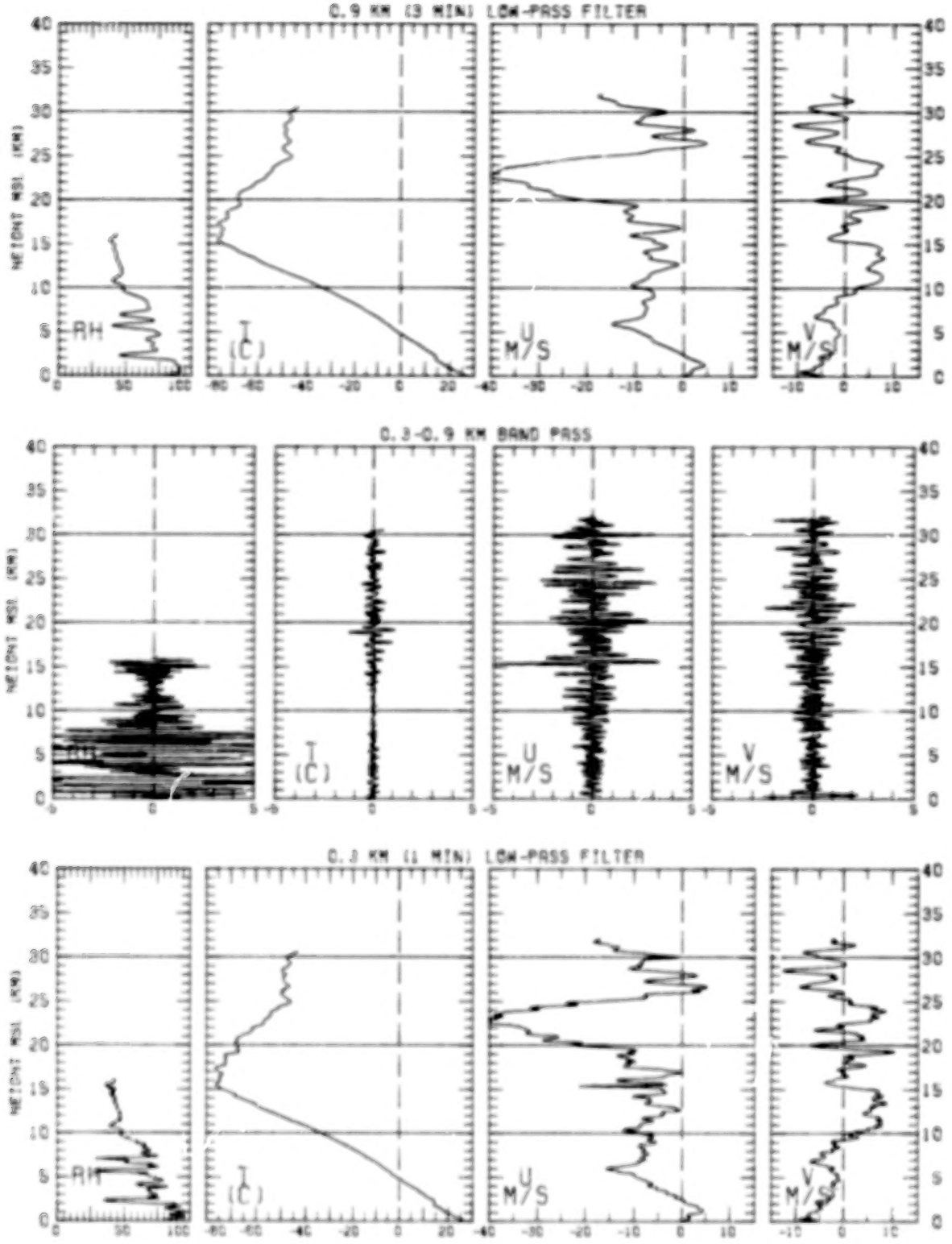
0.9 KM (3 MIN) LOW-PASS FILTER
0.3-0.9 KM BAND PASS
0.3 KM (1 MIN) LOW-PASS FILTER
HEIGHT MSL (KM)
RH
T (C)
U M/S
V M/S

Figure 43

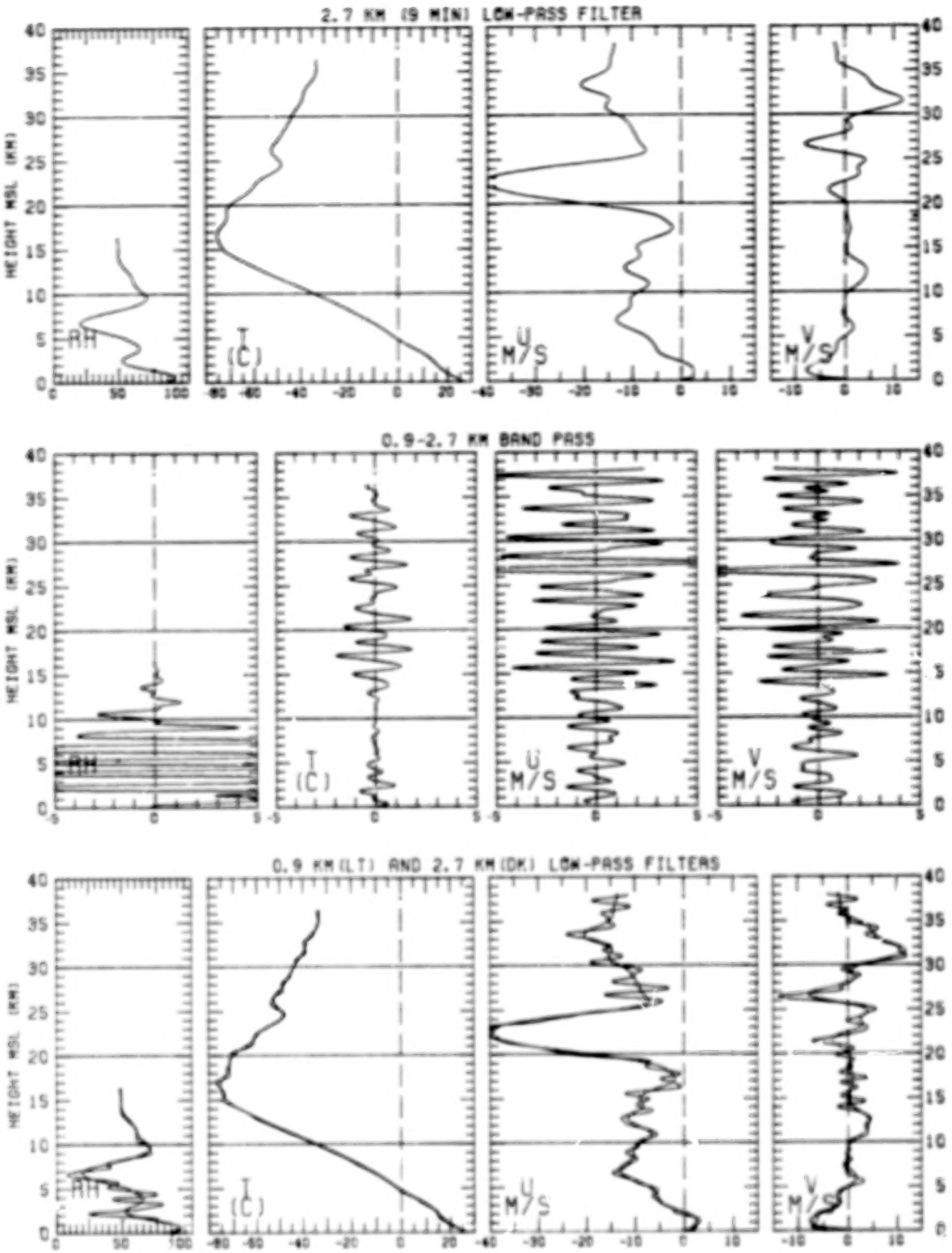
2.7 KM (9 MIN) LOW-PASS FILTER
0.9-2.7 KM BAND PASS
0.9 KM (LT) AND 2.7 KM (DK) LOW-PASS FILTERS
HEIGHT MSL (KM)
RH
T (C)
U M/S
V M/S

Figure 44

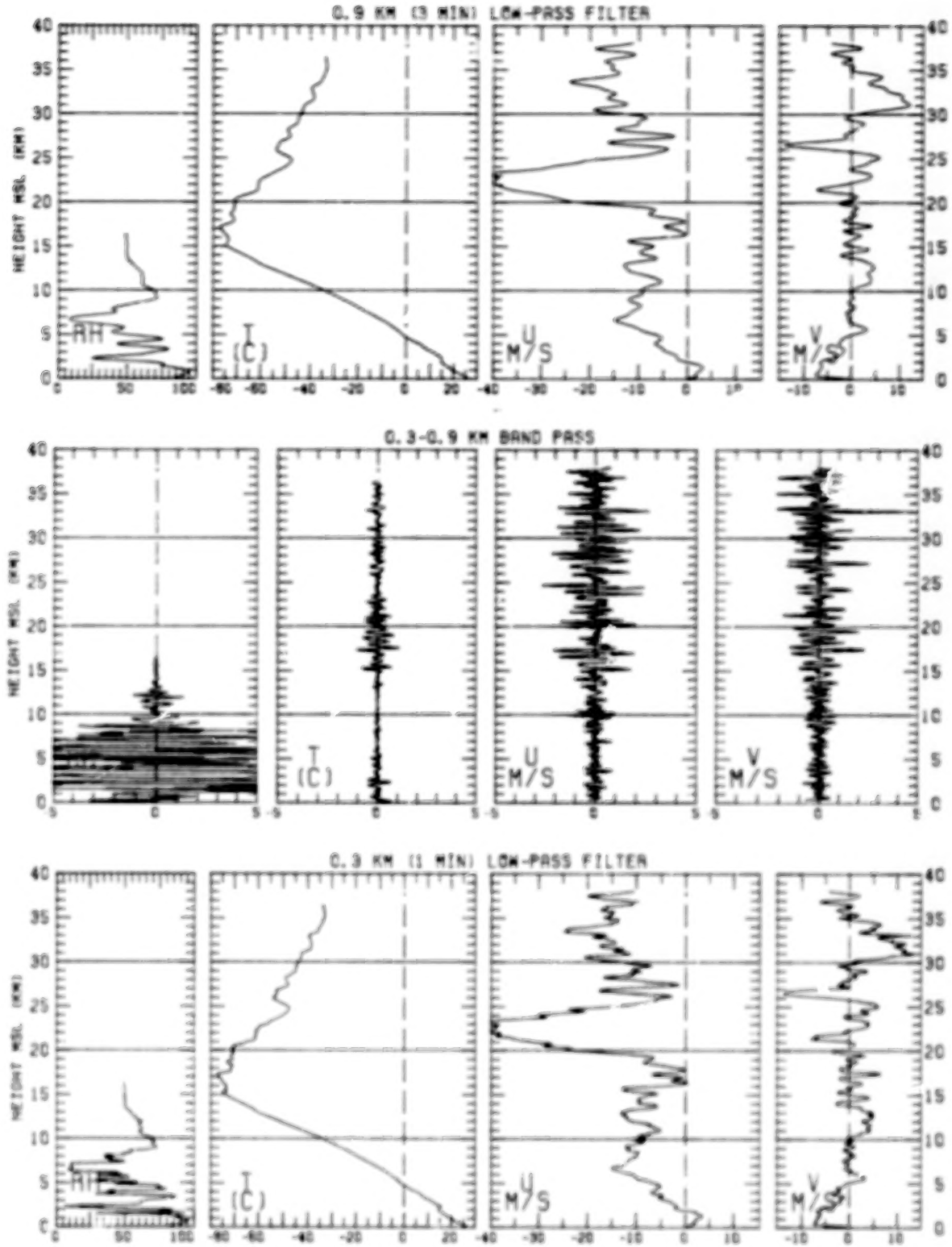
0.9 KM (3 MIN) LOW-PASS FILTER
0.3-0.9 KM BAND PASS
0.3 KM (1 MIN) LOW-PASS FILTER
HEIGHT MSL (KM)
RH
T (C)
U M/S
V M/S

Figure 44

PANAMA 27 JULY 1977 10:28UT

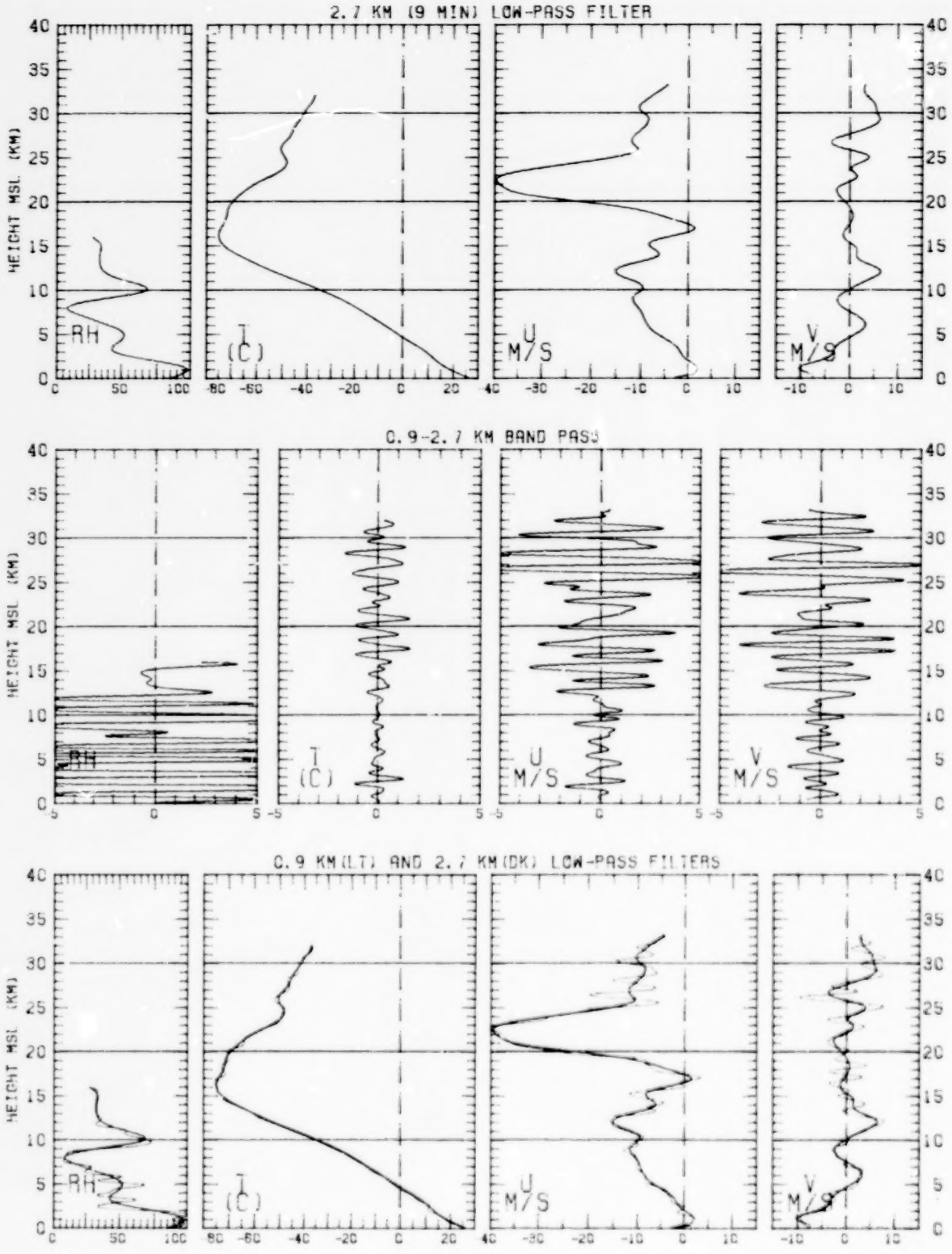

Figure 45

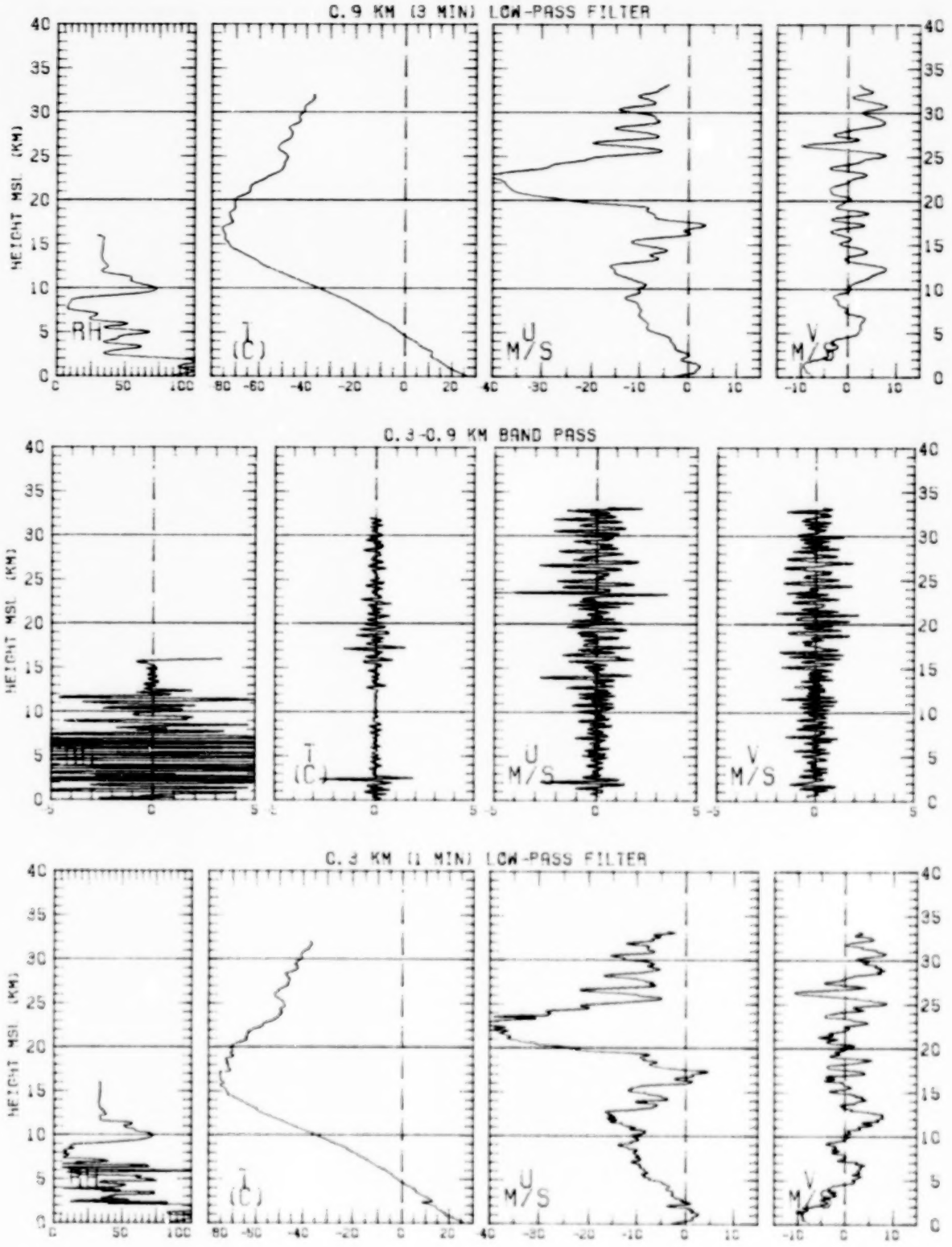
0.9 KM (3 MIN) LOW-PASS FILTER
0.3-0.9 KM BAND PASS
0.3 KM (1 MIN) LOW-PASS FILTER
HEIGHT MSL (KM)
RH
T (C)
U M/S
V M/S

Figure 45

PANAMA 27 JULY 1977 22:40UT

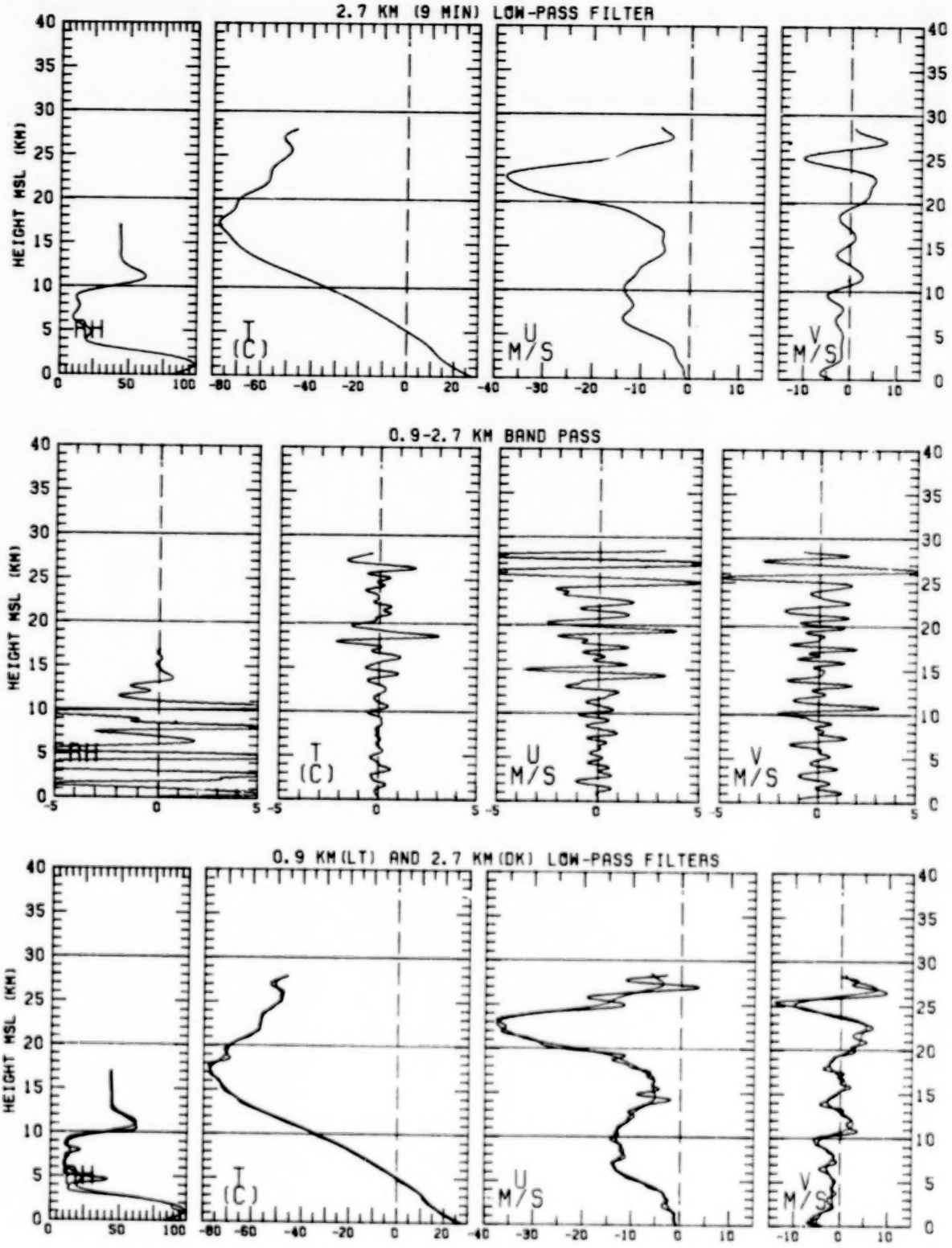

Figure 46

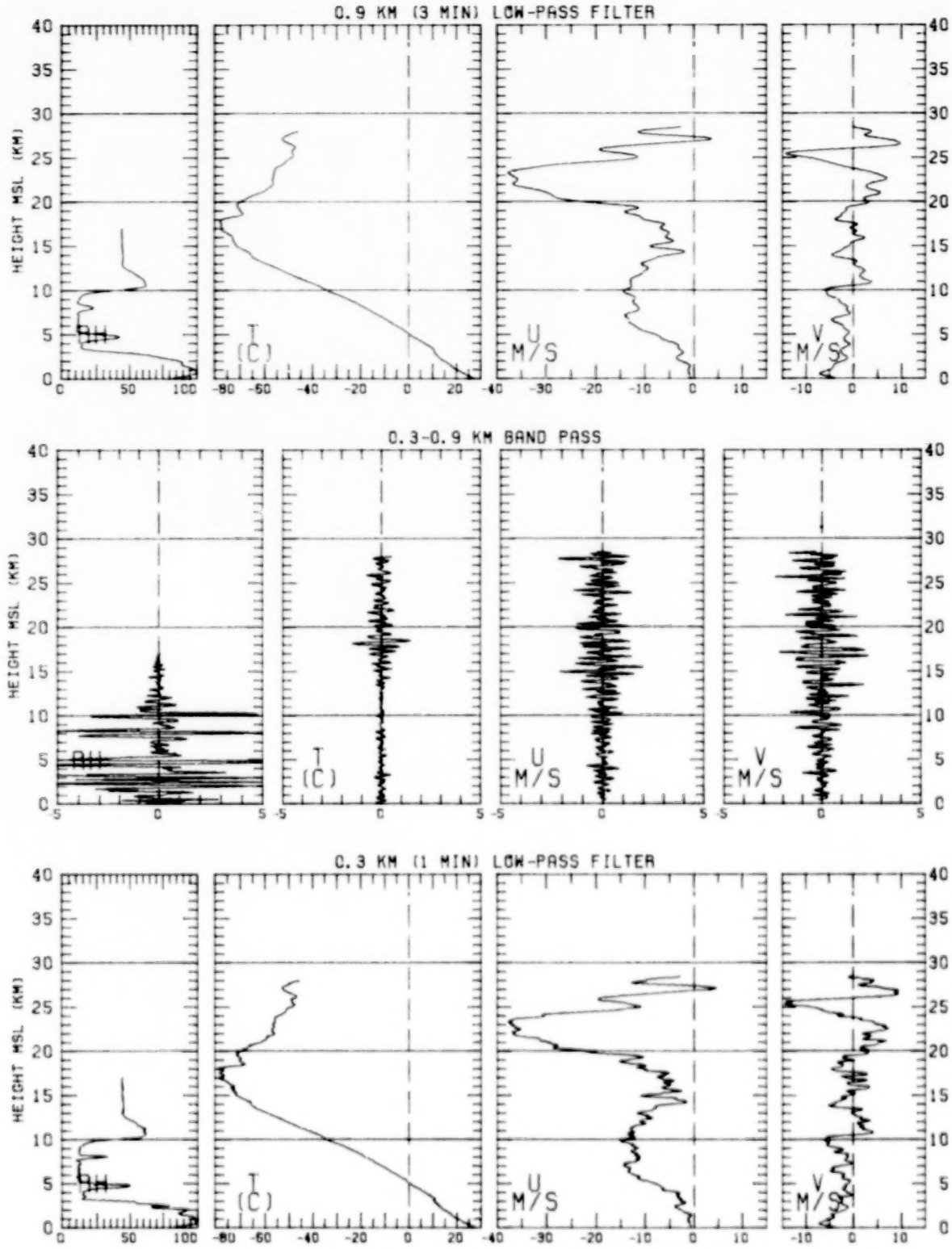
0.9 KM (3 MIN) LOW-PASS FILTER
0.3-0.9 KM BAND PASS
0.3 KM (1 MIN) LOW-PASS FILTER
HEIGHT MSL (KM)
RH
T (C)
U M/S
V M/S

Figure 46

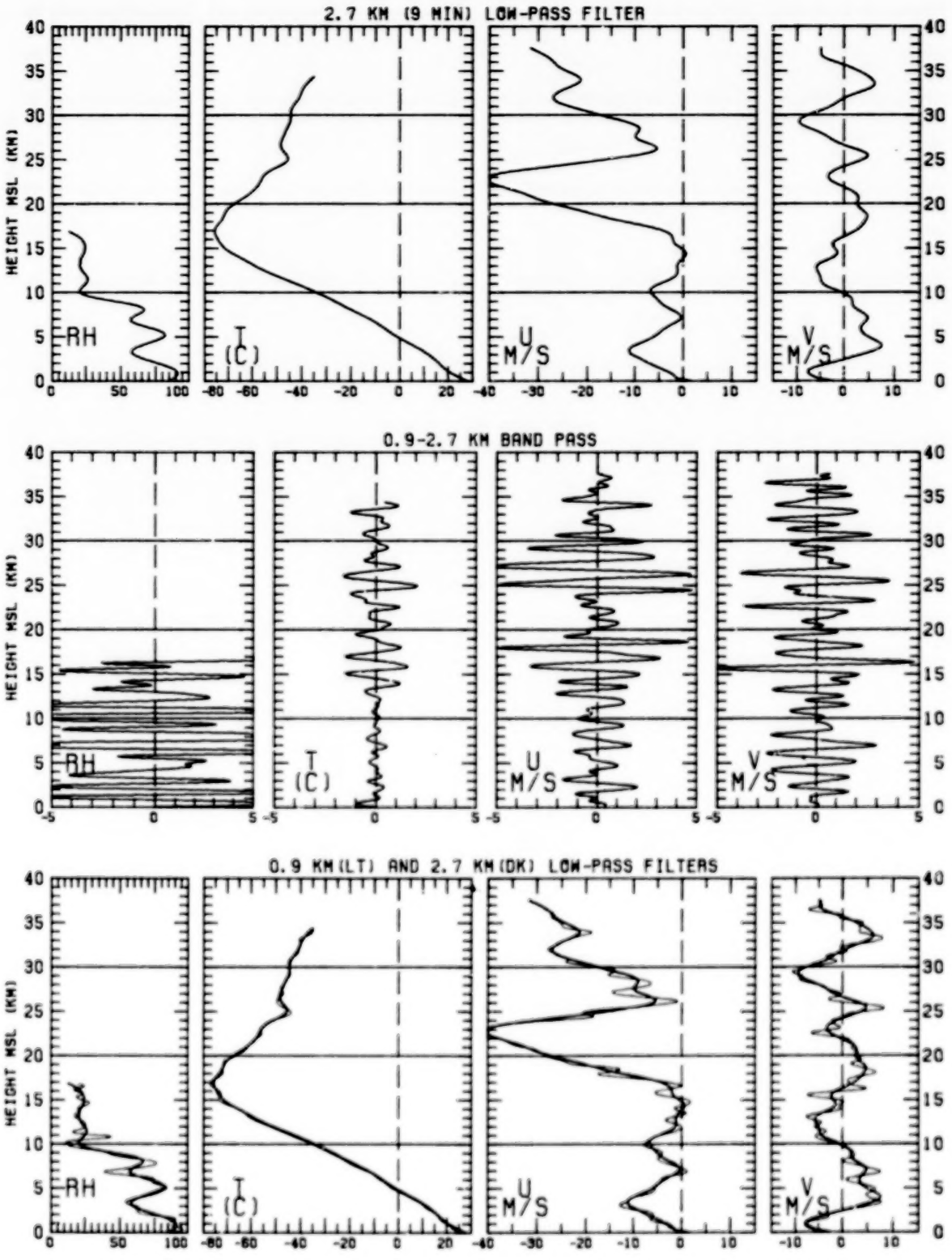
2.7 KM (9 MIN) LOW-PASS FILTER
0.9-2.7 KM BAND PASS
0.9 KM(LT) AND 2.7 KM(DK) LOW-PASS FILTERS
HEIGHT MSL (KM)
RH
T (C)
U M/S
V M/S

Figure 47

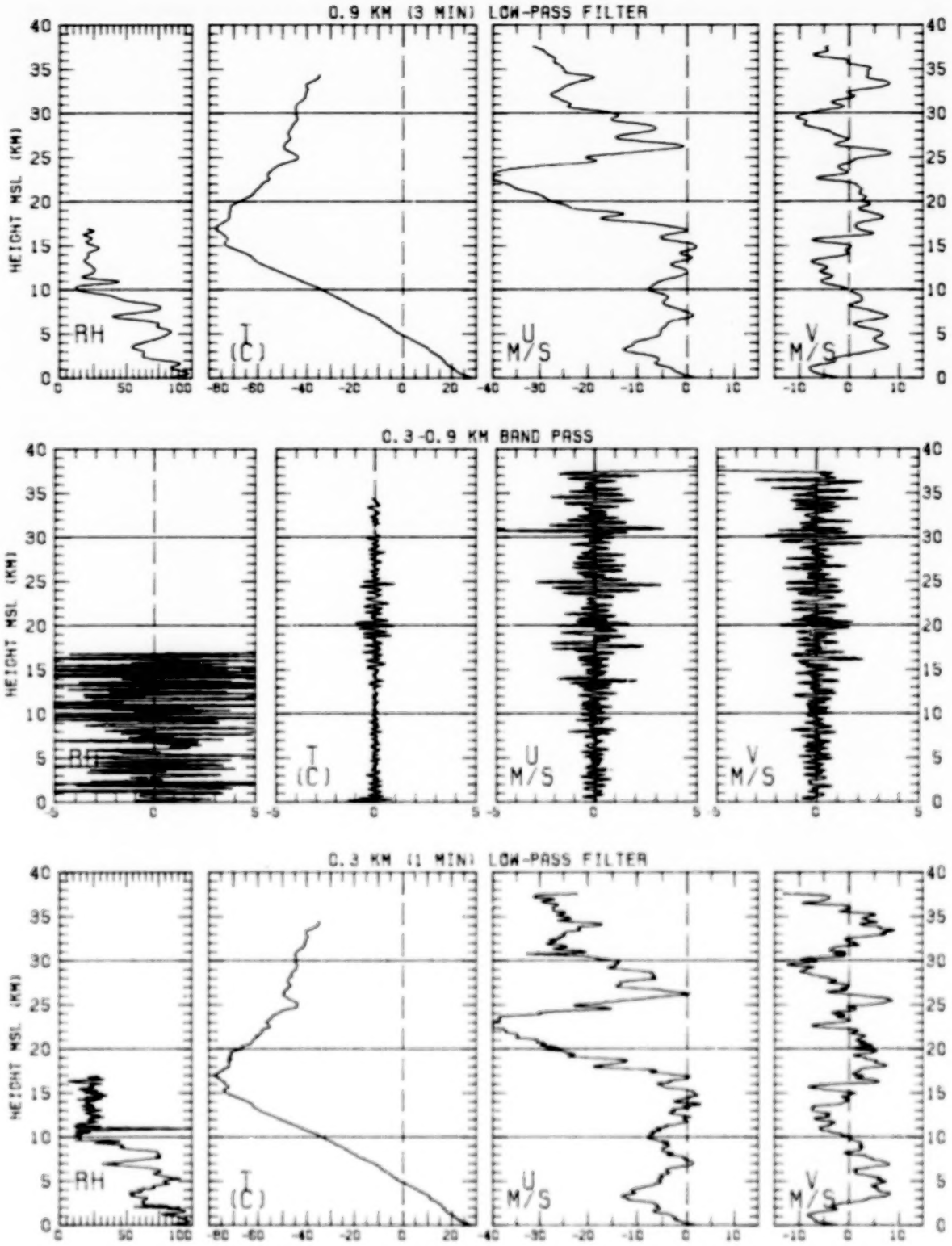
0.9 KM (3 MIN) LOW-PASS FILTER
0.3-0.9 KM BAND PASS
0.3 KM (1 MIN) LOW-PASS FILTER
HEIGHT MSL (KM)
RH
T (C)
U M/S
V M/S

Figure 47

PANAMA 29 JULY 1977 4:26UT

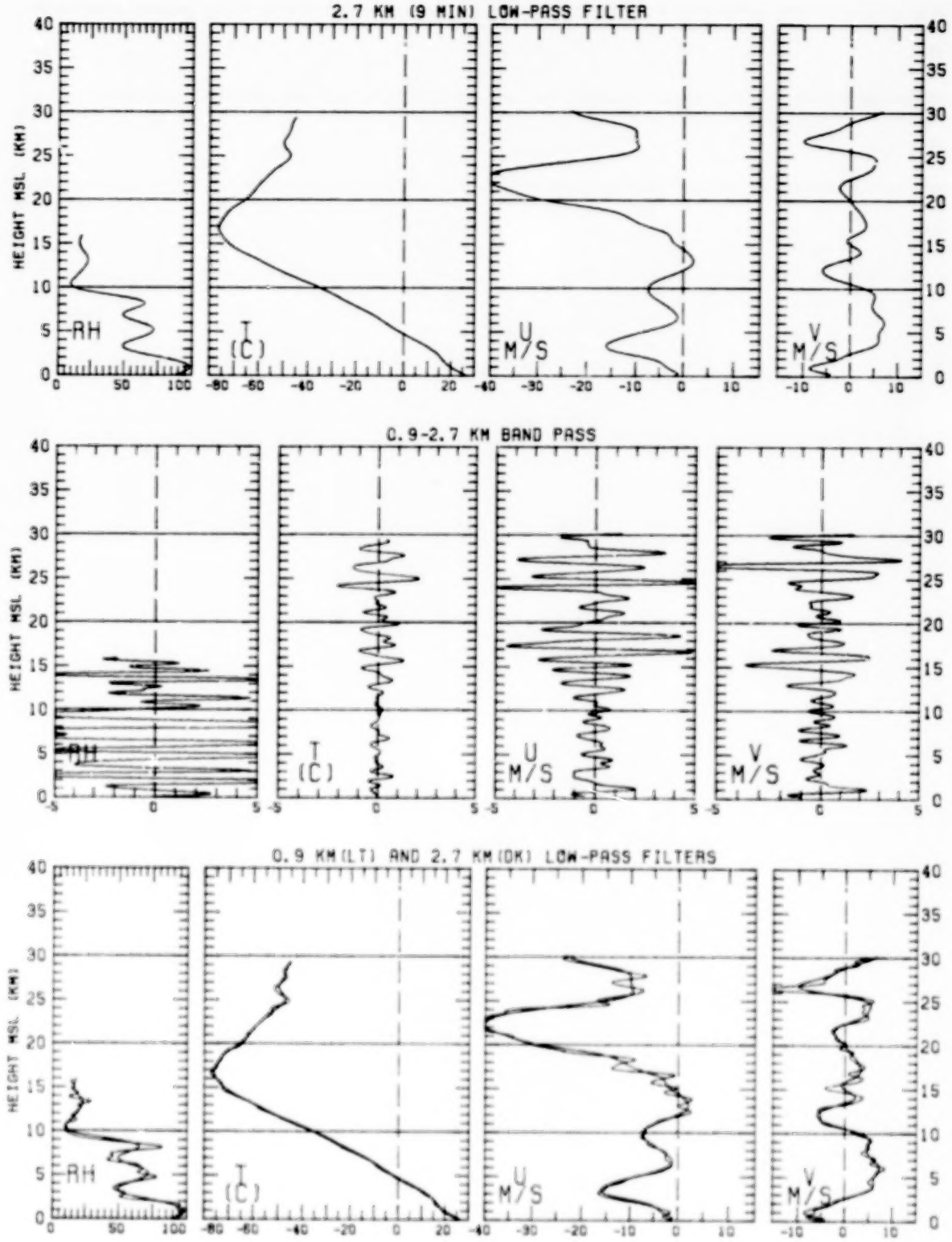

Figure 48

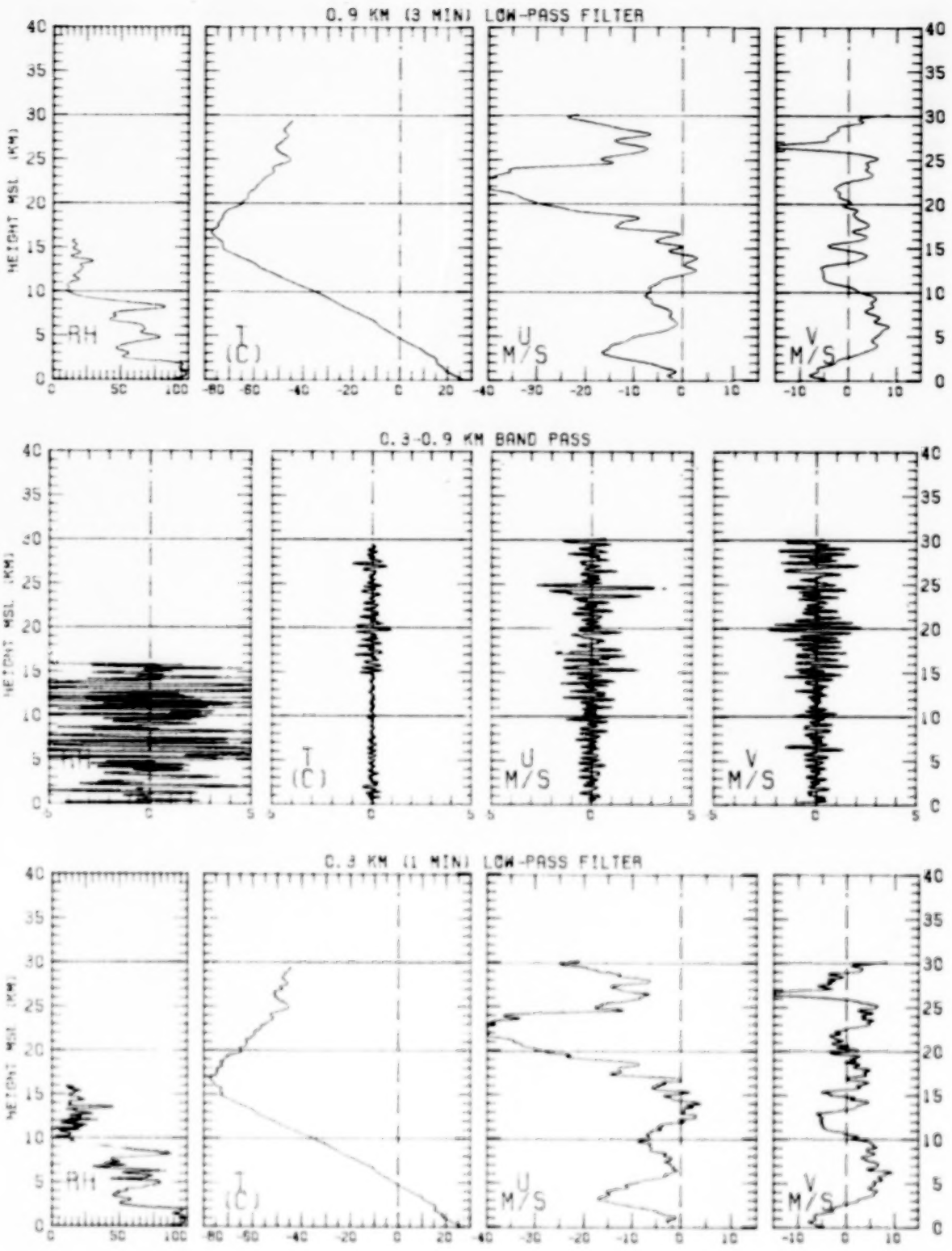
0.9 KM (3 MIN) LOW-PASS FILTER
0.3-0.9 KM BAND PASS
0.3 KM (1 MIN) LOW-PASS FILTER
HEIGHT MSL (KM)
RH
T (C)
U M/S
V M/S

Figure 48

PANAMA 29 JULY 1977 10:40UT

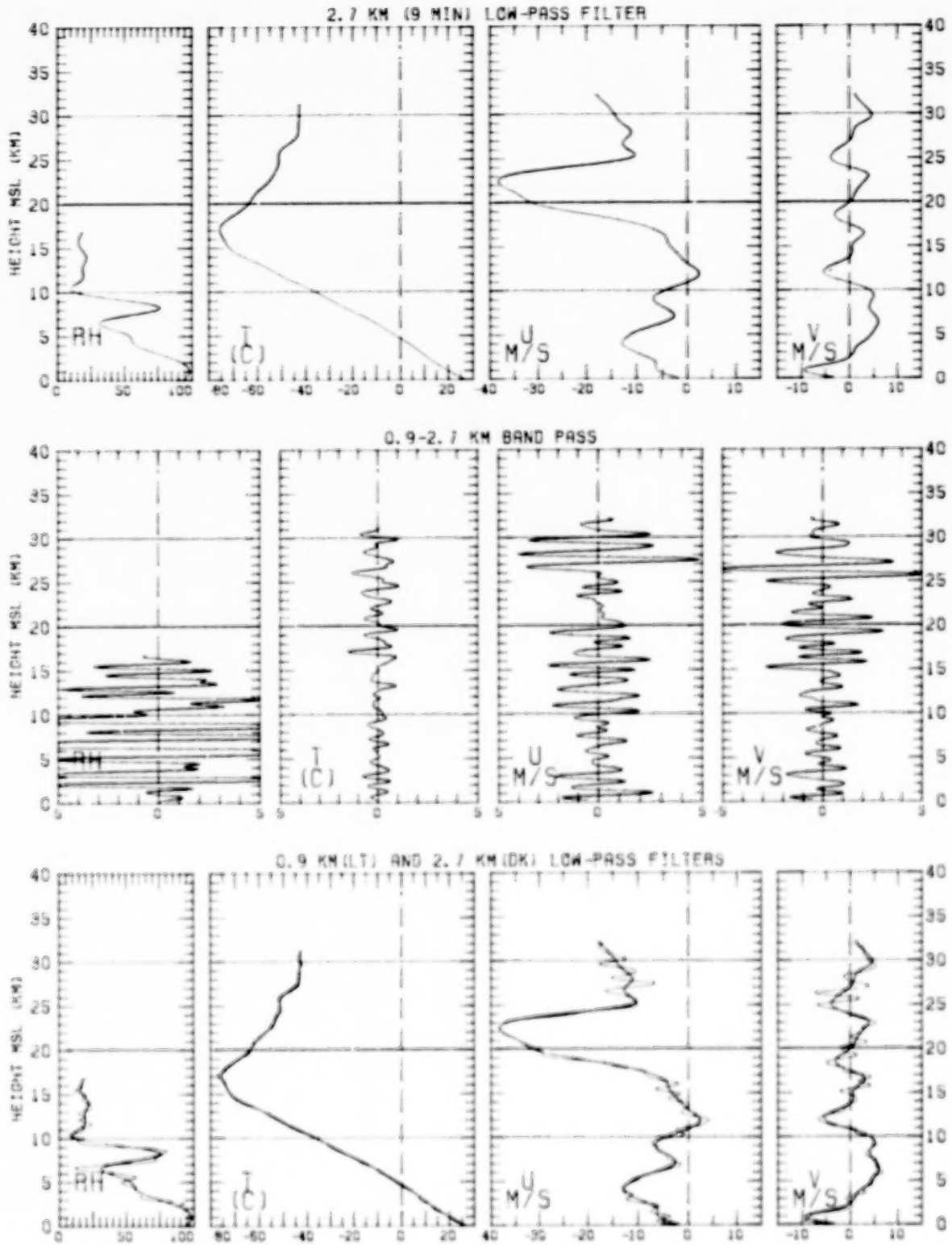

Figure 49

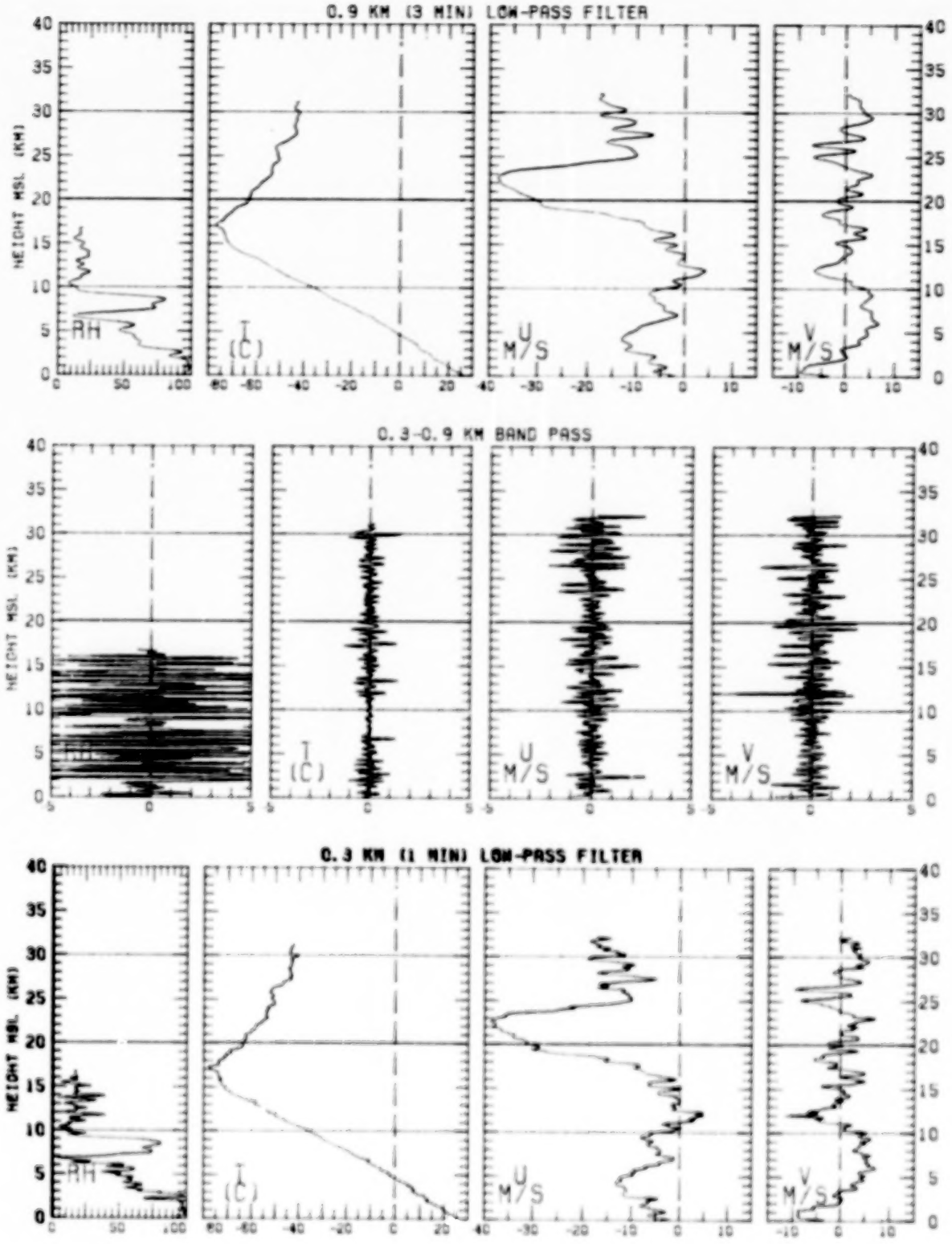
0.9 KM (3 MIN) LOW-PASS FILTER
HEIGHT MSL (KM)
RH
T (C)
U M/S
V M/S
0.3-0.9 KM BAND PASS
HEIGHT MSL (KM)
T (C)
U M/S
V M/S
0.3 KM (1 MIN) LOW-PASS FILTER
HEIGHT MSL (KM)
RH
T (C)
U M/S
V M/S

Figure 49

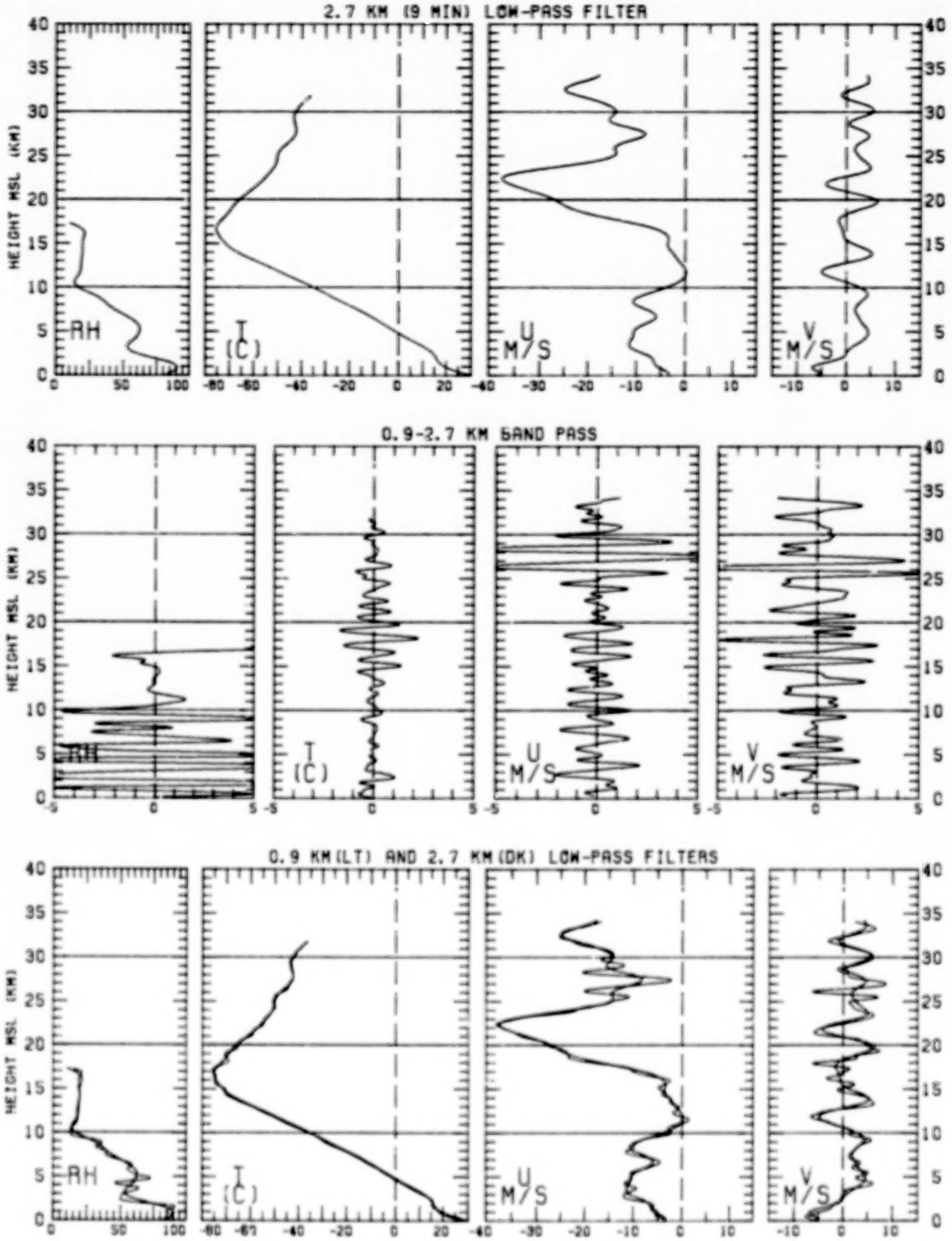
2.7 KM (9 MIN) LOW-PASS FILTER
HEIGHT MSL (KM)
RH
T (C)
U M/S
V M/S
0.9-2.7 KM BAND PASS
0.9 KM(LT) AND 2.7 KM(DK) LOW-PASS FILTERS

Figure 50

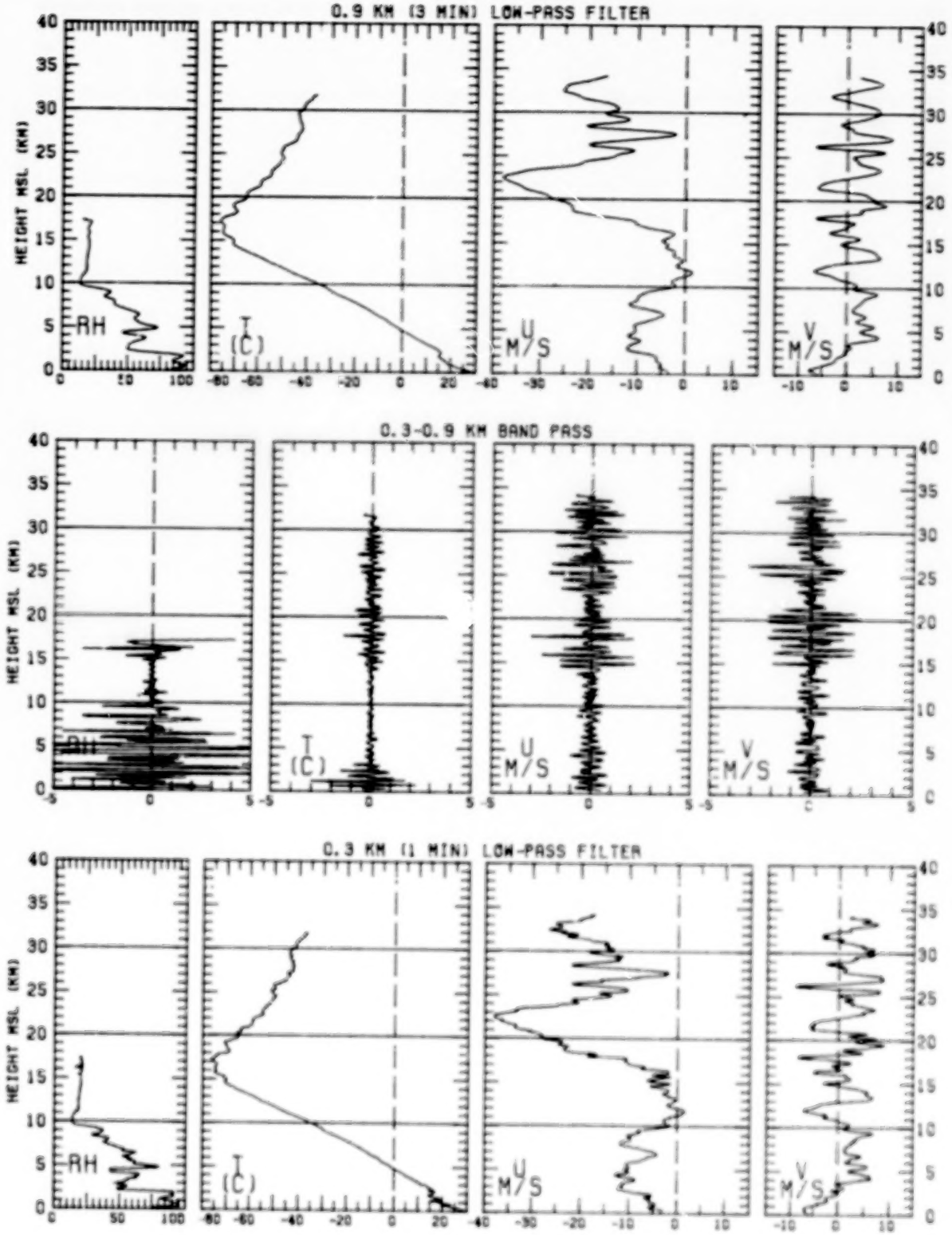
0.9 KM (3 MIN) LOW-PASS FILTER
HEIGHT MSL (KM)
RH
T (C)
U M/S
V M/S
0.3-0.9 KM BAND PASS
0.3 KM (1 MIN) LOW-PASS FILTER

Figure 50

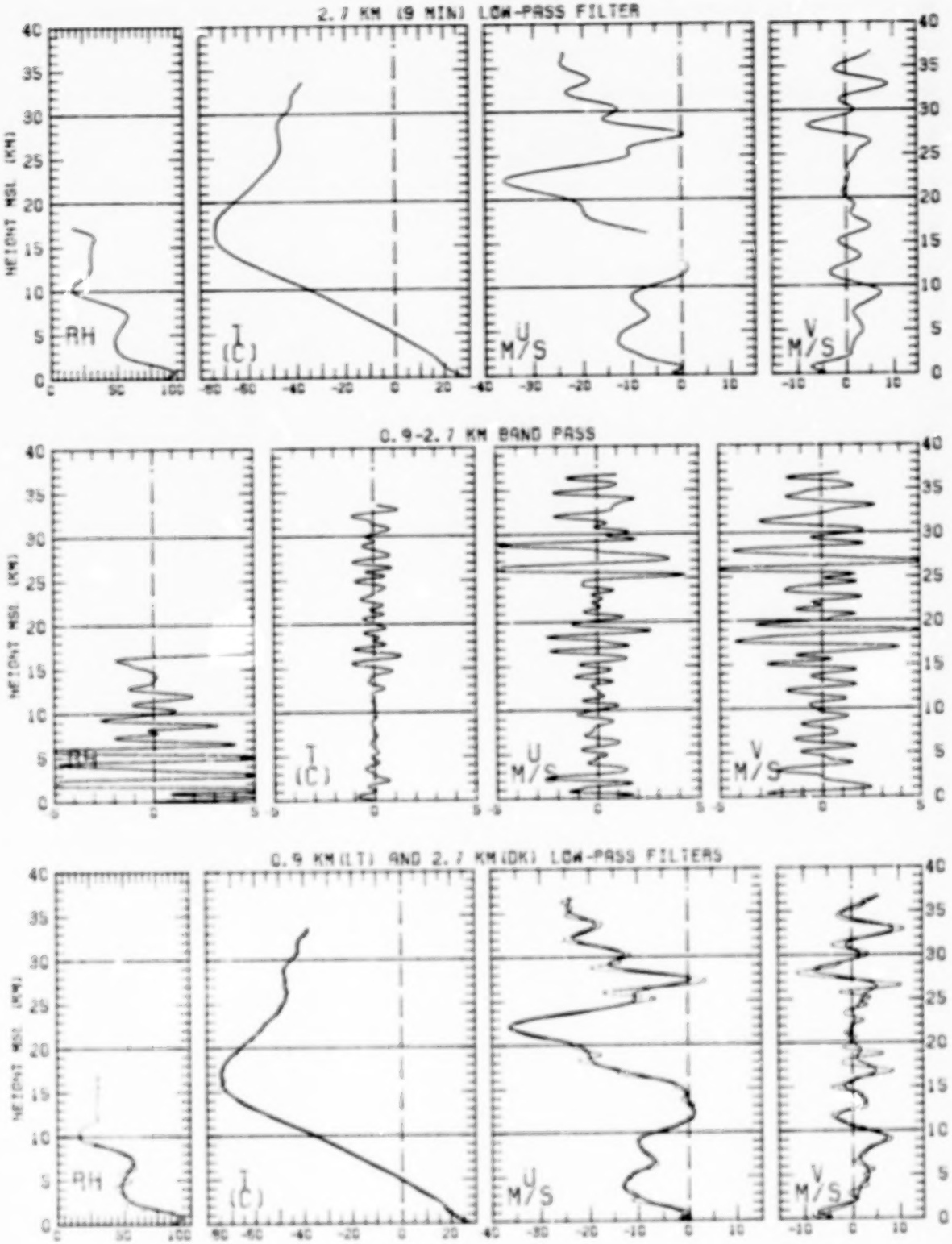
2.7 KM (9 MIN) LOW-PASS FILTER
HEIGHT MSL (KM)
RH
T (C)
U M/S
V M/S
0.9-2.7 KM BAND PASS
0.9 KM(LT) AND 2.7 KM(DK) LOW-PASS FILTERS

Figure 51

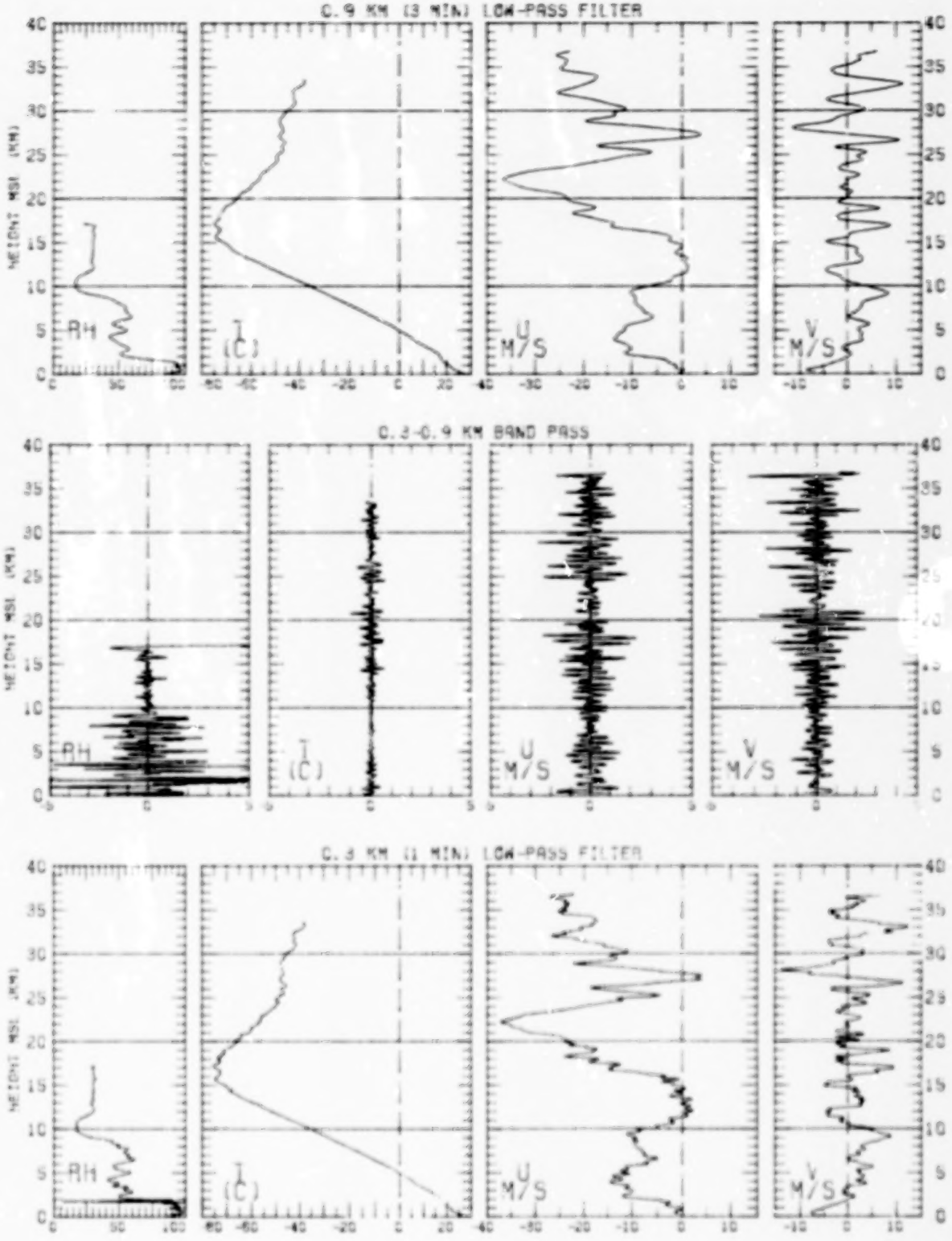
0.9 KM (3 MIN) LOW-PASS FILTER
0.3-0.9 KM BAND PASS
0.3 KM (1 MIN) LOW-PASS FILTER
HEIGHT MSL (KM)
RH
T (C)
U M/S
V M/S

Figure 51

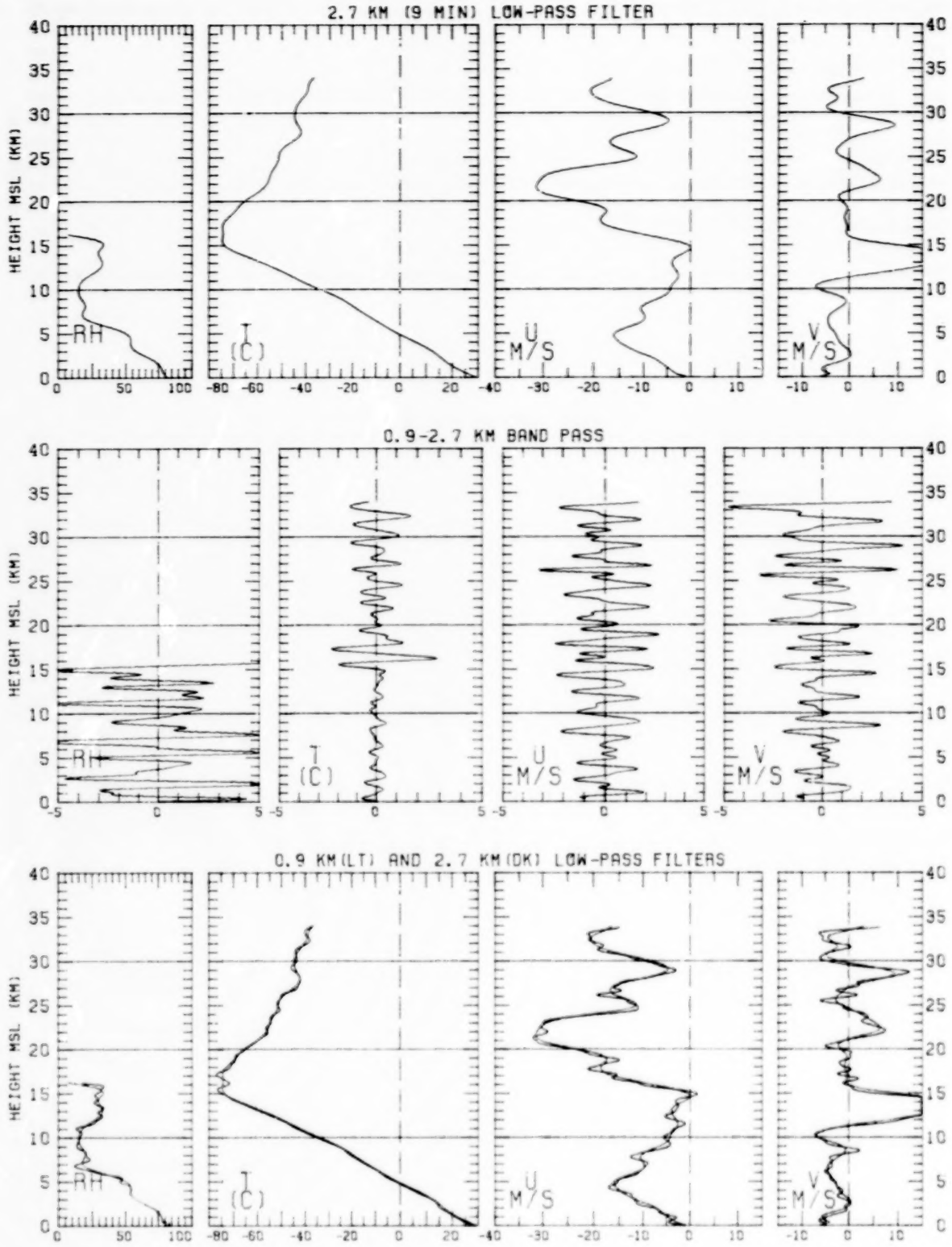
2.7 KM (9 MIN) LOW-PASS FILTER
HEIGHT MSL (KM)
RH
T (C)
U M/S
V M/S
0.9-2.7 KM BAND PASS
0.9 KM(LT) AND 2.7 KM(DK) LOW-PASS FILTERS

Figure 52

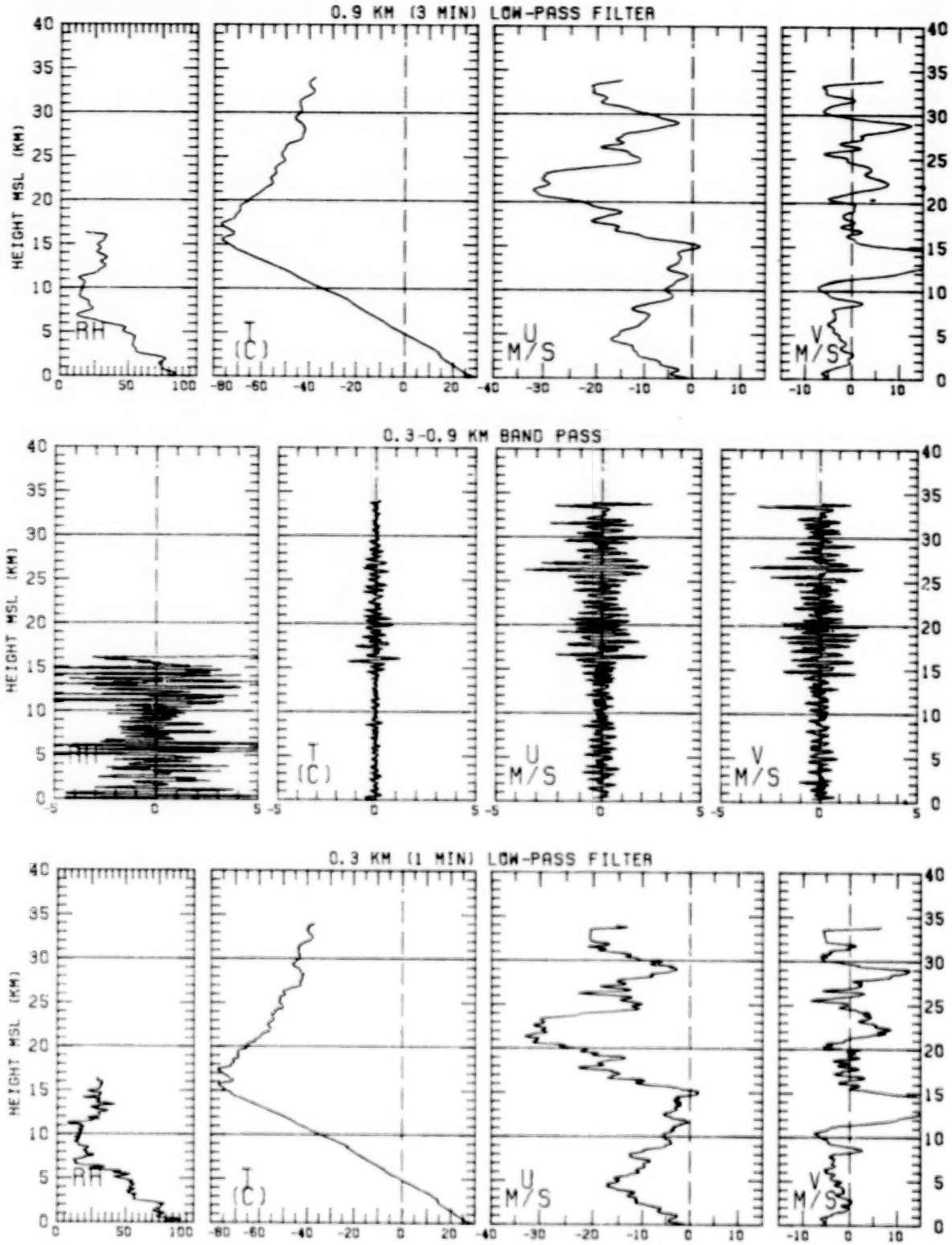
0.9 KM (3 MIN) LOW-PASS FILTER
HEIGHT MSL (KM)
RH
T (C)
U M/S
V M/S
0.3-0.9 KM BAND PASS
0.3 KM (1 MIN) LOW-PASS FILTER

Figure 52

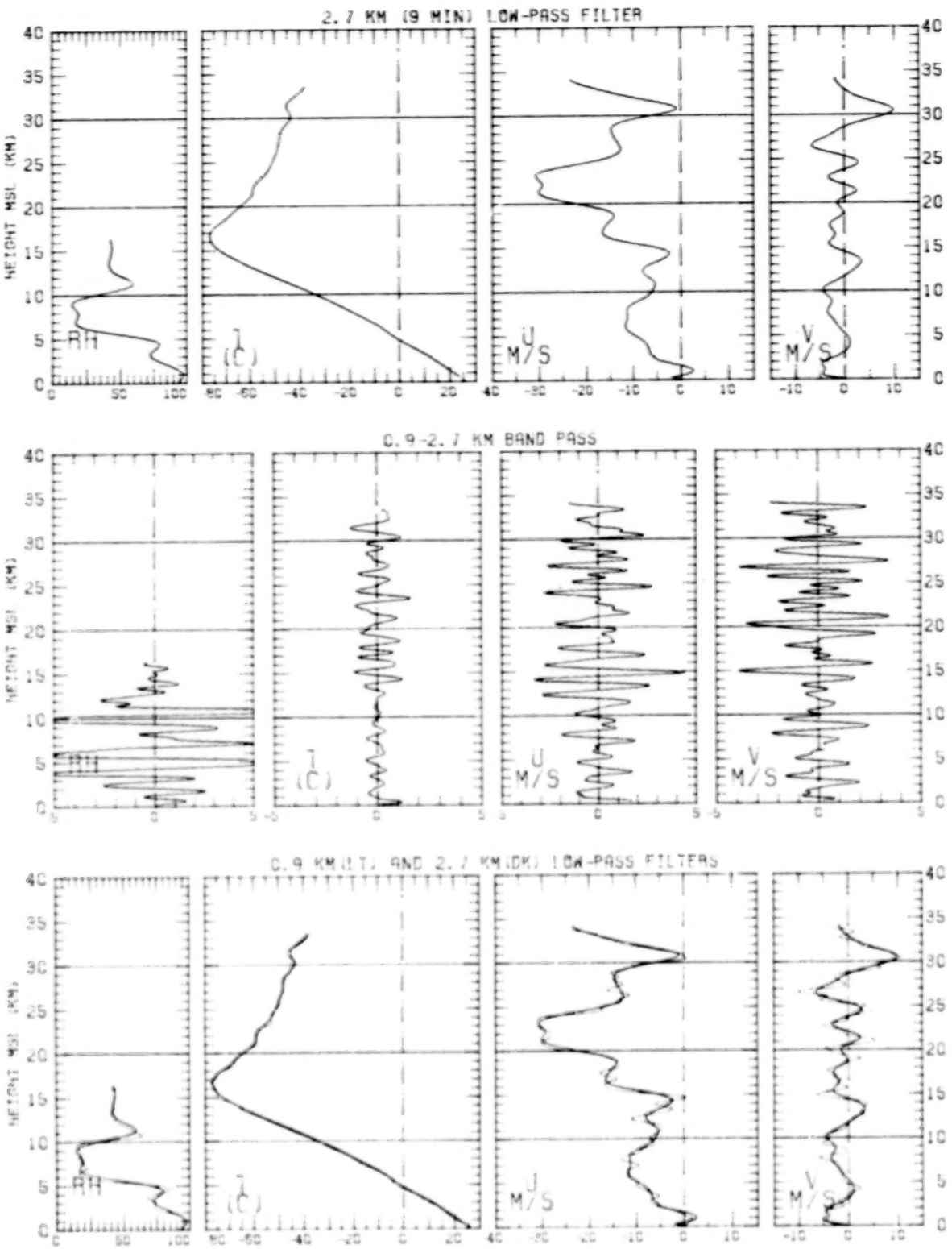
2.7 KM (9 MIN) LOW-PASS FILTER
HEIGHT MSL (KM)
RH
T (C)
U M/S
V M/S
0.9-2.7 KM BAND PASS
0.9 KM (LT) AND 2.7 KM (DK) LOW-PASS FILTERS

Figure 53

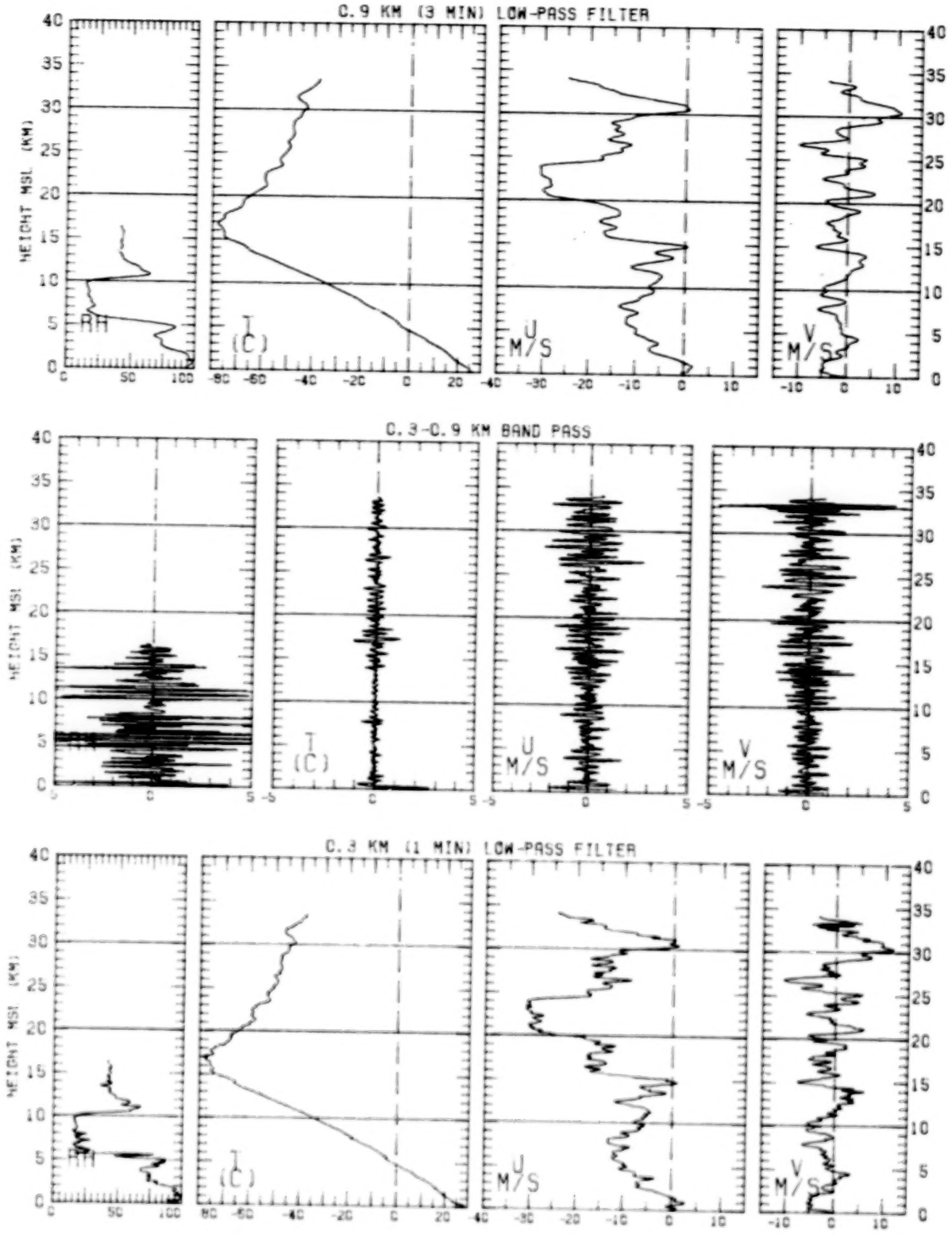
0.9 KM (3 MIN) LOW-PASS FILTER
HEIGHT MSL (KM)
RH
T (C)
U M/S
V M/S
0.3-0.9 KM BAND PASS
HEIGHT MSL (KM)
T (C)
U M/S
V M/S
0.3 KM (1 MIN) LOW-PASS FILTER
HEIGHT MSL (KM)
RH
T (C)
U M/S
V M/S

Figure 53

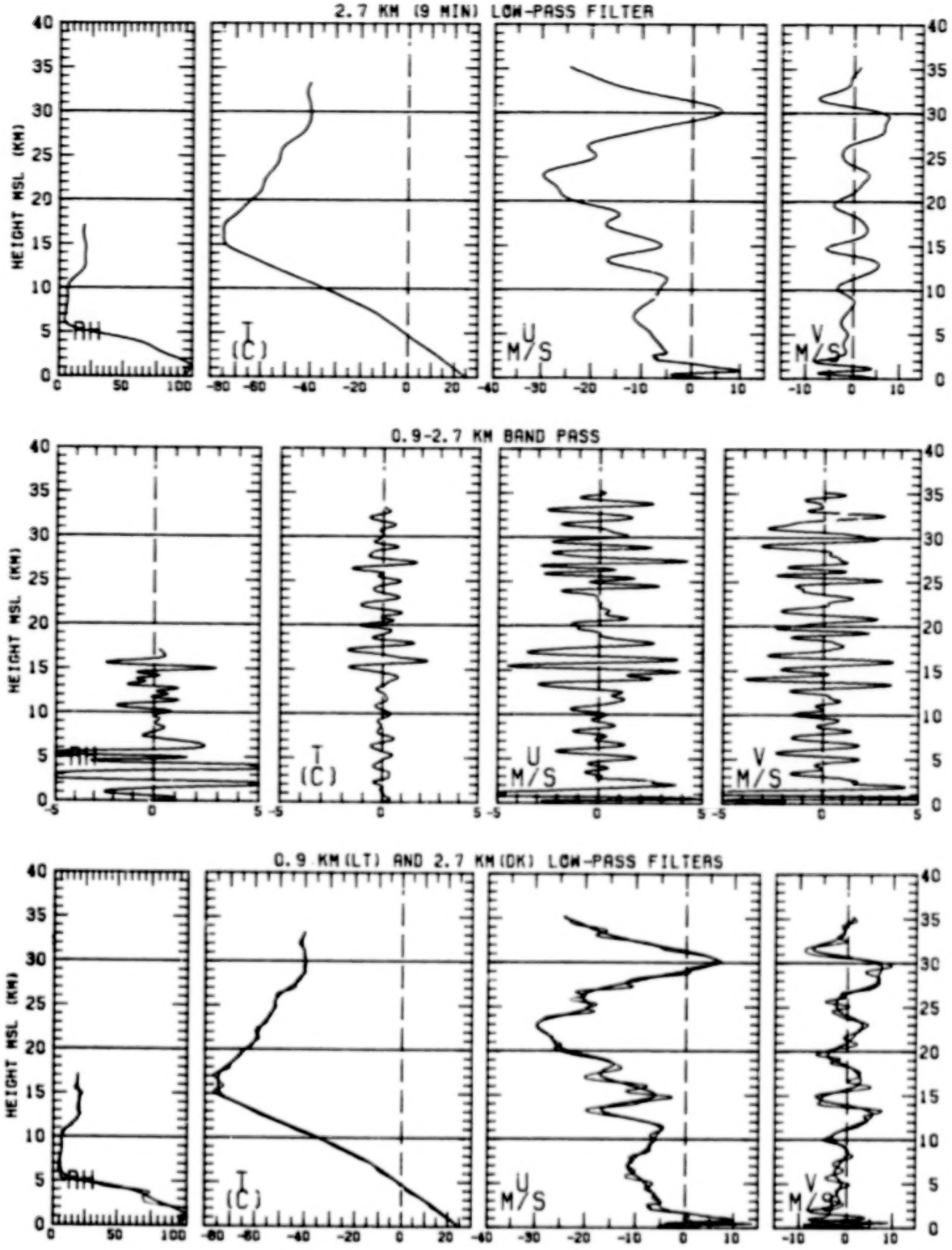
2.7 KM (9 MIN) LOW-PASS FILTER
HEIGHT MSL (KM)
RH
T (C)
U M/S
V M/S
0.9-2.7 KM BAND PASS
0.9 KM(LT) AND 2.7 KM(DK) LOW-PASS FILTERS

Figure 54

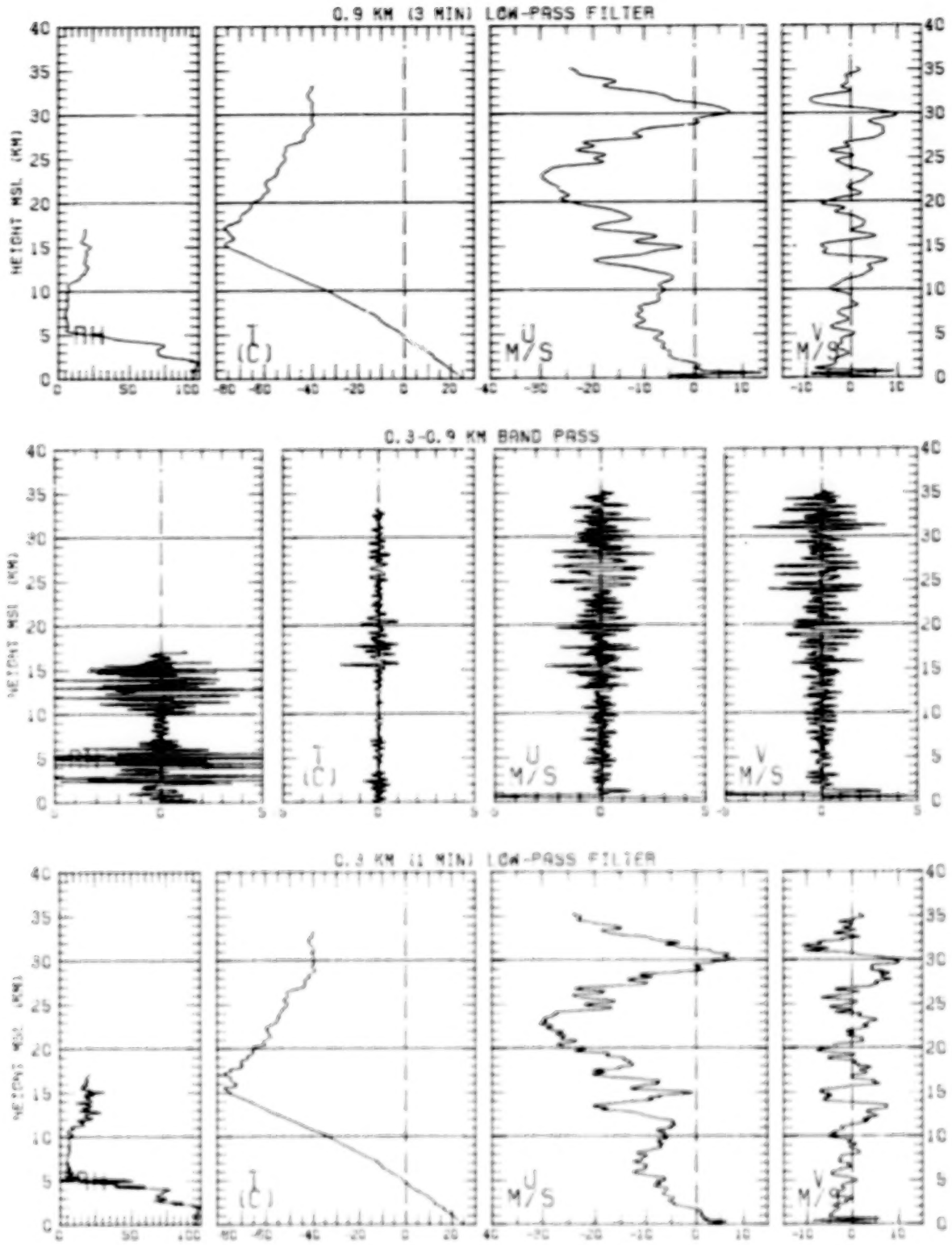
0.9 KM (3 MIN) LOW-PASS FILTER
HEIGHT MSL (KM)
RH
T (C)
U M/S
V M/S
0.3-0.9 KM BAND PASS
0.3 KM (1 MIN) LOW-PASS FILTER

Figure 54

REFERENCES

Danielsen, E. F., 1959: The Laminar Structure of the Atmosphere and Its Relation to the Concept of the Tropopause. Arch. Meterol. Geophys. Biokl., Ser. A, Bd. 11, 293-332

Danielsen, E. F., 1964: Report on Project Springfield. Defense Atomic Support Agency Contract DA-49-XZ-079, DASA 1517, Washington, D. C., 97 pp.

Danielsen, E. F., 1966: Atmospheric Waves of Small Vertical Scale that Affect the Wind and Temperature Profiles. Final Report, Phase II. Analyses of Time Variability of Atmospheric Parameters. NASA Contractor Report CR-61158, George C. Marshall Space Flight Center, 54 pp.

Danielsen, E. F. and R. T. Duquet, 1967: A Comparison of FPS-16 and GMD-1 Measurements of Methods for Processing Wind Data. J. Appl. Meteor., 6, 824-836.

Danielsen, E. F., 1968: Stratospheric-Tropospheric Exchange Based on Radioactivity, Ozone and Potential Vorticity. J. Atmos. Sci., 25, 502-518.

Danielsen, E. F. and R. Bleck, 1970: Tropospheric and Stratospheric Ducting of Stationary Mountain Lee Waves. J. Atmos. Sci., 27, 758-772.

Danielsen, E. F. and D. Deaven, 1974: Northern Hemispheric Analysis Methods for Deriving Two-Dimensional Transport Model From Isentropic Trajectories and Potential Vorticity. Proceedings of the International Conference on Structure, Composition and General Circulation of the Upper and Lower Stratosphere, Vol. II, Melbourne, Australia, 835-848.

Danielsen, E. F. and J. F. Louis, 1977: Transport in the Stratosphere, in Studies in Geophysics, The Upper Atmosphere and Magnetosphere. National Academy of Sciences, Washington, D.C., 141-155.

Louis, J. F., 1974: A Two-Dimensional Transport Model of the Atmosphere. Ph. D. Thesis, Dept. of Astrogeophysics, Univ. of Colorado, Boulder, Colorado.

Mahlman, J. D., 1965: Relation of Stratospheric-Tropospheric Mass Exchange Mechanisms to Surface Radioactivity Tests. Arch. Meterol. Geophys. Biokl., A, Bd. 15, 1-19.

Mahlman, J. D. and W. J. Moxim, 1978: Tracer Simulation Using a Global General Circulation Model: Results from a Midlatitude Instantaneous Source Experiment. J. Atmos. Sci., 35, 1340-1374.

Reiter, E. R., 1963: A Case Study of Radioactive Fallout. J. Appl. Meteor., 2(6), 691-705.

Reiter, E. R. and J. D. Mahlman, 1965: Heavy Radioactivity Fallout Over the Southern United States, November 1962. J. Geophys. Res., 70, 4501-4520.

Schmidlin, F. J. and G. Kloos, 1978: Balloon-Borne Ozonesonde and Rocket Temperature and Wind Data Gathered During the ITCZ Experiment - July 16-31, 1977. Internal NASA Report, NASA Wallops Flight Center.

Wallace, J. M. and V. E. Kousky, 1968: Observational Evidence of Kelvin Waves in the Tropical Stratosphere. J. Atmos. Sci., 25, 900-907.

Wallace, J. M., 1973: General Circulation of the Tropical Lower Stratosphere. Rev. Geophys. Space Phys., 11, 191-222.

1. Report No.	2. Government Accession No.	3. Recipient's Catalog No.
NASA CR-3269		

4. Title and Subtitle	5. Report Date
High Resolution Vertical Profiles of Wind, Temperature and Humidity Obtained by Computer Processing and Digital Filtering of Radiosonde and Radar Tracking Data From the ITCZ Experiment of 1977	April 1980
	6. Performing Organization Code
7. Author(s)	8. Performing Organization Report No.
Edwin F. Danielsen, R. Stephen Hipskind, and Steven E. Gaines	
9. Performing Organization Name and Address	10. Work Unit No.
Beam Engineering, Inc. Sunnyvale, CA	11. Contract or Grant No. NAS2-10023
12. Sponsoring Agency Name and Address	13. Type of Report and Period Covered
National Aeronautics and Space Administration Washington, D. C. 20546	Contractor Report
	14. Sponsoring Agency Code

15. Supplementary Notes

Ames Technical Monitor: William Page — Final Report

Edwin F. Danielsen: Beam Engineering, Inc.

R. Stephen Hipskind: Air Resources Center, Oregon State University, Corvallis, Oregon

Steven E. Gaines: San Jose State University, San Jose, California

16. Abstract

Results are presented from computer processing and digital filtering of radiosonde and radar tracking data obtained during the ITCZ experiment of July 1977 when coordinated measurements were taken daily over a 16-day period when the ITCZ moved across the Panama Canal Zone (NASA TM-78577). This report deals specifically with temperature, relative humidity, and wind velocity profiles. The wind velocities are derived directly from special radar tracking data which eliminate the major sources of errors that limit accuracy of the conventional rawinsonde system.

17. Key Words (Suggested by Author(s))	18. Distribution Statement
Intertropical Convergence Zone, Stratosphere, Troposphere-Stratosphere Exchange, Meteorology, Atmospheric Physics, Temperature, Relative Humidity, Wind Velocity Profile	Unclassified - Unlimited Star Category - 47

19. Security Classif. (of this report)	20. Security Classif. (of this page)	21. No. of Pages	22. Price*
Unclassified	Unclassified	116	$6.50

*For sale by the National Technical Information Service, Springfield, Virginia 22161

NASA-Langley, 1980

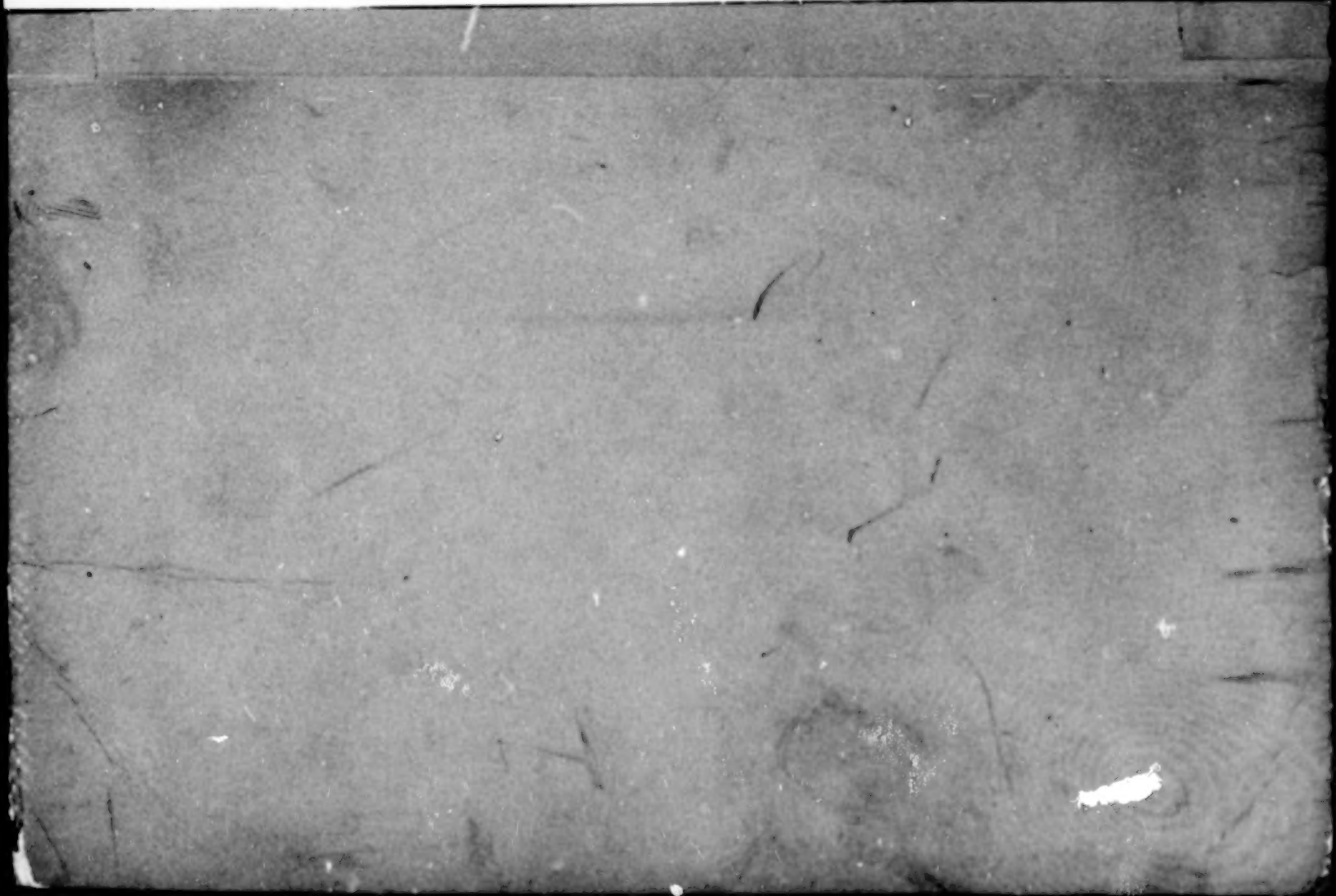

END

June 30, 1981